E-18-622

AFWAL-TR-82-1089

LOW VOLTAGE FIELD EMITTER ARRAYS

Georgia Institute of Technology
Schools of Ceramic and Electrical Engineering
Atlanta, Georgia 30332

July 1982

Final Report for Period 1 July 1979 to 30 June 1981

AVIONICS LABORATORY
AIR FORCE WRIGHT AERONAUTICAL LABORATORIES
AIR FORCE SYSTEMS COMMAND
WRIGHT-PATTERSON AFB, OHIO 45433

NOTICE

When Government drawings, specifications, or other data are used for any purpose other than in connection with a definitely related Government procurement operation, the United States Government thereby incurs no responsibility nor any obligation whatsoever; and the fact that the government may have formulated, furnished, or in any way supplied the said drawings, specifications, or other data, is not to be regarded by implication or otherwise as in any manner licensing the holder or any other person or corporation, or conveying any rights or permission to manufacture, use, or sell any patented invention that may in any way be related thereto.

This technical report has been reviewed and is approved for publication.

Raymond J. Bruns

RAYMOND J. BRUNS, Proj Engr
Microwave Devices Group
Electronic Technology Division
Avionics Laboratory

Richard L Remski

RICHARD L. REMSKI, Chief
Microwave Devices Group
Electronic Technology Division
Avionics Laboratory

53 25

FOR THE COMMANDER:

Donald S Rees

DONALD S. REES, Chief
Microwave Technology Branch
Avionics Laboratory

"If your address has changed, if you wish to be removed from our mailing list, or if the addressee is no longer employed by your organization please notify AFWAL/AADM-1, W-P AFB, OH 45433 to help maintain a current mailing list".

Copies of this report should not be returned unless return is required by security considerations, contractual obligations, or notice on a specific document.

Unclassified

SECURITY CLASSIFICATION OF THIS PAGE *(When Data Entered)*

REPORT DOCUMENTATION PAGE		READ INSTRUCTIONS BEFORE COMPLETING FORM
1. REPORT NUMBER AFWAL-TR-82-1089	2. GOVT ACCESSION NO. B-071-169-L	3. RECIPIENT'S CATALOG NUMBER
4. TITLE *(and Subtitle)* Low Voltage Field Emitter Arrays		5. TYPE OF REPORT & PERIOD COVERED Final Report for Period 1 July 1979 to 30 June 1981 6. PERFORMING ORG. REPORT NUMBER
7. AUTHOR(s) J. K. Cochran, A. T. Chapman, R. K. Feeney, D. N. Hill, K. J. Lee, R. D. Jones, R. V. Kolarik, K. H. Moh, J. P. Price		8. CONTRACT OR GRANT NUMBER(s) F33615-79-C-1832
9. PERFORMING ORGANIZATION NAME AND ADDRESS Georgia Institute of Technology Schools of Ceramic and Electrical Engineering Atlanta, Georgia 30332		10. PROGRAM ELEMENT, PROJECT, TASK AREA & WORK UNIT NUMBERS 2002 02 76
11. CONTROLLING OFFICE NAME AND ADDRESS Avionics Laboratory (AFWAL/AADM) AF Wright Aeronautical Laboratories, AFSC Wright-Patterson Air Force Base, Ohio 45433		12. REPORT DATE July 1982 13. NUMBER OF PAGES 226
14. MONITORING AGENCY NAME & ADDRESS*(if different from Controlling Office)*		15. SECURITY CLASS. *(of this report)* Unclassified 15a. DECLASSIFICATION/DOWNGRADING SCHEDULE

16. DISTRIBUTION STATEMENT *(of this Report)*

Distribution limited to U.S. Gov't agencies only; test and evaluation; July 1982. Other requests for this document must be referred to Air Force Wright Aeronautical Laboratories (AFWAL/AADM), Wright-Patterson Air Force Base, Ohio 45433.

17. DISTRIBUTION STATEMENT *(of the abstract entered in Block 20, if different from Report)*

18. SUPPLEMENTARY NOTES

19. KEY WORDS *(Continue on reverse side if necessary and identify by block number)*

Cathode, Field Emitter Arrays, Field Emission, Low Voltage, Thin Film, Tungsten Fiber Arrays, Unidirectional Solidified UO_2-W Composite, In situ Composite, Zirconia-Tungsten Composite.

20. ABSTRACT *(Continue on reverse side if necessary and identify by block number)*

The purpose of this contract was to characterize and optimize low voltage field emitter (LVFE) cathodes. LVFE arrays are fabricated using oxide matrix-tungsten fiber unidirectionally solidified, eutectic composites as a substrate. The composites consist of 10^7 single crystal tungsten fibers per cm^2 of oxide matrix. The fibers are continuous and parallel. After the composite has been processed to produce W fibers exposed above the oxide matrix, a thin film insulating layer is vapor deposited on the oxide matrix. Over the insulating layer

DD FORM 1 JAN 73 1473 EDITION OF 1 NOV 65 IS OBSOLETE

Unclassified

SECURITY CLASSIFICATION OF THIS PAGE *(When Data Entered)*

is deposited a metal layer (an extractor grid) and the process produces micron sized holes in the extractor grid which are concentric with the fiber tips. By having the extractor grid at the same height as the fiber tip and the tip at the center of micron sized holes, sufficient field gradients are produced with 100-200 volts grid bias to produce field emission from the fiber tip.

These field effect cathodes were optimized by three main thrusts: improving of LVFE structure, emission testing of the field emitters, and improvement of the oxide-metal composite growth process. An improved emitter structure was fabricated by providing better control of the vapor deposition process, changing the insulator material to a higher resistivity material, developing new post deposition techniques, and upgrading the composite etching. As a result, for UO_2-W leakage currents were reduced but remained a problem. Emission testing demonstrated 100 mA peak current pulsed (20 A/cm^2) and 0.94 A/cm^2 (2 mA) CW for UO_2-W LVFE's. Computer simulations of field potential aided in optimizing the structure. Improving the UO_2-W composite was attacked by installing a 50 kw composite growth facility to provide larger boule size. Increasing boule size resulted in poorer growth quality of the UO_2-W composite but with the higher power level, yttria stabilized zirconia matrix-tungsten fiber composites (ZYW) of good fiber quality were produced.

The zirconia-tungsten composite provided an insulating matrix as compared to the UO_2 semiconducting matrix. By changing the composite base to ZYW, leakage selected in LVFE's was substantially reduced to the point of elimination in the same samples. ZYW LVFE's were emission tested CW and produced 1-5 A/cm^2 for 200 μm diameter active areas. With improvements, emission levels should be advanced to even higher current densities.

FOREWORD

The Schools of Ceramic and Electrical Engineering of the Georgia Institute of Technology, Atlanta, Georgia, prepared this final report on Low Voltage Field Emitter Arrays. This is the Final Technical Report for Contract F33615-79-C-1832 covering the period 1 July 1979 to 30 June 1981.

The program was sponsored by the U.S. Air Force Microwave Device Group, Wright-Patternson Air Force Base, Ohio, and was monitored by Mr. Raymond J. Bruns. Dr. J. K. Cochran was the project director with co-principle investigators Dr. A. T. Chapman, Dr. R. K. Feeney, and Dr. D. N. Hill. Graduate students contributing to the project were K. J. Lee, R. D. Jones, R. V. Kolarik, K. H. Moh, and J. P. Price.

Dr. Cochran was responsible for overall fabrication of the LVFE devices with R. V. Kolarik providing the investigations in the area of electrical properties of thin film Al_2O_3, K. H. Moh studying etching characteristics of ZrO_2-W composites, and K. J. Lee contributing in etching of UO_2-W and electropolishing of the molybdenum extractor. Dr. Hill was responsible for emission testing of all the LVFE devices. Dr. Feeney provided calculations showing effects of LVFE geometry and space charge on emission and R. D. Jones provided circuit model considerations. Dr. Chapman and J. P. Price conducted investigations in unidirectional solidification of UO_2-W and ZYW composites.

TABLE OF CONTENTS

TABLE OF CONTENTS

LIST OF ILLUSTRATIONS

LIST OF ILLUSTRATIONS

LIST OF ILLUSTRATIONS

LIST OF ILLUSTRATIONS

LIST OF ILLUSTRATIONS

LIST OF ILLUSTRATIONS

LIST OF TABLES

SUMMARY

Low voltage field emitter array cathodes have the potential of supplying needed improvements in microwave tube technology. If the potential for this type of cathode is realized, it could solve many impending cathode requirements which are not expected to be satisfied by conventional thermionic cathodes.

The low voltage field emitter is fabricated using oxide matrix tungsten fiber unidirectionally solidified composites as a substrate. In cross-section, these composites are composed of 5-15 million, ∿0.5 μm diameter, single crystal tungsten fibers per square centimeter of oxide matrix. The fibers are continuous and parallel, and etches are available to expose the W fibers above the oxide matrix. Each exposed fiber provides a field effect electron gun in the fabrication process. Each electron gun consists of an extractor electrode supported on the oxide matrix by a thin film insulator and located about one micron from the tip of the tungsten fiber. Since the spacing is so close, electron emission is obtained from the tungsten fiber at a potential of approximately one hundred volts. The emission from a single tungsten fiber is in the microampere range. However, since the fiber density is in the range of ten million per square centimeter, the emission current potential is high.

Prior to the start of this contract, low voltage field emitters based on UO_2-W composites had demonstrated emission currents of 31 A/cm^2 in a pulsed mode with a gross peak current of 22 mA. The main impediment to this device was the poor electrical quality of the vapor deposited SiO_2 insulator. At operational voltage of 100 to 200 volts, leakage currents through the insulator of 2 to 20 mA were typical which precluded dc operation or even pulsed operation at a 1% duty cycle. Thus, the objective of this program was to characterize and

optimize field emission from UO_2-W low voltage field emitter (LVFE) arrays. This effort had three main thrusts: improvement of the LVFE structure, emission testing of the field emitters, and improvement of the UO_2-W composite growth process.

An improved emitter structure was fabricated by changing the insulator material to a higher resistivity material, developing new post deposition cleaning techniques, and upgrading the composite etching process. Addition of a microprocessor to the vapor deposition equipment enabled controlled deposition of thin film oxides at rates of 0.2 to 2.0 nm/sec ±20%. Aluminum oxide, Al_2O_3, was substituted for SiO_2 as the insulator which increased the bulk resistivity of the insulator four orders of magnitude. Phosphoric acid etching was successful in cleaning Al_2O_3 deposits from the W fibers and controllably dissolving the Al_2O_3 films to allow recessing of the insulator under the Mo extractor. Protrusions and rough surfaces on the Mo extractor were found to be removable by electropolishing in sulfuric acid. Finally, the UO_2-W etching process was improved by constructing a new etching facility which provided more laminar flow for the etch. This produced smoother UO_2 surfaces for thin film deposition. As a result of the combination of these improvements, one UO_2-W sample was tested with leakage current reduced to $\sim$10 μA at 120 volts in dc operation.

Emission testing for UO_2-W LVFE's was in pulsed mode for most samples, but with improvements in the insulator, a few samples were tested dc. Pulse testing of larger arrays increased demonstrated peak emission to 100 mA at 220 volts (20 A/cm^2). Also, with reduced leakage currents, a dc current density of 0.94 A/cm^2 at 125 volts was measured.

Computer predictions of field potentials and emission levels based on the LVFE geometry were utilized in guiding optimization of the structure. The most significant result was the prediction that positioning the W fiber tip below the extractor significantly reduces field potentials and emission. Emission testing tended to confirm the necessity of having the emitter tip at the level of or above the extractor.

Attempts were made to improve UO_2-W composite growth by increasing the unidirectionally solidified boule size. To increase boule size, a larger power (50 kw) growth facility was installed. Unfortunately, with increased boule size, lack of stoichiometric control of UO_{2+x} in the liquid caused the quality of fiber growth to vary to the extent that only six to eight samples/boule could be obtained. However, with the increased power, it was possible to grow 32 mm diameter yttria stabilized zirconia-tungsten composites (ZYW). Overall, the growth of ZYW compared to UO_2-W was more uniform, fiber continuity better, and growth more controllable.

Most emission failures for the UO_2-W LVFE were the result of high leakage currents through the electron beam evaporated Al_2O_3 insulator, resulting in ohmic heating of the insulator and shorting of the extractor of the UO_2 base. To solve this problem, the composite base used for the LVFE was switched from UO_2-W to ZYW. In the UO_2-W composite system, the UO_2 matrix is a semiconductor with a resistivity of 10^3 Ωcm. In the ZYW composite, the yttria stabilized ZrO_2 matrix is an insulator with the resistivity of 10^{14} Ωcm. Emission testing of the ZYW LVFE's resulted in leakage currents that were substantially reduced.

As a result of availability of good ZYW composites and the advantages of the insulating matrix, the last seven months of the contract were devoted to

fabricating and emission testing LVFE's employing ZYW composites as a substrate. Consequently, a number of changes were necessary for the fabrication of the LVFE, including developing new etchants to expose and point the W fibers. Emission testing for the first time was exclusively dc with emission current densities in the 1-5 A/cm^2 range and leakage in the μA range.

CHAPTER I

INTRODUCTION

Low voltage field emitter arrays have the potential of supplying needed improvements in microwave tube technology. In order to obtain desired operation at required power levels in the millimeter wave frequency range, current density requirements exceed the capability of conventional cathodes. Present practice compensates for the lack of available current density by increasing beam convergence. However, increased beam convergence leads to gun tolerance and alignment problems, and increased beam interception. Low voltage field emitter arrays have demonstrated a high probability of providing tens of amperes per square centimeter at reasonable values of applied voltage. These cathodes operate at ambient temperature, thus eliminating electron gun thermal stress problems and providing emission current immediately on application of electrode voltage.

If the potential for this type of cathode is realized, it could solve many impending cathode requirements which are not expected to be satisfied by conventional thermionic cathodes. In millimeter wave designs, scaling requires the cathode current density to increase with the square of the design frequency. Since present I-J band tube designs already require the maximum current density consistent with acceptable life, the only alternative to new cathode capabilities is to increase beam convergence in millimeter wave gun designs. Ambient temperature operation also offers the advantage of reduced thermal stress on metal-

ceramic bonds and seals in the gun. This will be expecially important because of the small dimensions involved in millimeter wave tubes. In addition, the field emitter array offers instant current upon application of voltage to the extractor, a feature of significance in short warm-up situations.

The low voltage field emitter[1] until now has been fabricated using UO_2-W unidirectionally solidified composites as a substrate. In cross-section, these composites are composed of 5-15 million, 0.5 μm diameter, single crystal tungsten fibers per square centimeter of UO_2 matrix. The fibers are continuous and parallel, and etches are available to expose the W fibers above the UO_2 matrix. Each exposed fiber provides a field effect electron gun in the fabrication process. Each electron gun, Figure I-1, consists of an extractor electrode located about one micron from the tip of a 0.5 micron diameter single crystal tungsten fiber. Since the spacing is so close, electron emission is obtained from the tungsten fiber at approximately one hundred volts potential. The emission from a single tungsten fiber is in the microampere range. However, since the fiber density is in the range of ten million per square centimeter, the emission current potential is high.

The objective of this program was to characterize and optimize field emission from UO_2-W low voltage field emitter (LVFE) arrays. This effort had three main thrusts: improvement of the LVFE structure, emission testing of the field emitters, and improvement of the UO_2-W crystal growth process. The emitter structure was improved by improving the vapor deposition process, changing the insulator material to a higher resisti-

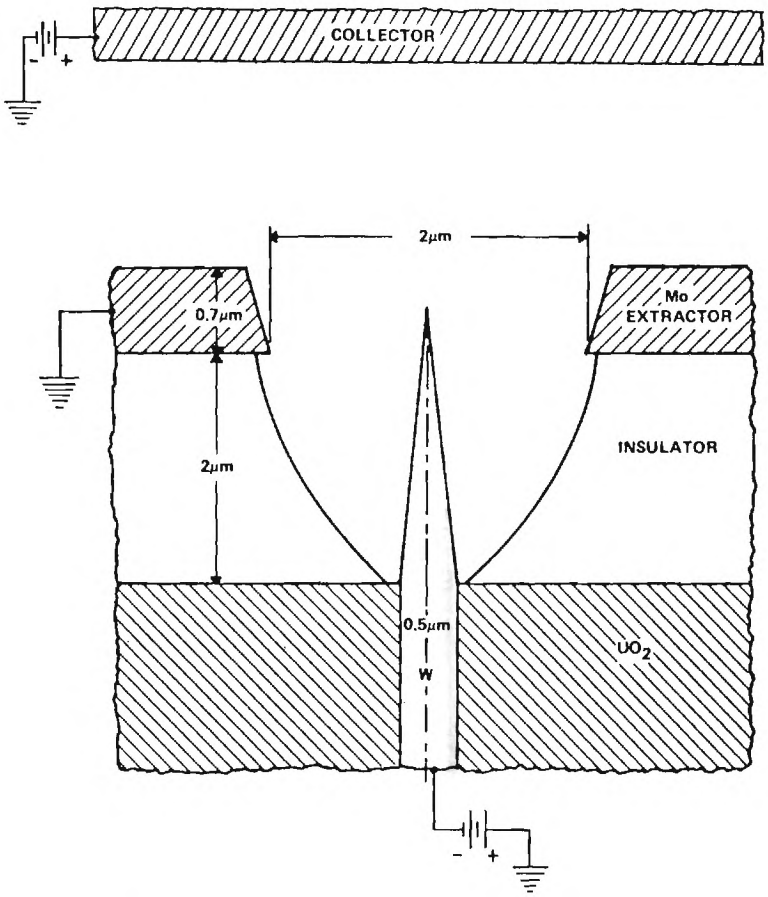

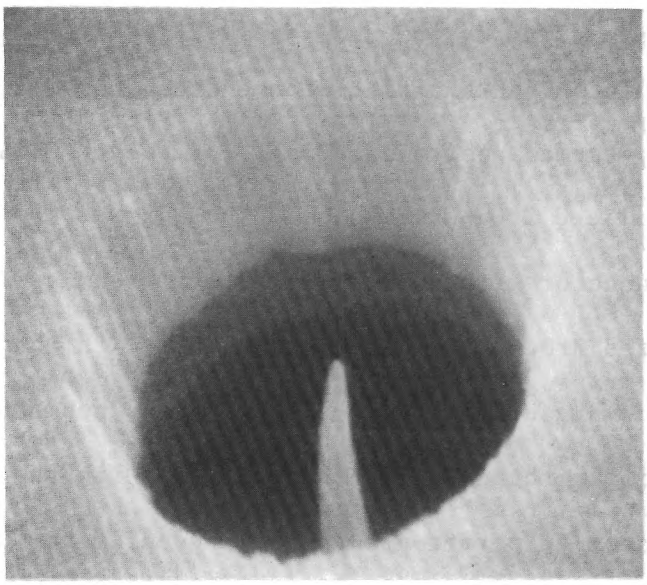

Figure I-1. Single Element of Low Voltage Field Emitter Array.

vity material, developing new post-deposition cleaning techniques, and upgrading the composite etching process. Emission testing for UO_2-W LVFE's was in a pulsed mode mainly and improvements in the insulator allowed a small amount of CW testing. In addition, emission testing has addressed life capabilities and tube atmosphere. Computer predicted emission calculations were useful in assessing the importance of device geometry, parameters such as fiber tip placement, extractor thickness, extractor orifice diameter and emitter tip radius. Improving the UO_2-W composite was attacked by installing a 50 kw crystal growth facility to provide larger boule size. The purpose of larger boule size was to provide larger UO_2 cell size, fibers more aligned with the growth direction, and larger crack-free areas. Before presenting efforts in the above areas, a background section has been included which presents the LVFE fabrication process prior to contract initiation. This permits easy delineation of new advances in LVFE processing.

Most failures for the LVFE have been the result of high leakage currents through the electron beam evaporated Al_2O_3 insulator, resulting in ohmic heating of the insulator and shorting of the extractor of the UO_2 base. To solve this problem, the composite base used for the LVFE was switched from UO_2-W to Y_2O_3 stabilized ZrO_2-W (ZYW). In the UO_2-W composite system, the UO_2 matrix is a semiconductor with a resistivity of 10^3 Ωcm. In the ZYW composite, the yttria stabilized ZrO_2 matrix is an insulator with the resistivity of 10^{14} Ωcm. As will be presented, leakage current was substantially reduced by use of a composite with an insulating matrix. With the installation of the 50 kw rf generator to permit growth of large diameter UO_2-W boules, it was possible to grow ZYW of the quality needed for LVFE fabrication. As a result of availability of good ZYW composites and for the reasons listed

above, the last seven months of the contract were devoted to fabricating and emission testing LVFE's employing ZYW composites as the substrate. As a result, a number of changes were necessary for the fabrication of the LVFE, including developing new etchants to expose and point the W fibers. Emission testing for the first time was exclusively dc with emission current densities in the 1-5 A/cm^2 range and leakage in the μA range.

CHAPTER II

LVFE FABRICATION AND GEOMETRY

Fabrication of the low voltage field emitters requires a variety of processes many of which are unique and not in practice anywhere else. Also, since the cathode is still an experimental device, any step to the process is subject to change and several processing changes and additions have been made in the past year. Therefore, to familiarize the reader with LVFE fabrication procedure and to document the state of the art in LVFE fabrication prior to the start of the contract, a detailed description of the process will be presented below with much of the chapter being exerpted heavily from Hill[2] and Lee[3]. After documenting the fabrication procedure, techniques used to define and vary the LVFE geometry have been presented.

A. LVFE FABRICATION

The key to the LVFE structure is the uranium dioxide-tungsten (UO_2-W) eutectic composite developed by Chapman and Clark[4]. Detailed descriptions of the growth process have been published[5,6], but because of its importance to the present work, a brief description of the process has been included below.

After slicing the composite to form a disc, the W fibers are exposed above the UO_2 matrix by selective etching. An active area is formed by dissolving fibers except for a masked area. After stripping the mask, the LVFE structure is formed by vapor depositing thin films on the exposed fibers forming the active area. Thus the fabrication can be conveniently broken into (1) UO_2-W Unidirectional Solidification,

(2) UO_2-W Substrate Processing, (3) Selective Etching, (4) Active Area Formation, and (5) Insulator and Extractor Deposition.

1. UO_2-W Unidirectional Solidification

The UO_2-W composites are grown from near eutectic compositions using a direct induction heating internal floating-zone technique. The usual containment and contamination problems are eliminated because the molten zone is self-contained within the pellet-shaped sample. Self-containment is imperative, since temperatures up to 2800°C are required to melt these refractory materials. Uniform composite structures are produced because of the well-defined liquid-solid interface associated with the inherent steep temperature gradients present in this internal floating-zone technique.

The UO_2-W composites which serve as substrates for the LVFE structures are fabricated by first dry-mixing the desired composition of UO_2 and tungsten powders. This mixture is dry pressed into cylindrical pellets up to 38 mm in diameter by about 60 mm in length, and sintered in a controlled atmosphere for stoichiometry control of the oxide. When the pellets are sufficiently densified, they are placed in the apparatus shown schematically in Figure II-1 and melted. The vitreous SiO_2 containment tube provides the neutral or reducing environment necessary to prevent the oxidation of the composite samples and the Mo preheater tube. Preheat temperatures of 1400-1500°C are required to increase the electrical conductivity of the samples sufficiently for direct rf heating at 3.5 MHz. In the configuration shown in Figure II-1, a single bottom Mo

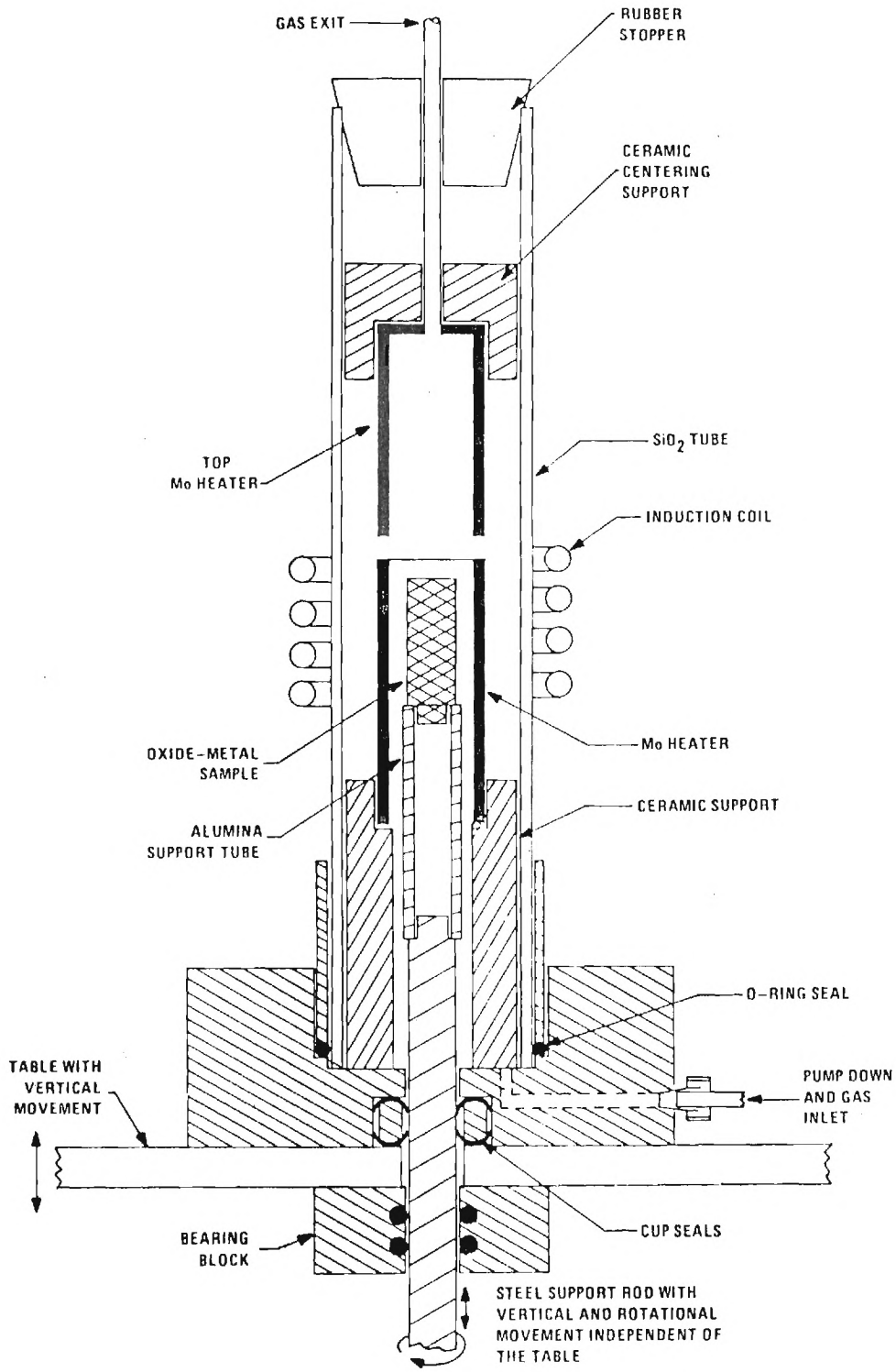

Figure II-1. Schematic Diagram of the Induction Furnace Used for Growth of the UO_2-W Composite.

preheater is used, and for internal zone melting the Mo tube is simply lowered out of the coil to expose the entire rod to the rf field. The concurrent increase of temperature, electrical conductivity, and resistance heating of the sample continues until the interior of the rod melts. The high radient heat loss from the surface of the rod and relatively low thermal conductivity of the oxide-metal mixture produces a steep thermal gradient across the skin of the rod so that, by controlling the input power, one can keep the surface temperature well below the melting point of the oxide-metal eutectic. Careful regulation of the oxygen potential in the growth atmosphere is required to maintain sufficient tungsten solubility in the molten urania.

Unidirectional solidification is achieved by lowering the sample and moving the internal molten zone upward through the rod at 20-40 mm/hr. A cavity forms over the molten zone because of the difference in density between the sintered rod and the nearly theoretically dense solidified composite. During the lowering, the oxide-metal mixture melts from the roof of the cavity, runs down the interior walls of the cavity into the molten pool, and is unidirectionally solidified at the base of the molten zone. To minimize thermal cracking, the rod is lowered into the bottom Mo preheat tube which is repositioned in the lower turns of the induction coil to act as a postheater operating at 1500°C. After the rod is lowered several centimeters, the Mo tube is raised to heat the entire length of the rod to control the cooling and reduce cracking due to thermal shock. After growth, the ingots are either longitudinally sectioned, Figure II-2, for analysis or sliced into waf-

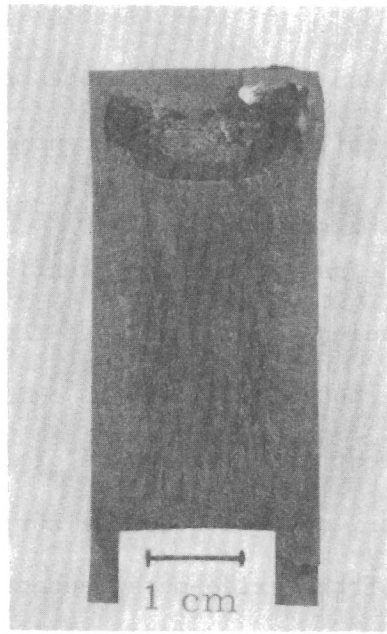

(a)

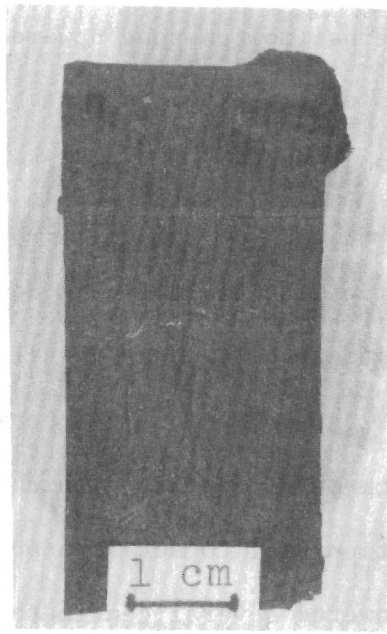

(b)

Figure II-2. Longitudinal Sections of Unidirectionally Solidified UO_2-W Composite Ingots.

ers for fabrication of the LVFE substrates.

2. UO_2-W Substrate Preparation

After removal from the rf furnace, the ingots were sliced perpendicular to the growth direction using a diamond saw. The resulting wafers were normally 1-2 mm thick, with 2 mm being the desired thickness (for ease in handling). The wafers were ground and polished and examined with a metallograph to determine whether the fiber growth was satisfactory.

Wafers which passed this test were then glued to a glass plate and chips 4.2 mm in diameter were cut from the wafer with a diamond core drill. The chips were cleaned thoroughly, then mounted on a plastic rod with a cyanoacrylate cement and polished to a 1 μm finish on a diamond lap. A brass fixture was used to insure that the faces of the chip remained parallel during the final grinding and polishing step. After the final polish, the chip was removed from the plastic rod and cleaned carefully in an ultrasonic cleaner in benzene followed by a methanol rinse.

3. Selective Etching Procedure

The next step in the fabrication process was the selective etching of the composite chip to expose the tungsten fibers and shape the tips to the desired geometry. Two etching solutions, developed in previous work on composites[3], were utilized for this purpose. The first etchant, designated the CAHN-P or pointing etch, was composed of the reagents shown in Table II-1. This etch attacks the UO_2 matrix and, to a lesser extent, the tungsten fibers. The result is that the fibers are exposed and at the same time etched to very fine points, Figure II-3.

Table II-1. Composition of CAHN-P Etch.

Reagent	Volume Percent
Chromic Acid (saturated)	39.7
Acetic Acid (Glacial)	26.5
Hydrofluoric Acid (49%)	15.3
Nitric Acid (70%)	18.5

For a pointed-pin geometry, the chip was gripped in a pair of nylon tweezers and held in a beaker while the CAHN-P etch solution was circulated past the chip by the stirring action of a teflon-coated spinbar. Rotation speed and position of the chip in the solution were carefully controlled to insure reproducible results. An etching time of fifteen minutes was usually sufficient to obtain pointed fibers 3-4 μm long, with cone angles of $\sim 10^{o}$, although the required etching time was somewhat dependent on the fiber diameter. Increasing the etching time generally resulted in longer fibers with reduced tip cone angles. Because the fiber diameter frequently varied somewhat along its length, the etched, pointed pins often varied in height, sometimes by as much as twenty percent.

Only the procedure for producing pointed fibers has been presented here because the conical shape has been the only geometry used for the past year. However, three other geometries have been used in the past. Cylindrical tipped fibers can be produced by the CAHN-L etch, a chromic-acetic-hydrofluoric-nitric acid solution that dissolves the UO_2 matrix without attaching the W fiber. Thus the cylinder shape remaining from polishing is maintained. Hemispherical tips can be produced by thermally

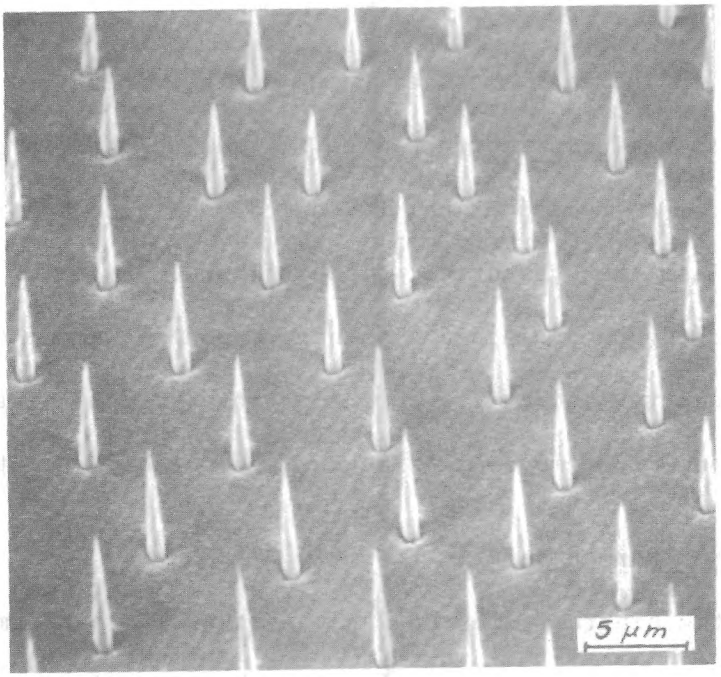

(a)

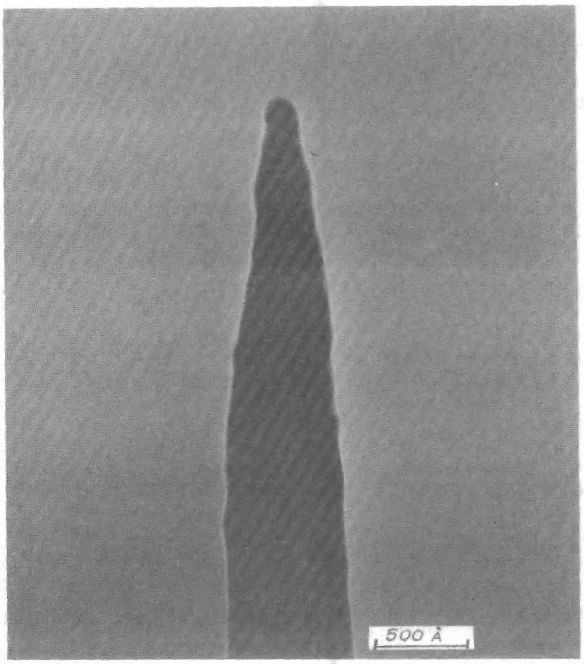

(b)

Figure II-3. Example of Pointed-Pin Geometry Available With CAHN-P Etch, (a) X2500, ϕ = 45°, (b) X340K, ϕ = 90°.

annealing the cylindrical tips, allowing surface energy to drive the tip geometry to a minimum surface area. A variety of tip geometries from cylindrical to hemispherical to conical can also be produced by argon ion milling the cylindrical tipped fibers.

After etching the chip and obtaining exposed pins of the desired height and geometry, the chip was rinsed thoroughly in distilled water and then methanol to remove all traces of the etching solution.

4. Active Area Formation

A schematic diagram illustrating the steps in the formation of the active area is given in Figure II-4. The chip was first examined with the metallograph to decide which cell(s) near the center contained the most uniform fiber growth. Once a suitable cell was selected, the chip was placed in a fixture under a 30X binocular microscope and a small circle of wax (Apiezon Wax W) dissolved in trichlorethylene (TCE) was placed on the surface in the center of the cell, using a micrometer syringe, to protect the pins which would form the active area (Figure II-4b). The viscosity of the wax solution was carefully controlled so that the mask, the diameter of which could be controlled down to $\sim$0.2 mm, was bonded tightly to the surface of the UO_2. The back of the chip was also coated with wax to protect the exposed pins there.

After the wax masks dried, the remaining pins on the surface and sides of the chip were removed to a depth of 10-100 μm (Figure II-4c) by etching with the alkaline ferricyanide solution of $K_3Fe(CN)_6$, 15 gm; NaOH, 5 gm; and sufficient distilled H_2O to make 100 ml. The wax was

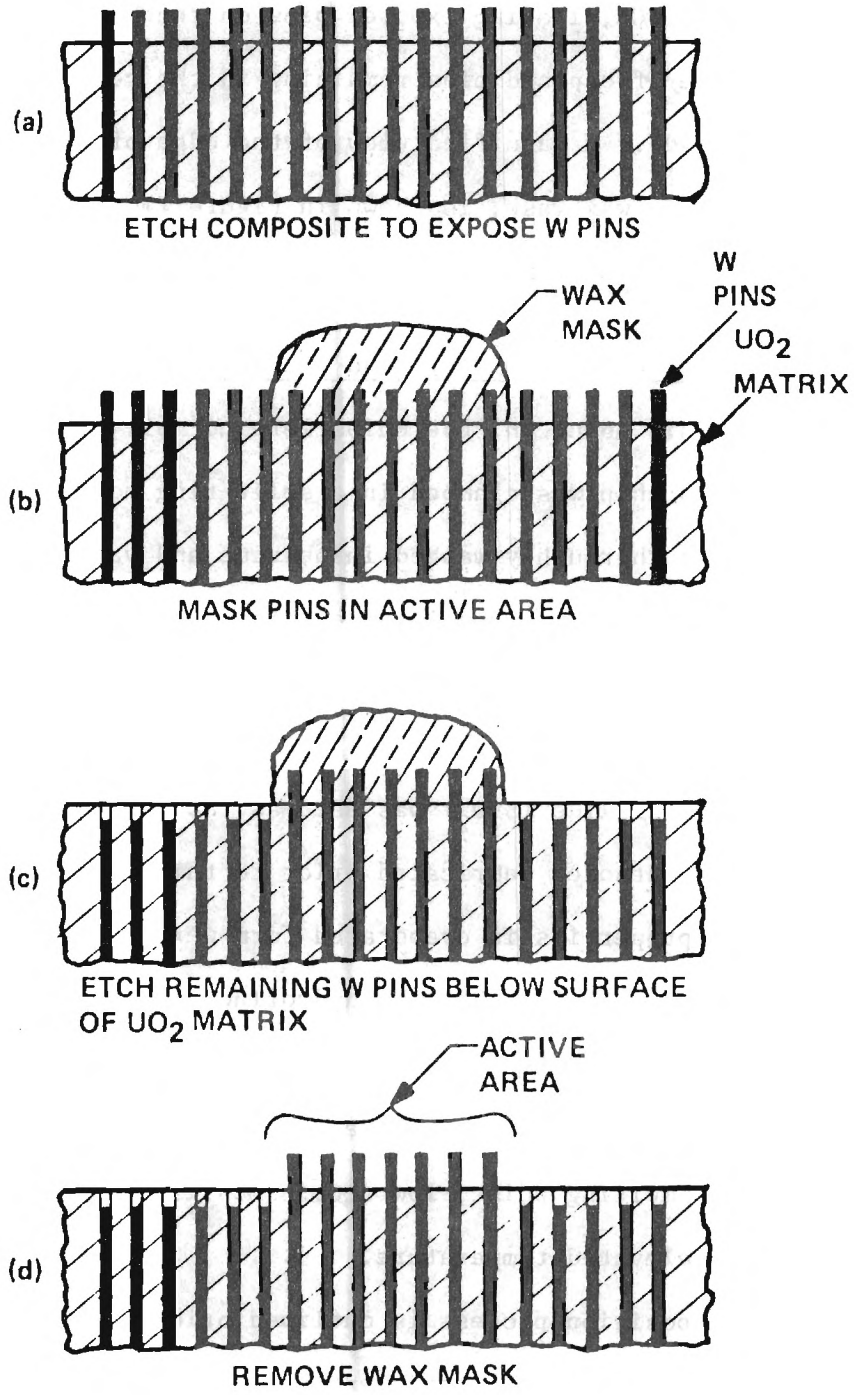

Figure II-4. Schematic Diagram Illustrating the Steps in the Formation of the Active Area.

removed with TCE, leaving exposed pins on the back of the chip and a small circle of exposed pins remaining in the center of the chip (Figure II-4d). A magnified view of the edge of an active area, after removal of the wax mask, is shown in Figure II-5. Note the holes where the tungsten have been removed by the alkaline $K_3Fe(CN)_6$ solution.

5. Deposition of Insulator and Extractor Films

From this point on, the chips were normally processed in groups of three. Each chip was clamped in a split-ring holder to facilitate handling and was thoroughly washed in benzene and vapor-degreased in TCE. The chips were then placed in an electron beam evaporation unit diagrammed schematically in Figure II-6, for deposition of the insulator and extractor films.

Silicon dioxide (SiO_2) was used as the insulating material for all of the LVFE cathodes fabricated prior to this contract. Although its electrical properties in evaporated form were only marginal, the advantage was the ease of etching by hydrofluoric acid (HF), an acid which attacks the other materials in the LVFE structure very slowly if at all. Molybdenum (Mo) was chosed as the material for the extractor film because of its high melting point, low atomic mobility on the surface, and high modulus at elevated temperature.

The deposition process is outlined briefly in the following paragraphs for the reader's convenience. A more detailed description of the deposition equipment and procedure is given by Lee[3].

The vapor deposition system consisted of a 6 kW, self-accelerating, 180 bent-beam gun and four selectable water-cooled copper hearths. The

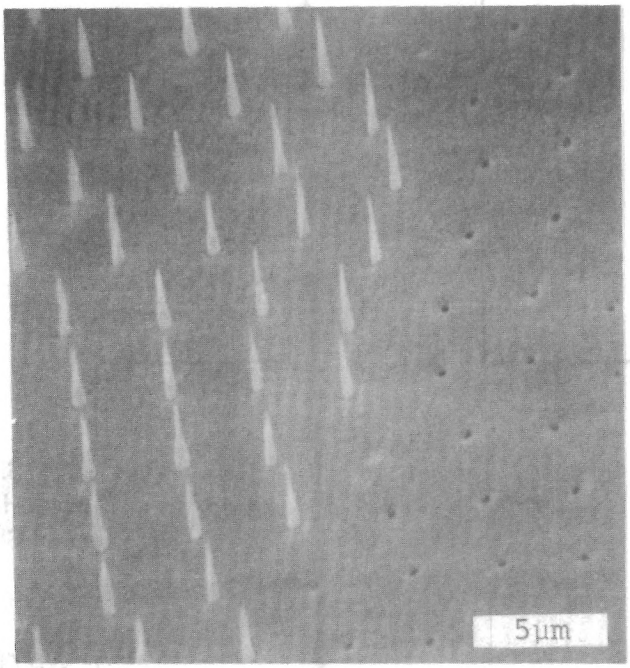

Figure II-5. Edge of a Typical Active Area Prior to Deposition of the Insulating and Extractor Films, X3500.

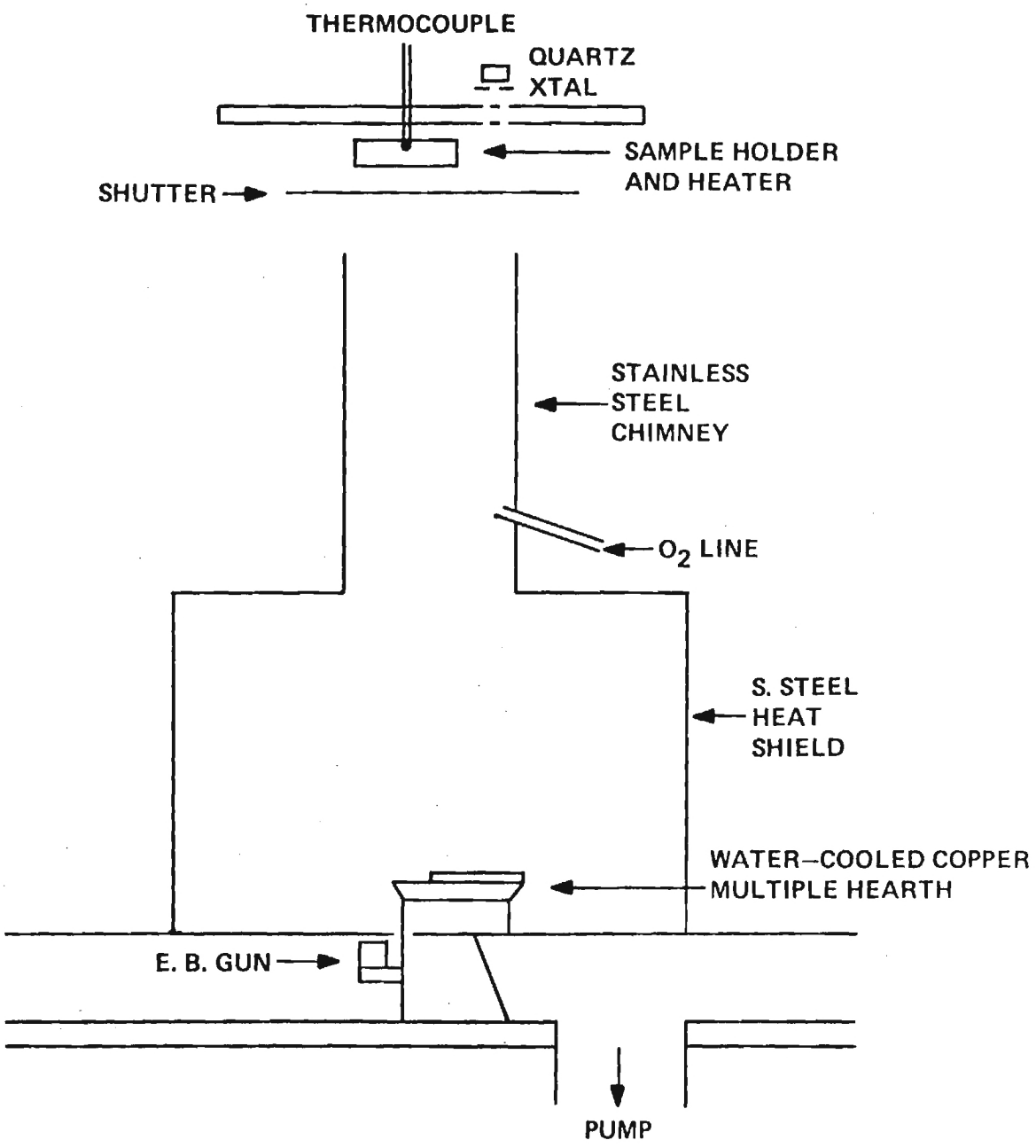

Figure II-6. Schematic Diagram of Vapor Deposition System.

gun was powered by a manually operated 5 kW DC power supply. Film thickness was monitored with a piezoelectric quartz crystal thickness monitor, which measured the change in frequency of the quartz crystal, operating initially at 5 MHz, as the crystal changed weight with increasing film thickness. The output of the thickness monitor was fed into a recorder to permit measurement of the deposition rate and to provide a record of the deposition run. The film thickness was calculated using the relation

$$t = c \frac{\Delta f}{\rho}, \qquad \text{(II-1)}$$

where t = film thickness in nanometers

ρ = film density in gm/cm^3

Δf = frequency change in Hz

c = calibration constant.

In addition, the film thickness was generally verified by SEM measurements. The LVFE chips were placed in the heater assembly and heated to 350° ±10°C, after the pressure in the bell jar had been reduced to 1×10^{-6} torr. (130 mPa). Oxygen was bled into the chamber, via a leak valve until the pressure stabilized at 5×10^{-5} torr. (6500 mPa). The SiO_2 was deposited, at ∿50nm/min, until the desired thickness in relationship to the pin height was achieved. Variations in deposition rate were very large, ±100%, due to manual control of deposition power. The oxygen leak was then closed, and when the pressure returned to its former value, the hearth was rotated to position the molybdenum for evaporation.

A mask was rotated into position to limit the deposition of the

molybdenum film to a circular area ∿2.5 mm in diameter in the center of the chip. Molybdenum was evaporated at 80 nm/min. usually to a thickness of 700-800 nm although this thickness was varied intentionally in some runs.

B. LVFE GEOMETRY

A field emission electron gun is formed at each exposed fiber during the deposition process, Figure II-7. Thin film deposition by evaporation is a line-of-site process and the UO_2-W substrate is positioned so the condensing vapor is perpendicularly incident on the UO_2 matrix and approximately parallel to the fiber axes. As deposition proceeds, the films on the UO_2 surface and the fiber tips increase in thickness parallel to the vapor stream. In addition, because the fiber tip is above the matrix, the deposit on the tip grows outward, at about a 15 to 50 degree angle to the vapor stream.

The result is the formation of a cone-shaped deposit on the pin tips, with a cone angle characteristic of a given material. As the cones grow, they shadow the area surrounding the pins and form inverted-cone holes, Figure II-7b. When the metal extractor film is deposited, the cones serve as a mask preventing metal deposition in the holes which electrically isolate the extractor from the fibers. After deposition, each chip was etched in a five percent HF solution for five seconds to partially undercut the cones at the pin tips and ultrasonically vibrated at 55 kHz for 15 seconds in distilled water to remove the cones, Figure II-7c. Examples of the structure in each stage of fabrication are shown in the SEM photomicrographs of Figure II-8.

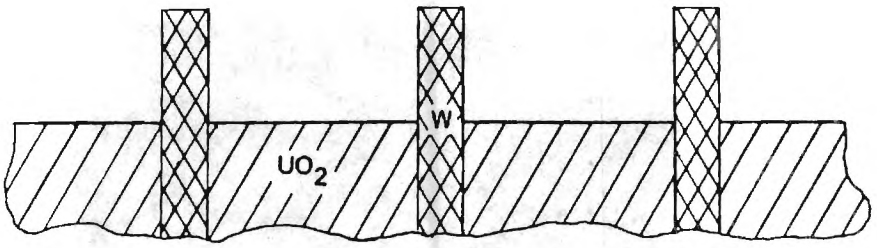

Step 1. Etch a polished UO_2 – W composite to produce free standing W pins (cathodes).

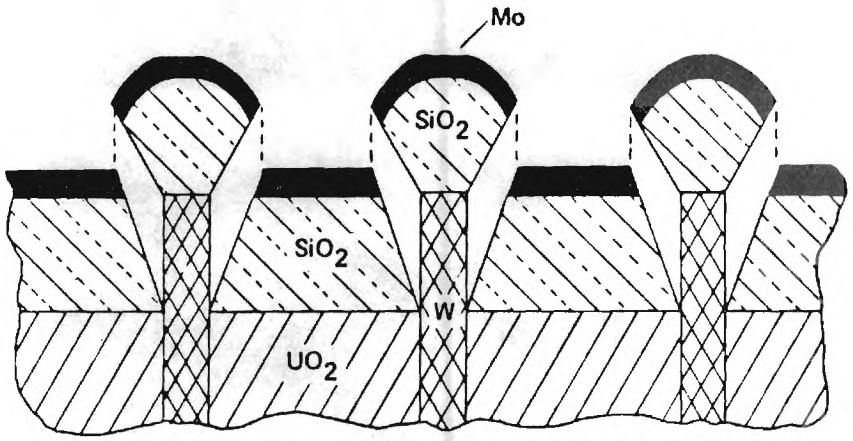

Step 2. Vapor deposit SiO_2 and Mo parallel to fiber axes to the desired thickness.

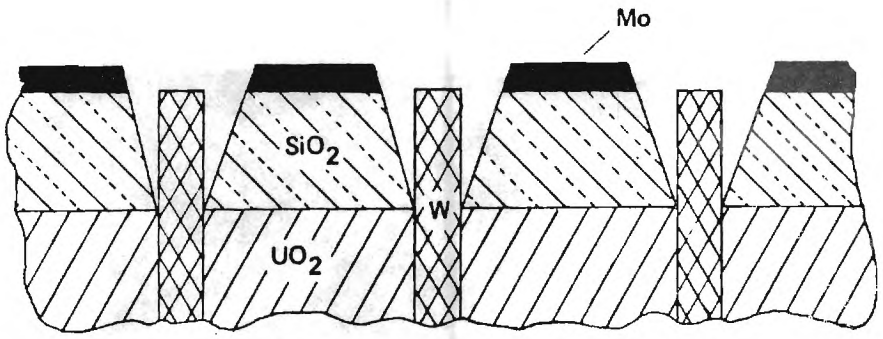

Steps 3 and 4. Ultrasonically vibrate in H_2O to remove cathode cones and clean remanent SiO_2 from cathode with hydrofluoric acid.

Figure II-7. Schematic Diagram Showing the Steps in the Formation of the LVFE Structure.

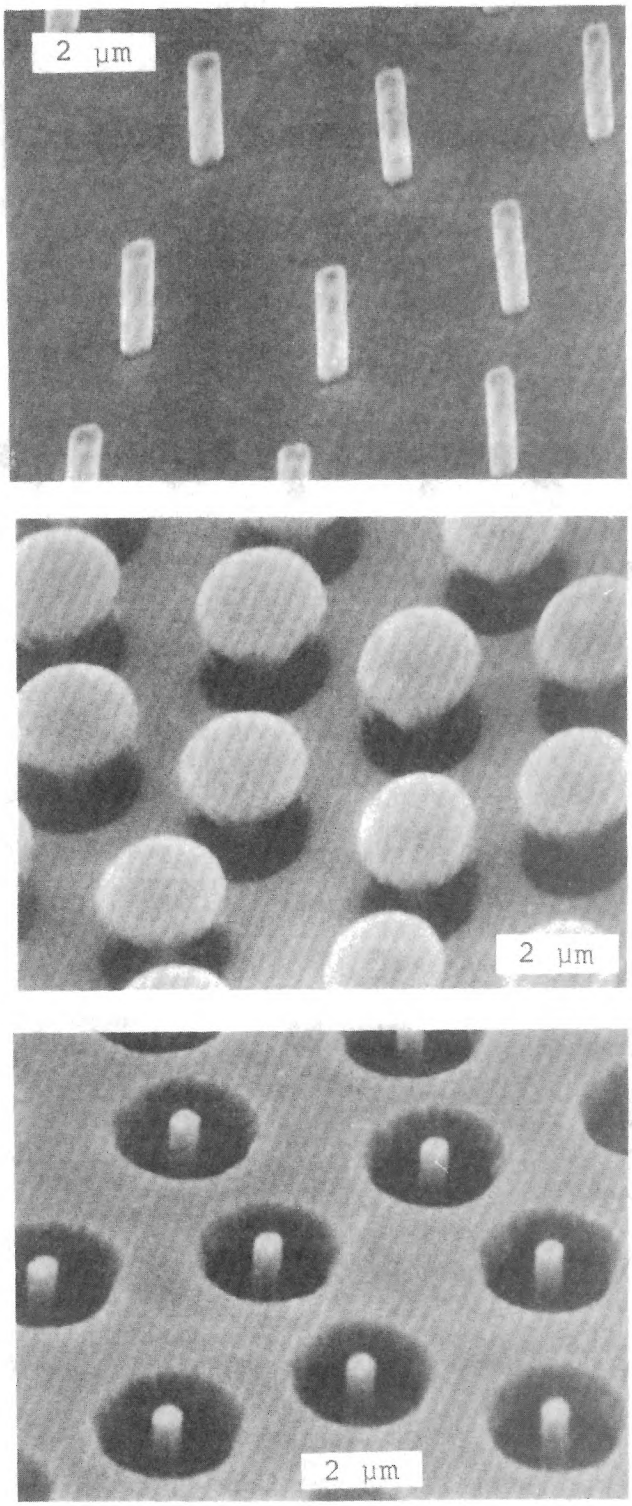

Figure II-8. Examples of the LVFE Structure During Each of the Fabrication Steps Illustrated in Figure II-7.

After cleaning, the active area was examined in the metallograph to see if all of the cones had been removed; if not, then the process was repeated, up to four or five times if necessary, until 90 percent or more of the cones had been removed. Those remaining were usually bound too tightly to remove without risking damage to the rest of the active area from the violent action of the ultrasonic cleaner. However, some cathodes were tested with up to 20 percent of the cones in the active area still in place, and no failures were associated with an unremoved cone.

After removal of the cones, each chip was etched for 15 seconds in the five percent HF solution to remove low-angle SiO_2 deposits from the hole and the pin tip. This was followed by a 15-second etch in 1 N HCl solution to dissolve low-angle molybdenum deposits in the hole, and to try to remove any ridges of molybdenum left around the rims of the holes when the cones were removed. Next, the chips were thoroughly rinsed in distilled water, followed by a rinse in electronic grade methanol. The shape and size of a completely processed active area is shown in Figure II-9.

1. Single Deposition

Because the cathode cone grows at constant angle, θ_c, the LVFE geometry is predictable, Figure II-10. The insulator cone angle, θ, is determined by the geometry of the cathode cone to be

$$\theta = \tan^{-1}[(Tz/T)\tan\theta_c] \qquad \text{(II-2)}$$

where the various parameters are defined on Figure II-10. Knowing the

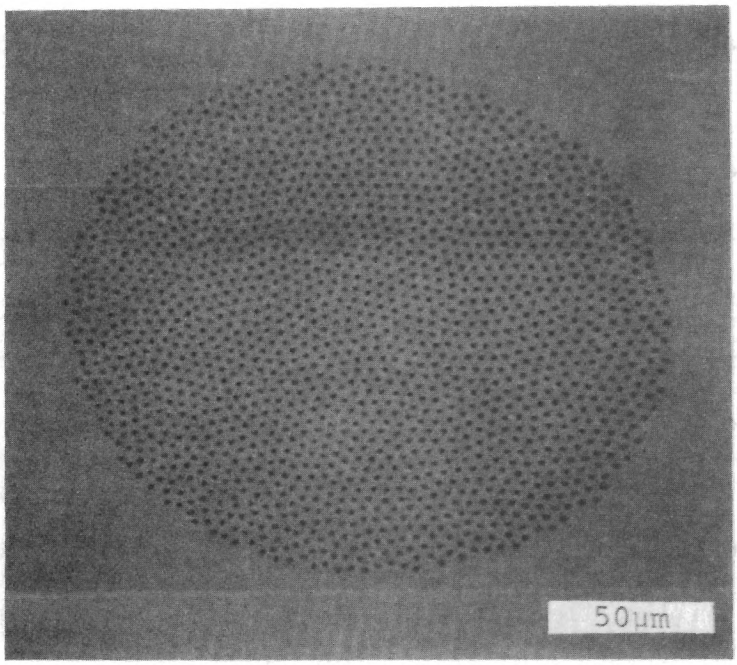

Figure II-9. Micrograph Showing the Shape and Size of a Typical Active Area, X320, $\phi = 30°$.

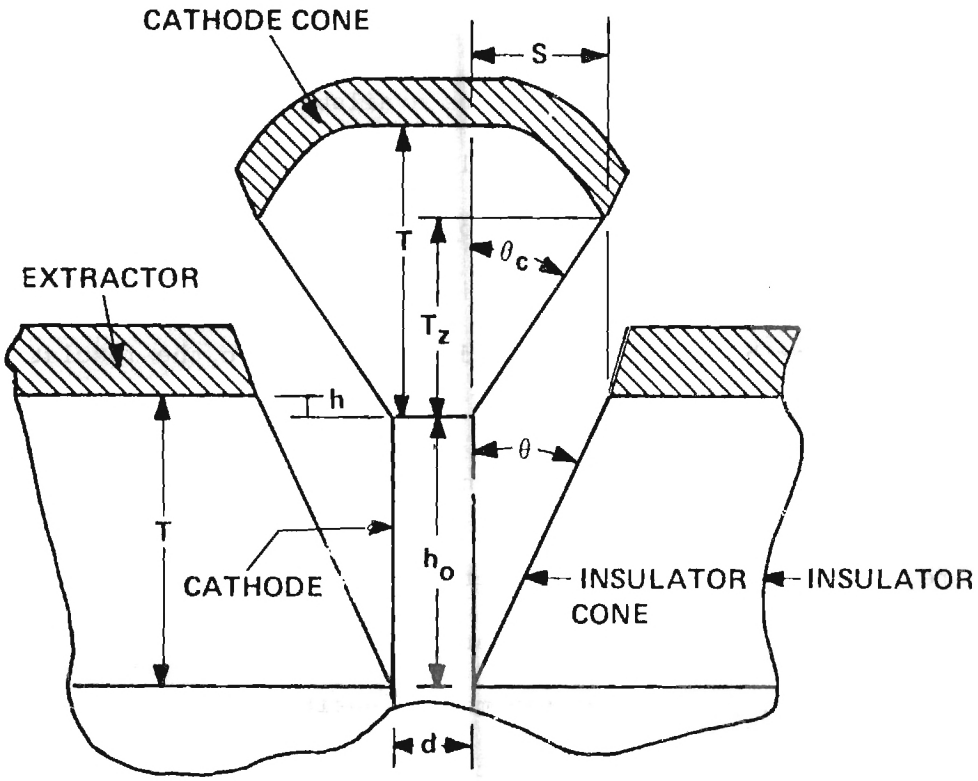

Figure II-10. Schematic Diagram Showing Parameters That Define the LVFE Geometry.

insulator cone angle, θ, allows calculation of the extractor hole diameter, D, at the insulator/extractor interface,

$$D = 2T \tan\theta + d, \qquad \text{(II-3)}$$

where d is the fiber diameter at the tip. For pointed fibers d $\sim$0, and for the Al_2O_3 and SiO_2, θ is $\sim$27° so that for pointed fibers, the extractor hole diameter is equal to the insulator thickness. Therefore during a single deposition, the only means available for varying the extractor hole diameter is to vary the insulator thickness. It should be noted that the cathode cone angle for molybdenum is smaller than the oxides so that the extractor cone angle is $\sim$20°.

The fiber height is expressed in relation to the insulator/extractor interface as

$$h = h_o - T \qquad \text{(II-4)}$$

where h is positive when the fiber tip is above the insulator/extractor interface. By varying the insulator thickness, T, in relation to the fiber length, h_o, the fiber tip may be positioned below, at the level of, or above the insulator/extractor interface.

2. Double Deposition

It would be desirable to be able to vary the extractor hole diameter independently of the insulator film thickness. For example, thicker insulator films may be necessary to reduce leakage current or, in the case of pointed pins, to locate the pin tip in the plane of the extractor and yet still maintain a small cone angle. Such an improvement in the geometry would normally be negated, however, by the increased interelectrode spacing.

The problem was solved by the development of a double-deposition process which provides control over the extractor hole diameter. The steps in this process are shown schematically in Figure II-11. Rather than depositing the insulator layer to the desired thickness the first time, deposition is halted at an intermediate stage (Figure II-11a).

The chip is removed from the bell jar (after cooling to room temperature), and the cones removed as described previously (Figure II-11b). The chip is etched for 15 seconds in the five percent HF solution to remove low-angle SiO_2 deposits in the holes. The chip is replaced in the bell jar, and a second deposit of SiO_2 is evaporated. The second deposit grows inward from the rim of the hole as the shadowing cone on the pin tip grows outward (Figure II-11c). At the halfway point, when the edge of the cone begins to shadow the ingrowing rim, it causes the rim to grow outward again as shown in Figure II-11d. The deposition is halted when the SiO_2 film has reached the desired thickness, and the Mo extractor film is deposited. The cones are then removed, and the resulting structure is shown in Figure II-11e. An example of the interelectrode spacing, S, which results when the entire insulator thickness is deposited in a single step is also shown in Figure II-11e, for comparison.

The diameter D of the extractor hole after the second SiO_2 deposition can be expressed, using simple geometric relationships, in terms of the thickness of the material deposited each time, the tangent of the growth angles of the cone and sidewall of the hole, and the pin diameter.

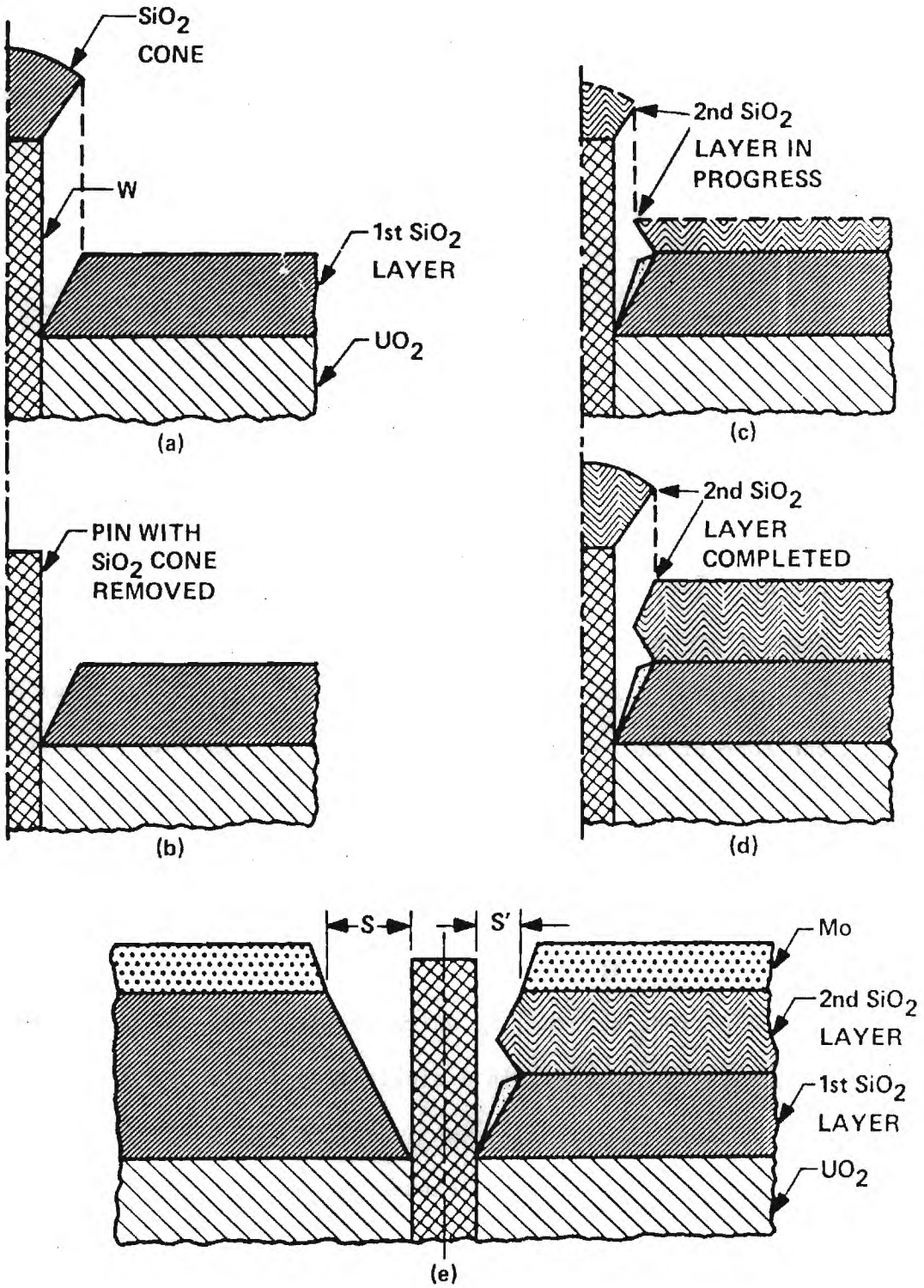

Figure II-11. Schematic Diagram Illustrating the Steps in the Double-Deposition Process.

It is given by

$$D = d + x\,2t_2 + t_1[(1 - \frac{x}{y})] \qquad \text{(II-5)}$$

where

$$t_2 > \frac{t_1 x}{2y} \qquad \text{(II-6)}$$

and t_1 = thickness of material (e.g., $SiO_2 + Al_2O_3$) deposited in the first deposition run

t_2 = thickness of material deposited in the second run

$x = \tan\theta$,

$y = \tan\theta_c$

d = pin diameter (assumed to be zero for pointed pins).

An example of an LVFE array produced using the double-deposition process is shown in Figure II-12.

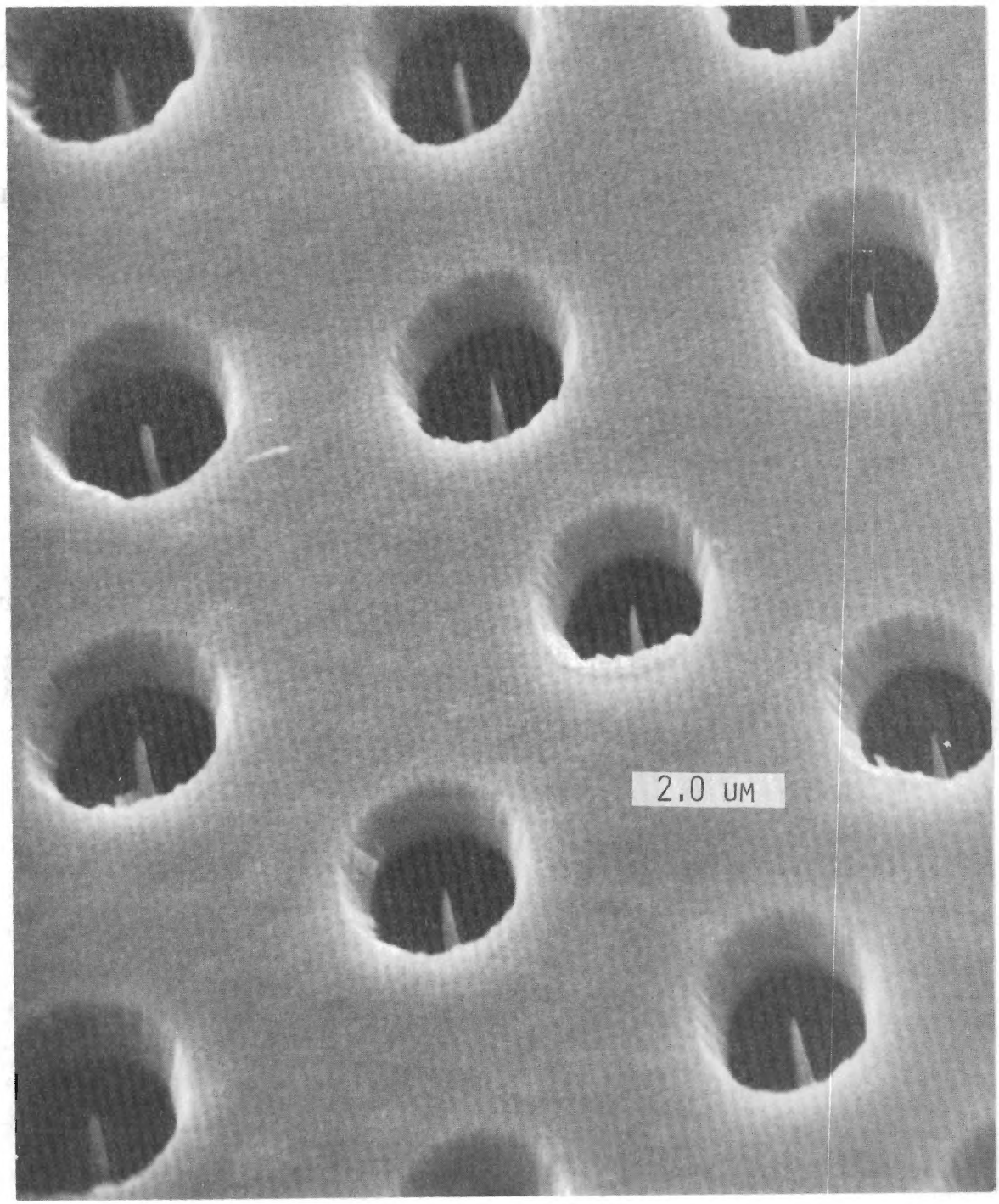

Figure II-12. Example of an LVFE Array Produced Using the Double-Deposition Process (Insulator Thickness is 3.3 μm) X12K.

CHAPTER III

IMPROVEMENT OF LVFE STRUCTURE

At the initiation of this contract a number of improvements needed to be made on the LVFE structure. As shown previously (1), multiple deposition allows independent control of extractor hole diameter and insulator thickness but poor thin film adhesion for samples exposed to air between depositions had been a problem. The adhesion problem was addressed successfully and is presented below.

The major effort of this section was to increase the resistance of the insulator with the goal of reducing leakage current to the low μA range. Insulator quality was improved by partially redesigning the thin film deposition facility, introducing changes in the deposition procedure, changing insulator material from SiO_2 to Al_2O_3, and by developing more effective post deposition cleaning techniques. Because improvements to the deposition facility affect both multiple deposition and insulator quality, deposition is described in Section A of this chapter and the multiple deposition and insulator quality experiments are described in Sections B and C.

Finally, better control of etching the UO_2-W composite was needed for more reproducible W fiber heights and for smoother UO_2 substrates. An etching apparatus designed to provide more laminar flow patterns was fabricated and variations in the CAHN-P etch compositions were investigated.

A. THIN FILM DEPOSITION FACILITY AND EVAPORATION PROCEDURE

During the first four months of the contract, the thin film deposition facility was almost completely redesigned and rebuilt. The first nine depositions were devoted mainly to learning the operation of the

new equipment and therefore will be described in this section.

At the start of this program, deposition was provided by a manually controlled electron beam evaporator capable of 6 kW at 10 kV and a water-cooled, four-hearth, 180° bent beam evaporation source. A microprocessor-based deposition rate controller was added to control the electron beam power supply via feedback from a water-cooled quartz crystal thickness monitor, Figure III-1. The rate controller has so far been shown to be capable of controlling oxide (SiO_2 and Al_2O_3) deposition rates between 0.20 and 2.0 nm/sec with deposition rate variation of ∿20%. At deposition rates greater than 2.0 nm/sec for the oxides, channeling becomes a problem and the localized excessive heating creates spitting and erratic deposition of the evaporant. Rates lower than 0.20 nm/sec have not beem attempted. Also, added to the facility was a fast response strip chart recorder to monitor deposition rate.

Several changes in the deposition system were made to reduce heating effects during deposition. An aluminum-collar heat sink and a short pyrex bell jar were installed. Secondly, the shielding of the hearth was improved to allow easy cleaning as well as providing heat shielding.

Attachment of a nitrogen gas supply to the deposition system was made to reduce the amount of down-time between deposition runs. This addition helped in two ways. First, adsorption of water vapor was reduced by backfilling the chamber with nitrogen before opening. Secondly, by admitting a small quantity of gas during the final stages of post deposition cooling, the temperature of the system could be reduced to room temperature more rapidly than if the chamber were held under vacuum.

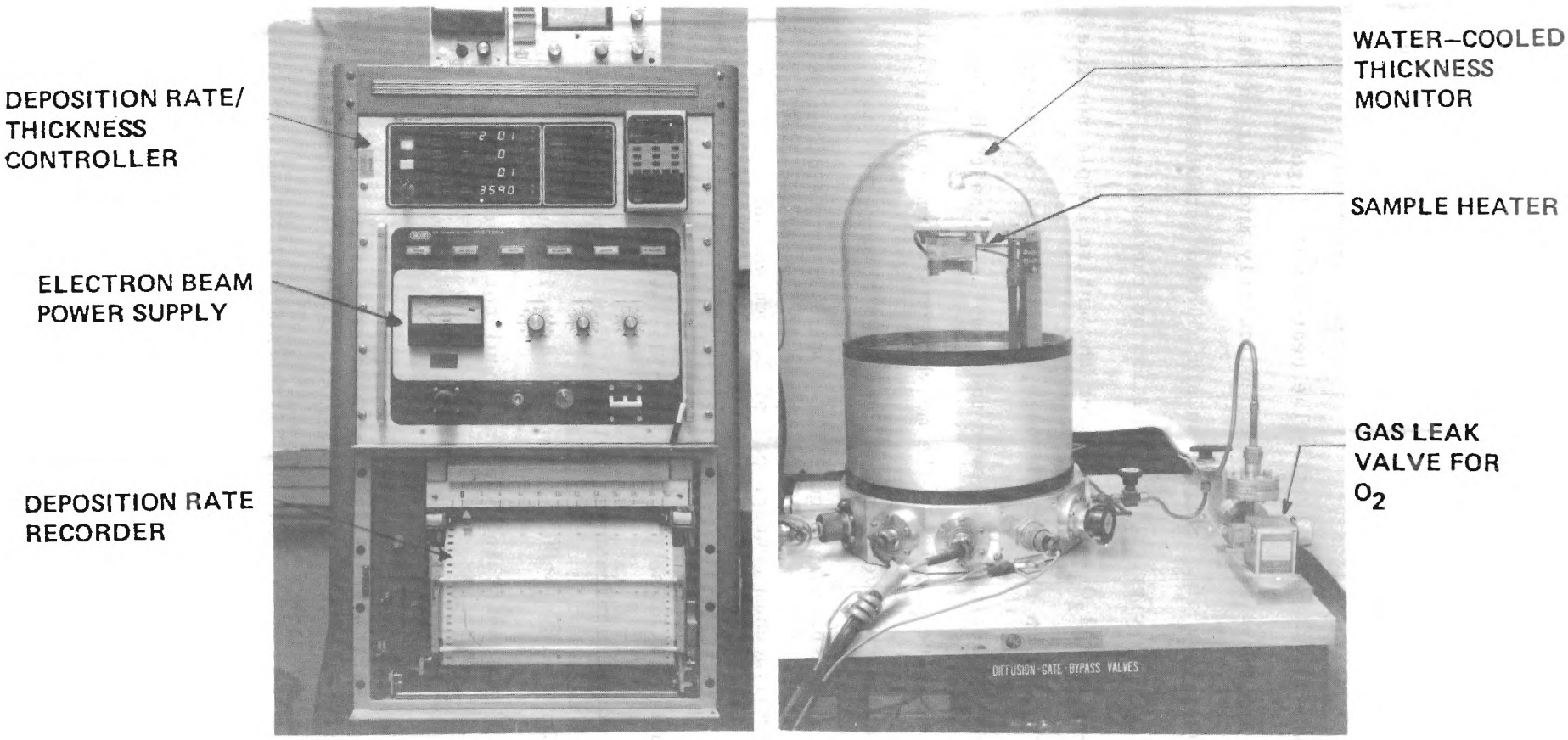

Figure III-1. Thin Film Deposition Facility.

A new sample heater/holder system capable of accommodating nine 4.2 mm diameter LVFE samples rather than three as in the previous deposition system was designed and constructed. The heater was aligned in the system so that the evaporant matter was perpendicularly incident on the UO_2 sample surface. Use of a movable shield allowed establishing the desired deposition rate prior to deposition on the sample. After depositing the insulator (Al_2O_3 or SiO_2) over the entire sample surface except for a support ring on the outside edge, a mask plate containing nine 2.5 mm dimaeter holes was slid over the samples so that the holes were centered on the nine samples. The molybdenum 2.6 mm diameter contact pad containing the active area was deposited through the mask. A typical LVFE chip shown in Figure III-2 was 4.2 mm in diameter by $\sim$1 mm thick with a molybdenum contact pad of 2.6 mm and an active area of 0.5 mm.

The heater in the sample heater/holder system was capable of 200 watts and could produce temperatures up to 700°C but excessive deposition system heating occurred above $\sim$600°C. For all depositions, O_2 pressure of 5×10^{-5} torr (6.5 mPa) was maintained during insulator deposition and an ambient pressure of $1\text{-}2 \times 10^{-5}$ (1.3-2.6 mPa) was present during the metal deposition for the extractor.

For characterization of the insulator films, metal-insulator-metal sandwich films were deposited on Al_2O_3 substrates 38 mm x 25 mm x 1.3 mm thick, Figure III-3. A copper sample holder for the Al_2O_3 substrate was fabricated to fit in the sample heater system. With the mask plate (described above) retracted from the sample holder, a layer of Mo

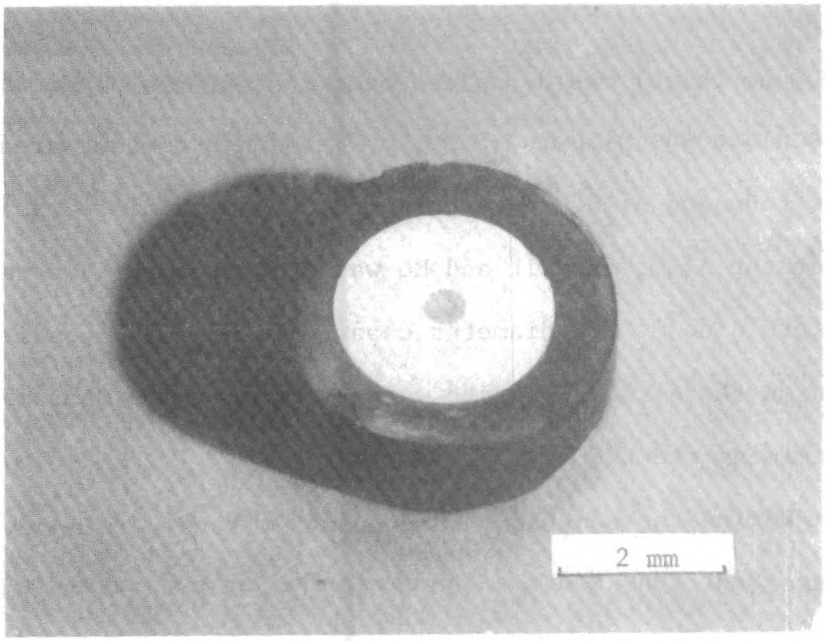

Figure III-2. Typical LVFE Chip Showing 2.6 mm Diameter Molybdenum Contact Pad and 0.5 mm Diameter Active Area, 11X.

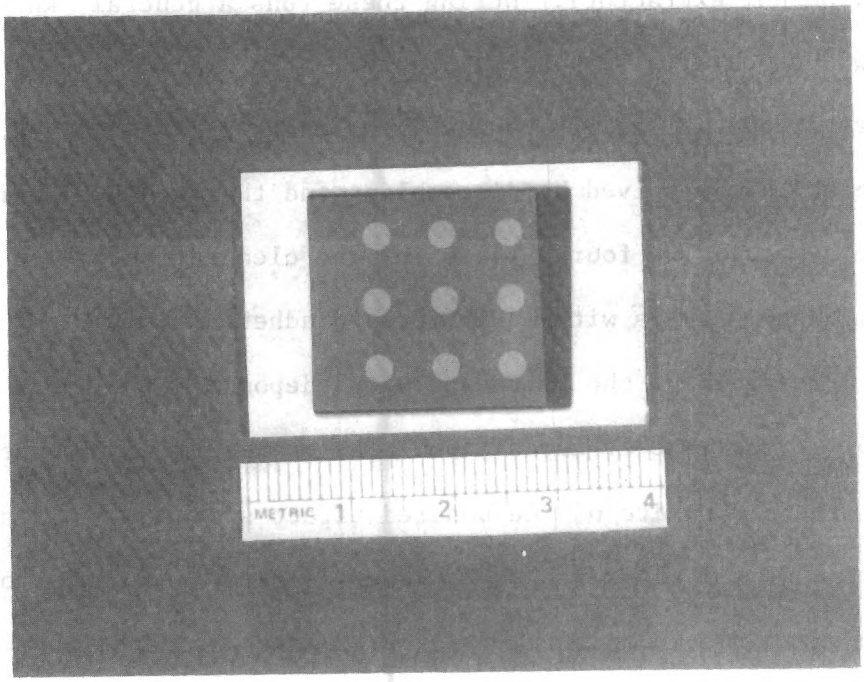

Figure III-3. Alumina Substrate for Insulator Conduction Measurement.

(∿200 nm thick) was deposited over most of the Al_2O_3 substrate. The mask plate was slid in ∿3 mm to shadow a contact area on the Mo electrode and Al_2O_3 was deposited. The mask plate was then slid to cover the Al_2O_3 deposit and Mo was deposited through the mask plate to form nine 2.6 mm diameter capacitor samples. Conditions for deposition on the Al_2O_3 substrate were as identical as possible to those used in forming the LVFE's.

During the contract, 39 deposition runs were made. A summary of the first eight runs and the changes made for the runs are presented below. The remaining thirty-one depositions will be presented later. The first three runs were attempts to duplicate the films produced with the old system (i.e. a two micron thick silica insulator and a one micron thick molybdenum extractor). During these runs a general knowledge of the new controller was obtained and the proper values for the variable settings were found. Films from these first three runs exhibited adhesions failure which was solved by dissembling and thoroughly cleaning the new sample heater. The fourth run using the cleaned system produced silica and molybdenum layers with much improved adherence.

The goal of the fifth and sixth deposition runs was to improve control of the rate of deposition. The changes made for the fifth run had an effect opposite of the desired effect so the appropriate corrections were made for the sixth run. The film structure was also changed for the sixth run. An 0.2 μm layer of silica was deposited, followed by 1.7 μm of Al_2O_3 and 0.6 μm of molybdenum. A thin silica layer was deposited first to allow the removal of the deposition cones by the methods used to remove silica cones, i.e., a five second immersion in 10% hydro-

fluoric acid followed by ultrasonic cleaning in water for fifteen seconds. Because of favorable emission tests results of samples from deposition six, the geometry and composition of the insulating and extractor layers were duplicated for deposition seven.

For deposition eight, nickel was substituted for molybdenum as the extractor layer. Because the melting point of nickel is less than that of molybdenum, the hearth could be kept at a lower temperature and less heat would be dissipated to the deposition system. While the substitution did reduce the system temperature, the geometry of the nickel extractor layer quality was inferior to that of a molybdenum layer due to larger ($\sim$0.5 μm) crystallization of nickel. The reduced quality was judged to be a result of the increased mobility of nickel atoms with respect to molybdenum.

As can be seen above, the first eight depositions were made to learn how to use new deposition equipment and to make improvements to the system. The remaining depositions fell into three basic categories: (a) depositions made to fabricate LVFE from UO_2-W composites for emission testing; (b) deposition for investigation of the electrical properties of the insulator by fabrication of thin film capacitors, and (c) depositions made to fabricate LVFE from ZYW composites during the last six months of the contract. Deposition conditions for evaporations 9-39 are summarized in Table III-1. Eight of the depositions were double depositions as will be discussed below.

B. MULTIPLE DEPOSITION

Much of the time, etching UO_2-W composites with the CAHN-P solutions results in pointed pins 3 to 5 μm in length. (The CAHN-P etch is discussed in Section III-D.) If single deposition is used the extractor hole diameter is

Table III-1. Summary of Deposition Parameters For LVFE and Capacitor Fabrication.

Deposition Number	Programmed Thickness Values		Actual Thickness Values		Programmed Insulator Deposition Rate	Substrate Temp.	Substrate	Comments
	Insulator (μm)	Extractor (μm)	Insulator (μm)	Extractor (μm)	(nm/sec)	(°C)		
9	0.1 SiO_2 1.9 Al_2O_3	0.5	----	----	1.0	350	UO_2-W	Emission Tested
10	1.0 Al_2O_3	0.3*	----	----	1.0	370	Al_2O_3	Capacitors for DC Conduction in Air
11	1.0 SiO_2	0.3*	----	----	1.0	437	Al_2O_3	Capacitors for DC Conduction in Air
12	0.1 SiO_2 2.0 Al_2O_3		----	----	1.0 1.0	404	UO_2-W	1st Deposition of Double Deposition
13	0.1 SiO_2 1.4 Al_2O_3	0.5 Mo	3.6	0.5	1.0 1.0	407	UO_2-W	2nd Deposition - Film Peeled
14	1.25 Al_2O_3		----	----	1.0	409	UO_2-W	1st Deposition of Double Deposition
15	1.25 Al_2O_3	0.6 Mo	2.5	0.3	1.0	400	UO_2-W	2nd Deposition - Good Adhesion, Emission Tested
16	1.0 Al_2O_3	0.3 Mo!	----	----	2.0	432	Al_2O_3	Capacitors for DC Conduction in Air
17	1.5 Al_2O_3	0.5 Mo	----	----	0.5	449	UO_2-W	Emission Tested
18	1.7 Al_2O_3	0.5 Mo	2.5	0.5	0.5	463	UO_2-W	Emission Tested
19	1.0 Al_2O_3	0.6 Mo	1.1	0.6	0.5	443	UO_2-W	Destroyed Learning to Electropolish
20	1.6 Al_2O_3	0.3 Mo	1.85	0.15	0.5	421	UO_2-W	Emission Tested
21	1.7 Al_2O_3	0.3 Mo	2.7	0.3	0.5	580	UO_2-W	Emission Tested
22	Aborted Run, System Pressure and Temperature Too High					700	UO_2-W	----------
23	1.0 Al_2O_3	0.3 Mo!	----	----	0.5	370	Al_2O_3	Capacitors, Linde Sapphire Source
24	Films Peeled Due to Oil Contamination From New Heat Shields					500	UO_2-W	Complete Deposition From #22
25	1.0 Al_2O_3	0.2 Mo!	1.8	0.2	0.2	370	Al_2O_3	Capacitors, Linde Sapphire Source
26	1.0 Al_2O_3	0.2 Mo!	----	----	0.5	450	Al_2O_3	Capacitors, Sapphire Source, Shorted

Table III-1. (Continued)

Deposition Number	Programmed Thickness Values: Insulator (μm)	Programmed Thickness Values: Extractor (μm)	Actual Thickness Values: Insulator (μm)	Actual Thickness Values: Extractor (μm)	Programmed Insulator Deposition Rate (nm/sec)	Substrate Temp. (°C)	Substrate	Comments
27	1.0 Al_2O_3	0.2 Mo!	----	----	0.5	450	Al_2O_3	Capacitors, Sapphire Source, Good Capacitors 198 pf
28	1.5 Al_2O_3	0.5 Mo	2.5	0.5	0.2	450	UO_2-W	Active Area Formed With Photoresist
29	Deposition Run to Test Evaporation Properties of Slip Cast Al_2O_3					-----		----------
30	1.2 Al_2O_3	------	----	----	0.2	450	UO_2-W	1st Deposition of Double Deposition
31	0.8 Al_2O_3	0.3 Mo	2.6	0.3	0.2	450	UO_2-W	2nd Deposition, Film Peeled Due to Phosphoric Acid Contamination
32	1.0 Al_2O_3	------	----	----	0.2	450	UO_2-W	1st Deposition of Double Deposition
33	0.5 Al_2O_3	0.5 Mo	2.6	0.5	0.2	450	UO_2-W	2nd Deposition, Good Adhesion
34	1.5 Al_2O_3	0.5 Mo	2.0	0.5	0.2	450	ZYW	Cylindrical Tips, No Leakage, CW
35	1.25 Al_2O_3	0.5 Mo	2.0	0.5	0.2	450	UO_2-W	Linde Powder Source, Samples Shorted
36	1.0 Al_2O_3	0.5 Mo	1.8	0.5	0.2	450	ZYW	Hemispherical Tips, No Leakage, CW
37	1.0 Al_2O_3	0.2 Mo!	1.6	0.2	0.2	450	Al_2O_3	Capacitors, Linde Powder Source
38	1.25 Al_2O_3	0.75 Mo	2.0	0.75	0.2	450	ZYW	Pointed Tips, No Leakage, CW
39	1.0 Al_2O_3	0.3 Mo	1.2	0.3	0.2	450	ZYW	Pointed Tips, Estractor Too Thin, Electropolished Too Long

*Bottom Electrode was Ni and Top Electrode was Mo.

!Both Bottom and Top Electrodes were Mo.

approximately equal to the insulator thickness. When the extractor hole diameter exceeds 2.0 μm, for LVFE's of 10^7 fibers/cm^2, many of the extractor holes overlap leaving only ribbons of Mo between the holes to carry voltage to the center of an active area. Thus, if insulator film thickness is to be matched with fiber heights of 4 μm or greater and an extractor hole diameter is to be maintained at or below 2.0 μm, double deposition must be used. Four sets of deposition runs, depositions 12/13, 14/15, 30/31, and 32/33 were devoted to double deposition.

In the first double deposition run, number 12, the insulator was composed of 0.1 μm of SiO_2 overlayed with 2.0 μm of Al_2O_3. The LVFE's were cleaned in 10% HF to remove the cathode cones and redeposited with 0.1 μm of SiO_2, 1.4 μm of Al_2O_3 and 0.5 μm of Mo. The purpose of the SiO_2 layer was to facilitate cone removal in 10% HF. However, the cathode cones were difficult to remove from both depositions and were in HF for longer than normal. Five of the six LVFE samples prepared in runs 12/13 exhibited film adhesion failure. It was not known whether the failure was due to excessive HF attack from contaminated sample surfaces, or to strain caused by thick films (~4.1 μm). Failure of the films was at the UO_2-SiO_2 interface. The only sample that did not exhibit film peeling, L19D-2, was emission tested and it also had adhesion failure in the active area when observed after emission. It should be noted that the extractor hole diameter was 2.2 μm whereas for a single deposition with 3.6 μm of insulator, the hole diameter would have been 3.8 μm.

For the second double deposition run, 14/15, Al_2O_3 was the only insulator material used and it was deposited to 1.25 μm thickness in both depositions 14 and 15. For the extractor, 0.3 μm of Mo was deposited. Between depositions,

the cathode cones were removed with ultrasonic vibration in 5% HF. Cone removal was very successful, Figure III-4. After the second deposition, the samples also cleaned well in the HF. Adhesion problems were not present as seven of the eight samples did not show any peeling and the one that did obviously had surface contamination problems due to several crevices that retained etching solutions. The double deposition of runs 14 and 15 were successful as an extractor hole size of 1.5 μm resulted compared to the 2.6 μm that would have been obtained with single deposition.

After double deposition 14/15, no double depositions were made until depositions 30/31 at which time it was desired to reduce extractor hole diameters to reduce emission voltage. Between 14/15 and 30/31, cleaning of the Al_2O_3 insulator with 85% phosphoric acid at 100°C had been adopted. In the first deposition, number 30, 1.2 μm of Al_2O_3 was deposited at 0.2 nm/sec and the cathode cones were removed by phosphoric acid etching for 10 seconds. The second deposition, number 31, consisted of 0.8 μm of Al_2O_3 and 0.3 μm of Mo. The process produced extractor hole diameters of 1.2 μm, which were the smallest produced during this program, Figure III-5. After deposition, the samples were cleaned for 40 sec in phosphoric acid and electropolished for 5 sec in H_2SO_4 which increased the extractor orifice diameter to 1.6 μm. Unfortunately, on six of the nine samples, the films peeled between the first and second Al_2O_3 deposition layers. This was attributed to phosphoric remaining on the surface after cone removal. In the UO_2-W composites from the 50.H2 boule, there was considerable "blue phase" at the UO_2 grain boundaries. After annealing and etching, this results in crevices 0.1 to 1.0 μm wide between grains. These crevices were thought to have retained phosphoric acid even after rinsing in distilled water.

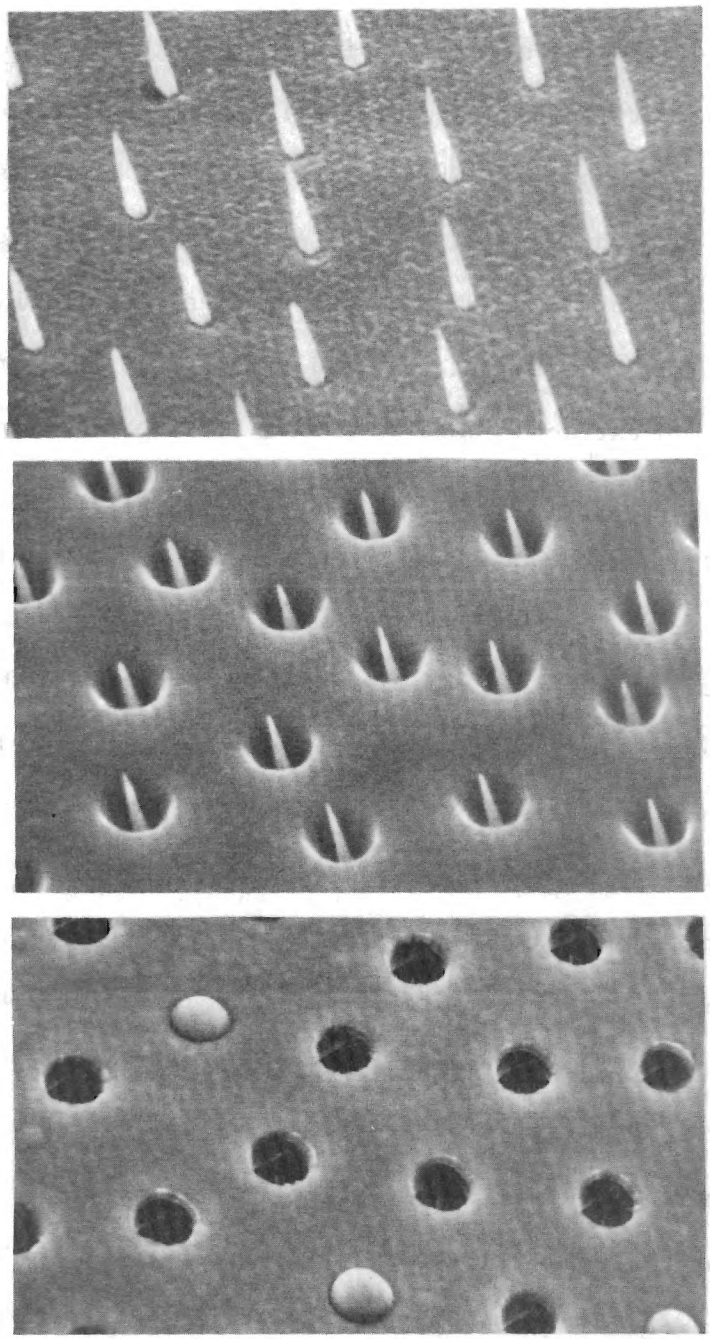

Figure III-4. SEM Sequence of Double Deposition 14/15 Showing (a) Pointed W Fibers, (b) After Depositing 1.25 μm Al_2O_3 and Cleaning, and (c) Final Structure After a Second 1.25 μm of Al_2O_3, 0.3 μm Mo and Cathode Cone Removal, 5000X, ϕ = 45°. (Sample JP9-1A2)

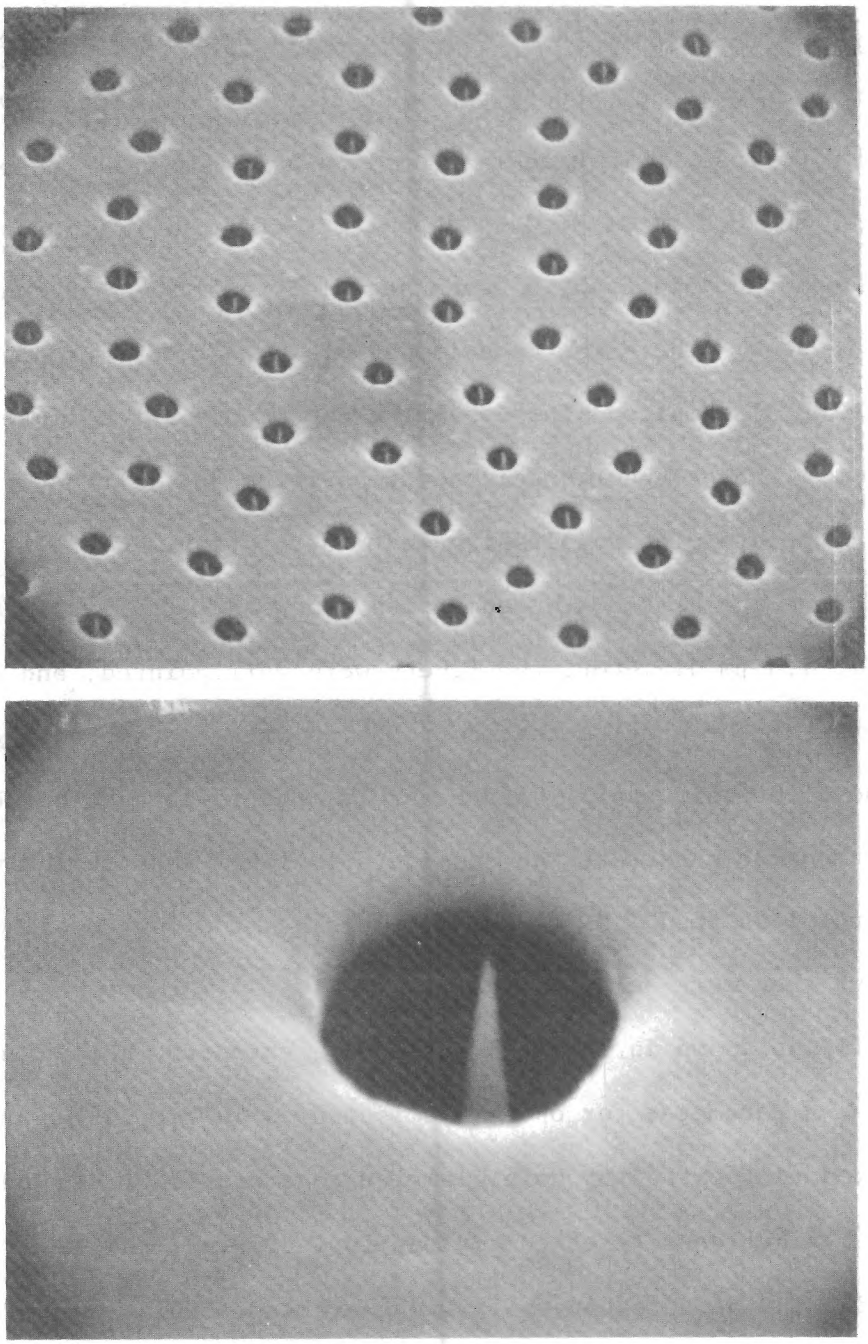

Figure III-5. SEM Photograph of Double Deposition Sample 50.H2-31-2D1 Showing 1.6 μm Extractor Orifice Diameters After Electropolishing.

For double depositions 32/33, processing consisted of depositing 1.0 μm of Al_2O_3 at 0.2 nm/sec in deposition 32 followed by a 10 second phosphoric acid etch to remove the cathode cones. After acid etching, five one minute distilled H_2O rinses were used for complete acid removal. In deposition 33, 0.5 μm of Al_2O_3 and 0.3 μm of Mo were deposited. Post deposition cleaning was a 45 sec phosphoric acid etch, a seven sec electropolish, and ten sec of phosphoric acid etch. There was no evidence of any adhesion problem as experienced in Deposition 31 samples. Thus the five one minute water rinses were sufficient to remove all the phosphoric acid for Deposition 32. Extractor hole diameters were 1.4 μm before electropolishing and 1.6 μm after. Overall, the LVFE epo-sition 33 were the best UO_2-W geometries produced. The extractor hole diameter were small, 1.6 μm diameter, the fibers were well pointed, and the fiber heights, h, for seven of the samples ranged from even with the top of the extractor to 1.4 μm above the extractor. Unfortunately, the resistance between the extractor and the composite substrate was considerably lower than recently experienced, ranging from less than 1 MΩ to 20 MΩ. This was too low to allow CW emission testing but they were pulse tested.

As will be shown in Chapters IV and V, extractor hole diameter is not as critical a parameter for optimum emission as is tip radius and work function. However, reducing extractor hole diameter does provide field enhancement and as the spacial fiber density of composites is increased, reduction of extractor orifice size may be necessary to prevent overlap. This section has demonstrated that double deposition can provide extractor orifice diameter reduction where needed as shown in Table III-2. Double deposition provided extractor orifice diameters an average of 52% of what would have been obtained with single deposition. Thus, the technique does work successfully and if proper attention is

Table III-2. Double Deposition Geometries.

Deposition	Insulator Thickness (μm)			Extractor Hole Diameter (μm)	
	Deposition 1	Deposition 2	Total Observed	Observed!	Single Deposition Equivalent
12/13*	2.1	1.5	3.6	2.2	3.8
14/15	1.25	1.25	2.5	1.6	2.6
30/31**	1.2	0.8	2.6	1.2	2.7
32/33	1.0	0.5	2.6	1.4	2.7

*SiO_2 was deposition to 0.1 μm thickness at the first of each deposition to act as a parting layer. The parting layer resulted in poor adhesion and was not used subsequently.

**Insufficient phosphoric acid removal between depositions 1 and 2 resulted in poor adhesion between the 1st and 2nd Al_2O_3 layers.

!Extractor hole diameter before electropolishing.

given to cleanliness and solvent removal, adhesion is sufficient to prevent peeling between layers. Note that an expected reduction of leakage current due to reduced hole diameter to insulator thickness ratios was not observed. The leakage exhibited by LVFE samples prepared by double deposition was not significantly different than that observed with single deposition samples.

C. INSULATOR QUALITY

The goal of the insulator quality section was to improve the insulator resistance to the point that leakage current would be reduced to a few μA with 100-200 volts applied across the insulator. At the start of the contract, the bulk resistivity of the SiO_2 insulator was low enough (10^8-10^{10} Ωcm) to provide leakage current in the mA range at 100-200 volts. Approximately six months after contract initiation, Al_2O_3 was substituted for SiO_2 as the insulator which provided an increase in resistivity to 10^{13}-15^{15} Ωcm at low voltages. However, the Al_2O_3 had to be chemically cleaned and 85% phosphoric acid at 100°C was found to work well. With an increase in insulator bulk resistivity a reasonable percentage of samples had high leakage due to mechanical shorts caused by molybdenum flash from leaning fibers. Thus, electropolishing the extractor in sulfuric acid was developed as a technique for cleaning the extractor. Finally, the electrical properties of electron beam evaporated Al_2O_3 was investigated to optimize deposition parameters to provide reduced leakage through the insulator. The Insulator Quality section is therefore divided into (1) Insulator (Al_2O_3) Cleaning, (2) Extractor (Mo) Electropolishing and (3) Insulator Conduction.

1. Insulator (Al_2O_3) Cleaning

For the first three months after switching to Al_2O_3 as the insulator, the Al_2O_3 was cleaned with 10% HF acid, and it did dissolve the high surface area Al_2O_3 deposits on the fibers and insulator cone walls. However, little or no attack could be observed on the bulk Al_2O_3 deposit. Thus smoothing or recessing the insulator under the Mo extractor was not possible.

After trying several etches, major improvement in cleaning Al_2O_3 was adopted. As reported in numerous references, 85% phosphoric acid etches Al_2O_3 and at a temperature of 100°C the amorphous Al_2O_3 was dissolved at a usable rate. The acid uniformly dissolved Al_2O_3 from the insulator cone walls without causing attack at the Al_2O_3/UO_2 interface. Using the 85% phosphoric acid at 100°C, the Al_2O_3 insulator, as deposited under the LVFE conditions (i.e. 0.2 and 0.5 nm/sec at 400°C), was dissolved at a rate of 10-15 nm/sec. Etching times of 15-30 seconds have been found to be satisfactory for cleaning Al_2O_3 from the W fibers and smoothing insulator cone walls without causing any adverse effects. It should be noted that for samples which showed increased electrical conductivity across the insulator after phosphoric acid etching, almost all had mechanical shorts visible in the SEM.

An example of the cleaning possible is shown in Figure III-6 where the Al_2O_3 was dissolved for 60 seconds. The insulator is recessed to the point that the extractor is being supported by post of Al_2O_3 at the largest areas of Mo between the extractor holes. It should be noted that samples from Deposition 21 were deposited at 580°C and after 100°C phosphoric acid etching bumps of material approximately 80 nm in diameter remained on the W fibers. After etching samples from Deposition 24 for 50 seconds in 100°C phosphoric

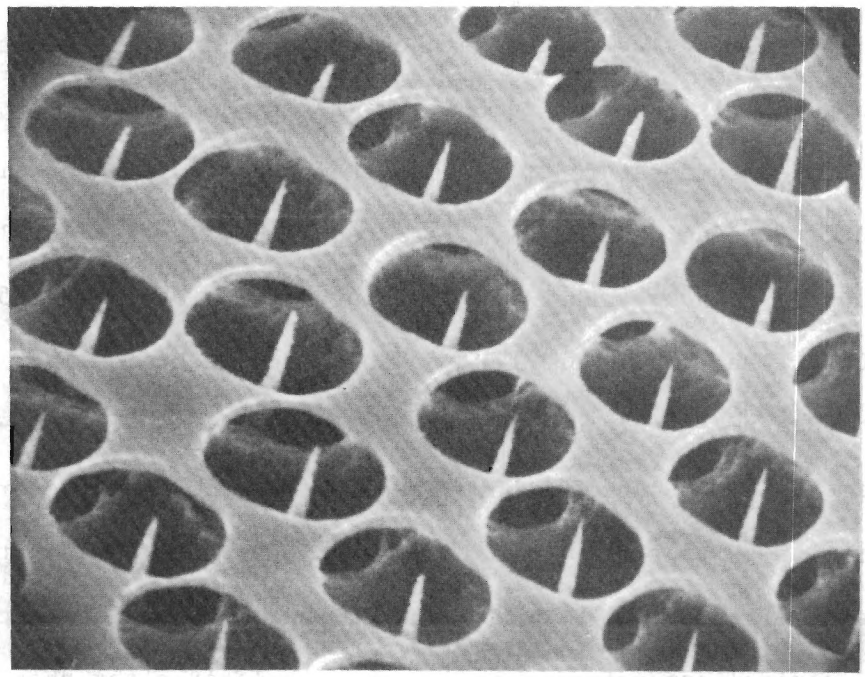

Figure III-6. SEM of Sample UNK-21-1A1 After Etching in 85% Phosphoric Acid for 60 Seconds at 100°C, 5.0KX, $\phi = 45°$. Note that the Al_2O_3 Insulator is Severely Recessed Under the Mo Extractor.

acid, an Al_2O_3 sheath still encapsulated the tungsten fibers. Deposition 24 had been deposited at 500°C but the samples contained 300 nm of Al_2O_3 deposited at 700°C in deposition 22. Normally, this length of etching would clean the fibers. The conclusion was drawn that at 580°C, a small amount of Al_2O_3 crystallization occurred on the fibers and the crystallized Al_2O_3 was much more resistant to acid solution. At 700°C (Deposition 22) all the Al_2O_3 deposited must have crystallized and was completely resistant to the 100°C phosphoric acid. The Al_2O_3 deposited in 24 at 500°C etched very well. Thus, in order to completely clean the Al_2O_3 insulator in the 100°C phosphoric acid etch, Al_2O_3 deposition must be made with the composite substrates below 580°C. All depositions subsequent to 24 were therefore deposited below 500°C to ensure proper Al_2O_3 post-deposition cleaning.

2. Extractor (Mo) Electropolishing

It had been realized for some time that it is highly desirable to clean Mo deposits from the sides of the extractor holes. These deposits are the result of W fibers that are not perpendicular to the UO_2 substrate surface. An example of these deposits in an extreme case is shown in Figure III-7a where sample UNK-21-1A1 was etched in phosphoric acid to clean the Al_2O_3 and shaken ultrasonically in H_2O to remove as many of the Mo caps as possible. However, as shown, the Mo caps were still present after ultrasonic cleaning and increased cleaning times does not remove caps of this type.

The first two techniques attempted for cleaning the Mo extractor were unsuccessful. These consisted of boiling in concentrated hydrochloric acid (HCl) for up to 3 minutes and ultrasonically vibrating in aqueous HNO_3 (diluted 1:3) for up to 3 mintues. Neither treatment appeared to provide any

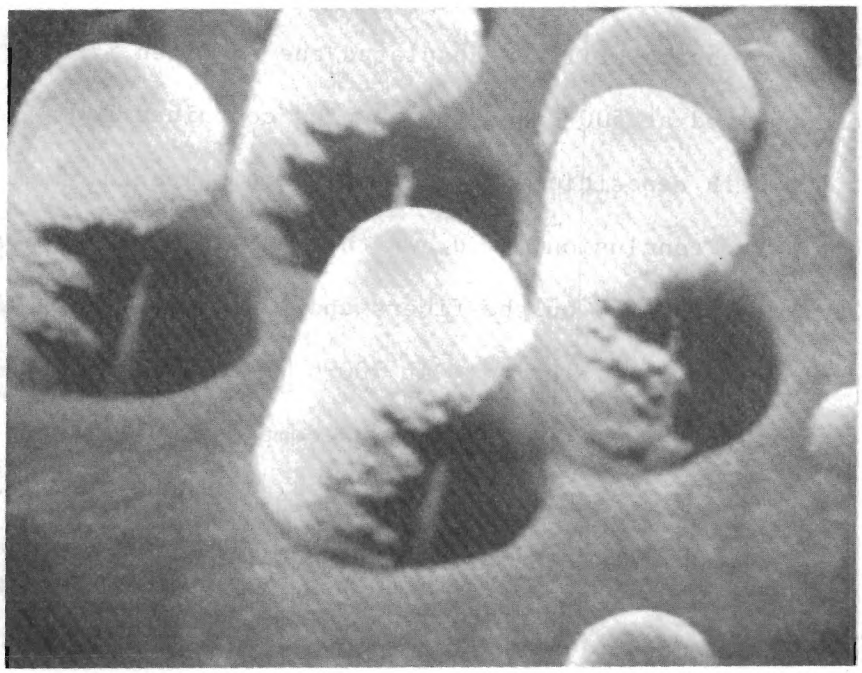

(a)

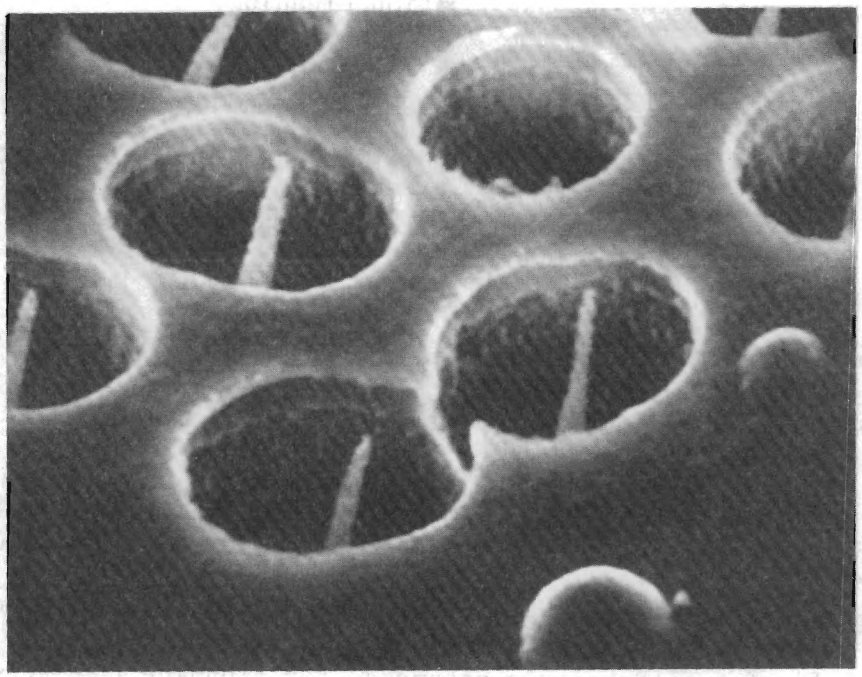

(b)

Figure III-7. SEM of Same Area of Sample UNK-21-1A1 (a) Before Electropolishing and (b) After Electropolishing 5 Seconds, 10 KX, $\phi = 45°$.

visible attack on the Mo extractor.

The technique developed, that was extremely successful in cleaning the extractor, consisted of electropolishing in 98% H_2SO_4 for 2-30 seconds with seven volts dc applied to the Mo extractor. The experimental apparatus is shown schematically in Figure III-8. A pair of teflon tweezers was adapted as a sample holder and equipped with a platinum electrode so that contact was made only to the Mo extractor, which served as the anode in the electropolishing cell. A platinum sheet fifty mm square served as the cathode. Best results were obtained by electropolishing while vibrating in an ultrasonic bath. The electropolish voltage was determined by measuring the I-V characteristics of the cell using bulk Mo as the anode, Figure III-9. The correct voltage occurs on the constant current plateau, at a voltage just below that necessary to cause increasing cell current. Since the current increases at $\sim$8 volts, seven was selected as the optimum electropolish voltage.

The results of electropolishing are shown in Figure III-7b where sample UNK-21-1A1 was electropolished for 10 seconds. Note that Figure III-7a and III-7b are of the same area. The improvement in the extractor geometry is evident as removal of Mo caps left by leaning fibers is not routine and complete.

During electropolishing the Mo extractor, which was 2.5 mm in diameter, the polishing current equilibrated at $\sim$2 mA, or at $\sim$40 mA/cm^2. For these conditions, the extractor hole radii increased at $\sim$10-20 nm/sec. Examples of an electropolished extractor may also be seen in Figure III-5 and may be compared to unpolished extractors in Figures II-12 and III-4. The electropolishing has been very successful in removing shorts between fibers and the extractor caused by broken Mo caps as shown in Figure III-7. In addition, with sharp

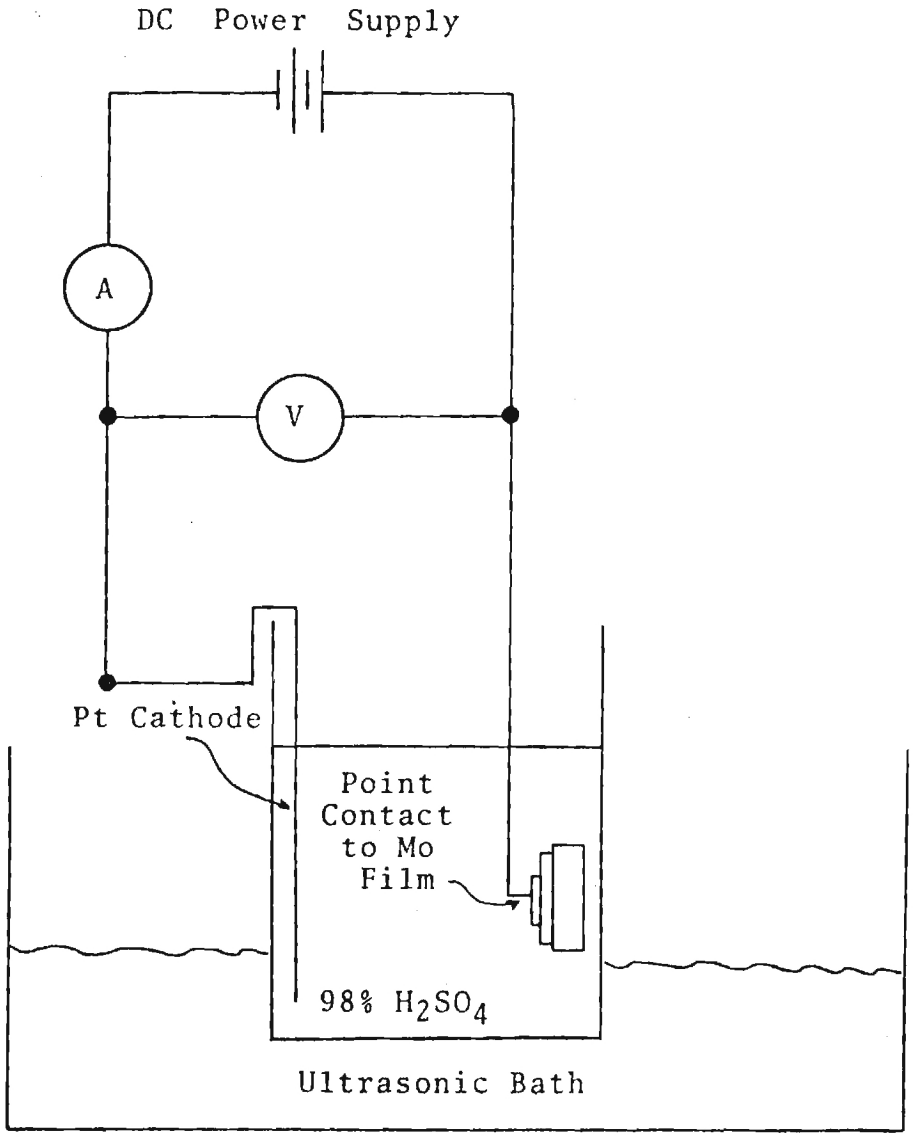

Figure III-8. Schematic Diagram of Molybdenum Extractor Electropolishing Apparatus.

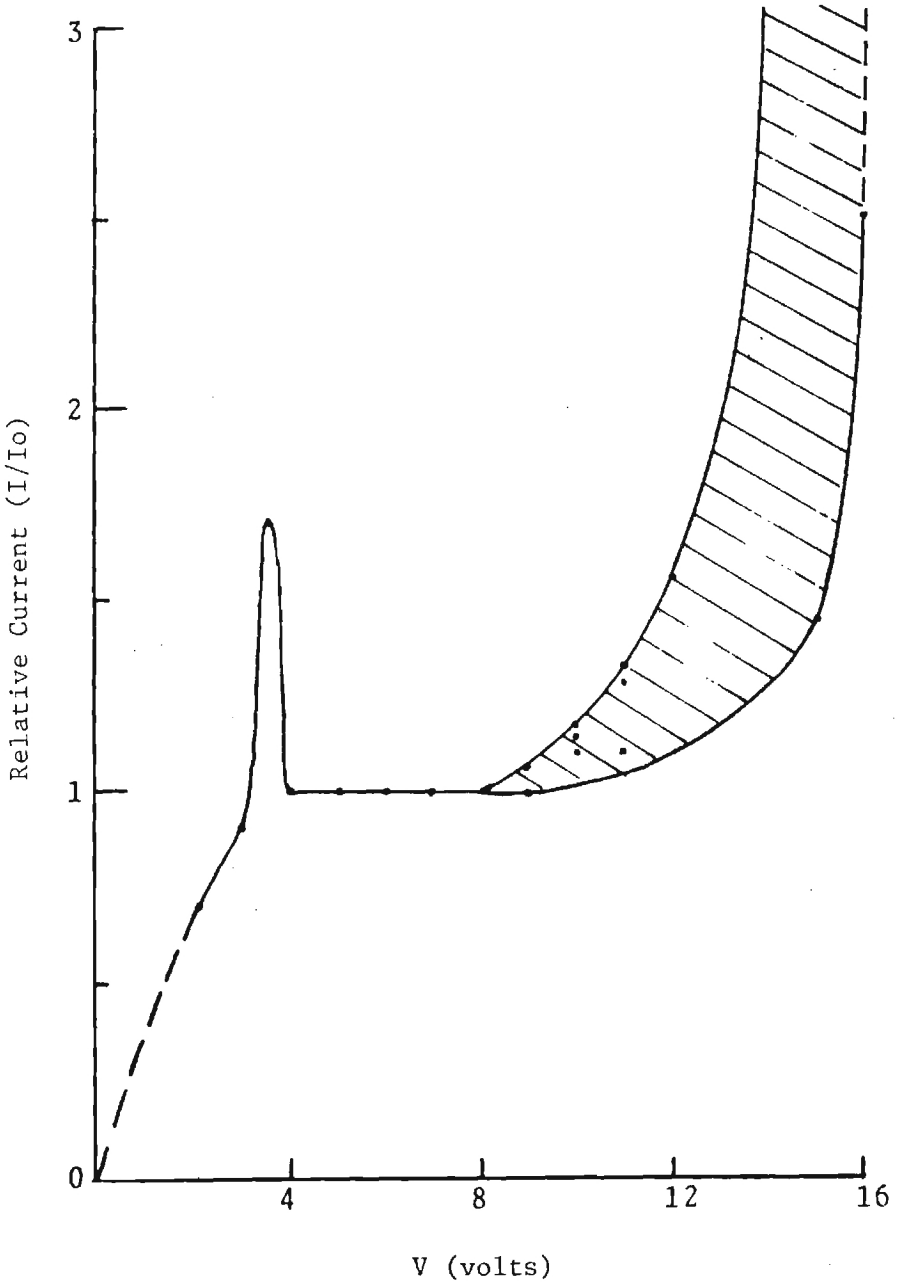

Figure III-9. Current-Voltage Relationship for Molybdenum Electropolishing in 98% H_2SO_4.

corners removed from the extractor, the tendance to arc must be reduced.

3. Insulator Conduction

At the start of the contract, electron beam evaporated SiO_2 was used as the insulator and leakage currents during LVFE emission testing were typically in the range 1-20 mA. During the first three months of the contract, the insulator was changed to Al_2O_3 primarily due to the V-I characteristics of capacitors fabricated from SiO_2 in Deposition 11 and Al_2O_3 in Depositions 10 and 16, Figure III-10. As can be seen, conduction through the Al_2O_3 appeared capable of dc operation to above 200 volts. Consequently, the electrical properties of electron beam evaporated Al_2O_3 were measured and published in a Ph.D. dissertation by R. V. Kolarik[7]. The results of this dissertation are summarized below. Concurrent with the measurement of Al_2O_3 electrical properties using capacitors, the insulator I-V characteristics of operating LVFE's were monitored for comparison. These results are also presented below and, as will be detailed, the capacitor properties were not indicative of the insulator characteristics in operating LVFE's.

a. Electrical Properties of Amorphous Al_2O_3

The primary objective of this work was to characterize the ac and dc conduction of the Al_2O_3 films produced under the same conditions as those in the LVFE device. Four evaporant sources of varying purity were used to produce metal-oxide-metal test capacitors on glazed substrates. These were: Linde C 1.0 μm Powder, 99.979 w/o Al_2O_3; Baikowski 1.0 μm Powder, 99.990 w/o; Linde Sapphire, 99.992 w/o, and Crystal Systems Sapphire, 99.996 w/o. The Al_2O_3 deposited at a substrate temperature of ∿460°C at 0.4 nm/sec was found by x-ray diffraction to be amorphous. Film density was determined by a

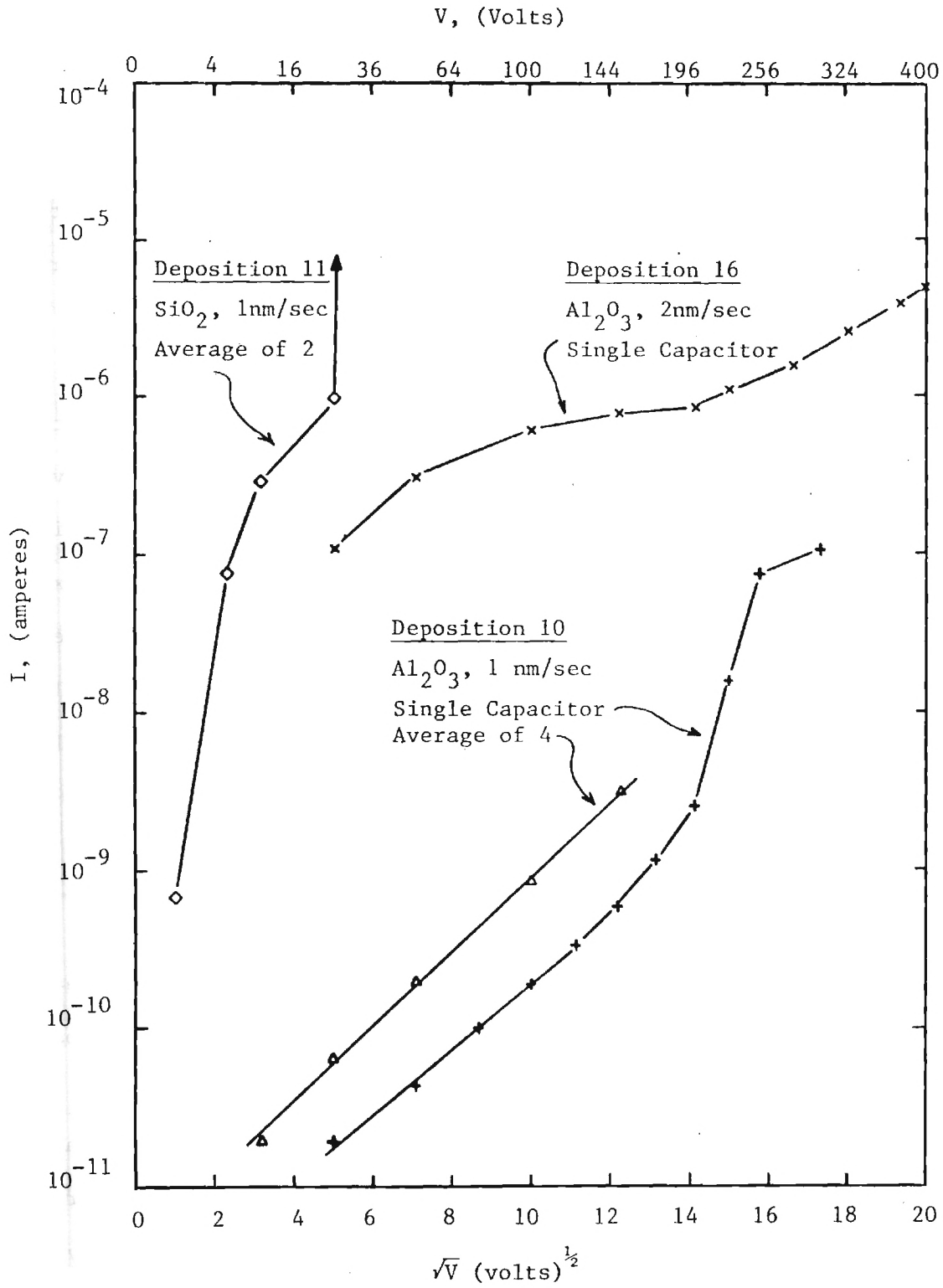

Figure III-10. Comparison of Conduction of 1 μm Thick SiO_2 And Al_2O_3 Films Deposited on Al_2O_3 Substrates.

weight-and-measure technique to be 2.7 gm/cm^3.

All conduction measurements were made in a vacuum of 10^{-4} torr (13 mPa) or better (normally $1x10^{-5}$ torr = 130 mPa) using a one point probe technique and the molybdenum-alumina-molybdenum capacitors described earlier. Both ac and dc measurements were made from 20° to 325°C and ac measurements over the frequency range 60 to 10^5 Hz at peak to peak voltage of 8 volts.

A general radio capacitance, an oscillator, and an oscilloscope, Figure III-11, were used to measure sample capacitance Cx from which the real dielectric constant, K', was calculated from Cx/Cv where Cv was vacuum capacitance for the device geometry. Analysis of the bridge circuit indicated that Cx was actually the parallel circuit capacitance so that Cx did provide the real component of the dielectric constant. The loss tangent, tan δ, was measured and the imaginary dielectric constant, K", was calculated from K' tan δ. The ac conductivity or dielectric conductivity was calculated from

$$r_d = \omega \varepsilon_o \varepsilon''$$

where ω is frequency, ε_o is vacuum permittivity, and ε'' is the imaginary permittivity equal in value to K". Dc measurements were with the apparatus shown schematically in Figure III-12.

Analysis of the ac data began with the examination of the loss as a function of frequency. The imaginary permittivity, which is a measure of the performance of a material as a dielectric, was used in this analysis rather than the loss. Plots of the imaginary dielectric constant, K" (equal to ε'', imaginary relative permittivity), were made for all samples tested

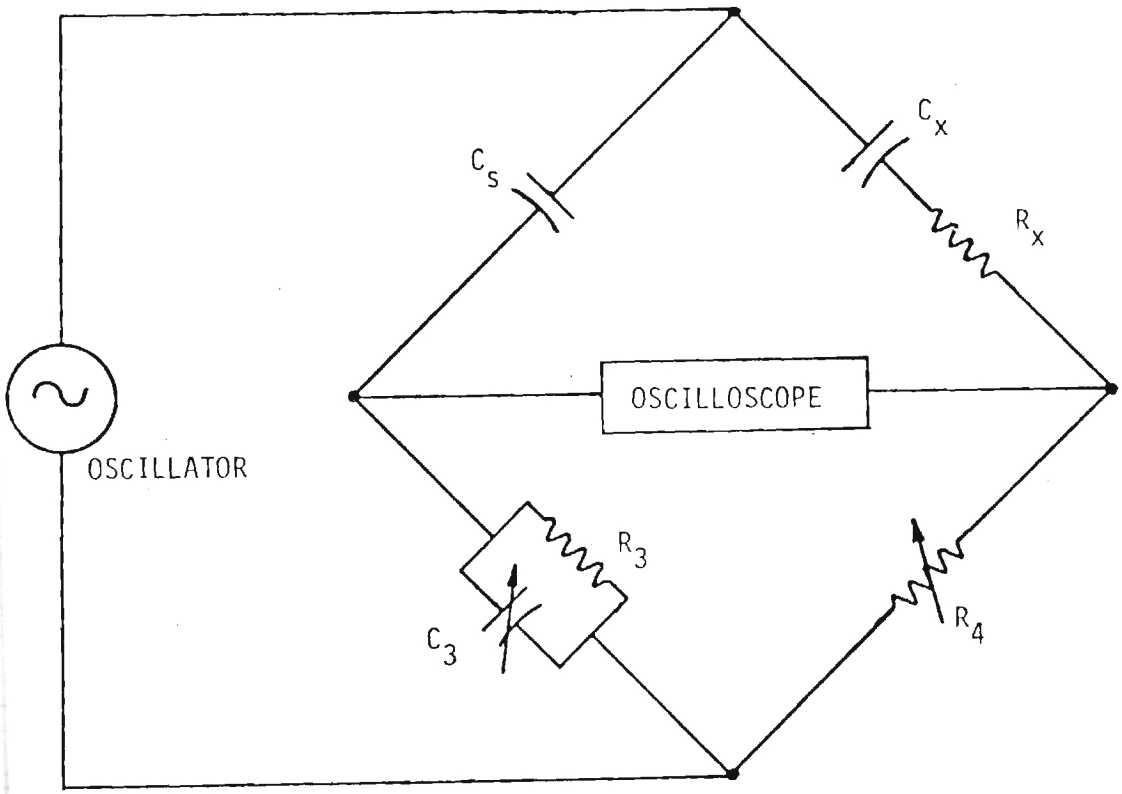

Figure III-11. Schematic Diagram Showing the Schering Bridge Circuit Used in the General Radio Type 716-C Capacitance Bridge.

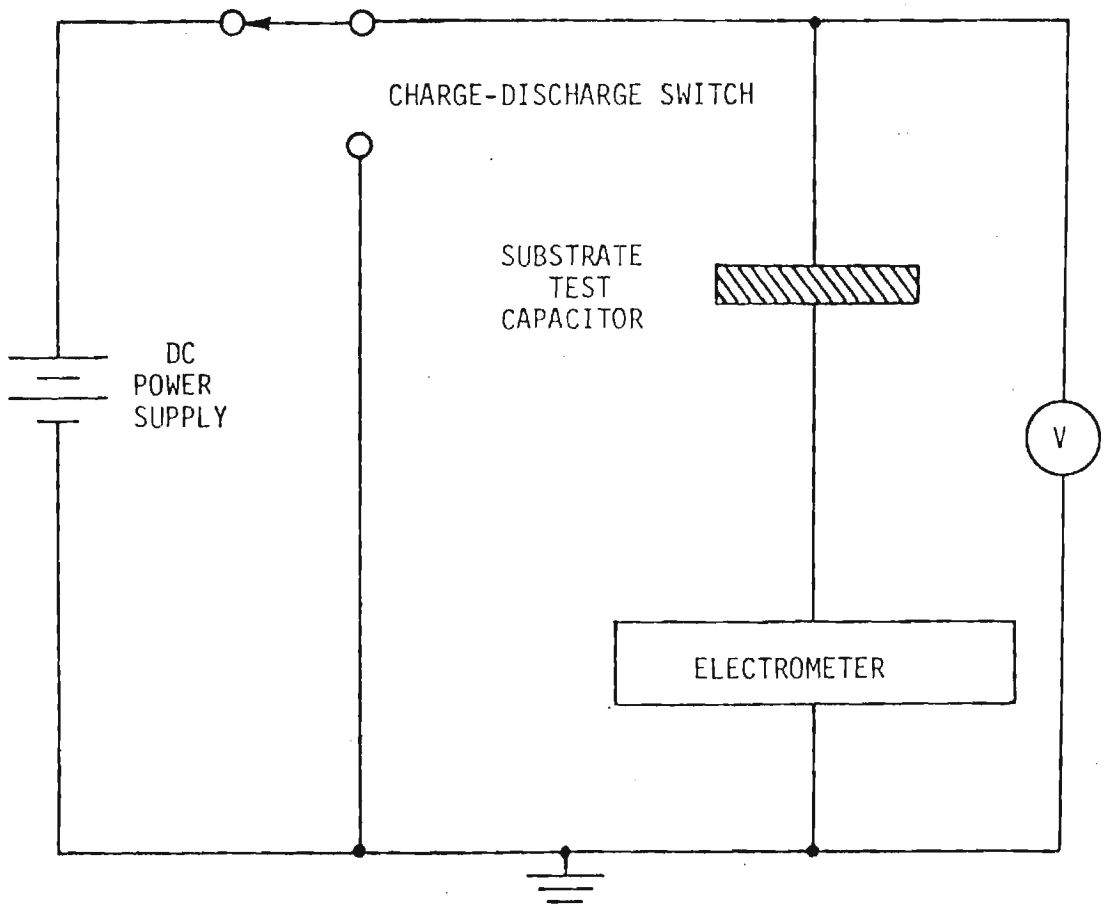

Figure III-12. Schematic Diagram of the Basic Circuit Used in the DC and Charge Storage Measurements.

for the temperature extremes. A typical plot is shown in Figure III-13. The curves at room temperature showed only a small increase, if any, as the frequency decreased. The K" for the 325°C data increased only slightly more than the room temperature values. The increasing trend with decreasing frequency was interpreted as the beginning of the migration of a low-frequency mechanism peak, such as interfacial polarization or ion hop into the measured frequency range.

The real dielectric constant, K' (equal to ε', the real relative permittivity), for the temperature extremes was included in the plot of K" as a function of frequency, Figure III-13. The K' value changed only slightly for all samples over the frequency range tested. This result agreed with the literature[8] and the trends seen by Birey.[9] Dielectric constants were higher than reported in the literature (13-16 compared to 9-12). This was probably a result of the density being lower than normal (2.7 compared to 3.1-3.2). Lower density films should allow greater polarizability of the oxygen ions, thereby increasing the dielectric constant.

Ac conductivity exhibited a frequency dependence as shown in Figure III-14. The slope, P, of the log σ_{ac} vs. log frequency curve was unity, within the error of the measurement, in nearly all tests conducted at room temperature. Very good correlation was seen in most of the data. The P values at 325°C, in general, were less than the room temperature values, but still near unity. Thus frequency-independent conduction was seen in most samples.

Arrhenius conductivity relationships, Figure III-15, generally provided activation energies between 0.05 and 0.10 eV. This activation energy range coupled with frequency independent conduction led to the conclusion that

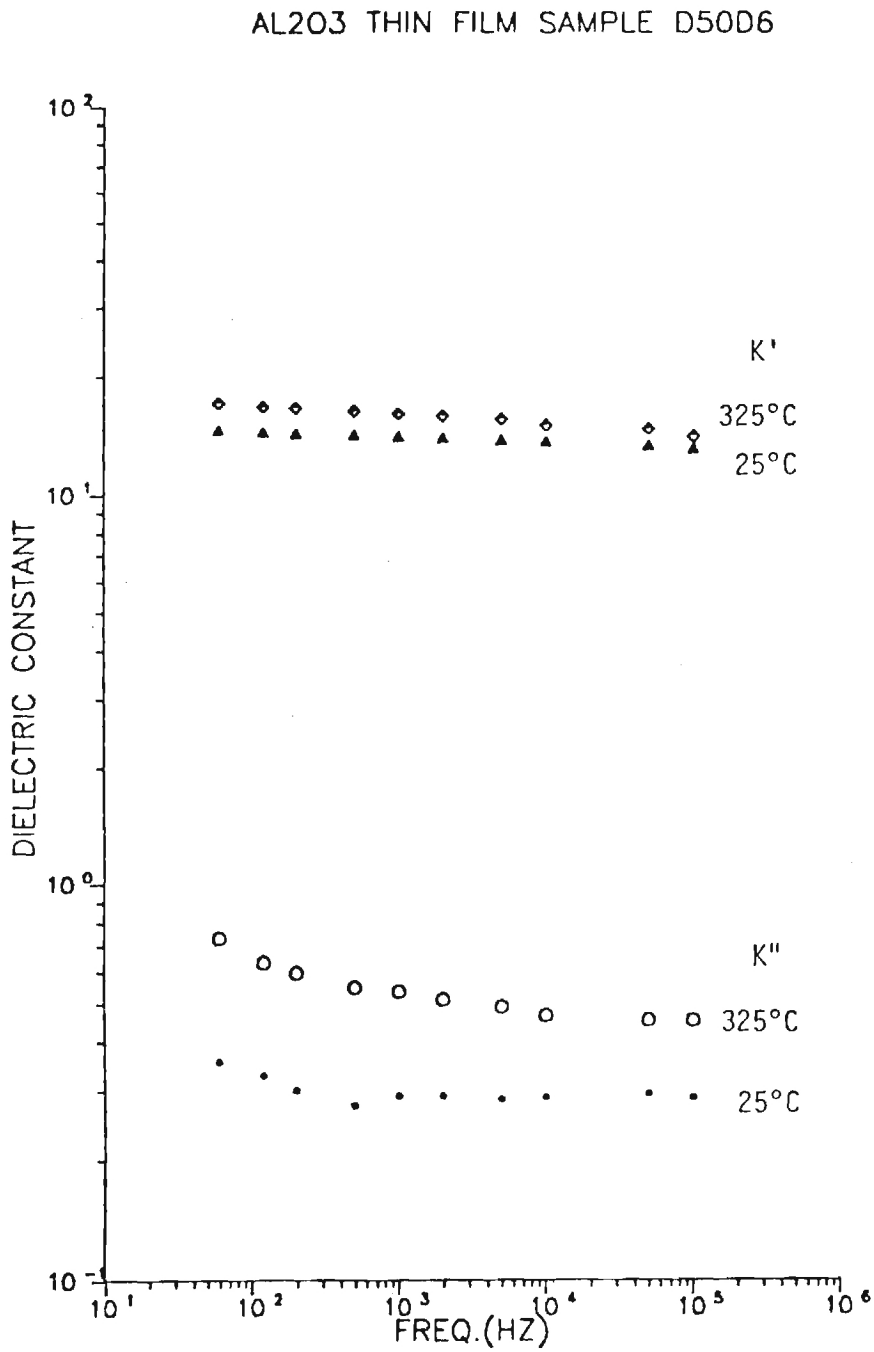

Figure III-13. Typical Plot of the Imaginary Dielectric Constant as a Function of Frequency at the Temperature Extremes. Also Included is the Real Dielectric Constant (D50d6).

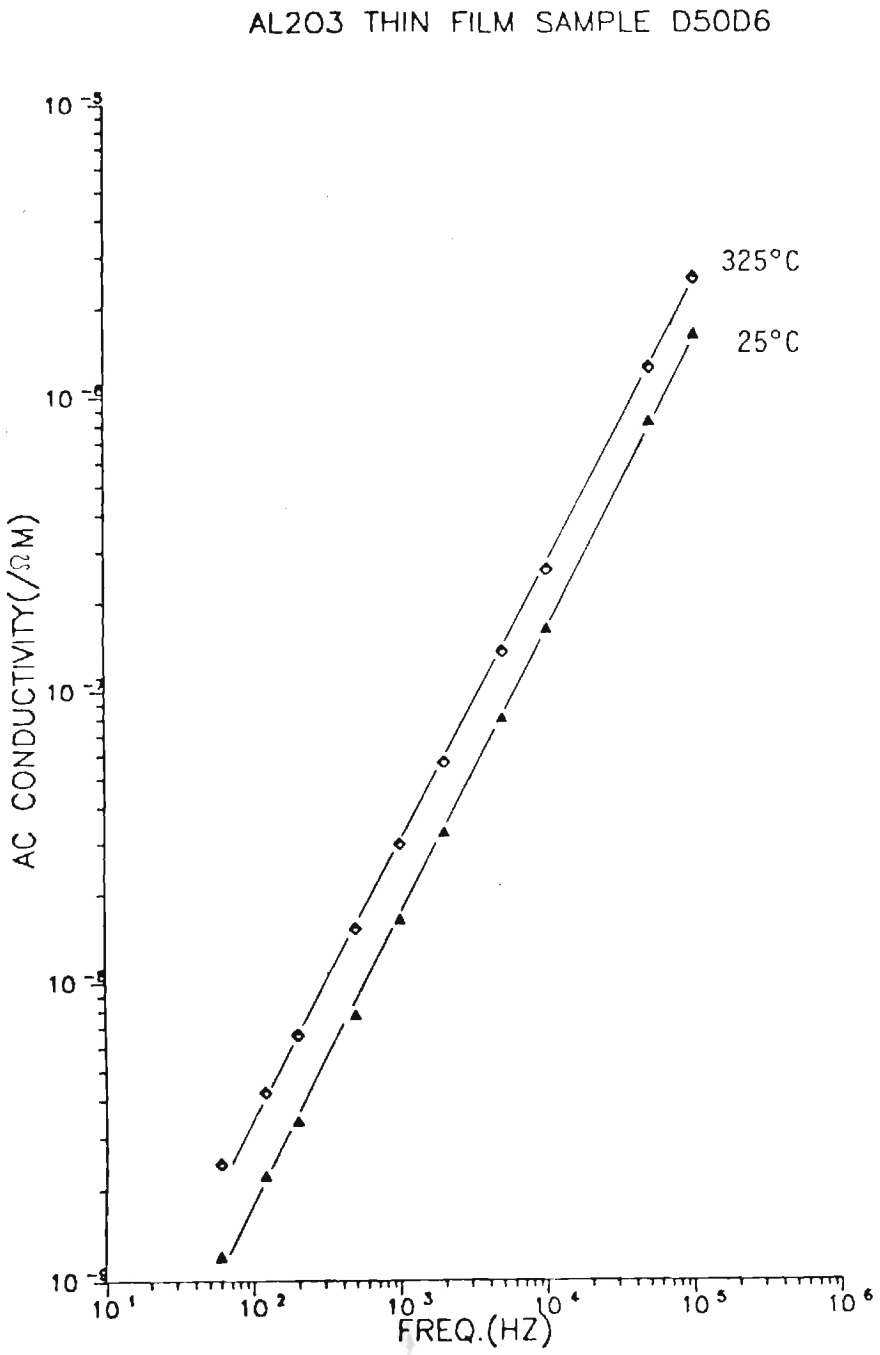

Figure III-14. Typical Ac Conductivity Plot as a Function of Frequency at the Temperature Extremes (D50d6).

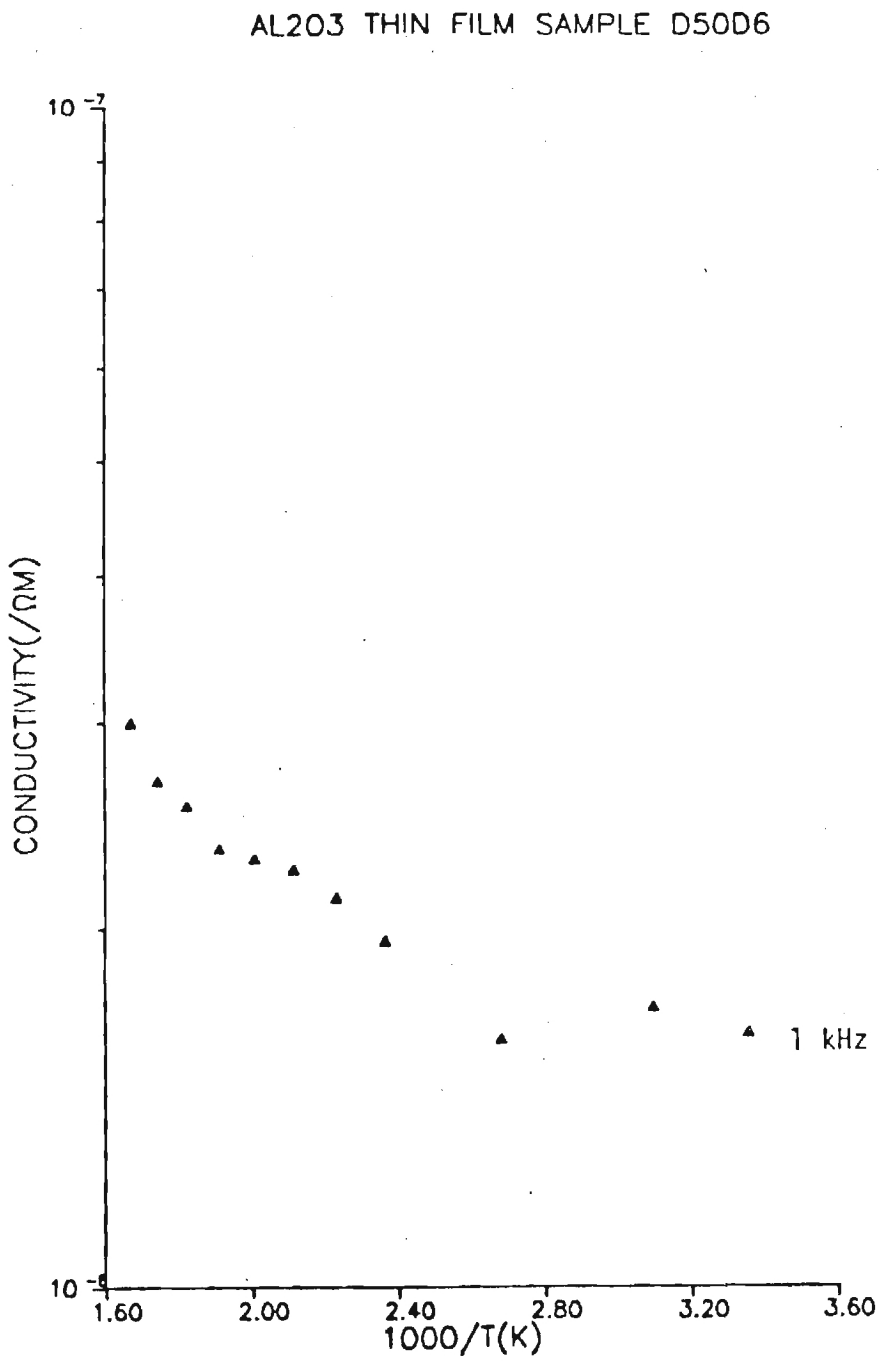

Figure III-15. Typical Ac Conductivity at 1 kHz as a Function of Reciprocal Temperature Plot (D50d6).

electron hop was the ac conduction mechanism present in the amorphous alumina. This was consistent with the low field conditions, 0.1 MV/cm, for the measurements. It should be noted that ac properties of all evaporant sources were very similar.

Analysis of dc conduction mechanisms indicated that at low fields, less than 0.1 MV/cm, space charge limited conduction was prevalent in many of the capacitors. As the field was increased (0.2 to 0.5 MV/cm) trap filling or electron movement into trapping levels in the conduction band was observed in the less pure evaporants, Figure III-16. At high levels (0.5-1.2 MV/cm), the higher purity Al_2O_3 sources exhibited either Poole-Frenkel or Schottky dominated conduction. An example of Poole-Frenkel conduction is shown by the linear portions of the curves for ln J/E vs $V^{\frac{1}{2}}$ in Figure III-17.

Energy barrier values from the slopes of log current density vs reciprocal temperature were used in conjunction with V-I characteristics to delineate the various conduction mechanisms. However, perhaps the best indicator of insulator quality can be seen from the log J vs 1/T plots of Figure III-18 where dc current at 25 volts applied to the capacitors is shown comparing all the Al_2O_3 sources. The Baikowski powder was consistently the best insulator, providing the lowest current for the highest temperature. Powder sources compared to single crystal also provided the best evaporation characteristics by forming large stable molten pools without exhibiting channeling during electron beam bombardment. Figure III-18 also shows some of the problems experienced with leakage in operating LVFE's as indicated by the large variation in conduction from evaporation to evaporation. As a result of these measurements, the Baikowski powder is being used exclusively for the insulator evaporant source.

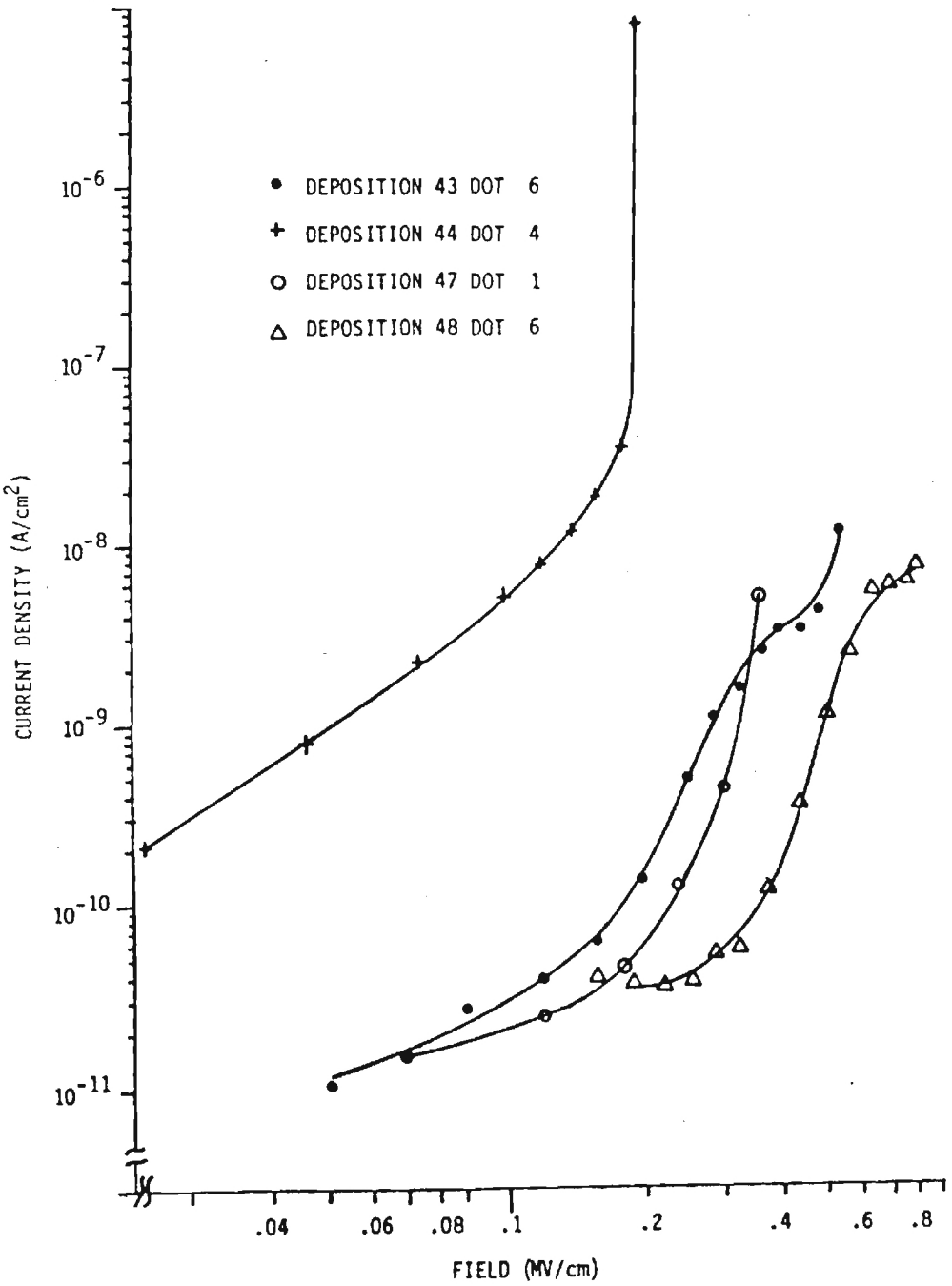

Figure III-16. Current as a Function of Field Plot for Samples From Depositions 43, 44, 47, and 48.

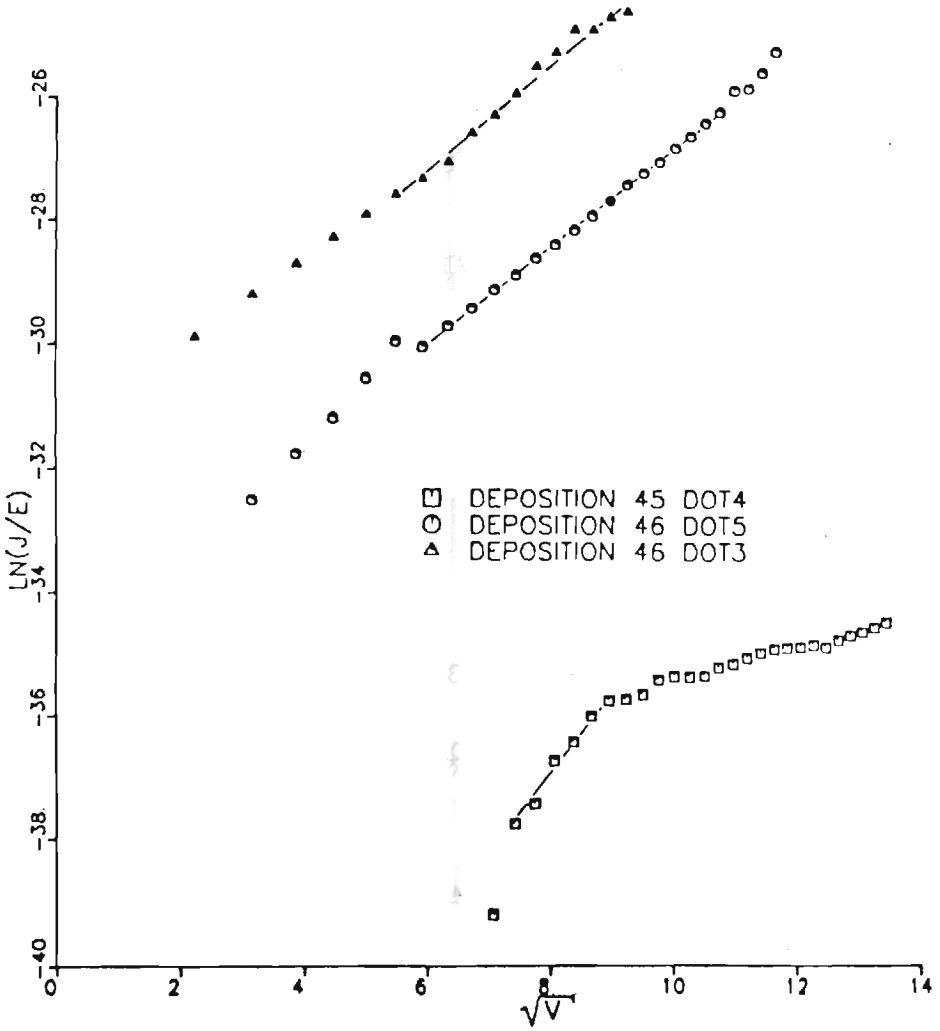

Figure III-17. I-V Dependence for Deposition 45 (Low-Field) and 46 Capacitors Using the Poole-Frenkel Analysis (In J/E vs. $V^{1/2}$).

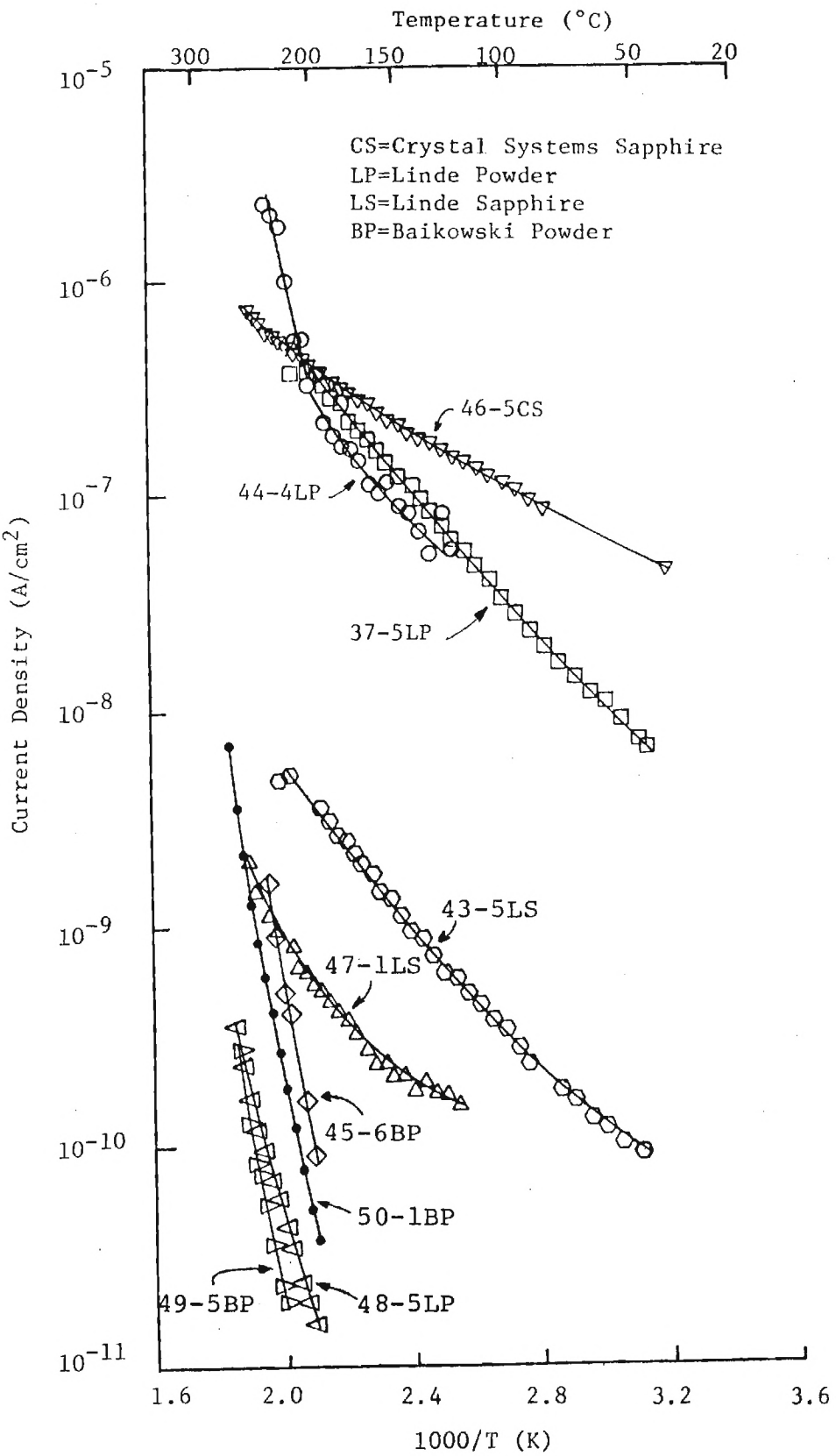

Figure III-18. Comparison Log of Current Density vs Reciprocal Temperature for Various Al_2O_3 Sources at 25 V Applied to ∿ 1.5μm Capacitors.

b. Leakage in LVFE's

At the start of the contract, leakage current was generally in the 1-20 mA range when LVFE's were operating in the 100-200 volt range. Use of Al_2O_3 as the insulator significantly reduced leakage current. Before deposition 20, mechanical shorts due to molybdenum from cathode cones bridging between a fiber and the extractor prevented emission testing of a high percentage of the LVFE's fabricated. After phosphoric acid cleaning of the Al_2O_3 and electropolishing of the extractor was developed, the V-I characteristics of the Al_2O_3 insulator was similar to the capacitors in the above discussion. With the initiation of emission in the voltage range of 60-80 volts (i.e. $\sim$0.3-0.4 mV/cm across the insulator), intercepted emission combined with the bulk conduction through the insulator made comparison of the LVFE insulator with the capacitors impossible. However, as extractor voltage was increased to the 120-150 volt range ($\sim$0.6-0.75 mV/cm) to obtain emission currents in the A/cm^2 range, the leakage current increased to the 0.1-5 mA range. Most of this leakage current was the result of degredation of the insulator under long term (2 days to 2 weeks) high field conditions. Some capacitors tested at high fields (0.5 to 1.0 mV/cm) maintained low conduction but the majority did not. For most UO_2-W LVFE's, emission was ultimately terminated by the excessive leakage current. It was primarily because of excessive leakage current that the LVFE base was changed from the conductive matrix UO_2-W composite to the insulating matrix ZrO_2-W composite, ZYW.

D. COMPOSITE ETCHING

In order to optimize the LVFE structure, exposed fiber arrays

exhibiting minimal variations in fiber height and oxide matrix roughness are required. At the start of the contract, the etching apparatus employed did not provide reproducible flow conditions and the surface of the samples was sufficiently rough to prevent thin film deposition on approximately 30% of the samples etched.

The apparatus shown in the schematic diagram in Figure III-19 was designed and constructed to provide reproducible flow conditions. It consisted of a regulated DC power supply, a variable-speed (0-30 rpm) DC motor and a digital voltmeter to monitor the voltage applied to the motor. The motor was used to rotate a platform holding a container (100mm diameter x 25mm deep) of the etching solution. Etching was produced by positioning the 4.2 mm diameter composite discs 38 mm from the center of rotation of the etch with the disc surface perpendicular to the etchout flow. Etchout velocity was varied from 20 to 120 mm/sec by controlling the rotation of the etchout container from 5 to 30 rpm respectively.

To allow etching of a large number of samples, and to ensure that the same technique was being used by all investigations, the etching facility was consolidiated into a single unit. A sample raising/lowering mechanism and the etch turntable were mounted to form a single unit. Two sample mounts each holding four samples were fabricated. An arm supporting the multiple sample mount attached to the raising/lowering mechanism and the support arm could rotate 90^{o} to allow rapid rinsing of the samples at the end of etching. With two sample mounts, four samples an hour could be etched continuously. Etching time for pointing was forty minutes, and thirty to forty minutes rinsing was required to completely remove the etch. Thus while one set of samples etched, the other rinsed.

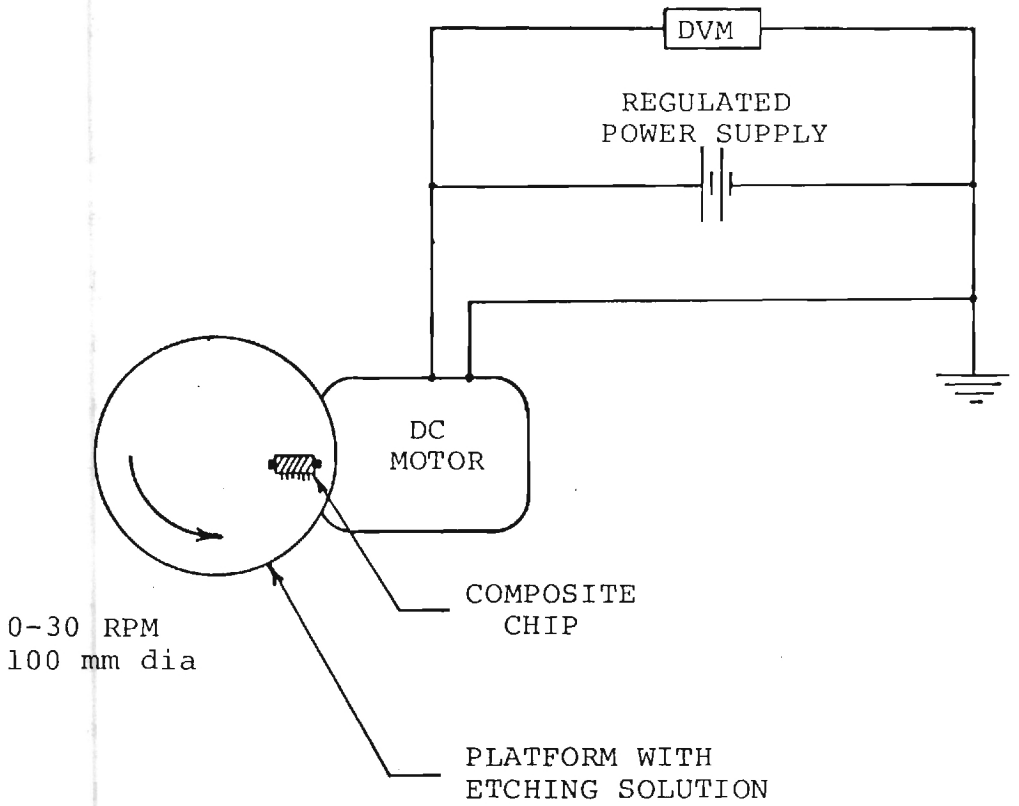

Figure III-19. Schematic Diagram of Etching Apparatus.

A dramatic improvement in smoothness of the UO_2 surface resulted. The flow condition was reproducible to the extent that no sample was rejected for surface roughness when etched at 50-60 mm/sec (12-16 rpm). If the etching flow rate was less than 40mm/sec (10 rpm), the UO_2 surface was rough, probably because a stagnant condition was created and localized variations in etch composition occurred as the reaction proceeded. Etching at flow rates greater than 120mm/sec also produced surface roughness probably due to turbulence.

Etch conditions for the CAHN-P etch were 15 rpm at 38 mm radius (60 mm/sec) for 40 minutes. These conditions produced pointed fiber cone angles ranging from 7 to 13 degrees. On an individual sample, the cone angle variation was generally $\pm 1^{o}$ but from sample to sample variations of $\pm 3^{o}$ did occur. The fiber diameters in UO_2-W ranged from 0.3 to 0.6 μm. On an individual sample the range of fiber diameters was small ± 0.02 μm but from growth run to growth run as experimental conditions changed so did fiber diameter. With the variation etched cone angle ($7-13^{o}$) and fiber diameter (0.3 to 0.6 μm), the range of pointed fiber lengths was 1.5 to 5.0 μm. On an individual sample slight variations in fiber diameter and etch rate of the fiber consistently produced variations of fiber lengths of $\pm 10\%$, i.e., for a sample with 5.0 μm fiber, the length variation would be from 4.5 to 5.5 μm.

Early in the contract, a series of samples were etched with variations in composition near the CAHN-P etch. It was thought that increasing the HNO_3 and HF contents of the etch would attack the tungsten fiber faster and increase the cone angle. Results did indicate that to be true, but the reproducibility of the results was insufficient to provide conclusive results.

The CAHN-P etch is a complicated chemical solution and some parameter (time after mixing, etch temperature, etc) may not have been controlled sufficiently to provide a narrow range of fiber lengths.

One UO_2-W boule, 50.H2, was grown with larger than normal fiber diameters (0.7 to 0.8 μm) which resulted in fiber lengths too large for LVFE fabrication. To reduce fiber lengths, compositional changes in the etch were made, Table III-3. Increasing the HF and HNO_3 content to 30 ml each (Etch B) resulted in too much attack on the W fibers. Etch A listed in Table III-3 provided fibers of a usable length. Although the effect of compositional changes in the etch are not understood fully, this does demonstrate that some controlled changes could be made to alter fiber cone angles and thus fiber lengths.

Table III-3. Composition of CAHN-P Etches and Fiber Lengths of UO_2-W Sample 50.H2.

	CAHN-P Etch Composition (ml)		
Reagent	Normal	A	B
Chromic Acid	60	60	60
Acetic Acid	40	40	40
HF	23.2	27	30
HNO_3	28.0	30	30
Fiber Length (μm)	5-7	3-4	1-2

CHAPTER IV

EMISSION TESTING

In this chapter, the various aspects of the emission testing program are discussed. The chapter is subdivided into five sections. The first describes the test vehicles and vacuum equipment used in the emission tests. This is followed by a description of the electronic test circuitry for both dc and pulse tests, and the testing procedures. The results of the emission tests are tabulated in the next section, which also includes a brief discussion of the results. The fourth section contains a detailed description of the life test program, including the facilities and electronic equipment. The final section contains an analysis of the residual atmosphere of the vacuum system in which the cathodes were tested and a brief description of the gas analyzer.

A number of UO_2-W LVFE cathodes were tested in a previous program, sponsored by the United States Army Missile Research and Development Command[1]. All of the cathodes were tested in pulse mode at low duty cycles to prevent failure of the SiO_2 insulating film. The test vehicles and procedures were similar to those used in the present program. Several cathodes fabricated during the Army program performed quite well, producing up to 15 A/cm^2 at 170 volts. The highest current density, however, was achieved with a cathode fabricated after that program ended. At an applied extractor potential of 318 V (pulsed), it produced a maximum emission current of 22 mA from an active area 0.3 mm in diameter, corresponding to a current density of 31 A/cm^2.

Part of the first year's work on this program was devoted to building up an LVFE test facility that would provide emission data on as many samples as possible. Since as many as nine cathodes are fabricated in a single deposition

run, it is desirable to obtain emission data on the cathodes as soon as possible, in order to provide adequate feedback to those responsible for cathode fabrication. Changes in fabrication which result in improved emission performance can thus be incorporated in the next deposition run, resulting in rapid optimization of the LVFE structure.

In the second year of the program, most of the time was devoted to emission testing, although minor improvements in the test facility continued. These included fabrication of the collector power supplies for CW operation and completion of the computer-controlled data acquisition system. Although some UO_2-W cathodes were tested in the second year of the program, the majority of the routine emission testing during that period was done with ZYW cathodes, as described in Chapter VI.

A. TEST VEHICLES

A photograph of the vacuum chamber used for the LVFE emission tests is shown in Figure IV-1. The 8 inch diameter chamber has four ports, which permit testing of four cathodes in a single pump down. The chamber is attached to a Perkin Elmer-ULTEK-D-I ion/sublimation pump, enabling rapid pumpdown, with a light bakeout, to pressures in the low 10^{-9} torr range. Pressure is monitored with a Veeco Bayard-Alpert ionization gauge and controller, with the gauge tube mounted in a port on top of the chamber.

There is no indication that an ultra-high-vacuum facility such as the one used here is necessary for operation of the LVFE device. On the contrary, there is evidence that the cathodes will operate at pressures even higher than those commonly found in thermionic-powered tubes today. Nevertheless, since the majority of the cathodes are run up to the point of failure, it is

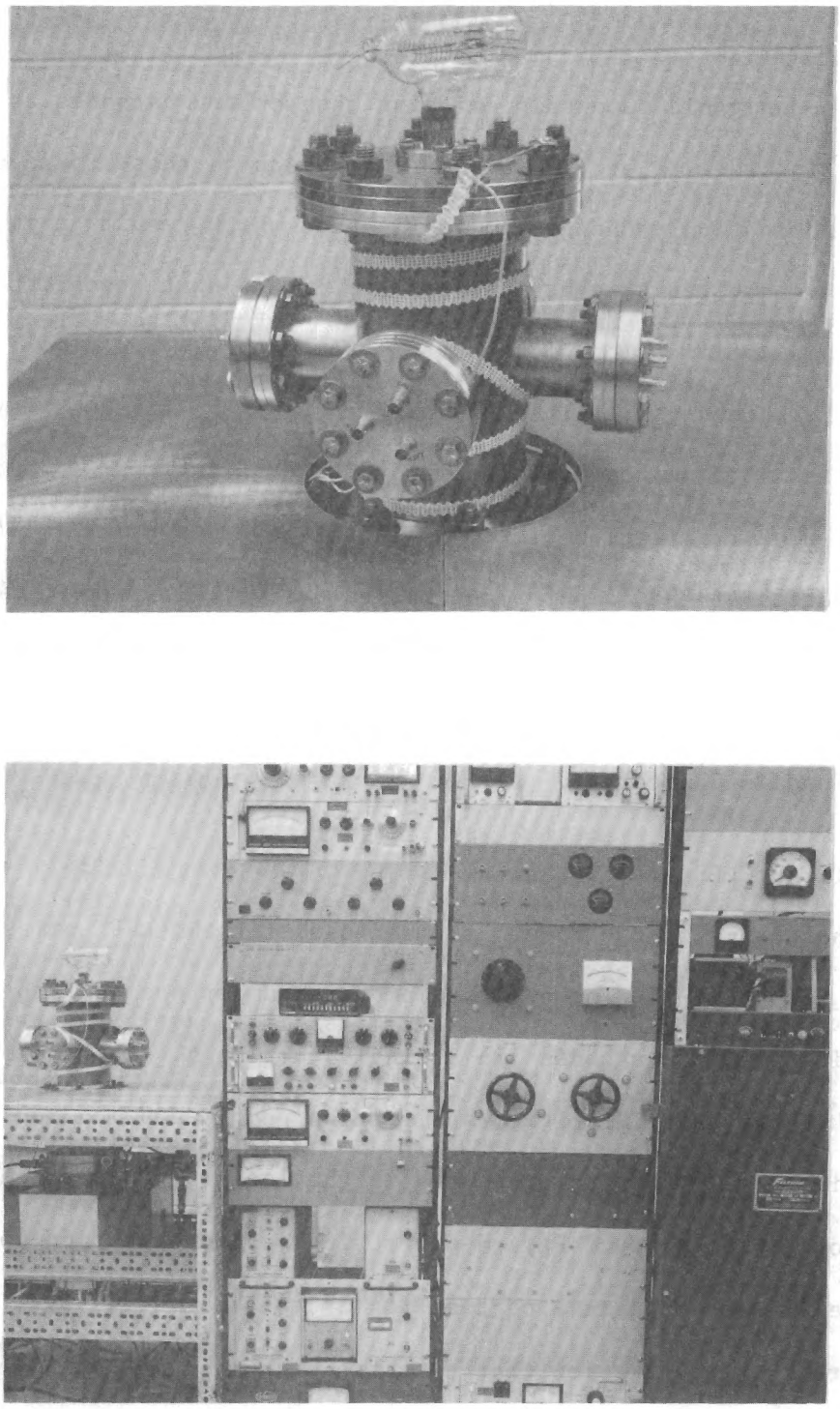

Figure IV-1. Vacuum Chamber and Electronic Test Equipment Used on Field Emission Tests.

desirable to test them under as ideal conditions as possible, eliminating poor vacuum as a possible cause of failure.

Four identical test vehicles, illustrated in Figure IV-2, were used to emission test the cathodes. Each test vehicle was mounted on a 4.5 inch o.d. Conflat flange, which could be bolted directly to the port on the test chamber. A photograph of one of the flange-mounted test vehicles is shown in Figure IV-3. One of the primary concerns in the design of the test vehicles was ease of changing cathodes. The 4 mm diameter cathode chips are affixed to the stainless steel support rod with a silver ink (Engelhard #16) containing a flexible, low-temperature-curing binder. The chip is spring-loaded against the extractor contact (either a wire, or an aperture in a steel plate) which is in turn connected to one of the electrical feedthrus mounted in the Conflat flange. The collector is simply a stainless steel rod, threaded to permit adjustment of the interelectrode spacing.

The strength of the silver ink is sufficient to hold the cathode chip in place for examination, yet low enough that the chip can be easily broken loose and replaced with another. Using these test vehicles, it is possible to remove four test samples from the vacuum chamber, replace them with new test samples, and have the chamber re-sealed in half a day. With a light bake-out (200^{o}C for 2 hours) it is possible to completely cycle the system in 24 hours and be ready to test four new cathodes.

B. ELECTRONICS

The electronic test circuitry can be divided into two broad categories: pulse and dc. Initially, it was necessary to test all of the LVFE devices in pulse mode to prevent heating and subsequent shorting of the insulating film.

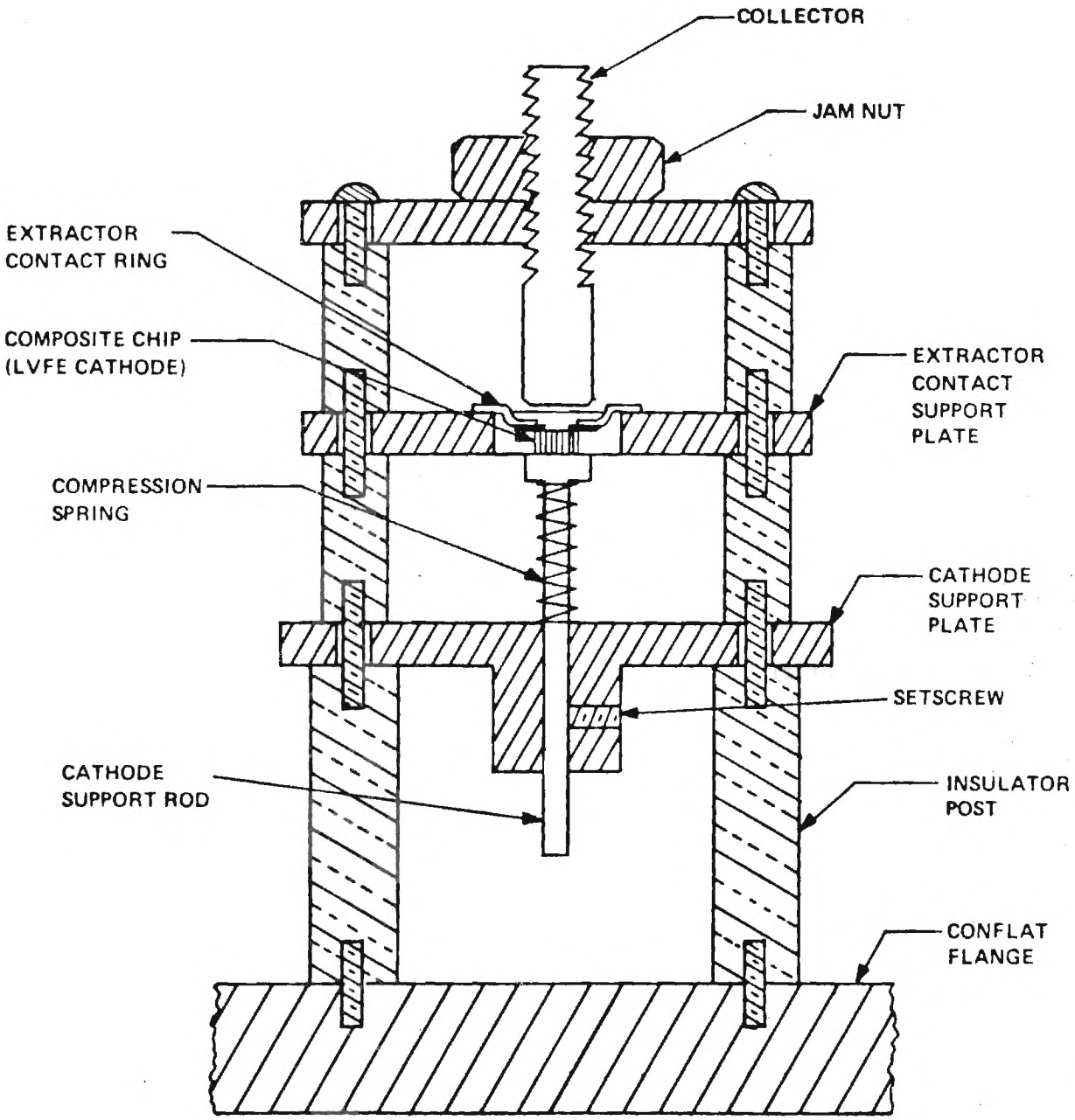

Figure IV-2. Section Drawing of LVFE Test Vehicle.

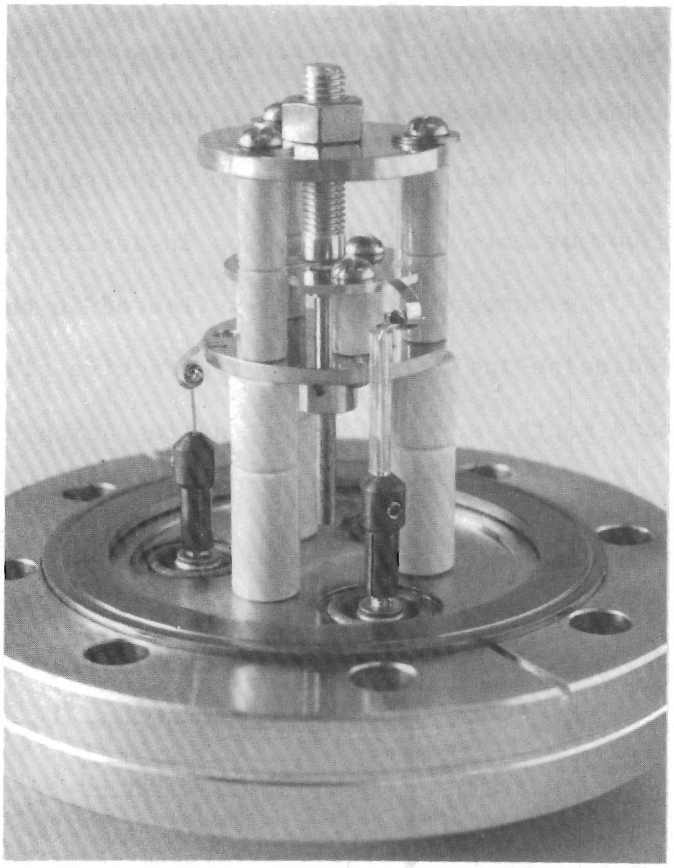

Figure IV-3. LVFE Test VEhicle, Mounted on 4.5 in o.d. Varian Conflat Flange.

A schematic diagram of the pulse test circuitry is shown in Figure IV-4. A pulse generator was designed which met the voltage, current, pulse width, and frequency requirements, and four such devices were constructed; thus up to four cathodes can be pulse tested simultaneously. However, it is necessary to use an oscilloscope to monitor the voltage, emission and leakage current pulses, and to avoid the need for more than two oscilloscopes (one with dual channels), it was necessary to build a switching network to permit monitoring of each cathode individually. The switching network is used for monitoring the pulsed life tests as well. The collector bias supply shown in Figure IV-4 consists of one or more 300 V batteries in series with the collector and a shunt resistor. The batteries are easily floated in the collector circuit; they produce no noise and are quite cost effective since, though expensive, they last many months at the low duty cycles being utilized in the pulse tests.

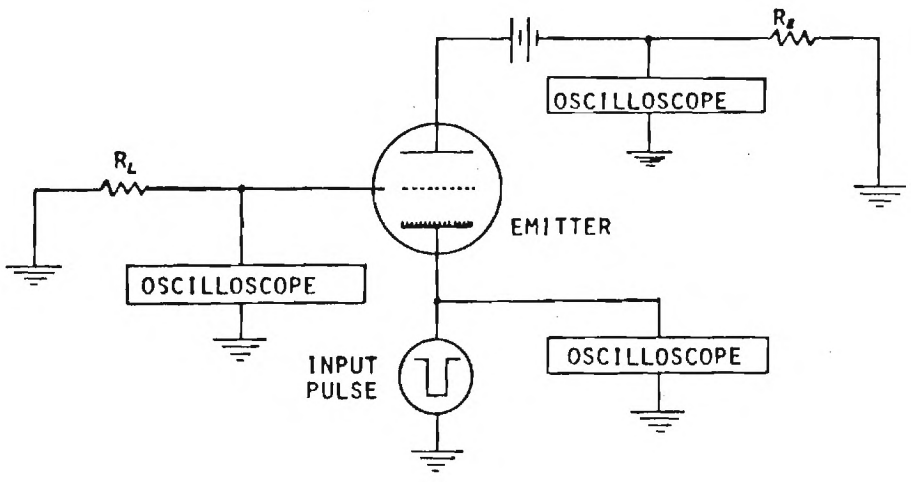

Figure IV-4. Schematic Diagram of LVFE Pulse Test Circuitry.

Continued improvements in the electrical properties of the insulating film eventually permitted the LVFE devices to be tested in a dc mode, and the dc test circuitry is shown in the schematic diagram in Figure IV-5. It is similar, of course, to the pulse test circuit; but instead of a pulse generator, a dc power supply is used to provide the necessary potential between the pins and extractor grid. A high-impedence digital voltmeter (Fluke 5000A) monitors the extractor potential, while electrometers (Keithley 610CR) are used to monitor leakage and emission current. The collector bias supply for the dc tests presented a slight problem since, at emission current levels in the milliampere range, the batteries discharged in a few days. This made it necessary to design an inexpensive, low noise, collector bias supply which could be floated in each collector circuit. A schematic diagram of this circuit is also shown in Figure IV-5.

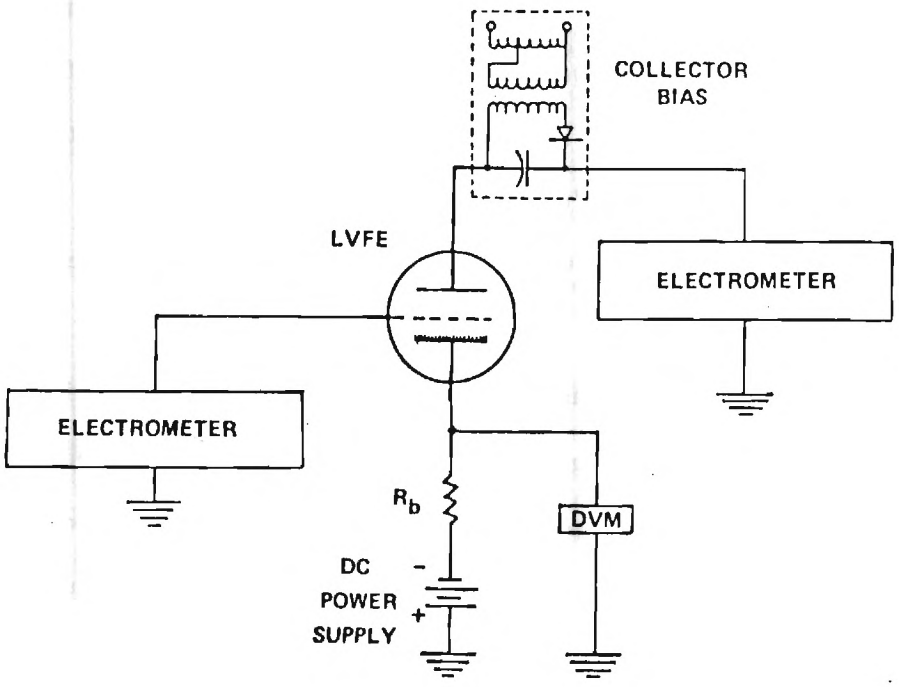

Figure IV-5. Schematic Diagram of LVFE CW Test Circuitry.

C. TEST PROCEDURE

The cathodes were tested as they became available after each deposition run. The first step was to measure the size of the active area from a photomicrograph taken in a Reichert Metallograph. A typical such photomicrograph is shown in Figure IV-6. The cathode was then attached to the stainless steel support stub described earlier and mounted in the test vehicle. The four test vehicles were bolted to the chamber, and the chamber was evacuated to $\sim 10^{-9}$ torr ($\sim$130 nPa) after a 2 hr/200°C bakeout. After the chamber was cooled to roo temperature, the cables were attached to the approriate electrical connectors on each flange, and voltage applied to the collector and extractor circuits.

The cathodes were normally tested by simply increasing the extractor voltage pulse amplitude until emission was observed (as an increase in amplitude of the voltage pulse across the precision shunt resistor in the collector circuit).

When the emission current had reached about 10 μA, it was normally left at that level for several hours. During this period, the current frequently increased, independent of voltage, by as much as an order of magnitude. This appears to be due to some type of "clean-up" phenomenon at the pin tips, and has been observed before, both by us and by other investigators testing field emitter arrays[2,7].

Once this initial stage had passed, the emission current was increased (by increasing the extractor voltage) at a more rapid pace. No specific schedule was followed, and the emission current was normally increased in increments of 10-100 percent over a period of several days. The current was increased until the cathode failed, which was almost always due to a short circuit between the extractor film and the UO_2-W composite. When testing

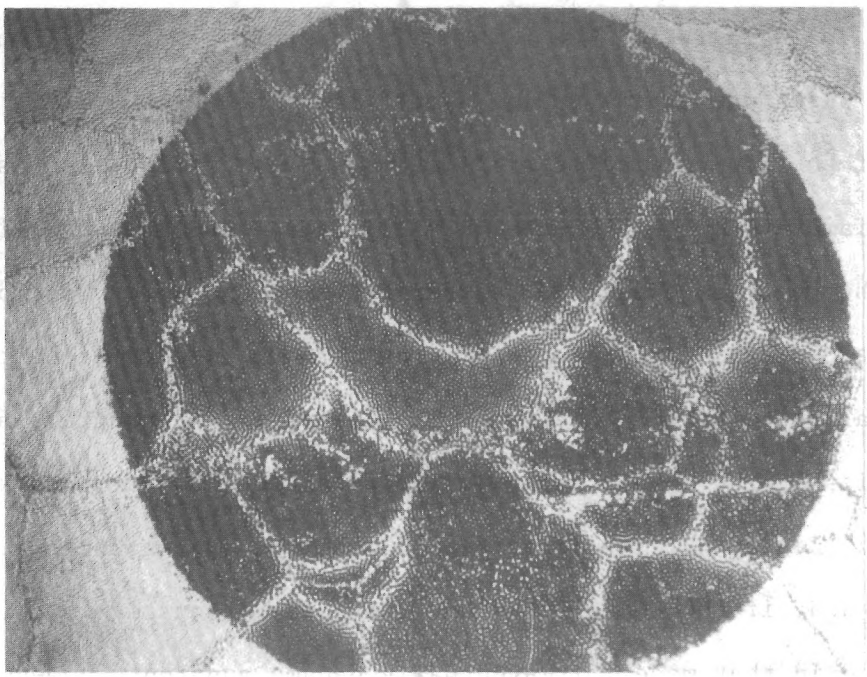

Figure IV-6. Photomicrograph of a Typical LVFE Active Area (X200).

was completed for all four cathodes, they were removed from the test vehicles and examined in the SEM. Normally one or more areas where the extractor film and composite were fused together by an arc revealed the point of failure.

D. EMISSION TEST RESULTS

The results of the UO_2-W emission tests run during the project are summarized in Table IV-1. The first column of the table gives the cathode designation, which was explained in Chapter II. The second column gives the diameter of the active area in millimeters; these varied from as small as 0.2 mm in diameter to as large as one millimeter. Column three lists the mode in which the test was conducted: either pulse, dc, or ac. Most of the early tests were made in a low-duty-cycle pulse mode to prevent heating and subsequent failure of the insulating film. Later in the program, as the electrical properties of the insulating film improved, several cathodes were operated in dc mode. Beginning with Deposition 20, all of the cathodes were turned on in dc mode and, if the leakage current remained reasonably low, the tests were continued in that mode. It eventually became apparent, however, that the Al_2O_3 insulator film could not withstand fields in excess of (20 V/μm) for extended time periods, so most of the cathodes were switched to pulse mode once emission current was observed. Two cathodes were driven by an ordinary 60 Hz ac sine wave and, although neither test gave spectacular results, they were about on a par with the dc tests in terms of leakage and emission current. Typical oscilloscope traces of extractor voltage and emission current traces are shown in Figure IV-7a, while those from a 60 Hz ac test appear in Figure IV-7b. For the pulse tests, the pulse width and duty cycle are

Table IV-1. Summary of Emission Test Results for UO_2-W LVFEA's.

CATHODE DESIGNATION	DIA. OF ACTIVE AREA (mm)	TEST MODE	PULSE WIDTH/ DUTY CYCLE (usec/%)	ARRAY CURRENT DENSITY @ 100V (A/cm^2)	LEAKAGE CURRENT @ 100V (mA)	MAX. ARRAY CURRENT DENSITY @ PK EXTRACTOR VOLTAGE (A/cm^2)	MAXIMUM EMISSION CURRENT (mA)
L19-09-1D2	0.32	PULSE	100/0.5	0.95	0.35	4.8 @ 141V	4.0
JP12-15-2C1	0.86	PULSE	200/1.0	3.16	12.5	8.5 @ 140V	50.0
JP12-15-2B1	0.88	PULSE	200/1.0	1.08	3.75	1.0 @ 94V	6.0
JP10-15-2A2	0.94	PULSE	200/1.0	0.56	0.16	1.4 @ 204V	10.0
JP9-15-1A2	0.75	PULSE	200/1.0	0.02	0.45	0.5 @ 235V	2.2
JP10-15-3A2	0.95	PULSE	200/1.0	**	SHORTED	- - -	-
50.05-17-3A1	0.85	PULSE	200/1.0	**	1.3	- - -	-
50.05-17-3B1	0.86	PULSE	200/1.0	<.01	1.8	1.2 @ 430V	7.2
50.05-17-3D1	1.02	PULSE	200/1.0	**	0.40	- - -	-
50.05-18-7C1	0.98	DC	- - -	0.03	0.07	0.2 @ 129V	1.6
50.05-18-7D1	0.98	PULSE	500/2.5	0.14	0.42	1.3 @ 157V	10.0
50-B3-18-3E1	0.64	PULSE	200/1.0	0.16	0.02	0.4 @ 250V	1.9
50-B3-18-3E1	0.64	DC	- - -	0.34	0.02	1.1 @ 120V	3.4
50-B3-18-3A1	0.78	PULSE	200/1.0	0.63	2.0	1.1 @ 120V	5.0
50-B3-18-3A1	0.78	PULSE	50/.25	0.63	2.0	4.6 @ 142V	22.0
50-B3-18-3A1	0.78	PULSE	1.5/.025	0.63	0.85	21.1 @ 226V	100.0
50.05-20-7A2	0.20	PULSE	50/.25	0.32	0.15	11.9 @ 255V	3.7
50.05-20-7B2	0.60	DC	- - -	0.02†	0.14†	0.02 @ 90V	0.06
50.05-20-9E2	0.54	DC	- - -	<.01	***	0.13 @ 70V	0.29
50.05-20-9F2	0.29	DC	- - -	0.04	0.23†	0.03 @ 95V	0.02
50.05-20-7F2	0.30	DC	- - -	<.01	***	.01 @ 75V	0.06
JP10-15-5A2	0.63	AC	60 Hz	0.02	1.9 pk	0.05 @ 105V	0.15
50-B3-18-3D1	0.64	AC	60 Hz	<.01	0.5 pk	0.03 @ 110V	0.10
50.05-21-9C1	0.33	DC	- - -	0.03	0.009	0.18 @ 130V	0.15
UNK-21-7A1	0.54	DC	- - -	0.02	0.06	0.07 @ 120V	0.16
UNK-21-1B1	0.52	DC	- - -	0.13	0.001	0.94 @ 124V	2.0
JP10-28-4B3	0.2	PULSE	200/1.0	0.05	0.15	0.3 @ 120V	0.09
UNK-28-7A2	0.2	PULSE	200/1.0	0.01	0.05	1.6 @ 260V	0.50
UNK-28-8A2	0.2	PULSE	200/1.0	0.01	0.22	0.1 @ 130V	0.03
JP9-28-1A3	0.2	PULSE	200/1.0	0.07	0.22	6.4 @ 250V	2.0
JP10-28-2A3	0.2	PULSE	200/1.0	<.01	0.65	0.1 @ 210V	0.03
E20-28-1A1	0.2	PULSE	200/1.0	<.01	1.0	1.0 @ 240V	0.30
E14-28-1A1	0.2	PULSE	200/1.0	0.04	0.20	1.6 @ 210V	0.50
50.H1-31-1B1	0.73	PULSE	200/1.0	0.09	0.3	2.4 @ 187V	10.0
50.H2-33-1C3	0.22	PULSE	200/1.0	0.21	2.8	1.0 @ 140V	0.40
L44-33-1A3	0.41	PULSE	200/1.0	0.05	0.3	0.3 @ 215V	0.40
JP10-33-4B4	0.45	PULSE	200/1.0	4.64*	2.9*	0.3 @ 74V	0.50

*Calculated by dividing total emission current by the size of the active area.
**These samples were later found to be shorted externally in the test fixture.
†Extrapolated value; sample failed at less than 100V.
***Unknown; sample failed well below 100V.

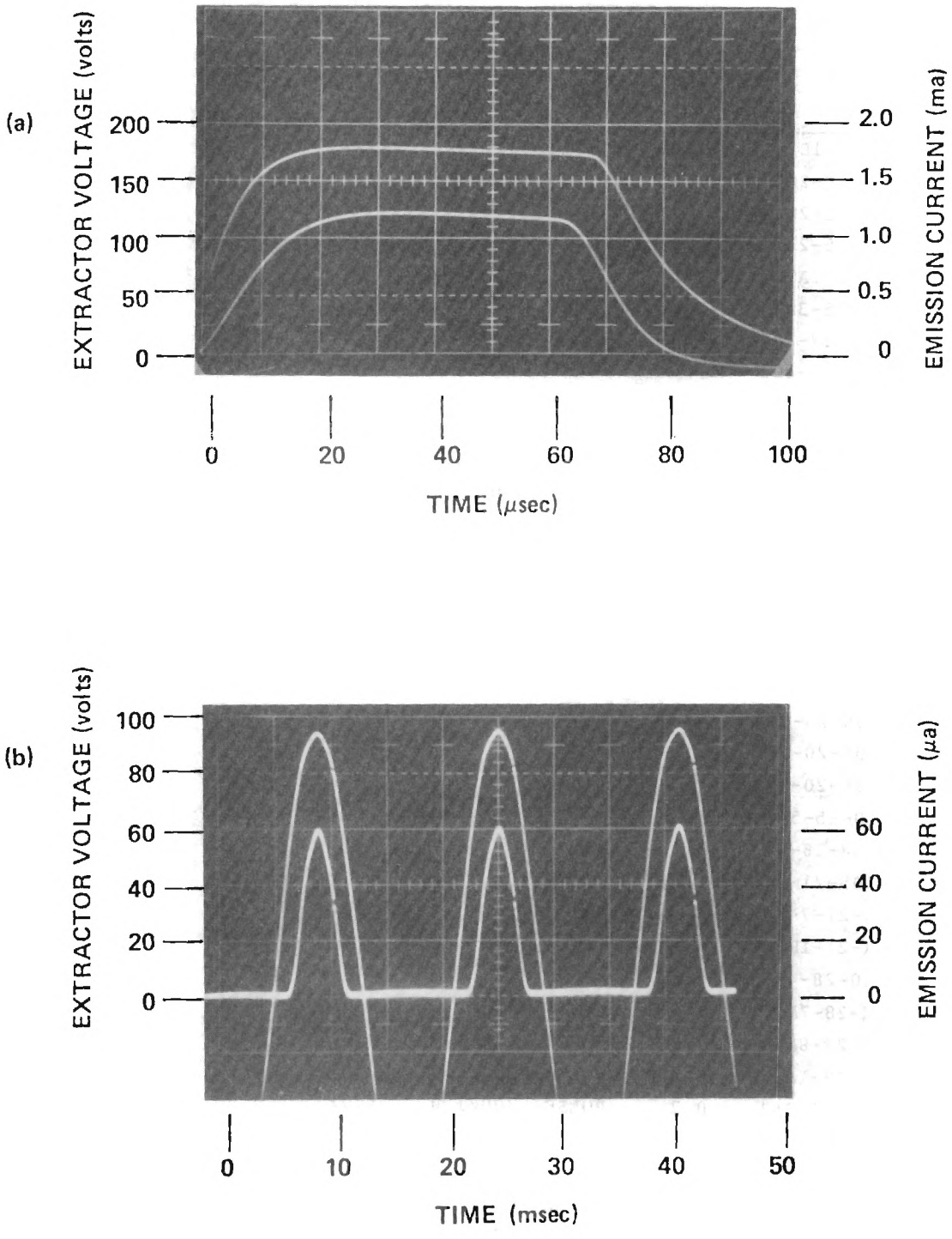

Figure IV-7. Examples of Oscilloscope Traces of Extractor Voltage and Emission Current, (a) Pulsed, (b) 60 Hz AC.

given in Column 4.

A convenient means for comparing the emission performance of the different cathodes is to calculate the array current density, J_{100}, the total emission current divided by the size of the active area at an extractor potential of 100 volts. (The value J is also frequently termed the macroscopic current density to differentiate it from the microscope current density, j, the current emitted by an individual pin divided by the actual emitting area at the pin tip.) Since the value of J_{100} is independent of array size, it gives a good measure of the effect of cathode geometry, and variations thereof, on emission performance.

The leakage current at 100 volts, listed in the next column for each cathode tested, gives a means for comparing the electrical properties of the insulating film. This was discussed in Chapter III, and will not be repeated here, except to note the obvious improvement shown by the samples fabricated in Deposition run 21. The maximum array current density achieved by each cathode is shown in the next column. For the pulse tests, this is the amplitude of the current pulse divided by the active area. The amplitude of the extractor voltage pulse is also given. The last column in the table lists the maximum emission current produced by each cathode, the value from which the array current density in the previous column was calculated.

Several of the test results listed in Table IV-1 represent significant advances in the state-of-the-art, and these will be discussed briefly here. Tests JP12-15-2C1 and -2B1 were the first of several cathodes with larger active areas - 0.8-1.0 mm in diameter. The large-area cathodes were fabricated and tested to see whether emission currents of 100 mA or more could be

obtained. Unfortunately, most of the large-area cathodes failed prematurely, apparently due to insulating film defects in the active area. After several such failures, the decision was made to reduce the active area diameter back to 0.5 mm or less for the remaining tests, until the electrical properties of the insulating film could be improved.

Before JP12-2C1 and -2B1 failed, they exhibited outstanding V-I characteristics, producing a higher array current density for a given extractor voltage than any LVFE device tested to date. Plots of emission current as a function of voltage are shown in Figure IV-8 for JP12-2C1 and for S-14, the cathode producing the highest array current density to date (tested prior to the beginning of this program). Fowler-Nordheim plots for JP12-2C1, JP12-2B1, and S-14 are compared in Figure IV-9. The 50 mA of emission current produced by JP12-15-2C1 is also the largest emission current produced by an LVFE device at a one percent or greater duty cycle. It is not clear whether the superior performance of the JP12 samples was due to extractor/pin geometry or to some unique property of the chips themselves.

Tests of cathode 50-B3-18-3E1 produced some rather puzzling results. It was initially tested in pulse mode, producing an array current density of 150 mA/cm^2 at 100 V, and 400 mA/cm^2 at 250 V. Because the leakage current was so low (20 μA @ 100V), it was tested dc as well. Surprisingly, the dc emission current was more than 100 percent greater at 100 V than the pulsed emission current and over four times the pulsed current at 120 V. Part of the reason for this can be explained by a glance at the respective Fowler-Nordheim plots in Figures IV-10 and -11. Note that the pulsed emission appears to become space-charge-limited at a current density of about 20 mA/cm^2, while the dc emission shows no signs of such an effect.

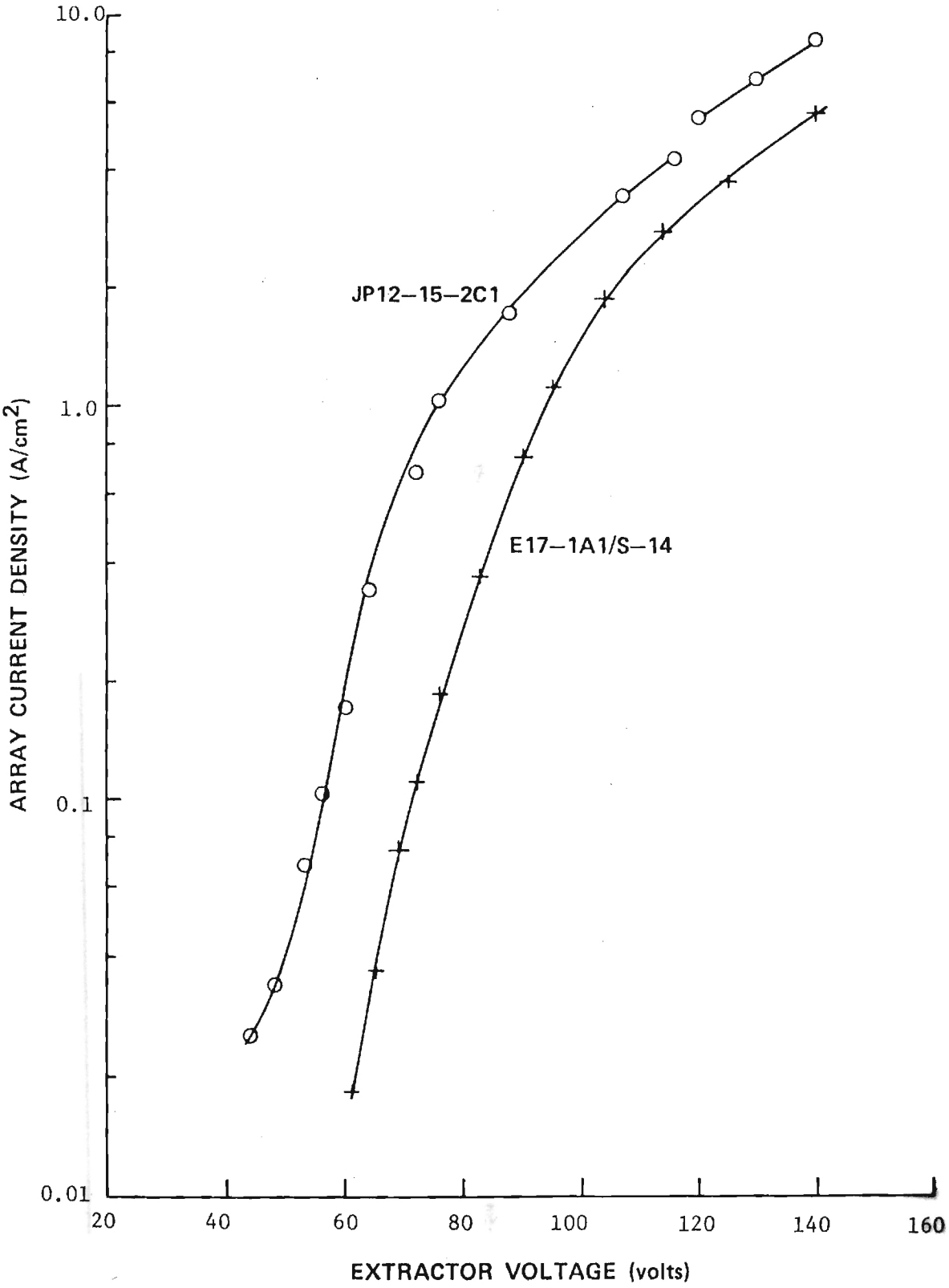

Figure IV-8. Emission Current as a Function of Voltage For Cathodes JP12-15-2C1 and S-14.

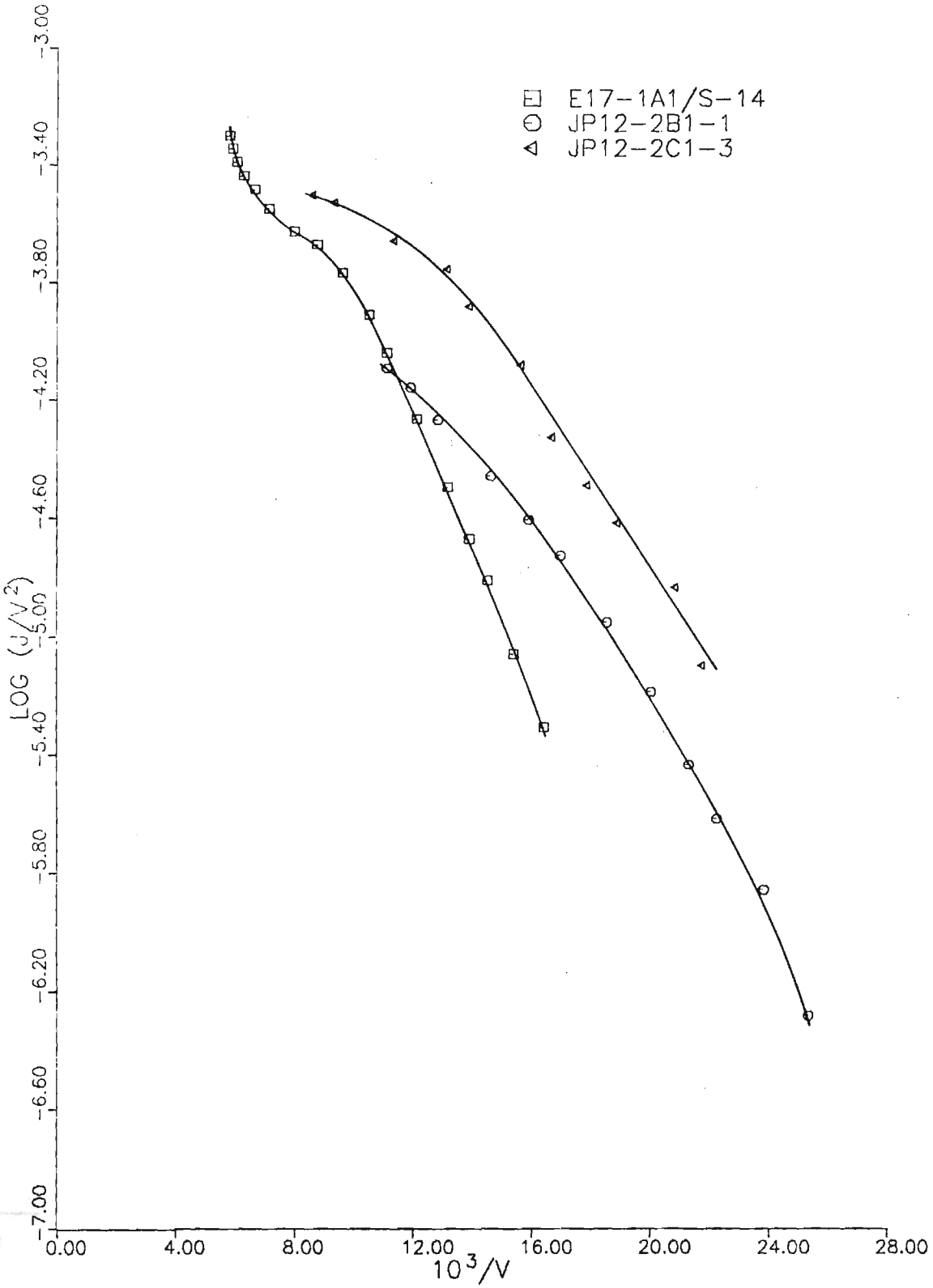

Figure IV-9. Fowler-Nordheim Plots for Cathodes JP12-15-2C1, JP12-15-2B1, and S-14. (Non-linearity in Upper Parts of Curves Indicates Beginning of Space-Charge Effects.)

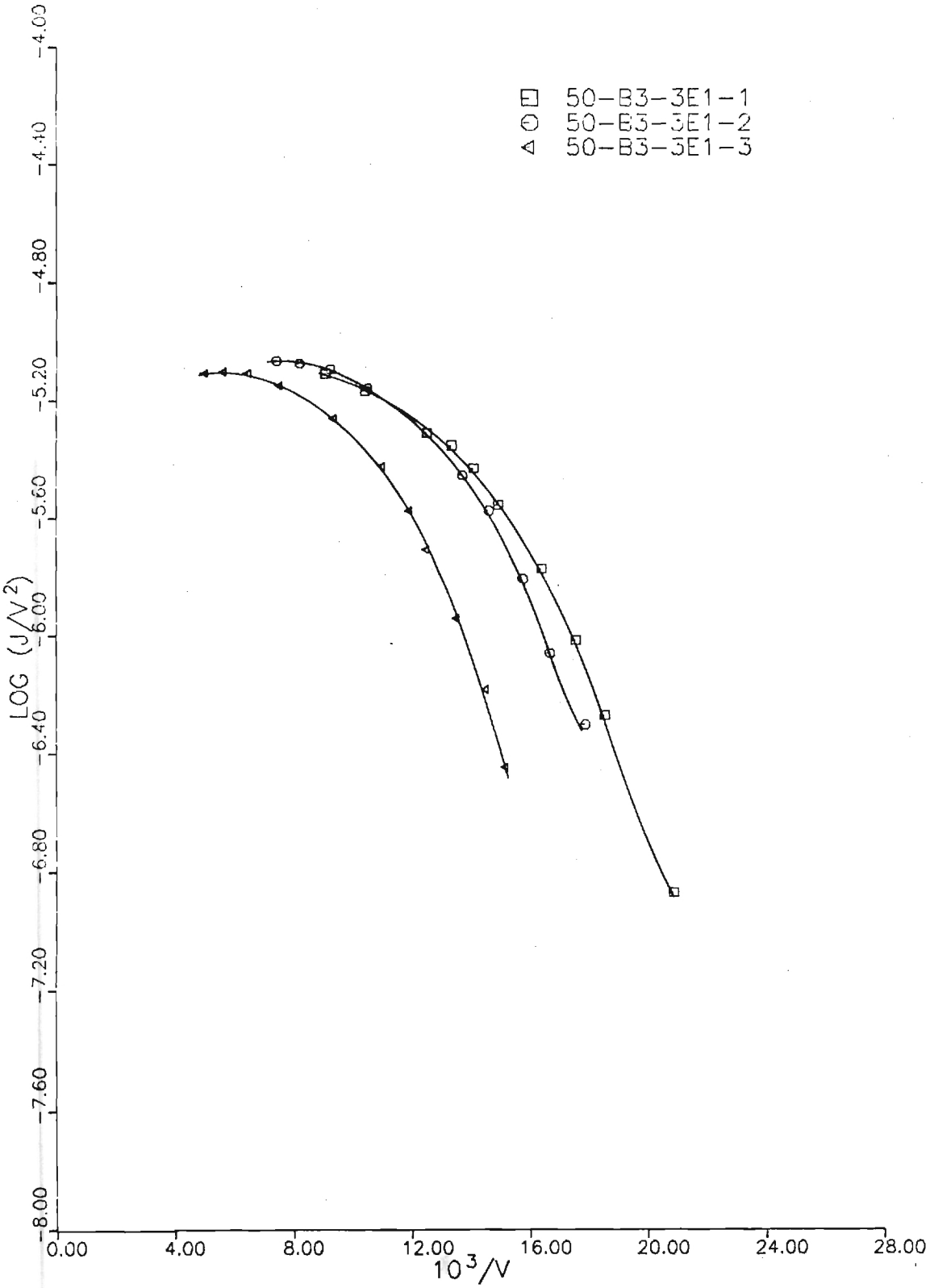

Figure IV-10. Fowler-Nordheim Plots for Cathode 50-B3-3E1 in Pulse Test Mode.

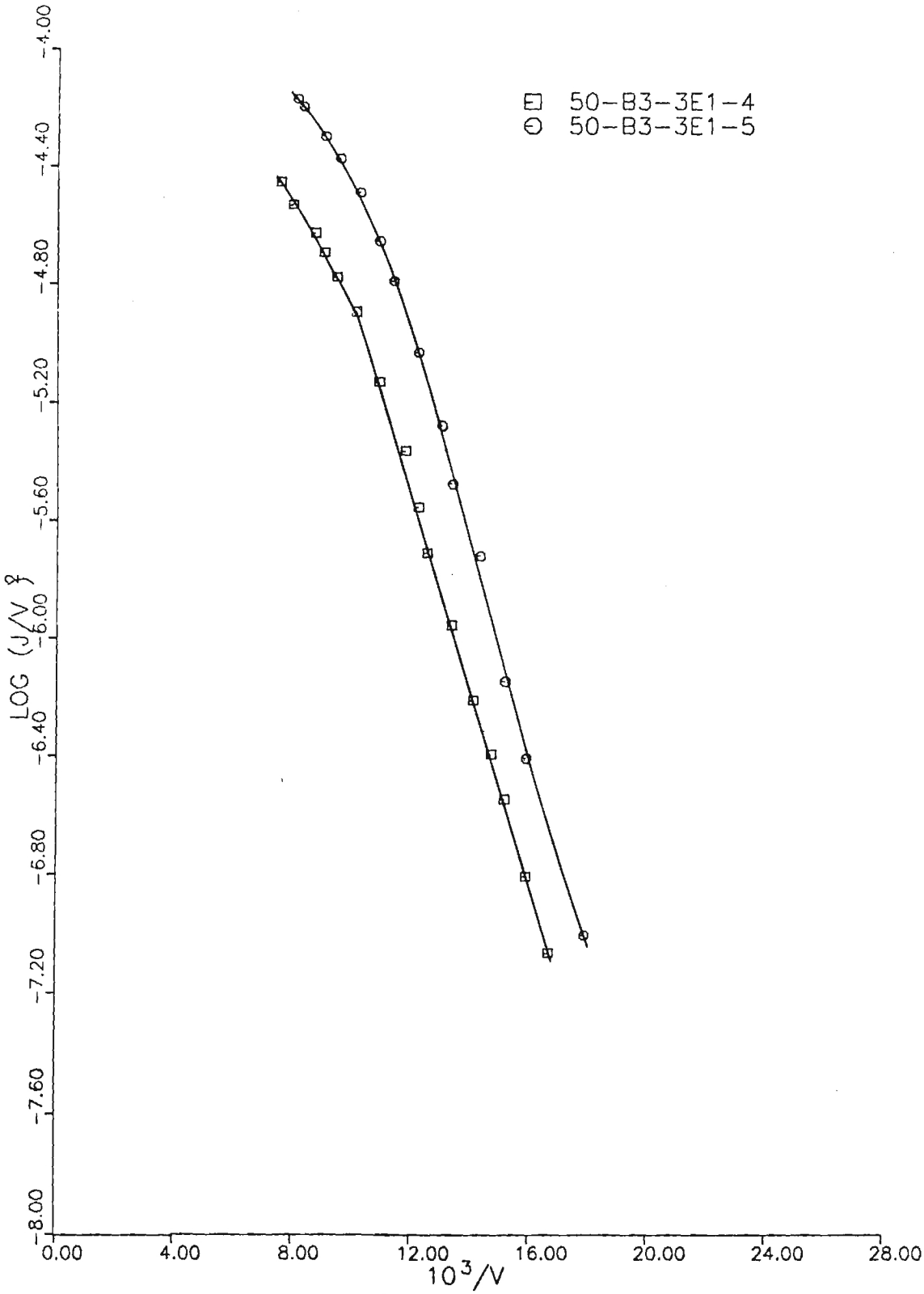

Figure IV-11. Fowler-Nordheim Plots for Cathode 50-B3-3E1 in DC Test Mode.

One possible explanation for this phenomenon is that operation in the dc mode maintains the pin tips in a "cleaner" condition, producing a low-work-function surface over a larger percentage of the pin tip surface. This provides a larger microscopic emitting area, with a proportionately lower microscopic current density. The effect is more pronounced with some cathodes than with others, indicating that tip geometry, and/or some other variable, may also play an important role.

Cathode 50-B3-18-3A1, with an active area 0.78 mm in diameter, produced the most emission current of any LVFE device to date. It was tested initially in the more or less standard pulse mode of 200 μsec pulses at a 1% duty cycle. Although the leakage current was high (∿2 mA @ 100V), ruling out dc testing, the intercept of the F-N plots were also reasonably high, indicating a greater than average microscopic emitting area (50-B3-3A1-2 & 4, Figure IV-12). The decision was made to see whether shortening the pulse width to 50μsec, thus reducing the duty cycle by a factor of four and lessening insulator heating due to leakage current, might permit much larger voltage pulses to be applied. This proved to be the case, resulting in 22 mA of emission (4.6 A/cm^2) at 142 V with ∿10 mA of leakage current. A F-N plot taken at this point (50-B3-3A1-6) is shown in Figure IV-12. The pulse width was further reduced to 1.5μsec, and the pulse amplitude increased until, at a peak voltage of 205 V, the measured emission current was 50 mA (10 A/cm^2); the leakage was also 50 mA. The peak capacitive charging current measured at the extractor was 300 mA, with a duration of 2μsec. The collector bias was 300 V to ground.

The cathode was left to operate overnight, and the next morning the current was found to be unchanged from the previous readings. This is the

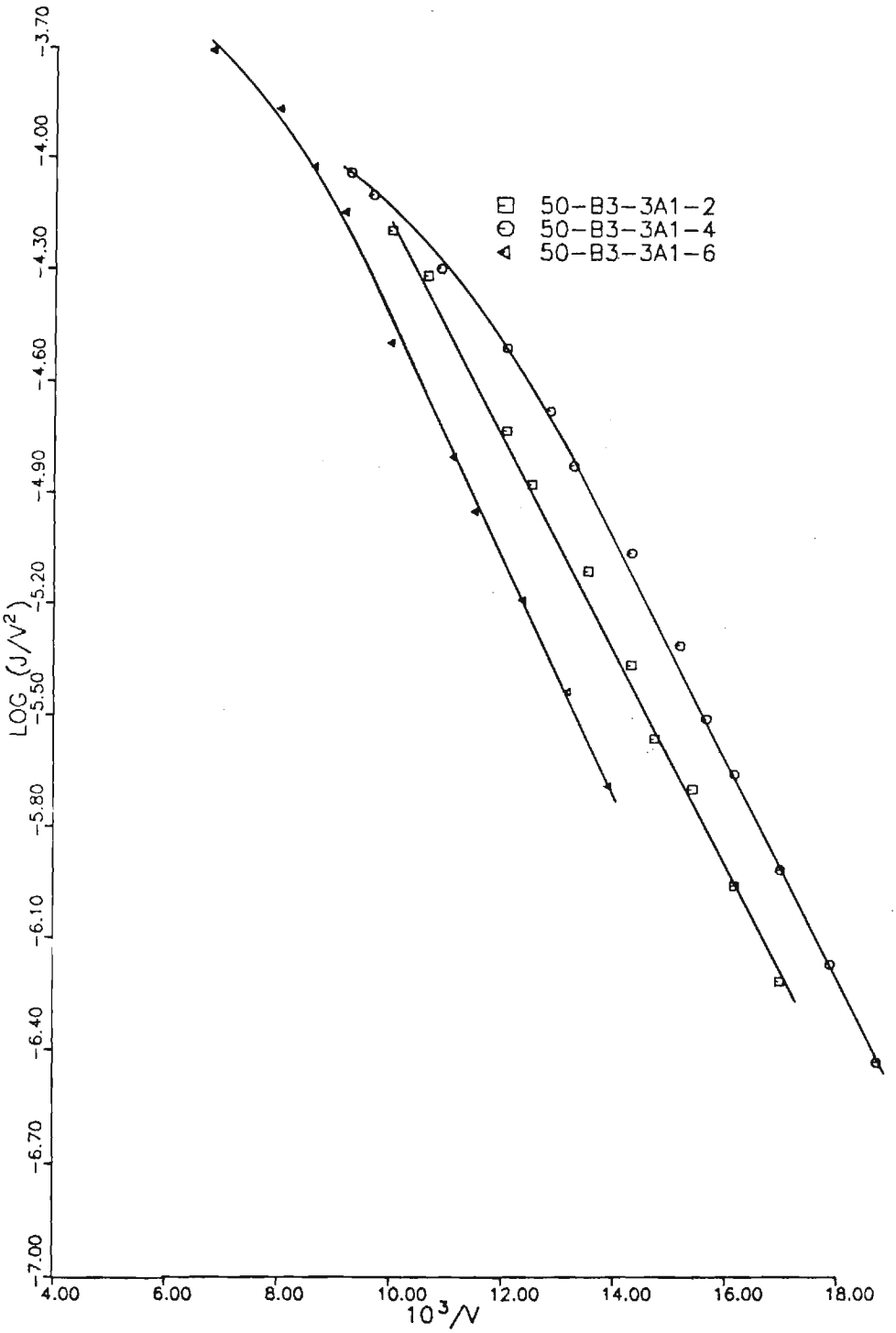

Figure IV-12. Fowler-Norheim Plots for Cathode 50-B3-18-3A1 Prior to Reduction of Pulse Width.

longest any LVFE cathode has operated at this current level. A Fowler-Nordheim plot (50-B3-3A2-SP1) taken at this point (Figure IV-13) revealed that the cathode was operating space-charge-limited. The extractor voltage was then held constant at 200 V, producing 36 mA of emission current and 50 mA leakage current, and the collector voltage was increased in 200 V increments from 300 V to 2 kV. This produced an increase in emission current to 67 mA (14 A/cm^2) and a 70% decrease in leakage current, to 15 mA. Further increases in collector voltage produced no more emission current, so presumably at this point the cathode was no longer operating space-charge-limited.

The extractor voltage was next increased to 225 V peak, resulting in 100 mA of emission current ($\sim$20 A/cm^2) with a leakage current of 25 mA. Data for another Fowler-Nordheim plot (50-B3-3A2-SP2) was taken at this time, and this plot is also shown in Figure IV-13. Note that at the higher emission level, the cathode is once more operating in the space-charge regime. After $\sim$15 minutes, an arc reduced the emission current to 80 mA at 225 V, and the test was terminated a short time later. Nevertheless, a milestone had been reached, for this is the highest overall emission current produced by an LVFE device to date.

Cathode 50.05-20-7A2 contained a small active area, only 0.2 mm in diameter; like -3A1, however, the microscopic emitting area was relatively large, producing 11.9 A/cm^2 (3.7 mA) at 225 V (pulsed). Although the leakage current was not extremely high, it was sufficient to make further voltage increases without failure unlikely. Since samples were needed for life testing, the decision was made to place it in a life-test vehicle. Its performance is discussed further in Section E.

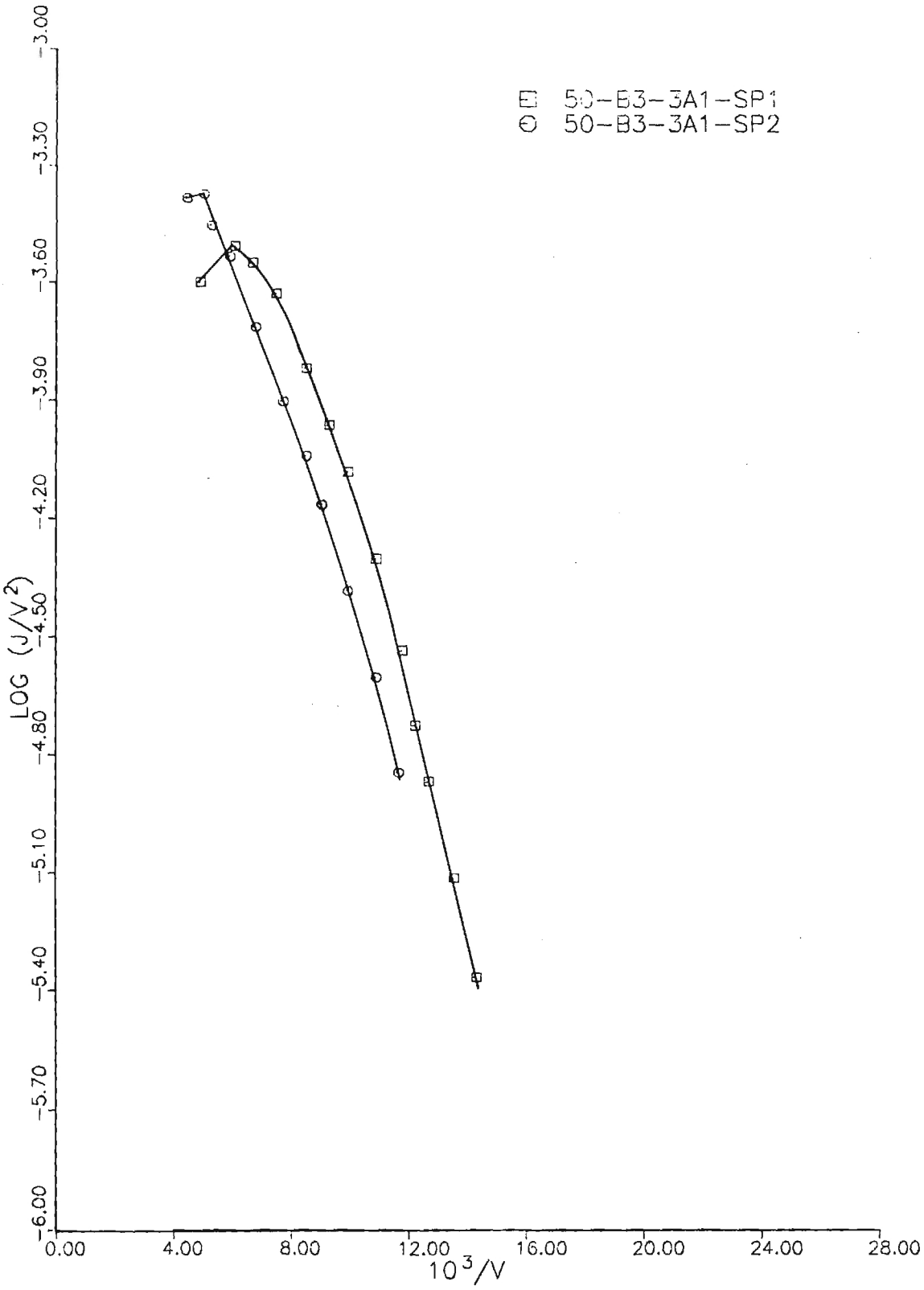

Figure IV-13. Fowler-Nordheim Plots for Cathode 50-B3-18-3A1 With Pulse Width Reduced to 1.5 μsec.

A series of cathodes from Deposition runs 20 and 21 were tested in dc mode, since initial measurements of leakage current indicated substantial improvement in the electrical properties of the insulator film, particularly the samples from Deposition run 21. Unfortunately, the fiber growth in all of the 50.05 samples was poor; hence, there was considerable variability in the shape and height of the etched tungsten pins. As a result, the emission performance of these samples was disappointing. On the other hand, the leakage current of all of these samples was significantly lower than anything tested previously.

One sample fabricated in Deposition run 21, UNK-21-1B1, was not from Growth run 50.05 and had much better pin uniformity. The emission performance was also better, reaching 940 mA/cm^2 dc at 124 V. The leakage current at 100 V was less than one microampere, and was less than 10 μA at 124 volts. F-N plots for the cathode are shown in Figure IV-14. The cathode failed when an apparent switching error suddenly applied over 200 V to the extractor; the resultant arc fused one small portion of the active area (Figure IV-15) and shorted the extractor film. Nevertheless, the data obtained from the test was extremely encouraging, for it gave an indication of the potential of the LVFE device for dc operation as the properties of the insulating film continue to be improved.

In testing sample UNK-21-1B1, it soon became apparent that, for dc emission currents of much more than 2 mA, collector heating would be a serious problem. Thus, future dc test cathodes will either have to be limited in size of active area, and hence total emission current, or some means must be found for dissipating enough of the power generated at the collector by the electron beam to prevent it from overheating.

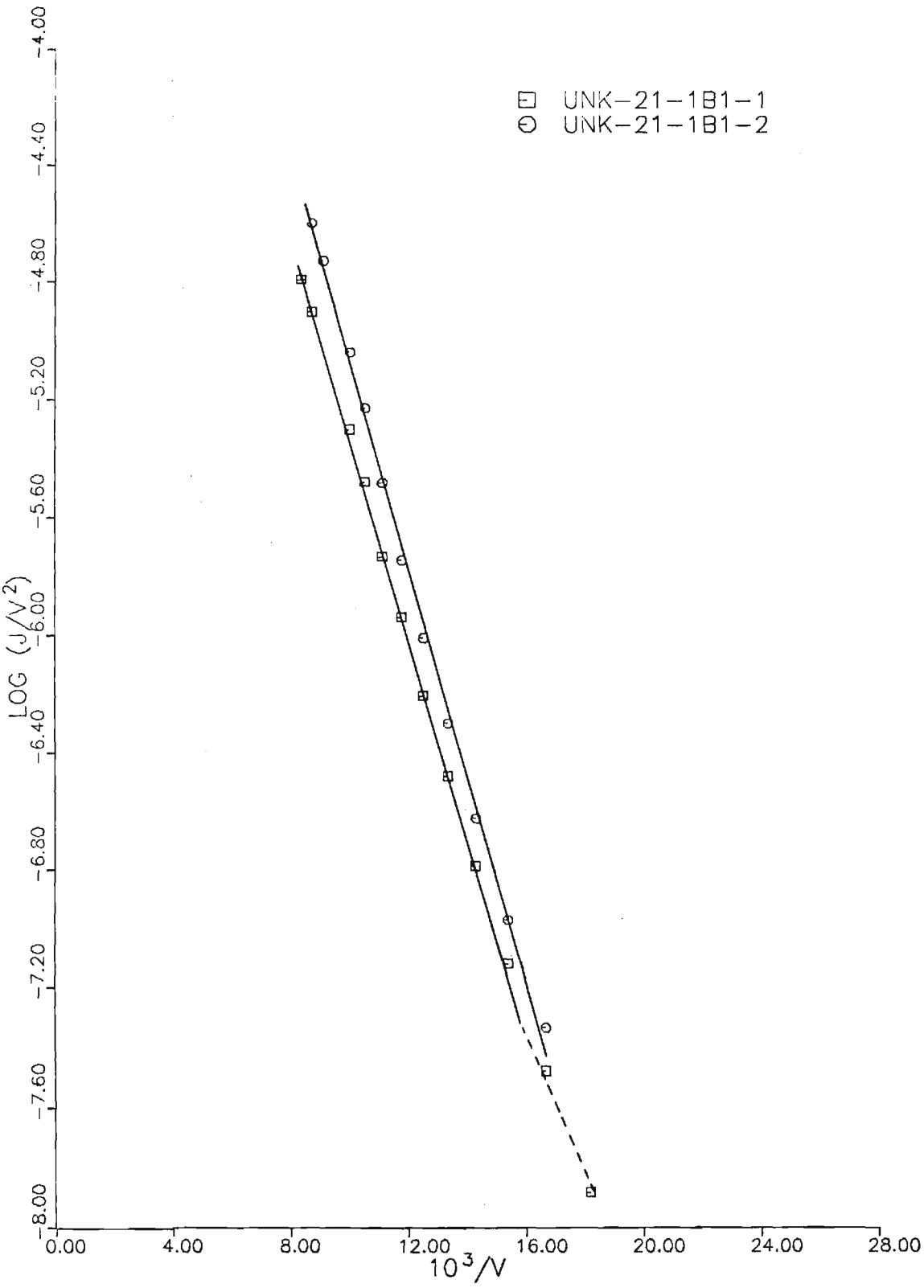

Figure IV-14. Fowler-Nordheim Plots for Cathodes UNK-21-1B1, Operating in CW Mode.

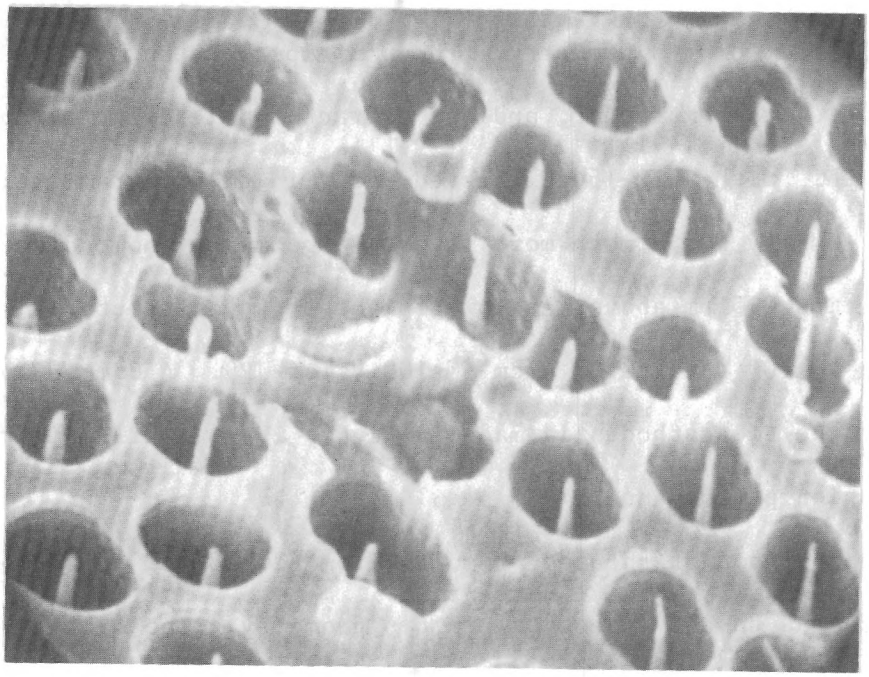

Figure IV-15. Fused Spot in the Active Area of Cathode UNK-21-1B1 That Shorted the Extractor Film, X5000.

Unfortunately, the excellent electrical properties of the insulating films in Deposition run 21 were not reproducible, and a number of samples from succeeding runs were discarded because the resistance of the insulating film was too low. Seven cathodes from Deposition run 28 were tested in pulse mode, but of these only one, JP9-1A3, produced significant emission current, and this at relatively high voltage. Although this sample had relatively uniform pin heights throughout the active area, that was the only favorable part of its geometry. The pin tips were an average of 0.5 μm below the plane of the extractor, and the extractor hole diameter averaged 3.6 μm. Compare this with JP12-15-2C1 tested early in the program, which had a similar pin density but a much more favorable geometry (hole diameter of 1.6 μm and pin tips 0.5 μm above the lower plane of the extractor). JP12 produced 3.2 A/cm^2 @ 100 V vs. 0.07 A/cm^2 @ 100 V for JP9. A comparison of the geometry of the two cathodes is made in Figure IV-16, while Figure IV-17 compares the emission performance.

A comparison of the test results from E20-28-1A1 and JP9-28-1A3 may give some clues as to the effect of pin tip geometry. The overall geometry of these two samples was similar, i.e., extractor hole diameter and pin tip position. However, JP9 had relatively sharp pins, whereas most of the pin tips of E20 had been accidently removed by the alkaline $K_3Fe(CN)_6$ etchant, forming truncated cones. The slope of the F-N plots for JP9 was about 40 percent lower than those for E20 (Figure IV-18). Since the field enhancement at the pin tips, β, is calculated from the relation

$$\beta = -2.97 \times 10^7 \frac{\phi^{3/2}}{m},$$

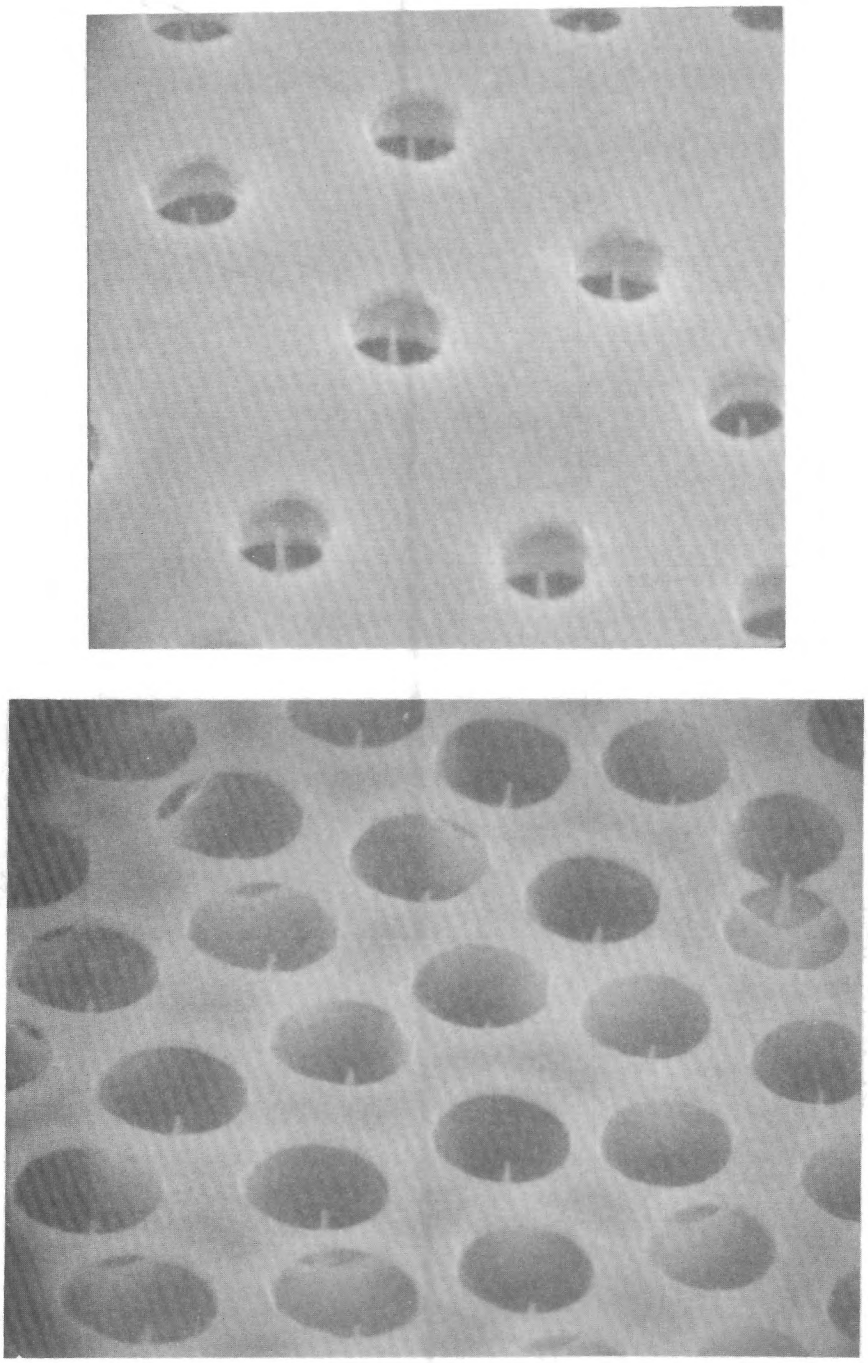

Figure IV-16. Comparative Cathode Geometries of JP12-15-2C1 (Upper Photo, X7500) and JP9-28-1A3 (Lower Photo, X5000).

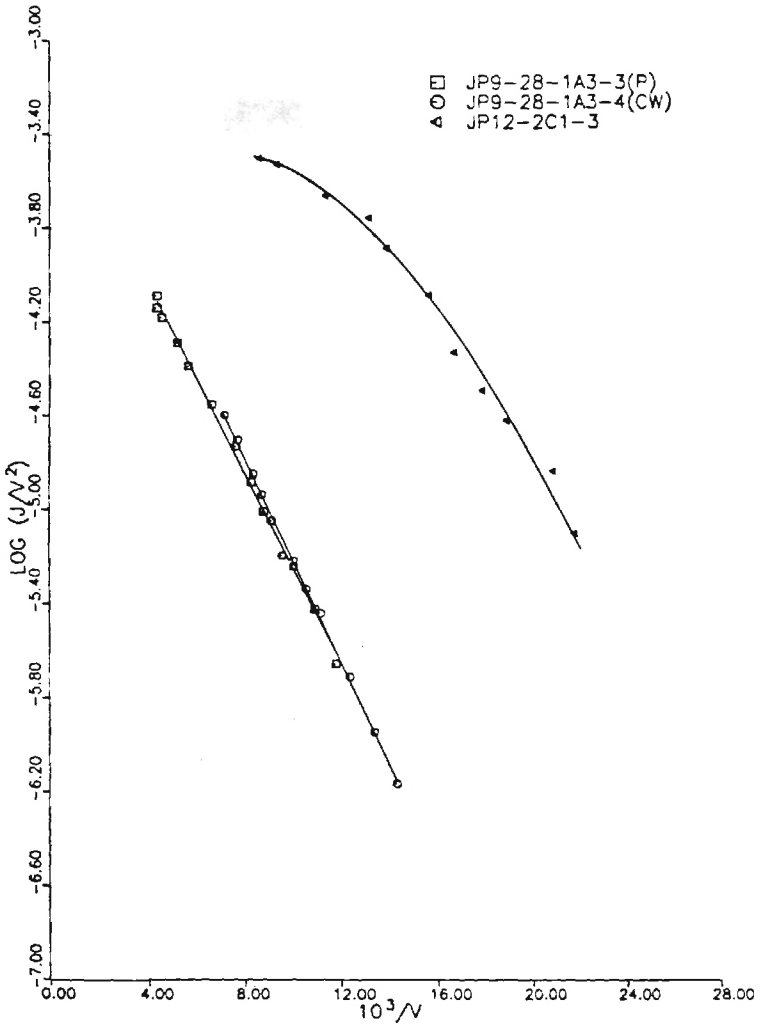

Figure IV-17. Comparison of Emission Test Results for Cathodes JP12-15-2C1 and JP9-28-1A3.

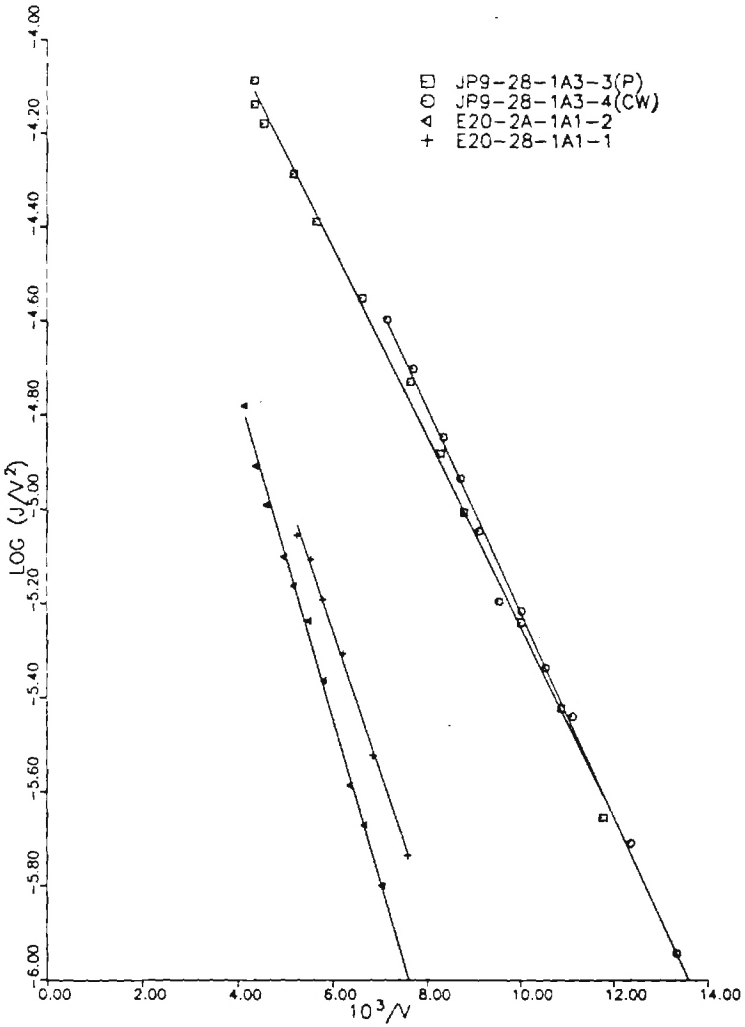

Figure IV-18. Comparison of F-N Plots for JP9-28-1A3 and E20-28-1A1, Illustrating the Effect of Pin Geometry on Slope of the F-N Plot.

where ϕ is the work function and m is the slope, a similar increase in field enhancement for JP9 would be expected. This should, of course, produce a corresponding increase in current density and, in fact, the array current density for cathode JP9 was at least an order of magnitude greater than E20 at the same voltage.

Cathode JP9 and JP10 were removed and examined in the SEM, and neither showed any evidence of arc damage. Cathodes E14 and E20, on the other hand, failed by shorting; SEM examination revealed arc damage, involving 6-10 neighboring pins, in the active area of both cathodes.

E. LIFE TESTING

In planning the life test program, the intention was to initiate life tests early in the contract to permit evaluation of cathode performance for 10,000 hours or more. Unfortunately, unexpectedly long delays in delivery of equipment and hardware delayed completion of the test facility until near the end of the first year.

The life test vehicles are similar in design to the routine test vehicles, except they are reduced in size. The size reduction permits them to be mounted on 2.75 in. Conflat flanges, which are in turn mounted on a 1.5 in o.d. Varian TEE. A 2 liter/sec Varian appendage ion pump is mounted on the opposite end of the TEE, while a copper pinch-off tube (the roughing line) is bolted to the center port. A diagram of the test vehicle mounted in a TEE is shown in Figure IV-19, and a photograph of the test facility appears in Figure IV-20. The photograph shows the rack-mounted panel on which four life test vehicles will be installed although only two are in place at the present time. Below this panel two pulse generators are mounted in the rack; and

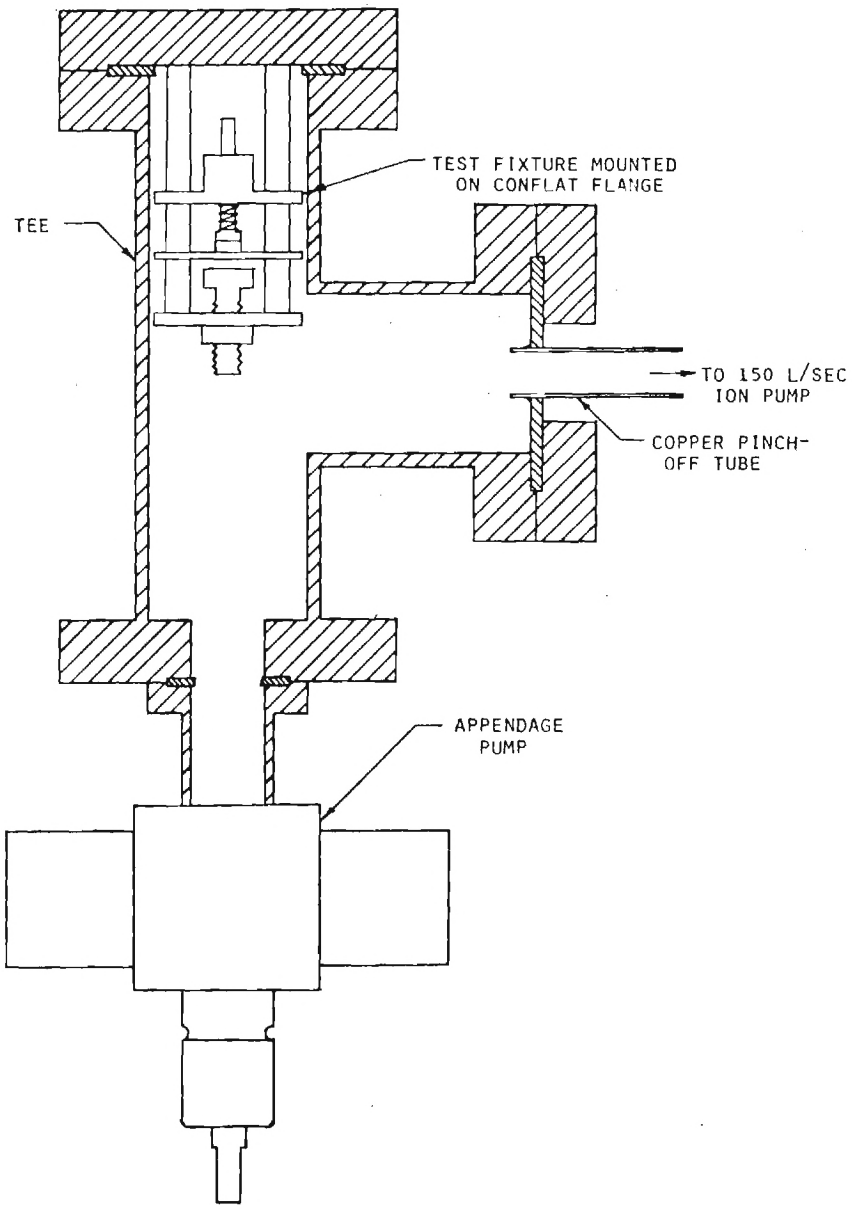

Figure IV-19. Section Drawing of LVFE Life Test Vehicle Mounted on Varian 1.5 in. o.d. TEE, Showing Location of Pinch-Off Tube and Appendage Ion Pump.

below these is the power supply for the appendage ion pumps. (It has capability for controlling and monitoring up to ten such pumps.) Four test vehicles have been completed, and as the need rises (and samples become available), additional test vehicles can be added at a cost of about $700, including pump. A close-up of the rack-mounted test vehicle and appendate pump is shown in Figure IV-21.

The procedure for initiating a life test was to first install the cathode in the test vehicle and assemble the flange and appendage pump to the VARIAN TEE, as shown in Figure IV-19. This assembly was then attached to the main test chamber where it could be pumped by the large capacity ion pump during a 24 hour/400°C bakeout. At the conclusion of the bakeout, the appendate pump was started and the cathode turned on.

The original plan was to condition the cathodes at 12-15 A/cm^2 for several days, pinch off the TEE from the main system, install it on the life test rack, and operate the cathode at 10 A/cm^2 until it failed or changed operating characteristics. In mid-April, 1980, cathode number 50.05-20-7A2 reached a current density of 12 A/cm^2 @ 250 V (pulsed), with a leakage current of ∿2 mA, and was transferred to a life test vehicle. The cathode apparently suffered some damage in the transfer, because the leakage current was much higher than before (∿6 mA). Because of the high leakage current, the cathode was operated at a reduced level of 5 A/cm^2 for the life test.

The cathode was operated coninuously in the life test facility from 6-3-80 until 2-10-81, accumulating a total of ∿6000 hours at 5 A/cm^2. The extractor voltage pulse amplitude remained fairly constant at 200 volts, varying less than 3% during the period of the test. The voltage pulse length was 40 μsec, and the frequency was maintained at 60 Hz throughout the test.

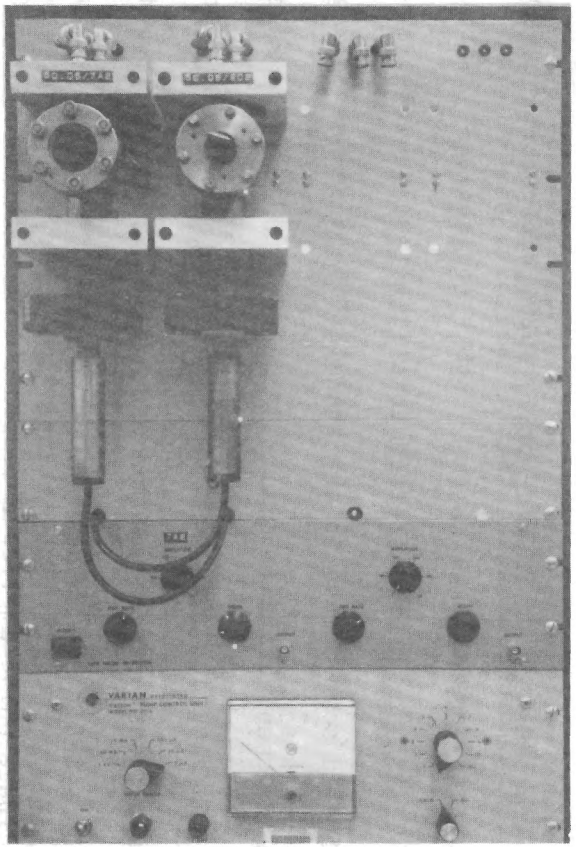

Figure IV-20. LVFE Life Test Facility With Two Test Vehicles Installed.

Figure IV-21. LVFE Life Test Vehicles.

On 2-10-81, the emission current suddenly dropped from 1.75 mA to 660 μA (∿2 A/cm^2), indicating some damage had occurred in the active area. This was believed to be due to a brief power outage, which may have generated a voltage spike when the power supply re-started. The cathode continued to run at the 2 A/cm^2 level (with a leakage current of 10 mA) until 8-23-81, when the test was voluntarily terminated after 11,400 hours at 2 A/cm^2.

A number of other cathodes were installed in life test vehicles and turned on while connected to the main test chamber. Unfortunately, only one of these 50.05-20-9D2, achieved a high enough current density for a meaningful life test. It was operated under the same conditions as 50.05-7A2, at a current density of 2 A/cm^2 @ 165 V (pulsed), for about 1500 hours. At that point the emission current suddenly dropped by approximately 50 percent and the test was terminated.

F. ANALYSIS OF TESTING ATMOSPHERE

A VEECO Model SPI-10 Monopole Residual Gas Analyzer was used to determine the components at the atmosphere in the vacuum system during an emission test. The analyzer tube was mounted in the top flange of the chamber in place of the ionization gauge (Figure IV-1), which was moved to another port. The collector was thus located equidistant from each of the four ports of the system.

After calibration and alignment, using a N_2 source gas, the system was pumped down, baked out (24 hrs/300°C), and the pressure reduced to 76 nPa (5×10^{-10} torr). Unfortunately, the instrument was not sensitive enough to measure gas species at this pressure, so air was bled into the system until the pressure rose and stabilized at 3 μPa (2×10^{-8} torr). This was typical of the

pressure level at which the LVFEA cathodes were normally tested.

The spectrum shown in Figure IV-22 was obtained at 3μPa (2×10^{-8} torr). One of the cathodes was then activated and a second spectrum run. The two spectra were identical in all respects, indicating that the LVFEA produced no detectable gas species during operation at this pressure. This is to be expected, of course, for low power operation. At higher power levels, there is substantial rise in the system pressure due to outgassing of the collector, and the residual gas spectrum would be expected to change accordingly. The question of what gas species are desorbed from the collector, and what effect they have on cathode operation, will have to be addressed in future investigation.

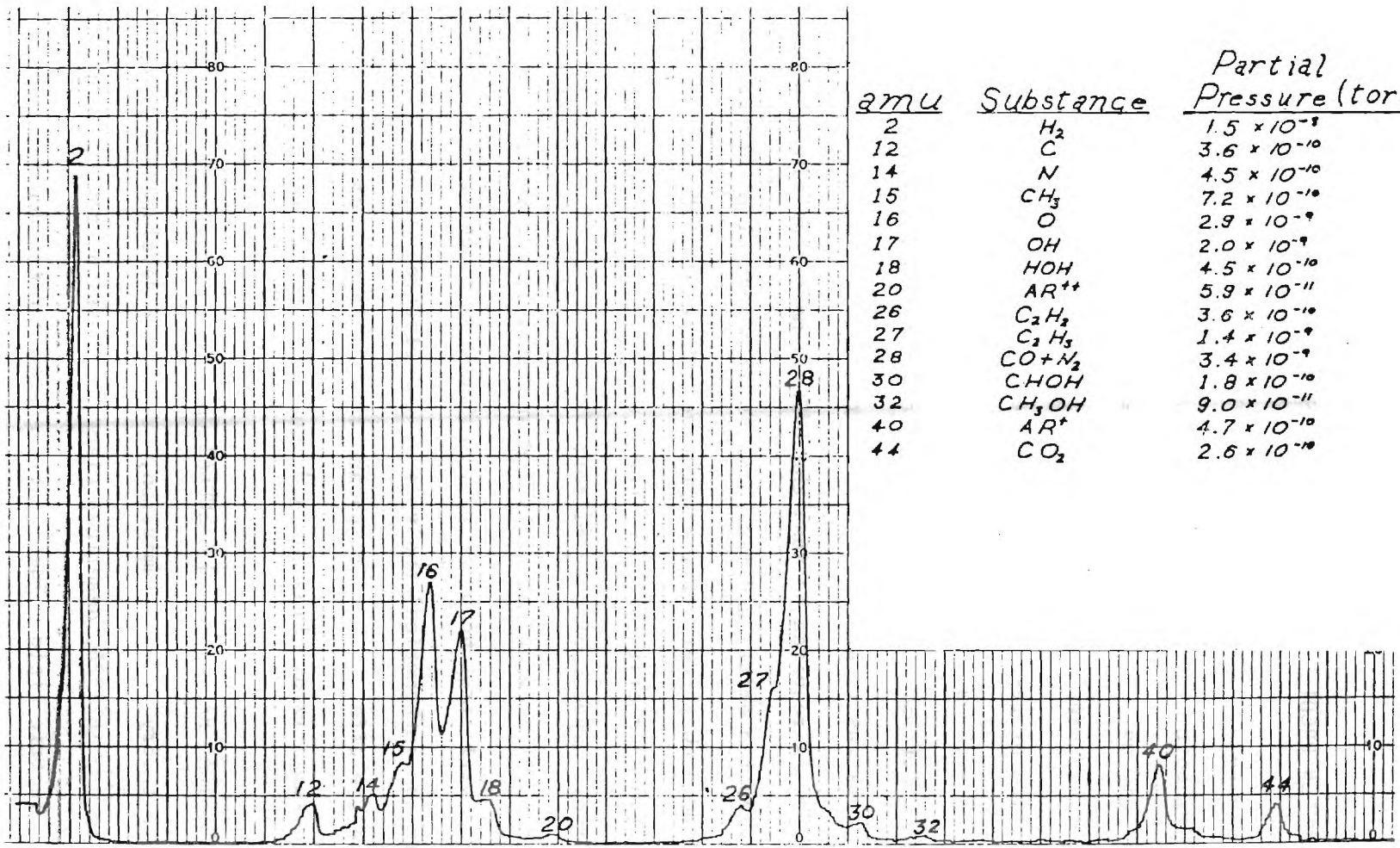

amu	Substance	Partial Pressure (torr)
2	H_2	1.5×10^{-8}
12	C	3.6×10^{-10}
14	N	4.5×10^{-10}
15	CH_3	7.2×10^{-10}
16	O	2.9×10^{-9}
17	OH	2.0×10^{-9}
18	HOH	4.5×10^{-10}
20	AR^{++}	5.9×10^{-11}
26	C_2H_2	3.6×10^{-10}
27	C_2H_3	1.4×10^{-9}
28	$CO+N_2$	3.4×10^{-9}
30	CHOH	1.8×10^{-10}
32	CH_3OH	9.0×10^{-11}
40	AR^{+}	4.7×10^{-10}
44	CO_2	2.6×10^{-10}

Figure IV-22. Mass Spectrum of Residual Atmosphere on Vacuum System.

CHAPTER V

COMPUTER PREDICTED GEOMETRY EFFECTS AND CIRCUIT MODEL OF THE LVFE

This chapter describes efforts to simulate the total device performance including both the effects of geometry on electron emission and the electrical circuit aspects of the LVFE module. The primary goal of the work was to provide guidance for the optimization of controllable parameters of the fabrication process. The effects on emission and electron trajectories of variables such as emitter tip radius, pin cone angle, extractor thickness, and pin position relative to the extractor were examined. The second goal of the work was to develop a valid circuit model of the LVFE device. A circuit model is required because the LVFE is more than simply a cathode; it is an electron emitting device possessing a control electrode and a unique volt-ampere characteristic. Effective utilization of the LVFE in practical applications is critically dependent upon an accurate characterization of the circuit aspects of the emitter.

In the following material, a discussion of the physical basis of field emission will first be presented, followed by a description of the techniques used in the mathematical analysis of the electron emission. Next, results showing the effect of device parameters on electron emission and trajectories will be summarized. Finally, a discussion of the circuit model will be given.

A. PHYSICAL BASIS OF THE CALCULATIONS

The theory of field emission, originally developed by Fowler and Nordheim [11] in 1926, describes electron emission from cold metals into a high electric field. The theory relates current density, J, in A/cm^2, field strength E, in V/cm, and the work function according to the

expression:

$$J = \frac{1.54 \times 10^{-6} E^2}{\phi t^2(y)} \exp \frac{-6.83 \times 10^{7} \phi^{3/2} f(y)}{E} \qquad \text{(V-1)}$$

where f(y) and t(y) are slowly varying elliptic functions of

$$y = \frac{(e^3 E)^{1/2}}{\phi} = \frac{3.79 \times 10^{-4} E^{1/2}}{\phi}. \qquad \text{(V-2)}$$

The substitution of typical numbers for ϕ shows that negligible field emission results until the electric field strength exceeds about 10^9V/m (1kV/μm or 10^7V/cm). The high value of electric field precludes the existence of a significant space charge region in the vicinity of the emitter tip until the current density approaches 10^8A/cm^2 (1μA/nm^2). The effect of space charge is to cause a reduction of the local electric field, an attendent decrease in emitted current, and a divergence in the electron trajectories. However, because of the high current density required for significant space charge, most of the normal range of field emitter operation can be described by a space-charge-free model. This allows the potential distribution within the device to be obtained from a solution of Laplace's equation which is considerably simpler to implement than Poisson's equation which considers space charge. The simplicity of Laplace's equation is offset by the need for extremely fine spatial resolution to represent the electric field near the very small pin tip. Mesh sizes of about 1nm (10 A) are needed to give sufficient detail in the electric field on the field emitter as compared with about 25 μm for the usual thermionic emitter.

Because the objective of the present work was the steering of the device fabrication procedures, it was important that a large number of quite different

structures should be analyzed. In order to reduce computation time and costs, comparisons among these varied structures were made on the basis of space-charge-free calculations. However, once the "standard" geometry had been selected, a limited number of calculations including the effects of space charge were made. These results, together with the space-charge-free data are presented later in this chapter.

The next sections are organized so that those calculations and results that do not include space charge are separate from those that do include space charge. The space-charge-free material is presented first and later the modifications necessary to account for space charge are given. This procedure is followed to clearly separate the two types of analyses.

B. SPACE-CHARGE-FREE ANALYSIS PROCEDURE

Most of the emitter simulations were done with the space-charge-free model. For this case, a procedure involving the solution of Laplace's equation and integration of the equation of electron motion was developed. This technique, which was later modified to account for the effects of space charge is as follows:

1. Laplace's equation is solved for a single emitter device placed below a biased collector.
2. The portion of the potential mesh including the emitter tip is expanded to provide increased resolution. Laplace's equation is solved for more detailed mesh. The border with the original mesh and the electrodes constitutes the required boundary conditions.
3. Step 2 is repeated several times until a final mesh size of less than 1nm (10 Å) is obtained.

4. The electric field along the surface of the emitter is calculated. This calculation is made over the surface of the emitter described in the finest mesh.
5. The electric field is used to calculate the field emitted electron current as a function of position on the emitter tip.
6. Trajectory starting points are assigned to specified fractions of the total emitted current.
7. Trajectories are calculated in the final (finest) mesh of the generated starting points.
8. Using the final velocity and position of these trajectories as initial conditions, trajectories in the next larger mesh are determined.
9. Step 8 is repeated until the trajectories have been followed through all meshes and intercepted by the collector.

The above procedure will now be examined in detail and all important techniques and assumptions will be discussed.

1. Potential Calculation

The electrostatic potential within the interelectrode space is calculated using a difference equation approximation of Laplace's equation.

Laplace's equation for the cylindrically symmetric case is

$$\frac{1}{r}\frac{\partial}{\partial r}\left(r\frac{V}{\partial r}\right) + \frac{\partial^2 V}{\partial V^2} = 0 \qquad \text{(V-3)}$$

The equation can be approximated at discrete points by the difference equation,[12,13]

$$\frac{V_{i,\,j+1} - 2V_{i,\,j} + V_{i,\,j-1}}{(\Delta r)^2} + \frac{1}{r_j}\,\frac{V_{i,\,j+1} - V_{i,j-1}}{2\Delta r}$$

$$+ \frac{V_{i+1,j} - 2V_{i,j} + V_{i-1,j}}{(\Delta z)^2} = 0 \qquad \text{(V-4)}$$

where (i,j) is the point in (z,r) space, r is the size of the r-mesh and Δz is the size of the z-mesh. If Equation V-4 is solved for V_{ij} and the assumption made that a square mesh is used, i.e., $\Delta r = \Delta z$, the following expression for the potential at any interior point (i,j) is obtained.

$$V_{ij} = \frac{1}{4}\,(V_{i,j-1} + V_{i,j-1} + V_{i+1,j} + V_{i-1,j})$$

$$+ \frac{\Delta r}{8r_j}\,(V_{i,j+1} - V_{i,j-1}) \qquad \text{(V-5)}$$

This equation is a weighted average of the four neighboring potential values plus a term dependent upon the gradient in the r-direction. Equation V-5 is not valid for points along the axis of the cylinder, but the required representation is easily obtained by taking the limit of Equation V-3 as r approaches zero and noting that no line charge is present on the axis. The procedure yields the equation for the potential on the axis of the cylinder to be,

$$V_{i,j} = \frac{1}{6}\,(4\,V_{i,j+1} + V_{i+1,j} + V_{i-1,j}).$$

These equations with the boundary conditions are solved to obtain the potential matrix.

Two types of boundary conditions are possible. The first of these (Dirichlet) specifies the potential at the boundary. The second type of boundary condition specifies the normal derivative of the potential. For the present case, conductive electrodes represent boundaries of the first kind while dielectric boundaries such as between the substrate and gate electrode must be treated as those of the second kind. The condition,

$$\frac{dV}{dr} = 0 \qquad \text{(V-7)}$$

simulates an insulating boundary of infinite radial extent. This constraint is adopted for the dielectric boundaries. The boundary condition is implemented by taking the difference formulation for the derivative and setting it equal to zero. The outermost potential is then obtained in terms of the interior value. This result is substituted into Equation V-5 to yield the required expression for the potential at the boundary. The result is,

$$V_{ij} = \frac{1}{4} (2V_{i,j-1} + V_{i+1,j} + V_{i-1,j}). \qquad \text{(V-8)}$$

An additional complication arises if the potential boundaries are not r = constant or z = constant surfaces. If a piecewise approximation is not acceptable, some method of representing a smooth boundary must be included. This is accomplished by adjusting mesh points so that they properly reflect the actual boundary potential position. An

extrapolation/interpolation scheme is used to implement this procedure[12]. Give four matrix points with the boundary located between points P and Q

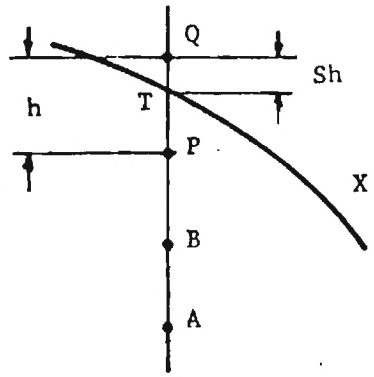

If the potential is known along the boundary X, the value at the nearer mesh point Q can be found by

$$V_Q = \frac{6}{(1-S)(2-S)(3-S)} V(X) - \frac{3S}{1-S} V(P) + \frac{3S}{2-S} V(A) - \frac{S}{3-S} V(B). \qquad (V-9)$$

In the equation S is the fractional distance into the mesh or $S = \overline{QT}/h$. If the nearer mesh point Q were on the other side of the boundary, the directed distance S would be negative. Equation IV-9 implements the procedure using a cubic approximation. This can be replaced by a lesser order expression if insufficient interior points are available.

The numerical solution is accomplished by repeatedly applying the potential equations to the potential matrix until the desired degree of convergence is obtained. The calculation is terminated when the values of successive iterations satisfy,

$$V_{ij}(k+1) - V_{ij}(k) \leq \varepsilon_v \qquad \text{(V-10)}$$

where ε_v is the voltage convergence value. A typical value of ε_v in this work is 0.001 V.

When the convergence condition is satisfied, the discrete matrix points along the smooth boundaries are modified to account for the actual boundary. Potentials are then recalculated and the discrete boundary modified again. After about five iterations negligible changes in the boundary values are noted.

2. Electric Field Calculation

The electric field is obtained from the potential by a difference equation approximation. The electric field near a matrix point (i,j) is given to second order by

$$E_r = \frac{V_{i,j+1} - V_{i,j-1}}{2\Delta r} - \frac{V_{i,j+1} - 2V_{i,j} + V_{i,j-1}}{(\Delta r)^2} h_r \qquad \text{(V-11)}$$

$$E_r = \frac{V_{i+1,j} - V_{i-1,j}}{2\Delta z} - \frac{V_{i+1,j} - 2V_{i,j} + V_{i-1,j}}{(\Delta z)^2} h_r \qquad \text{(V-12)}$$

where h_r and h_z represent the distance between the matrix point (i,j) and the point at which the electric field is to be determined. The second order correction is necessary since the trajectories are not

constrained to pass through mesh points.

3. Calculation of the Emitted Current

The emitted current is obtained by numerically evaluating

$$I = \int j \cdot dA = \sum_i J_i A_i . \qquad \text{(V-13)}$$

The current densities are given by the Equation V-1 using the electric field values along the surface of the emitter.

For a conical or spherical pin the area elements of area A_i are given by

$$A_i = \pi(r_{i+1} - r_i) \left[(z_{i+1} - z_i)^2 + (r_{i+1} - r_i)^2 \right]^{\frac{1}{2}} . \qquad \text{(V-14)}$$

This expression is exact for the conical regions and is approximately correct on the sphere. It is easily shown that the error in area is less than 0.1% if twenty subdivisions are chosen over a hemisphere.

The emitter surface is usually divided into fifty intervals. Twenty-five are selected at increments of equal polar angle around the spherical tip while twenty-five are equally spaced along the conical shank. It should be recalled that these calculations are made in the finest mesh and, therefore, only a small portion of the conical shank is represented. Because of the falloff of the electric field, a negligible error in the emitted current results from neglecting the remainder of the pin surface.

4. Trajectory Starting Points

The trajectory starting points are assigned to indicate speci-

fied fractions of the emitted current. This is done by comparing the total current, calculated as described above, with the cumulative current starting from the emitter tip. A trajectory is initiated for every five percent increase in cumulative current. A polynomial is fitted to the current calculations with the cumulative current as the independent variable and the emitter position as the dependent variable. The polynomial coefficients are then used to determine the starting location of each trajectory for the specified fraction of emitted current.

5. Trajectory Calculations

Once the potential arrays are determined and the starting points selected the trajectories can be calculated. The equations of motion for the electrons moving within the device are,

$$m\ddot{r} = -eE_r \qquad \text{(V-15)}$$

$$m\ddot{z} = -eEz \qquad \text{(V-16)}$$

where E_r and E_z are, respectively, the r- and z-components of the electric field. The electric field is obtained from Equations V-11 and V-12.

Once the field values are obtained, the equations of motion can be solved subject to the appropriate initial conditions. The initial conditions are either,

$$\dot{r}(0) = 0, \quad r(0) = r_o$$

$$\dot{z}(0) = 0, \quad z(0) = z_o \qquad \text{(V-17)}$$

for the emission at the surface of the emitter pin, or

$$\dot{r}(t_n) = \dot{r}_f, \qquad r(t_n) = r_f$$

$$\dot{z}(t_n) = \dot{z}_f, \qquad z(t_n) = z_f \tag{V-18}$$

at the points where the trajectories leave one expanded mesh for another. The subscript, o, indicates the initial starting locations where the subscript, f, designates the final values in the previous mesh.

The equations of motion are solved using the Runge-Kutta technique[12,13]. This method has the advantage of being self starting. It is probably slower than some other techniques and lacks a well-defined error estimate[12,13]. However, it is simple to implement and if proper precautions are observed, it provides good results. The routine was checked by solving differential equations with known analytical solutions. Trajectory results were confirmed by calculating them for different step sizes and verifying that the trajectories were essentially unchanged.

C. DISCUSSION OF RESULTS OBTAINED FROM SPACE-CHARGE-FREE CALCULATIONS

The techniques outlined in the previous material were utilized to perform a parametric study of the field effect emitters. The details of the simulation and a discussion of the results will not be presented.

The initial representation of a typical emitter geometry is shown in Figure IV-16. These basic dimensions were used for all simulations with device parameters varied as desired. The collector was situated

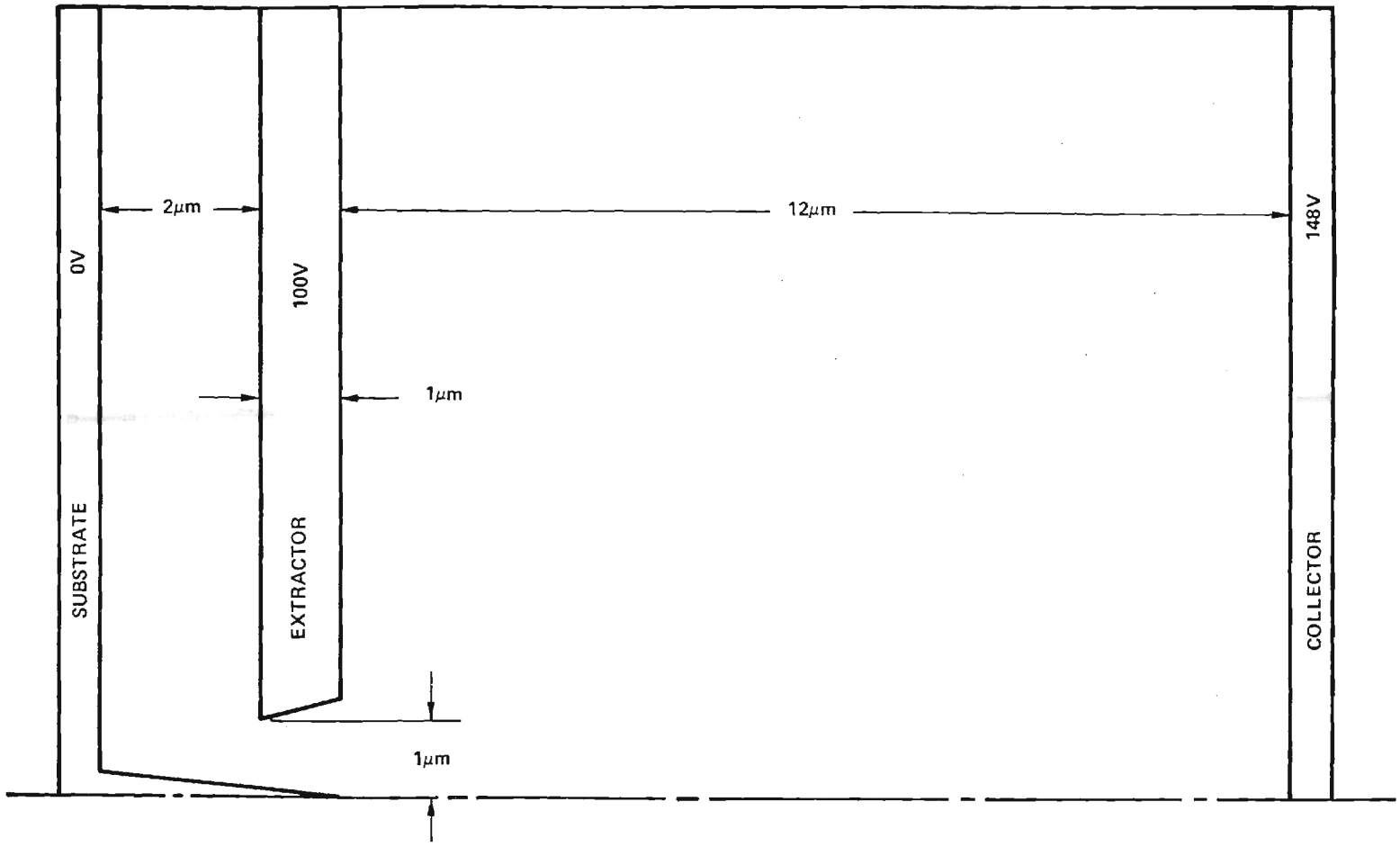

Figure V-1. Reference Geometry and Potentials for Simulation. Pin Radius is 10 nm (100 Å) and Cone-Half-Angle is 6 Degrees.

as far as possible while providing some resolution at the emitter and extractor. The collector potential of 148 V was selected to provide the same electric field that would be obtained from a collector biased 1000 V above the extractor and located 0.01 inch away. Figure IV-17 presents a plot of equipotentials for the reference device.

The initial representation of the emitter was made using 60 x 40 mesh. Resolution was, therefore, 0.25 μm. Three 5X expansions were made in the 60 x 40 mesh. Resolution in the final mesh was increased by a factor of three to 180 x 120 before the electric field was calculated. Thus, one mesh unit was equivalent to 0.25 μm in the initial simulation and 6.67 $\mathring{A}$ in the final mesh.

As discussed previously, trajectory calculations were initiated in the fine mesh and followed through successively larger meshes. Normalized time increments were chosen so about fifty steps per trajectory per mesh were calculated. Hence each complete trajectory was determined in 200 increments. This was an adequate number to ensure a valid solution by the Runge-Kutta method. A set of trajectories for the reference geometry is given in Figure V-18.

The emitted current was calculated using Equations V-1 and V-13. A work function of 8.0 eV, corresponding to oxygenated tungsten, was selected. The functions f(y) and t(y) were generated as discussed elsewhere[13]. The use of this work function resulted in a calculated current considerably lower than the measured value. This difference is probably attributable to the enhancement of the local electric field by atomic-size protrusions on the emitter pin.

Figure V-2. Plot of Equipotentials for Reference Device.

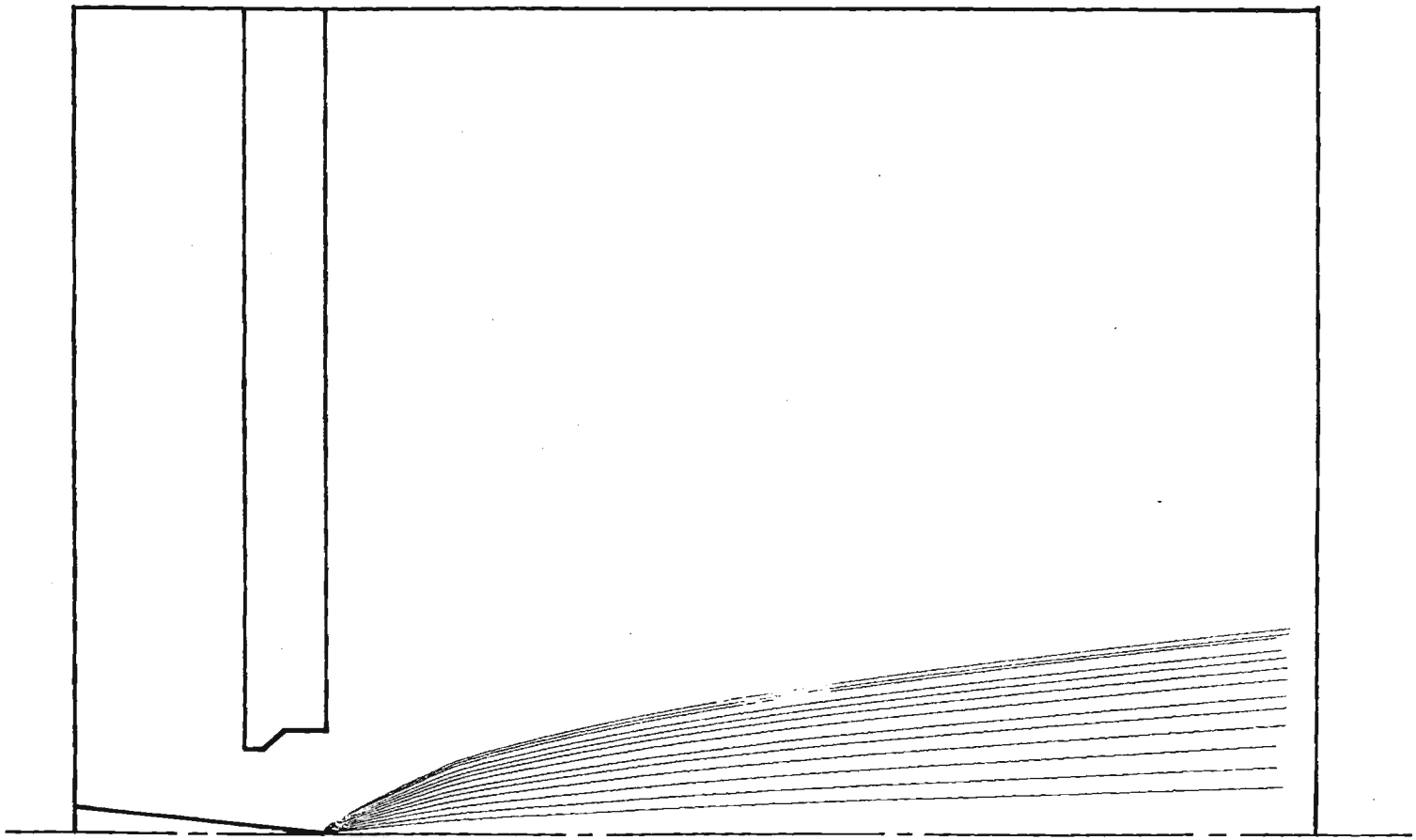

Figure V-3. Electron Trajectories for the Reference LVFE Configurations.

The results of the extensive simulations will now be summarized and discussed. A bench mark or nominal device geometry will be used when presenting results which are not strongly dependent upon the LVFE parameters. For example, the variation of pin-tip electric field position along the pin is of similar shape for all pin radii and cone angles. Hence, a single presentation of these results for a representative geometry conveys adequate information. The geometry and dimensions of the standard device are shown in Figure V-1.

1. Variation of Electric Field on Emitter Surface

Figure V-19 shows the variation of the electric field as a function of pin tip polar angle. These results indicate that the electric field is slowly varying near the pin tip, but falls off rapidly along the shank. Results for other pin radii and cone angles show a similar variation. It should be noted that these data are qualitatively similar to those for other low voltage field emitters, but often exhibit a significantly larger electric field[10].

2. Effect of Pin-Tip Radius on Peak Electric Field

One advantage of the composite LVFE devices over other types of emitter arrays is the very small pin tip radius obtainable from the tungsten pins by use of chemical etchants. Pin tip radii of less than 5nm (50 Å) can be produced. It was important to ascertain if such small tips could lead to the significant improvements in device performance and to evaluate the sensitivity of electron emission to small variations of pin radii.

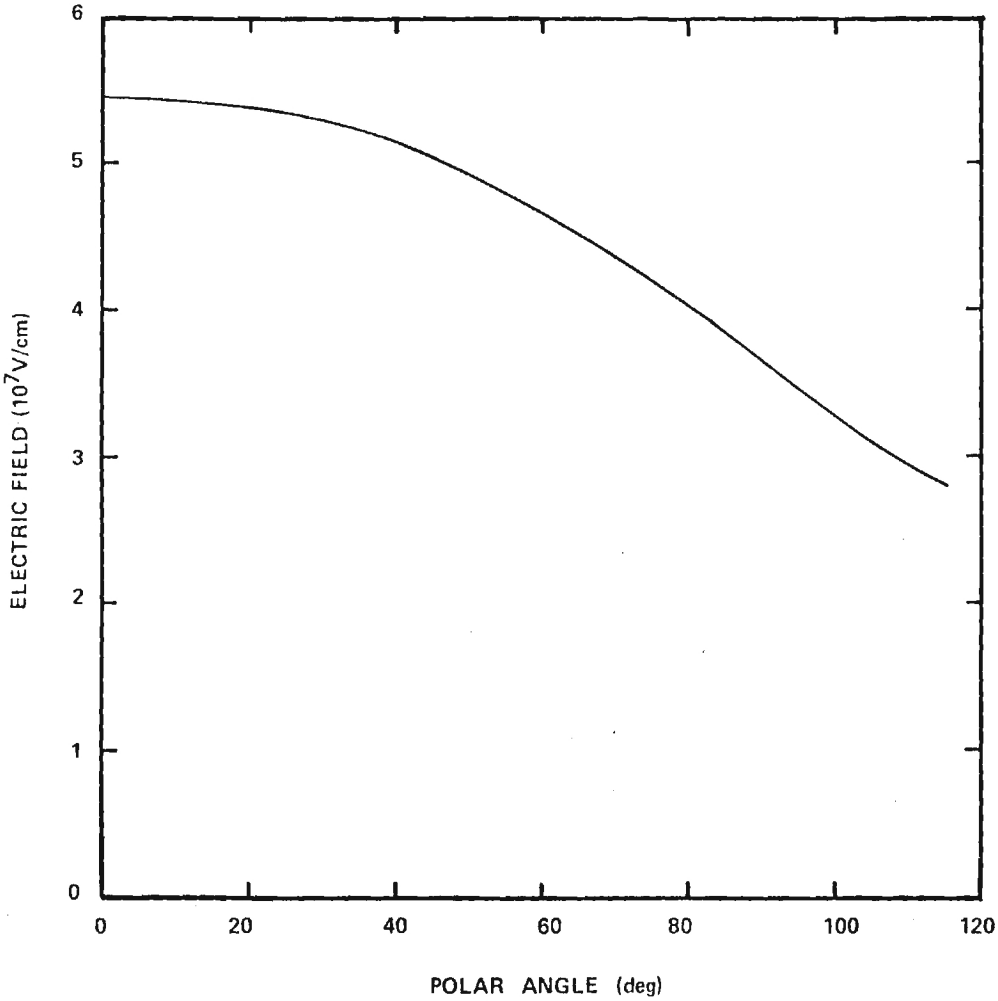

Figure V-4. Electric Field as a Function of Polar Angle. Pin Radius 10 nm (100 Å). Pin level, upper width edge of extractor. Data are for the reference geometry.

A simple way to estimate the effect of pin tip radius is to consider a single isolated pin placed below a spherical collector. For this simple case the electric field has been shown to be approximately,

$$E = \frac{2V}{r \log(R/r)}, \qquad \text{(V-19)}$$

where V is the applied voltage, r is the radius of the emitter, and R is the collector radius. Since the function log(R/r) is slowly varying, one can write,

$$Er \simeq \text{const.} \qquad \text{(V-20)}$$

This simple theory suggests that any reduction in the emitter radius will be accompanied by a proportional increase in electric field. This approximation was compared with the numerically calculated LVFE pin-tip electric field.

Results of the numerical calculations are given in Figure V-5 These data show the expected strong dependence of the electric field on the tip radius. Also presented in Figure V-5 is a plot of the field-tip-radius product. This quantity is seen to be slowly varying and thus in qualitative agreement with the simple theory.

From these calculations it can be concluded that the small radii of the composite LVFE device pins result in a significantly larger electric field than obtainable with the usual 25-75 nm (250-750 Å) radii of thin film type emitters. A second conclusion is that the size distribution of pin tip radii must be carefully controlled if spatially uniform emission is to be achieved.

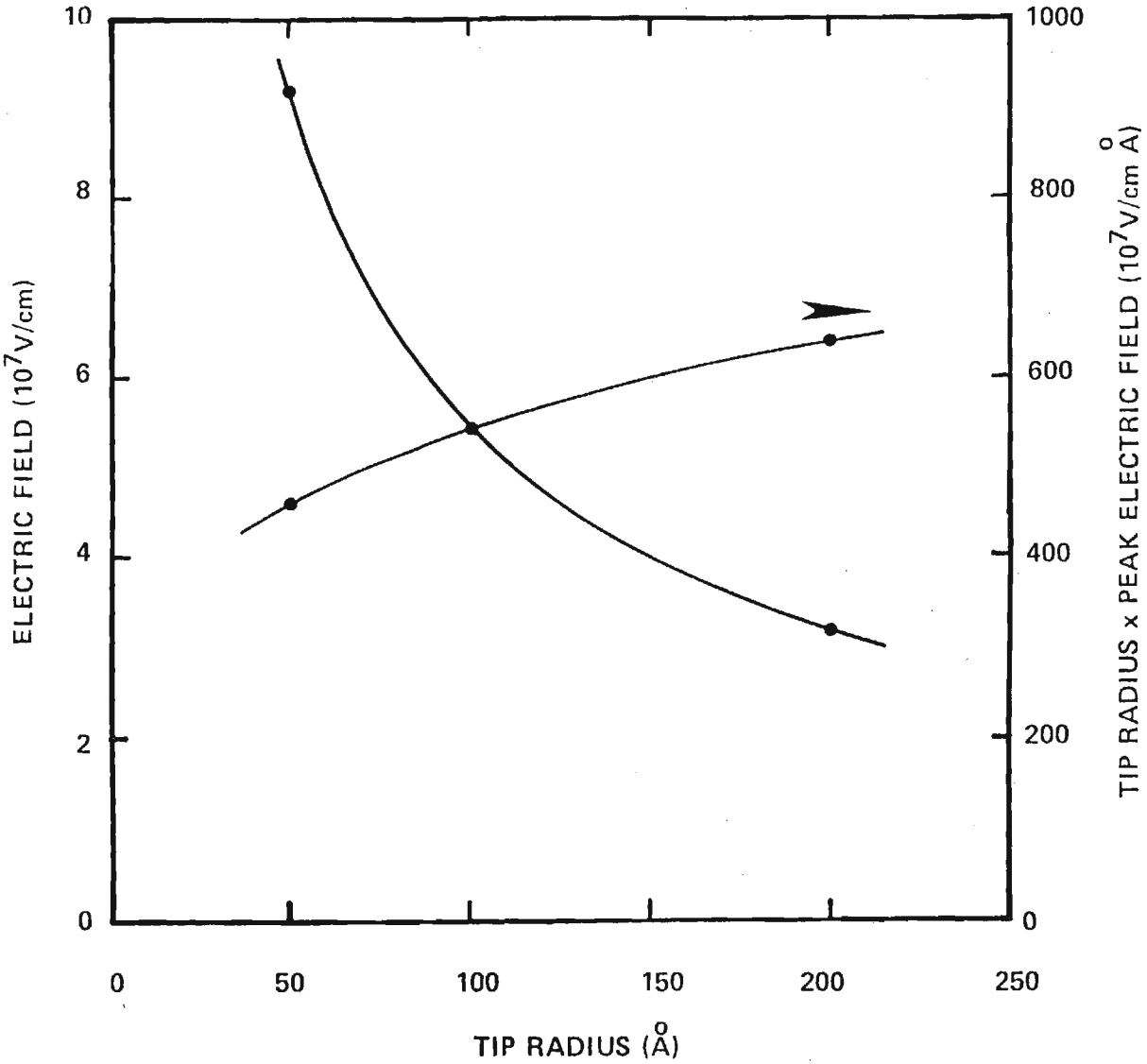

Figure V-5. Plots of Pin-Tip Electric Field and the Tip Radius-Electric Field Product as a Function of Tip Radius. Data are for the reference geometry.

3. Effect of Pin Cone-Angle on Peak Electric Field

The LVFE fabrication process yields emitter pins significantly sharper than those obtained by other methods. Calculations were made to assess the effect of the pin cone-angle of the peak electric field and hence electron emission. The results of this study are shown in Figure V-6. It is apparent that the small cone-half-angle (6^{o}) results in a significant increase in electric field over the larger angle (30^{o}) characteristic of other low voltage arrays. It can thus be concluded that the present fabrication techniques are yielding an emitter pin that is reasonably optimized with respect to pin cone-angle.

4. Effect of Extractor Hole Size on Peak Electric Field

The size of the extractor hole is one parameter that is expected to influence the performance of the LVFE device. The extractor hole radius is determined by the thickness of the insulator film and the number of deposition sequences. Multiple deposition offers a way to reduce the extractor radius. However, multiple deposition entails a more complex fabrication process.

The effect of extractor hole radius on pin tip electric field is shown in Figure V-7. The result indicates that the peak field is relatively insensitive to the hole radius, and suggests that the more complicated double deposition fabrication process used to reduce the hole diameter will offer only minor improvements in the LVFE performance.

5. Effect of Pin Position Relative to Extractor

Because of variations in effective etching rates, the preci-

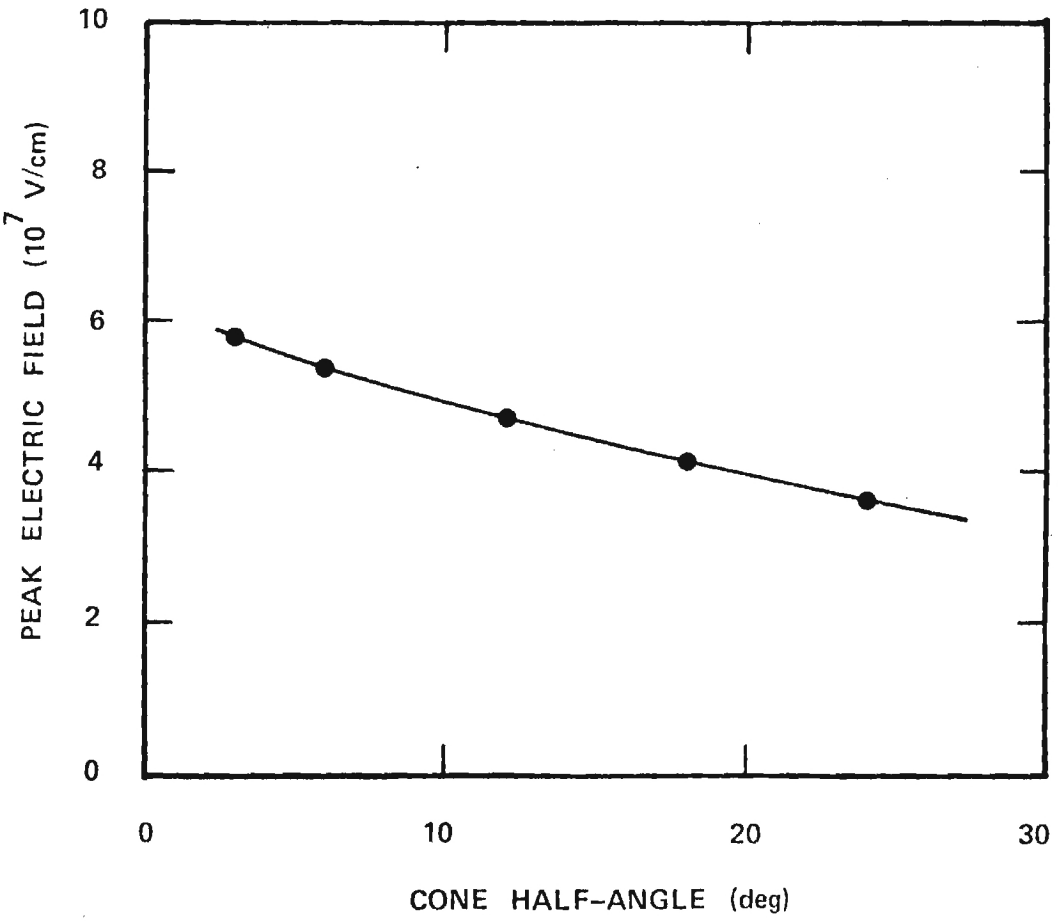

Figure V-6. Variation of Pin-Tip Electric Field as a Function of Cone Half-Angle. Data are for the reference geometry.

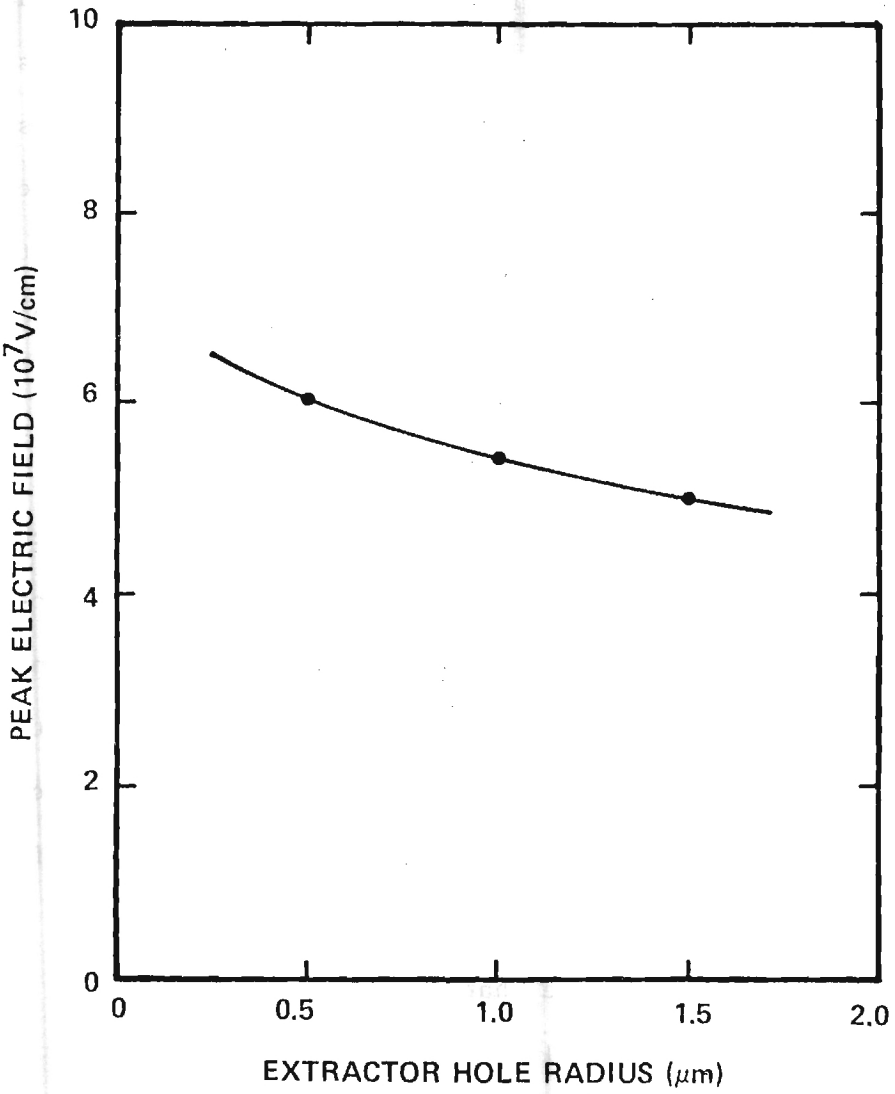

Figure V-7. Peak Pin-Tip Electric Field as a Function of Extractor Hole Radius. Data are for the reference geometry.

sion with which emitter pin length can be controlled is somewhat limited. It is thus very important to assess the effect of variations. These results are shown in Figure V-8. The figure plots the peak electric field as a function of the position of the emitter pin relative to the base of the extractor with extractor thickness as a parameter. The calculations lead to the important conclusion that the peak electric field, and hence emission, is insensitive to the position of the pin tip provided that the tip is positioned at least midway in the extractor. It is also apparent that there is negligible effect on the electric field from variations in extractor thickness. This allows other considerations such as extractor current capacity, to determine the actual thickness of the extractor.

D. ANALYSIS INCLUDING THE EFFECTS OF SPACE CHARGE

Although most of the device simulations were made using a space-charge-free model, a few representative calculations that included the effects of space charge were made. This section discusses these calculations including the mathematical methods used and the results obtained. Because of the large amount of material that is common to the discussion of the space-charge-free calculations, only the necessary modifications to include the effects of space charge will be presented.

The calculations including space charge proceed as follows:

1. The space-charge-free potentials, electric fields emission current and trajectories are calculated using the procedure described earlier.
2. An estimate of the space charge is made from the trajectories and the emission current.
3. New potentials, electric fields, emission currents and trajectories are calculated.

different situations. This was accomplished by adjusting the emitter work function over the range of 3.5 to 6.0 eV. All other device parameters and potentials were held at the reference values given in Figure V-1. For the indicated change in work function, the emission current changed from about 150 μA to about 0.2 μA. Space charge effects became significant with emission currents of about 20 μA. Results of the calculations including space charge are given in Figures V-9 and V-10. Figure V-9 shows the effect of space charge on the pin-tip electric field, while Figure V-10 indicates how increases in current and space charge affect the trajectories.

Figure V-10 presents a plot of the electric field over the surface of the emitter pin as a function of polar angle. The figure shows that the peak electric field is about 5.4×10^7 V/cm at the apex of the pin when space charge is not included. When the pin current reaches about 150 μA, the accumulated space charge reduces the electric field to the lower of the two curves, resulting in a peak value of about 4.25×10^7 V/cm. The field down on the side of the pin, where little emission occurs and hence little space charge, is very nearly equal to the space-charge-free value. One result of space charge is thus to cause a more uniform electric field and hence a more uniform electron emission from the pin. However, the space charge induced reduction is a small effect and probably cannot be relied upon to stabilize the emission from the LVFE array. A current of 15 μA per pin corresponds to an array current density of 150-1500 A/cm^2. Thus if all pins were emitting uniformly, it is unlikely that space charge effects would be observed in normal operation.

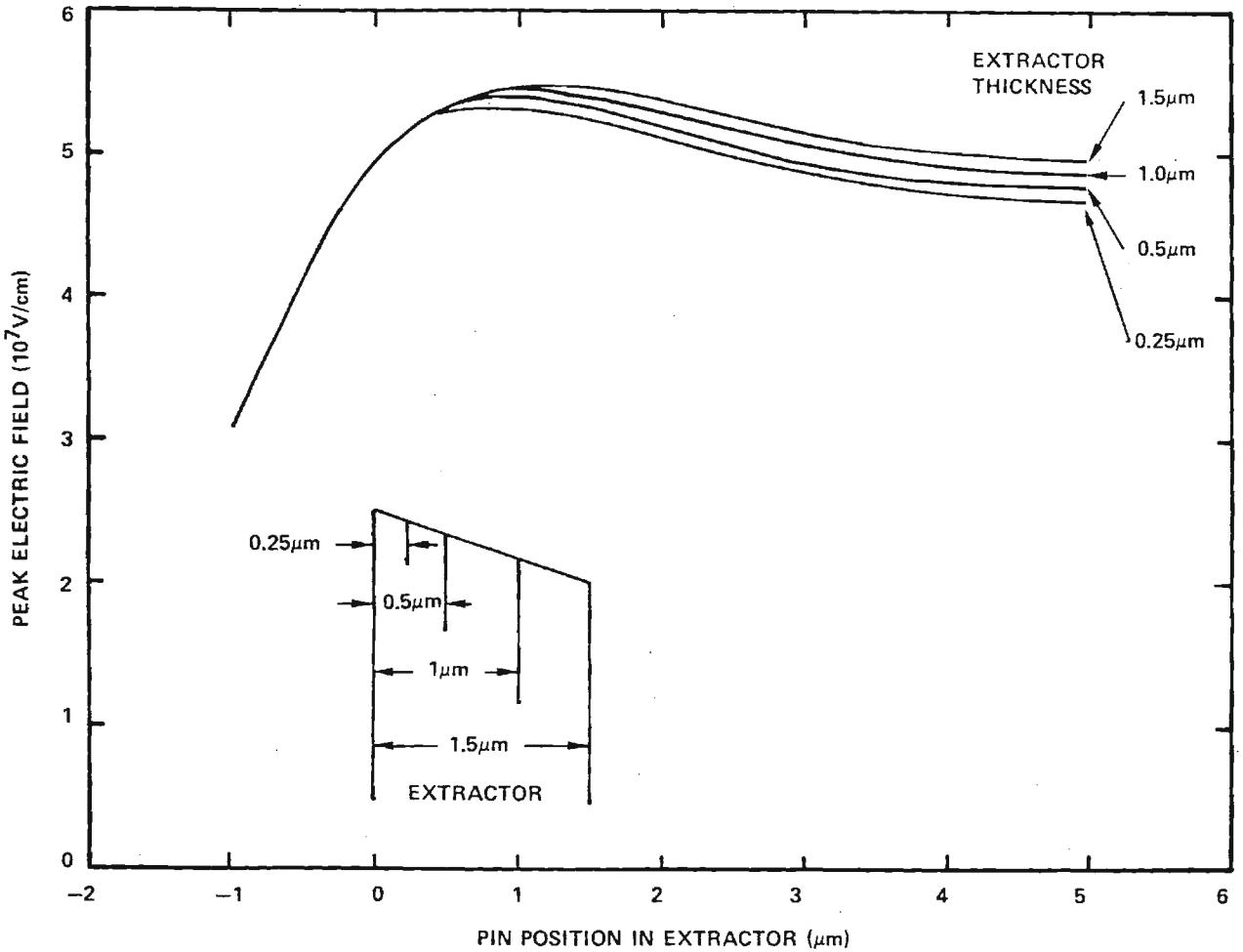

Figure V-8. Pin Tip Peak Electric Field as a Function of Pin Position in the Extractor with Thickness as a Parameter. Data are for the reference geometry.

4. A new estimate of the space charge is determined.

5. Steps 3 and 4 are repeated until the trajectories remain essentially unchanged.

The only new calculations introduced by the above procedure are those for the electric potential in the presence of space charge and the determination of the space charge from the trajectory information. These two tasks will now be examined in detail.

1. Potential and Space Charge Calculations

The electric potential within the cylindrically symmetric LVFE structure is exactly described by Poisson's equation,

$$\frac{1}{r}\frac{\partial}{\partial r}\left(r\frac{V}{\partial r}\right) + \frac{\partial^2 V}{\partial V^2} = -\frac{\rho}{\varepsilon_o}. \qquad \text{(V-21)}$$

If the equation is reduced to difference formulation and solved for V with the assumption made that a square mesh is used, i.e., $\Delta r = \Delta z$, the following expression for the potential at any interior point (i,j) is obtained:

$$V_{ij} = \tfrac{1}{4}(V_{i,j-1} + V_{i,j-1} + V_{i+1,j} + V_{i-1,j})$$

$$+ \frac{\Delta r}{8r_j}(V_{i,j+1} - V_{i,j-1}) + P_{ij} \qquad \text{(V-22)}$$

where

$$\rho_{ij} = \frac{(\Delta r)^2 \rho}{4\varepsilon_o} \qquad \text{(V-23)}$$

In this equation ρ is the charge density, and ε_o is the permittivity of free space. Using a similar analysis equations for points on Z-axis and boundary

points can be found.

Since at a given point the current density, J , is related to the volume space charge, ρ, and velocity, v, of the electron by,

$$J = \frac{\rho}{v}. \tag{V-24}$$

we can write

$$\rho_{ij} = \frac{(\Delta r)^2 J_k}{4v\varepsilon_o} \tag{V-25}$$

where J_k is the current density associated with the trajectory k through the point i,j.

The current density J_{ij} is obtained in terms of the current J_k carried by each trajectory from

$$J_{ij} = \frac{I_k}{A_{ij}} \tag{V-26}$$

Here A_{ij} is the surface area normal to the trajectory passing close to the ith matrix point. Calculations proceed by moving along a trajectory and assigning a space charge density to all points that lie within one Δr or Δz of the trajectory. Figure V-9 shows the geometry for these calculations. Using this idea, it can be shown that the additions to the space charge matrix for each trajectory crossing a horizontal line (z-direction line) at the point i,j are

$$\rho_{i,j} = \rho_{i,j} + \frac{\Delta r^2 \, I_K}{8\pi\varepsilon_o r \sin\theta \, \Delta z \sqrt{v_r^2 + v_z^2}} R_z \tag{V-27}$$

$$\rho_{i+1,j} = \rho_{i+1,j} + \frac{\Delta r^2 \, I_k}{8\pi\varepsilon_o r \sin\theta \, \Delta z \sqrt{v_r^2 + v_z^2}} (1-R_z) \qquad \text{(V-28)}$$

The additions to the space charge matrix for each trajectory crossing a vertical line (r-direction line) are given by,

$$\rho_{i,j} = \rho_{i,j} + \frac{\Delta r^2 \, I_k}{8\pi\varepsilon_o r \cos\theta \, \Delta z \sqrt{v_r^2 + v_z^2}} R_r \qquad \text{(V-29)}$$

$$\rho_{i,j+1} = \rho_{i,j+1} + \frac{\Delta r^2 \, I_k}{8\pi\varepsilon_o r \cos\theta \, \Delta z \sqrt{v_r^2 + v_z^2}} (1-R_r) \qquad \text{(V-30)}$$

In these equations R_r and R_z are the normalized (to mesh units) r- and z-distance to the point i,j; r is the radial distance to where the trajectory crosses either the horizontal or vertical line, and v_z and v_r are the z- and r-direction velocity components.

Using the above equations, the space charge associated with each matrix point near a trajectory is determined. These data are used to calculate a new potential distribution and a new set of trajectories. Since the electric field at the emitter tip is affected by the new potential distribution, the emitted current changes. This results in a different space charge distribution. After several iterations, the process converges resulting in the final values of the space charge distribution, the final potential distribution and the final emitted current.

2. Results of the Space Charge Calculations

Space charge effects were introduced using the techniques outlined above. In order to present an unambiguous representation of the effects of space charge, only the emitted current and consequently the space charge was changed for

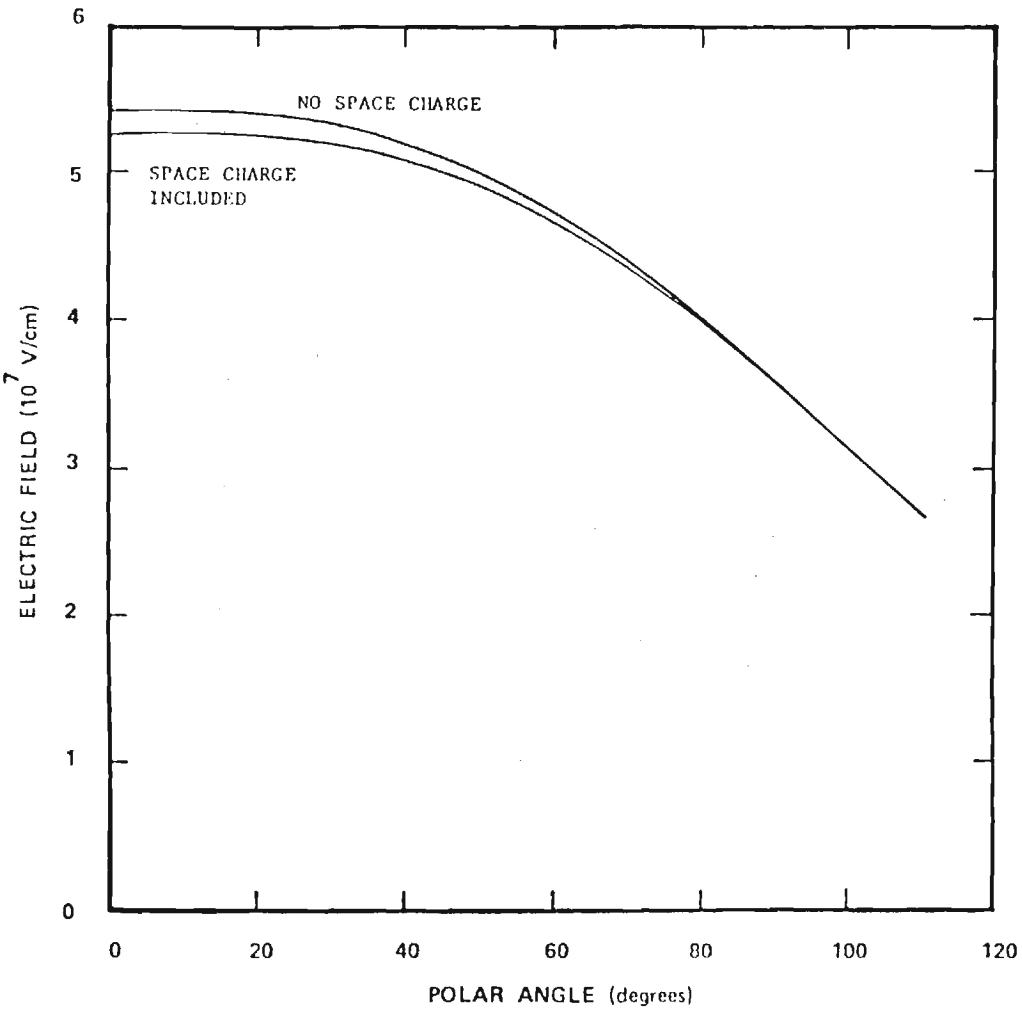

Figure V-9. Electric Field as a Function of Polar Angle. The Emission Current for the Space Charge Included Case is 150.5 Microamperes. Pin has the Reference Geometry.

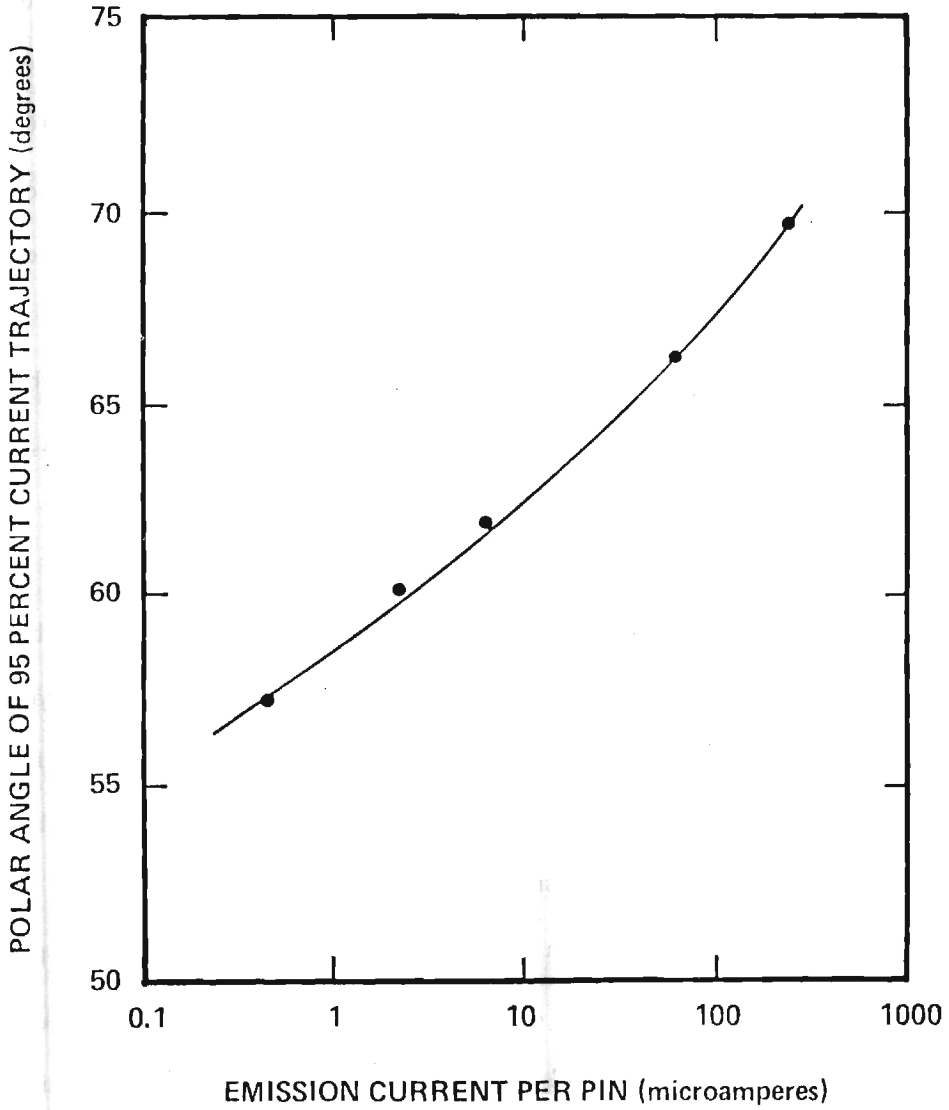

Figure V-10. Polar Angle of the 95 Percent Current Trajectory as a Function of Emission Current.

different situations. This was accomplished by adjusting the emitter work function over the range of 3.5 to 6.0 eV. All other device parameters and potentials were held at the reference values given in Figure V-1. For the indicated change in work function, the emission current changed from about 150 μA to about 0.2 μA. Space charge effects became significant with emission currents of about 20 μA. Results of the calculations including space charge are given in Figures V-9 and V-10. Figure V-9 shows the effect of space charge on the pin-tip electric field, while Figure V-10 indicates how increases in current and space charge affect the trajectories.

Figure V-9 presents a plot of the electric field over the surface of the emitter pin as a function of polar angle. The figure shows that the peak electric field is about 5.4×10^7 V/cm at the apex of the pin when space charge is not included. When pin current reaches about 150 μA, the accumulated space charge reduces the electric field to the lower of the two curves, resulting in a peak value of about 4.25×10^7 V/cm. The field down on the side of the pin, where little emission occurs and hence little space charge, is very nearly equal to the space-charge-free value. One result of space charge is thus to cause a more uniform electric field and hence a more uniform electron emission from the pin. However, the space charge induced reduction is a small effect and probably cannot be relied upon to stabilize the emission from the LVFE array. A current of 15 μA per pin from a $10^7/cm^2$ density array corresponds to an array current density 150 A/cm^2. Thus, if all pins were emitting uniformly, it is unlikely that space charge effects would be observed in normal operation.

Since space charge effects are observed experimentally, it must be concluded that a few emitter pins are emitting very strongly while most are quiescent. Such a conclusion seems to be confirmed by the observations with the field emission microscope.

The effect of space charge and increasing emission current on the electron trajectories is shown in Figure V-10. Here, the polar angle corresponding to 95 percent of the emitted current is given as a function of the total emission current. As explained earlier in this chapter, starting points for the trajectories were assigned at five percent current increments. For example, the first trajectory was started at the point on the pin where the current density integrated over the surface of the pin from the pin apex was five percent of the total current. The next trajectory started at ten percent of the total current, etc. The 95 percent trajectory thus includes approximately 95 percent of the total emission current. The total current (100%) includes the entire surface of the pin as described in the finest mesh.

From Figure V-10, it is seen that the half angle of the emitted current trajectory (the polar angle) increases significantly with increasing emission current. This leads to emission interception by the extractor if the pin is placed too low in the extractor. More importantly, it presents difficulties in the design of focussed electron beams.

E. LVFE CIRCUIT MODEL

A circuit model of the Low Voltage Field Emitter has been developed to aid in characterization of the LVFE and to permit effective application of the LVFE as an electron source in practical devices. The operating characteristics and driving requirements of the LVFE are represented by the circuit model. Inclusion of interelectrode capacitances in the model allows it to represent the frequency dependence and transient behavior of the device. The noise behavior of the LVFE has also been investigated and incorporated into the model.

The configuration of the circuit model has been determined from the physical properties and construction of the LVFE device. The extractor film and emitter pin resistance have been characterized using theoretical techniques. Preliminary theoretical investigations have been conducted for the device capacitances. Preliminary experimental noise measurements have been performed to determine applicable experimental techniques and equipment.

The theoretical derivations and calculations involve the use of a typical LVFE device structure to define the geometry being modeled and specify the dimensions used to calculate representative values for the circuit model elements. This typical device is constructed on a UO_2-W die with a radius r_d of 2.1 mm, a thickness ℓ_d of 2 mm, a fiber density N of 10^5 pins/mm^2, and a fiber radius r_p of 0.5 μm. The emitting pins are cone shaped with a spherical tip and have an exposed height of 2.5 μm, a tip radius r_t of 10nm, and a base radius equal to the fiber radius. The pins stand exposed over an active area with a radius r_{aa} of 0.25 mm. The molybdenum extractor layer has a

thickness h_e of 0.5 μm with the hole around each emitting pin having a radius r_h of 1 μm. The extractor is separated from the substrate by an Al_2O_3 insulator layer with a thickness ℓ_i of 2 μm.

1. Circuit Model Configuration

The circuit model is based upon the physical construction of the LVFE device, its expected characteristics, and the known properties of field emission. The diagram in Figure V-11 shows the basic structure of the LVFE with the parameters to be modeled superimposed over the corresponding part of the device structure. A schematic diagram of the equivalent circuit model configuration proposed for the LVFE is shown in Figure V-12.

The extractor terminal E of the circuit model corresponds to the perimeter of the extractor film. The cathode terminal K is the bottom surface of the UO_2-W composite die which has the ends of the fibers exposed outside the matrix to ensure that a good contact is made to all fibers. The anode terminal A is not an actual part of the LVFE structure, but must be provided in the model to receive the useful portion of the emission current. For all testing of the LVFE done for this research the anode will be a metal electrode located above the LVFE and physically separated from it.

The extractor resistor R_e of the LVFE circuit model represents the resistance of the thin molybdenum film forming the extractor. The cathode resistor R_k corresponds to the resistance of the UO_2 matrix and tungsten fibers within the matrix which together comprise the UO_2-W composite structure. The resistance of exposed portions of the tungsten fibers standing above the matrix to form the emitting pins is represented by the pin resistor R_p. No anode resistance is included in the circuit model since the anode

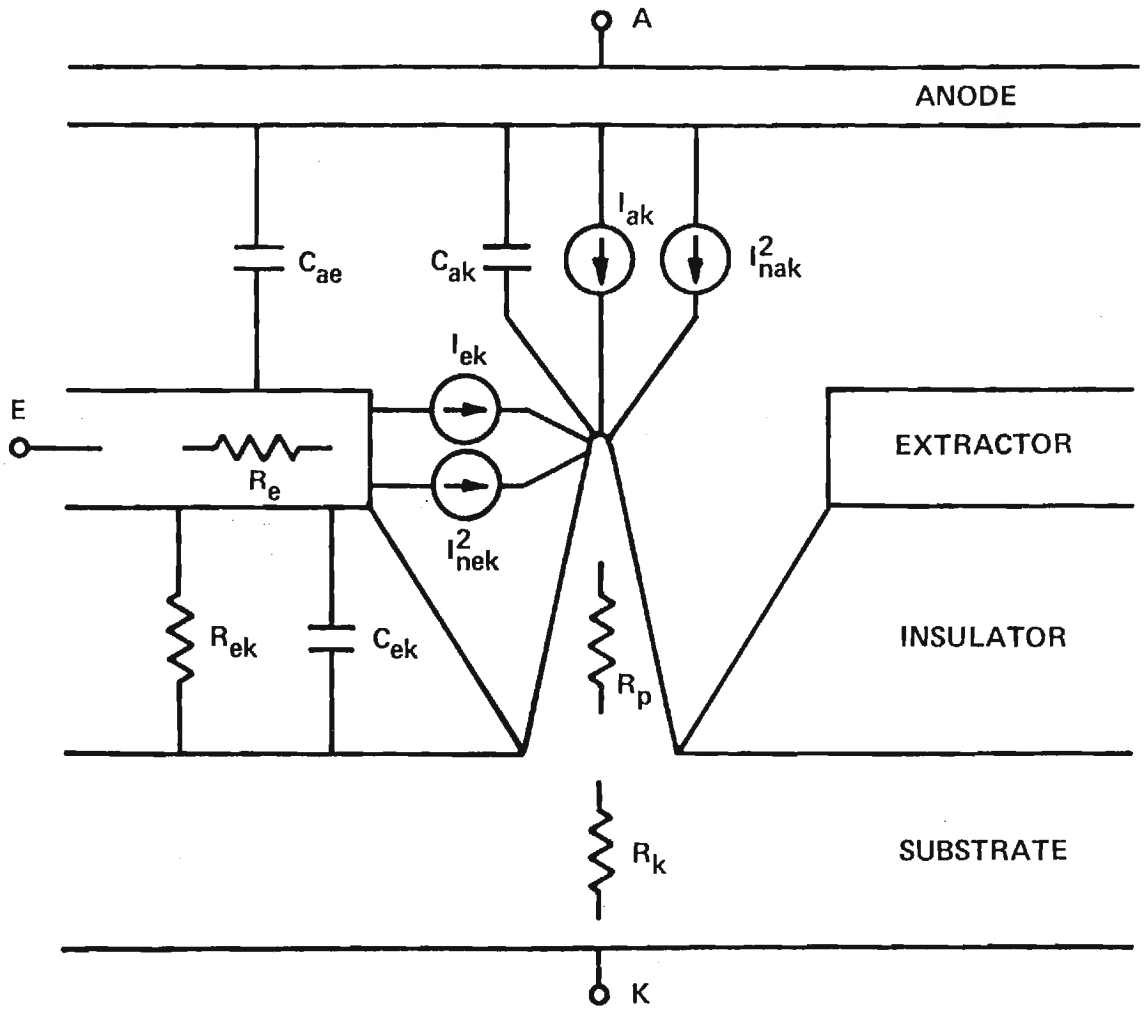

Figure V-11. Schematic of LVFE Structure Showing Circuit Model Parameters.

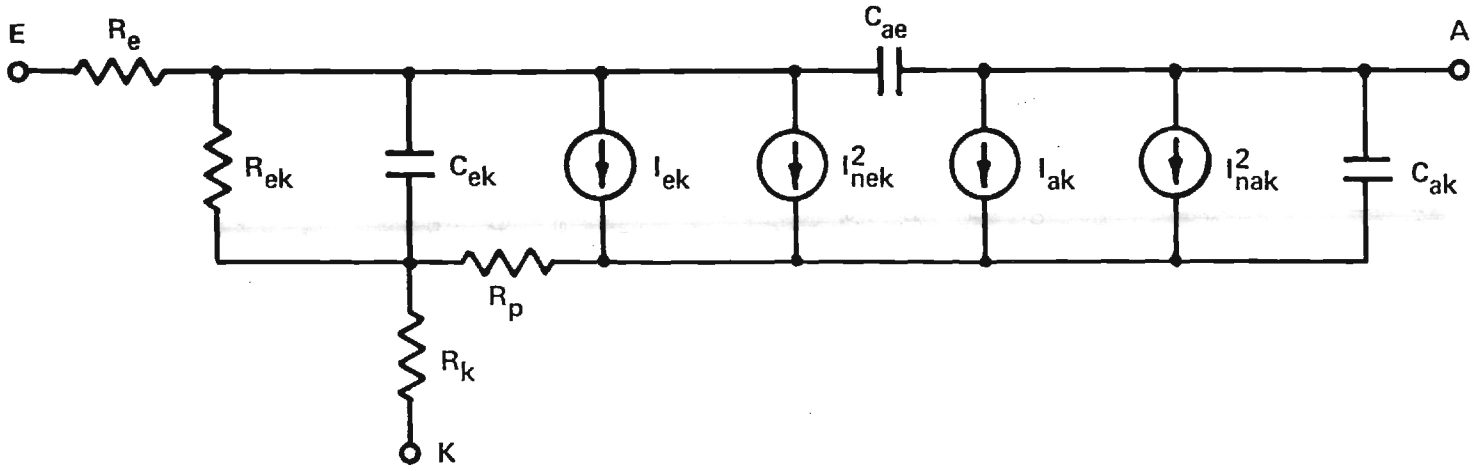

Figure V-12. Schematic Diagram of Equivalent Circuit Model.

electrode is a relatively large cross section metal structure.

The resistor R_{ek} characterizes the leakage current through the insulator separating the extractor film and the substrate. The capacitance between the extractor film and the substrate is represented by the capacitor C_{ek}. The capacitors C_{ae} and C_{ak} model the anode to extractor capacitance and the anode to cathode capacitance.

The combined current of sources I_{ak} and I_{ek} represent the average field emission currents emitted from the pin tips as a result of the field created by the potential difference between the pin tip and the extractor. The current source I_{ak} is the useful portion of the field emission current which goes to the anode. The current source I_{ek} is the portion of the field emission current which is intercepted by the extractor and therefore not available to the anode circuit. The noise current sources I^2_{nak} and I^2_{nek} represent the noise content of the emission current, which results from random fluctuations in the rate of electron emission from the pin surface.

2. Extractor Resistance

The extractor resistor R_e has been characterized using theoretical techniques. An expression for the extractor resistance has been derived and a representative value for the resistance has been calculated using the characteristics of a typical LVFE device.

The extractor resistor R_e in the circuit model represents the resistance of the thin molybdenum film which is vapor deposited on top of the insulator to form the extractor. The extractor film over the active area has holes through the film around each emitting pin and therefore has an effective resistivity which is increased by a factor that is inversely proportional

to the fraction of material remaining outside the holes. An expression for the extractor resistance is found by deriving the resistance of a thin circular plate with two concentric regions of differing resistivities where the current enters through one of the flat faces and exits at the perimeter. The center region of the plate represents the extractor film over the active area, while the outside region represents the extractor film outside the active area. The plate resistance is derived by determining the ohmic power dissipation in the plate for some terminal current I, and then using the $P = I^2R$ relation to find the resistance. The extractor resistance is expressed by

$$R_e = \frac{\rho_{Mo}}{8\pi h_e}\left[1 + \frac{N_p \pi r_h^2}{1 - N_p \pi r_h^2}\left[\frac{r_{aa}}{r_e}\right]^4\right] \qquad \text{(V-31)}$$

where ρ_{Mo} is the resistivity of molybdenum. The representative value of resistance calculated for the extractor resistor is 4.61 milliohms.

3. Extractor Current Density

The current densities within the extractor were also investigated. This investigation was concerned with the current density in extractor material without holes, the average current density in an extractor with holes, and the maximum current density occurring in extractor material between the holes. There was also some concern with the magnitude of current density that could cause destruction of the extractor.

The current density in extractor material without holes at a radius, r, from the center of the extractor is given by the relationship

$$J(r) = \frac{I(r)}{2\pi r h} \qquad \text{(V-32)}$$

I(r) is the current flowing out of a circular section of radius, r, and is dependent on what process produces the current. The variable, h, is the thickness of the extractor.

The current density in the molybdenum extractor material will be greater in the active area than the current density calculated for extractor material without holes. The average current density is inversely proportional to the area of the molybdenum left around the holes. The ratio of the average current density in the extractor film to the current density computed without holes can be expressed by

$$\frac{J_{avg}}{J} = \frac{1}{1 - \frac{\pi}{4} D_h^2 N_p} \qquad \text{(V-33)}$$

where D_h is the hole diameter and N_p is the pin density. Note that this ratio goes to infinity as $D_h (N_p)^{\frac{1}{2}}$ approaches $(4/\pi)^{\frac{1}{2}} = 1.13$.

The above relationship does not account for the fact that, as the holes become large with respect to the pin spacing, the current density in the material between the pins can be much larger than the average current density. This effect can be investigated with the use of simplifying assumption: the holes are uniformly spaced over a square lattice and current flow is linear rather than cylindrical. The relative current density can then be derived as a function of the angle between the direction of current flow and the axis of the lattice. The first and second derivatives of the relative current density function are used to determine the angle at which the current denstiy is maximum.

It has been found that the maximum current density is highest when the current flow is along either axis of the lattice. The ratio of the

maximum current density to the current density computed without holes can be expressed by

$$\frac{J_{max}}{J} = \frac{1}{1 - D_H \sqrt{N_p}} \qquad \text{(V-34)}$$

Note that this ratio increases rapidly as the hole diameter becomes an appreciable fraction of the pin spacing $1/(N_p)^{\frac{1}{2}}$.

Calculations of the average and maximum current density ratios can be done for a typical LVFE samples. Using a pin density of 10^7 cm^{-2} and a hole diameter of 2 μm makes the product $D_h\sqrt{N_p}$ equal to 0.632. Calculations of the current density ratios yield J_{avg}/J equal to 1.46 and J_{max}/J equal to 2.72.

Using estimated maximum values of leakage and displacement currents through the insulator film, current densities in the extractor film can be calculated and compared with fusing current densities for wires. Choosing a leakage current of 1 mA through an extractor film 0.5 μm thick, yields a current density (without holes) of 127 A/cm^2 at the edge of the 0.5mm diameter active area. Since it is believed that most of the leakage current originates in the active area, the area outside the active area will contribute little to leakage current. Under this assumption, the current density at the edge of the molybdenum layer is smaller, ∿31 A/cm^2.

The displacement currents can be caluclated using a value of capacitance of a parallel plate capacitor with a uniform dielectric. For a capacitor with 2μm thick Al O dielectric, the capacitance is 10 pF for the 0.5 μm diameter active area. For the extractor layer diameter of 2 mm the capacitance is estimated at 170 pf. Choosing a voltage rise of 100 volts in 1 μsec, the current denstiy in a 0.5 μm-thick extractor film can be calculated. At the

edge of the active area the current density is calculated to be 130 A/cm^2 and 540 A/cm^2 at the edge of the extractor film.

Fusing currents of wires have been determined and tabulated in handbooks. For small wire with a diameter of 0.1 mm , the current density required for fusing is on the order of 10^4 A/cm^2. Calculating the fusing current for a 1 μm wire yields a current density on the order of 10^5 A/cm^2. These results indicate that the expected extractor current densities are much less than those which could cause melting of the extractor layer. Also, some pinching of the current between the holes should not cause problems.

4. Substrate Resistance

Investigation of substrate resistor R_k has been completed using theoretical techniques. An expression for the substrate resistance has been found and a representative value of resistance has been calculated using the characteristics of a typical LVFE device.

The substrate resistor R_k represents the resistance of the disc of UO_2-W composite material comprising the substrate on which the thin film structure is fabricated. An expression for the substrate resistance is found by deriving the resistance of a cylinder formed from two different materials where each material has a constant proportion of the cross-sectional area along the axis of the cylinder. The proportion of the cross-sectional composed of tungsten is equal to the pin density times the cross-sectional area of a tungsten fiber. The expression for the substrate resistance is

$$R_k = \left[\frac{N_p \pi r_p^2}{\rho_W} + \frac{1 - N_p \pi r_p^2}{\rho_{UO_2}} \right]^{-1} \frac{\ell_d}{\pi r_e^2} \qquad \text{(V-35)}$$

where ρ_W and ρ_{UO_2} are the resistivities of tungsten and UO_2. A resistance of 1.77 milliohms is calculated for the representative value of the substrate resistance.

5. Pin Resistance

The exposed pin resistor R_p has been specified using theoretical techniques. An expression for the pin resistance has been derived and a representative resistance value has been calculated using the characteristics of a typical LVFE device.

The pin resistor R_p in the circuit model represents the resistance of the exposed portion of the tungsten fibers forming the emitting pins standing above the UO_2 matrix. The expression for the pin resistance is derived by first determining the resistance of a single pin and then dividing by the number of pins which are emitting. The resistance of a single pin is found to be approximating the pin geometry as a truncated cone topped by a hemispherical cap at the tip. Since virtually all of the current in the pin exits from the tip, the resistance of the truncated cone can be found by straightforward techniques. The resistance of the hemispherical tips is found by assuming that the current density is uniform in the hemisphere. The power loss in the hemisphere is determined for some current I entering the base of the hemisphere, and the resistance is obtained from the $P = I^2R$ relation.

The sum of the cone resistance and tip resistance divided by the number of emitting pins yields the pin resistance. The expression for the exposed pin resistance is

$$R_p = \frac{1}{n\pi r_{aa}^2 N_p}\left[\frac{\rho_W h}{\pi r_t r_p} + \frac{2\rho_W}{3\pi r_t}\right] \qquad \text{(V-36)}$$

where n is the fraction of avaiable pins that contribute to the emission current. For an estimated value of 0.1 for the fraction of emitting pins, the representative value of pin resistance is 7.94 milliohms.

6. Extractor-Cathode Resistance

A theoretical prediction of the extractor to cathode resistance R_{ek} resulting from bulk conduction through the insulator has been made. This treatment yields the best case resistance where the leakage current is the result of only bulk conduction. The resistance R_{ek} is derived from the standard equation for the resistance of conductor with constant cross section area, $R = \rho \ell / A$, where the cross sectional area is the area of the die minus the area occupied by the holes in the active area. The resulting expression is

$$R_{ek} = \frac{\rho_i \ell_i}{\pi r_d^2 - N_p \pi^2 r_{aa} r_h^2} \qquad \text{(V-37)}$$

where ρ_i is the resistivity of the alumina insulator material. Test films produced in the LVFE deposition equipment have exhibited resistivities ranging between 10^{11} and 10^{16} ohm-cm. For an insulator current caused only by bulk conduction, the representative resistance of R_{ek} would be at least 1.45×10^{8} ohms and possible as high as 1.45×10^{13} ohms.

7. Interelectrode Capacitances

Preliminary theoretical investigations of the capacitors C_{ek}, C_{ak}, and C_{ae} have been performed using electric field strength data obtained from an emitting pin computer simulation program. These investigations indicate that C_{ak} is less than 0.3 femtofarads and that C_{ae} is approximately 30 femtofarads for the anode geometry of a typical test fixture with an anode spacing

of 1 mm. Thus, both of the anode capacitance C_{ak} and C_{ae} are too small to permit practical experimental measurement of their values. The preliminary theoretical investigation of the extractor to cathode capacitance C_{ek} indicates a capacitance of approximately 160 picofarads for the typical LVFE device.

8. Noise Measurement

A preliminary noise measurement system has been assembled to check out system design, determine representative device noise levels, and measure the amplitude of the background noise present in the system. This system uses a Keithley Model 103 Low Noise Ac Amplifier, one Khron-Hite 3202 Filter, and one HP 3400A RMS Voltmeter. The filter is manually tuned to cover each half decade at a time and the output voltage is recorded manually from the RMS voltmeter. The Keithley amplifier determines the upper frequency limit of 100 KHz while the Khrone-Hite 3202 filter determines the lower limit of 18 Hz.

The results of noise voltage measurements are shown in Figure V-13. Noise voltage levels were found by measuring the RMS voltage output of the half decade filter and dividing by the amplifier gain. The device noise voltage levels were obtained with a one megohm anode series resistor and a 100 μA device emission current. The background noise measurements were also made with a one megohm resistor, but with no emission current. These measurements demonstrate that background noise in the system will not present any problems in making device noise measurements.

The preliminary noise measurement system was used to make a series of noise measurements on sample UNK-21-1B1 which was capable of dc operation with

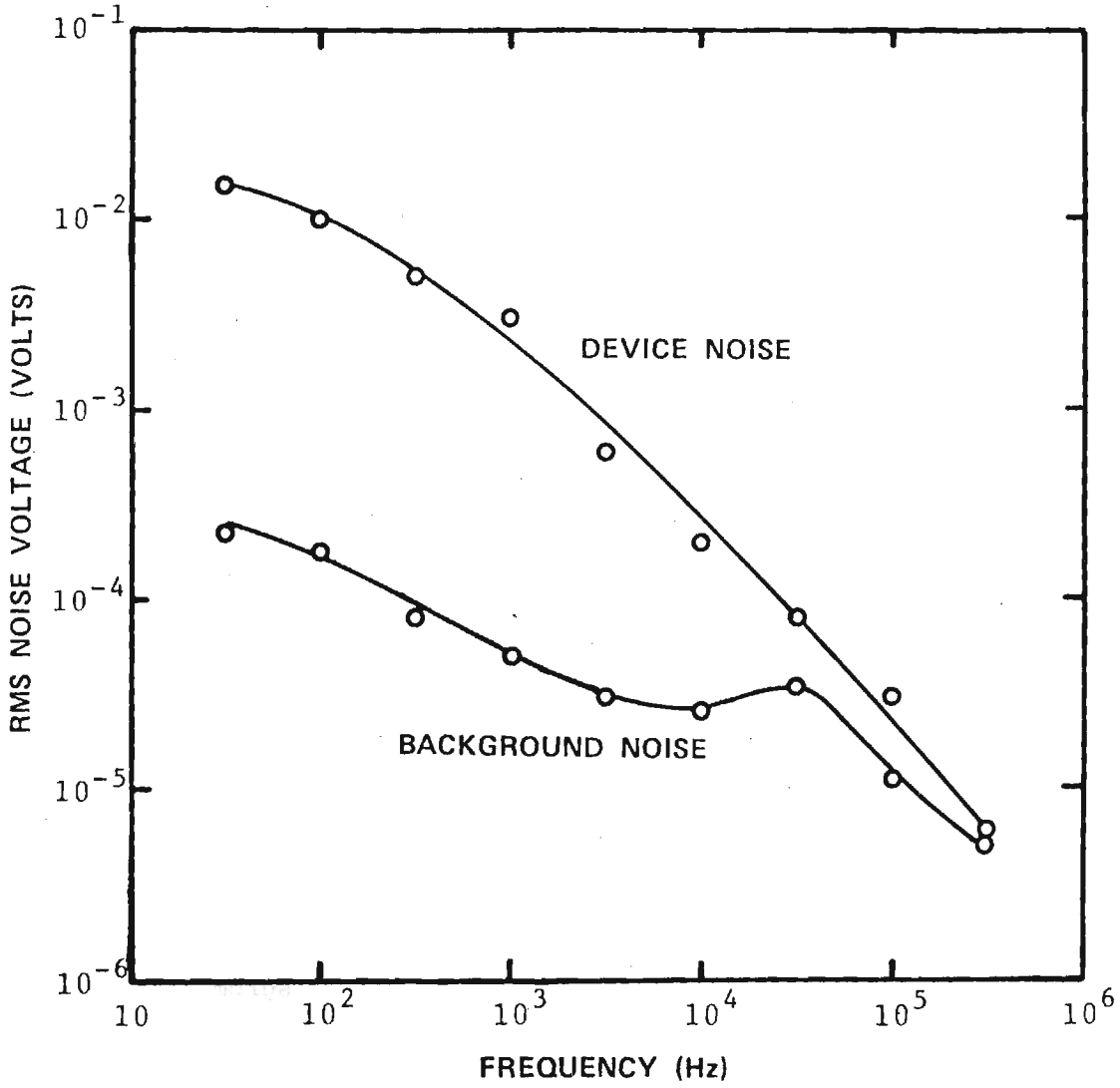

Figure V-13. Comparison of Background and Device Noise as a Function of Frequency.

appreciable currents. Noise measurements were made with emission currents of 50 μA, 100 μA, 200 μA, 500 μA, and 1 mA. Results of these measurements are plotted in Figure V-14. The data are shown in terms of noise current, obtained by dividing the noise voltage by the anode series resistance.

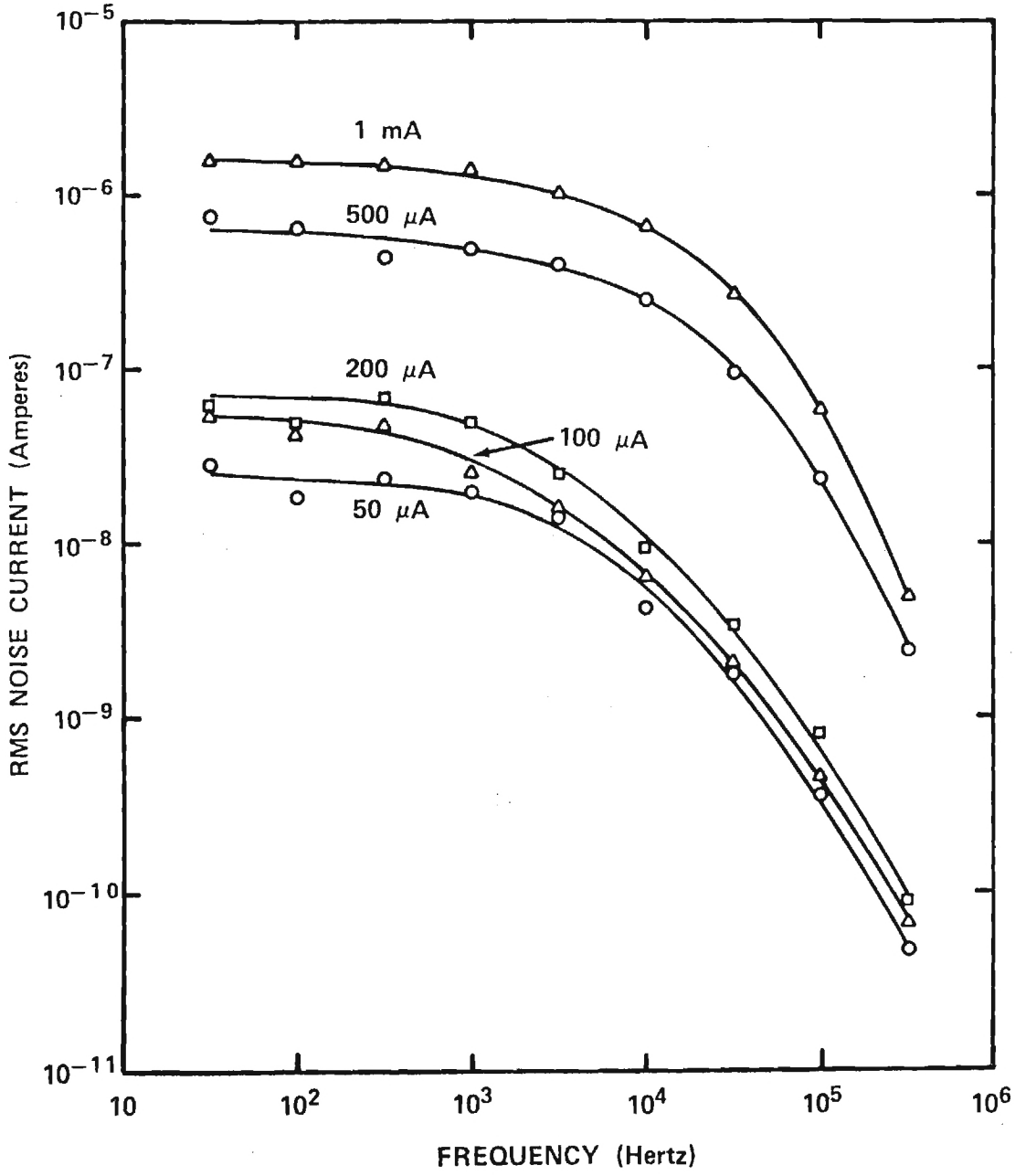

Figure V-14. LVFE Emission Noise for Various Emission Levels.

CHAPTER VI

INSULATING MATRIX COMPOSITE LVFE FROM ZYW

Most failures for the LVFE have been the result of high leakage currents through the electron beam evaporated Al_2O_3 insulator, resulting in ohmic heating of the insulator and shorting of the extractor of the UO_2 base. Under this contract, improvements have been made in insulator resistance and a few samples were tested dc with one sample reaching 1 A/cm^2 emission at 120 volts. However, high leakage continued to be the major obstacle of successful LVFEA operation.

In an effort to solve this problem, the composite base used for the LVFE was switched from UO_2-W to yttria stabilized ZrO_2-W or ZYW. In the UO_2-W composite system, the UO_2 matrix is a semiconductor with a resistivity of 10^3 Ωcm. Thus, for practical purposes, considering the close spacing of the fibers, UO_2 acts as a conductor. In the ZYW composite, the yttria stabilized ZrO_2 matrix is an insulator with the resistivity of 10^{14} Ωcm. As will be presented, leakage current was substantially reduced by use of a composite with an insulating matrix.

Use of an insulating matrix composite for the LVFE presented a unique opportunity since all other field emission arrays under development are based on an electrically conductive substrate. In addition to reduced leakage current, switching to ZYW offers advantages in other areas. First, the capacitance of the device could be significantly reduced which would reduce the charging current of the device in the pulsed mode, and permit rapid voltage times. With the conductive UO_2 matrix, the capacitance is the charge storage across the 1 μm Al_2O_3 insulator for the entire area of the Mo extractor pad.

With the ZYW, the fibers outside the active area may be removed to depths of 50-100 μm with no problem. Thus, the capacitance would be mainly that attributable to the active area.

Second, with an insulating matrix, some increase in field enhancement at the fiber tip is expected since the fiber becomes infinitely long as compared to the conducting matrix where the fiber is a 2-3 μm protrusion and the field is affected by the conducting substrate. No attempt has been made access the extent of field enhancement to be expected.

Finally, since the fibers are electrically isolated, there exists the possibility of current limiting individual fibers. By depositing a thin film resistor on the back of the LVFE substrate and overlaying a metal film, each fiber would have a current limiting series resistor. Thus, preferentially emitting fibers which might ultimately melt and short could be restricted to safe current levels.

In summary, converting from UO_2-W to ZYW as the unidirectional composite base for the LVFE should (a) reduce leakage current, (b) reduce device capacitance, (c) provide increased field enhancement, and (d) offer the possibility of current limitations on individual fiber emitters. In addition to advantages in the emission area, ZYW provided major advantages in composite growth, sample handling, and availability of samples.

Unidirectional solidification of UO_2-W oxide metal composites provided the substrate for LVFE's for the first seventeen months of the contract. Unfortunately, over the last seven months of that time, it became increasingly apparent that stoichiometric control of UO_{2+x} in the liquid was a major impediment to growing production quantities of UO_2-W composites.

During that time, short lengths (2-5 mm) of UO_2-W composite usable for LVFE application were being obtained from solidified boules (60-80 mm) in length. Thus, only six to eight samples/boule could be obtained from those growth runs and the quality of the growth varied considerably.

With the installation of the 50 kw rf generator to permit growth of large diameter UO_2-W boules, it was possible to grow 32 mm diameter ZYW samples. The results of initial growth runs with ZYW were very encouraging. ZYW does not have the oxygen stoichiometry problems experienced with UO_2-W and several cm of growth suitable for LVFEA have been obtained in a boule. Overall, the growth of the ZYW compared to UO_2-W has been more uniform, fiber continuity better, and growth more controllable. The mechanical strength of the ZYW is greater than the UO_2-W which has permitted easier handling, cutting of thinner chips (which promotes fiber continuity in an individual sample), and obtaining a larger number of samples from the same volume. From a recent ZYW boule (ZYW-14), 72 LVFE chips, 3 mm x 3 mm x 0.75 mm, were cut. Out of the 72 chips, 53 or 74% contained continuous fibers as determined by electrical continuity and were suitable for LVFE fabrication. This is an accomplishment unattained with UO_2-W composites.

As a result of availability of good ZYW composite and for the reasons listed above, the last seven months of the contract were devoted to fabricating and emission testing LVFE's with ZYW as the base rather than UO_2-W. As will be described in this chapter, a number of changes were made in the fabrication area, new chemical etchs were developed for exposing W fibers in ZYW and one for pointing was partially developed. Emission testing for the first time was exclusively dc with emission current densities with the 1-5A/cm^2 range and leakage in the μA range.

A. FABRICATION OF ZYW LVFE

With the availability of ZYW composites of a reasonable size and containing continuous fibers, ZYW LVFE's were fabricated for the last seven months of the contract. A number of processing changes were made compared to UO_2-W. First, the sample shape was changed to square chips 3.0 x 3.0 x 0.75 mm, Figure VI-1. These thinner, square samples facilitated easier handling, matched well with the crack patterns in the composite boule, and due to the reduced thickness increased the probability of continuous fibers in the samples. The samples were polished to 1 μm diamond finishes on both sides and 0.3 μm of Mo was vapor deposited on the back side to make electrical contact to the W fibers. (For vapor deposition a new sample holder was made which held eighteen samples. With the square shape, the chips could be packed side-by-side in slots so more samples can be placed in a smaller area compared to the round UO_2-W chips.)

After depositing the back surface Mo contact, the samples were etched as described in the next section. This provided W fibers ∿2.5 μm with either cylindrical, hemispherical or pointed tips. Active areas 200 μm in diameter were formed with photoresist and fibers outside the active area were removed by ultrasonic vibration in aqueous potassium ferrocyanide for 60 seconds.

The extractor was formed by vapor depositing Al_2O_3 to 1.5 μm thickness and molybdenum to 0.5 μm thickness in the same manner as for UO_2-W fabrication. For the ZYW deposition, no mask was needed for Mo deposition since no shorts can occur outside the active area due to the fiber removal and the insulating matrix. Post-deposition processing consisted of etching the Al_2O_3 insulator in phosphoric acid to remove the cathode cones, electropolishing the extractor,

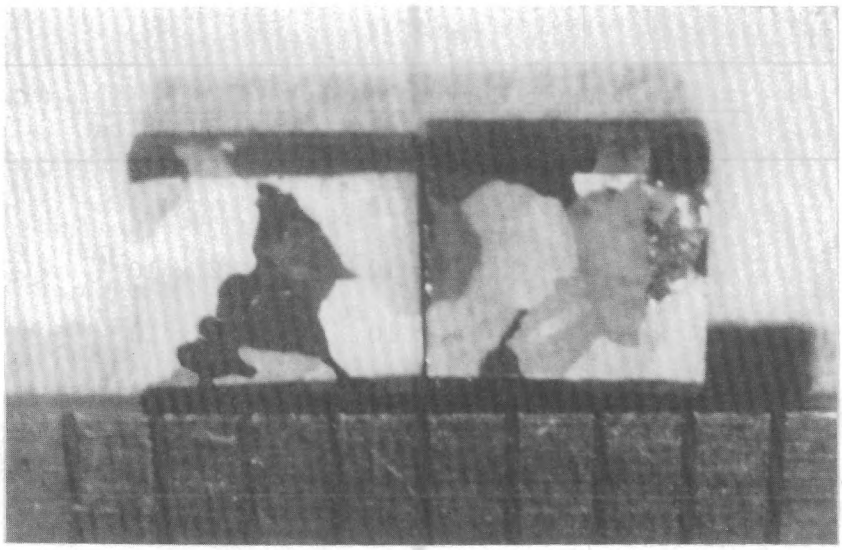

Figure VI-1. ZYW LVFE Chips After Final Processing, 11X.

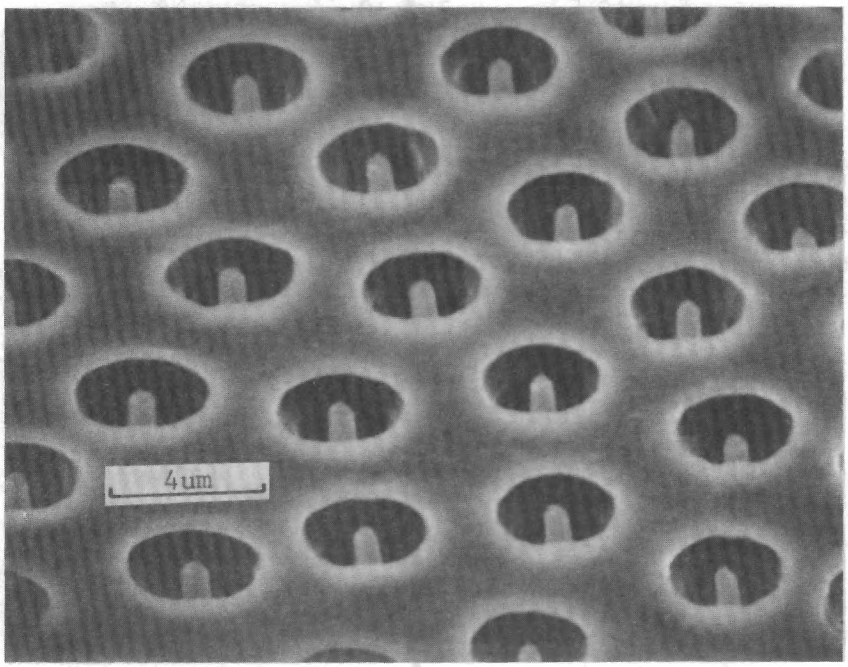

Figure VI-2. Portion of LVFE Z14-34-5 Active Area, 5,000X, 45°.

Table VI-1. Leakage Current and Capacitance for ZYW LVFEA Samples Z14-34.

Sample	Leakage Current (Amps) 50 Volts	80 Volts	130 Volts	Capacitance (pf)
1	2×10^{-10}	3×10^{-10}	NA	98
2*	1×10^{-9}	2×10^{-9}	$<2 \times 10^{-7}$	127
3*	4×10^{-10}	1×10^{-9}	6×10^{-7}	150
4*	4×10^{-10}	7×10^{-10}	1×10^{-6}	149
5	1×10^{-8}	2×10^{-8}	NA	133
6	4×10^{-12}	3×10^{-10}	NA	122
7	1×10^{-10}	2×10^{-10}	NA	98
8*	5×10^{-10}	1×10^{-9}	6×10^{-7}	129
9	5×10^{-10}	7×10^{-10}	NA	-
10*	4×10^{-9}	4×10^{-10}	$<2 \times 10^{-7}$	105
11*	2×10^{-9}	3×10^{-9}	$<1 \times 10^{-5}$	101
12	2×10^{-10}	1×10^{-9}	NA	160

*Samples that were emission tested.

and a final etch in phosphoric acid to recess the insulator. The final structure for cylindrical tipped fibers is shown in Figure VI-2.

Leakage measurements on the samples were most encouraging. Table VI-1 shows leakage for twelve samples from Deposition 34 where eleven samples had between 0.3 and 3.0 nA leakage at 80 volts, Table VI-1. Six samples were emission tested and at 130 volts the leakage was 1 μA or less for five of them. The sixth had 10 μA measured leakage but the majority of this current was intercepted emission. Leakage at these levels demonstrated that switching from UO_2-W to ZYW for the base improved leakage significantly.

B. EMITTER TIP GEOMETRY CONTROL

To provide ZYW composites with exposed fibers of controlled tip geometry a three pronged investigation was undertaken. First a program to investigate the etching characteristics of the yttria stabilized ZrO_2 matrix in phosphoric acid was initiated with the purpose of producing exposed tungsten fibers with cylindrical tips. Next, thermal annealing of exposed cylindrically tipped W fiber in H_2 was studied to produce fibers with hemispherical tips. Last, HF and HNO_3 was added to the phosphoric acid etch to slowly attack the W fibers and produce pointed tips. The etching studies were reported in a Master's thesis by Mr. K. H. Moh[14] and the results will be summarized below.

1. Phosphoric Acid Etching of ZYW

Boiling phosphoric acid was the only chemical etchant found to be satisfactory on all cubic solid solutions of stabilized zirconia that were studied. The effect of phosphoric acid concentration and temperature

effects were investigated in the reflux system shown in Figure VI-3. In this apparatus, temperature was maintained to $\pm 10^{o}C$ with a proportional band controller. An iron-constantan thermocouple was used for sensing the temperature.

Etching time was varied from 0.25 hours to 14 hours in the temperature range of 135^{o}-$260^{o}C$. Concentration of phosphoric acid was varied from 85% to 99.9% at particular temperatures. The different H_3PO_4 concentrations were produced by boiling an 85% H_3PO_4 solution. Evaporation taking place during boiling raised both the boiling temperature and concentration of the solution. Boiling was sustained until the desired boiling temperature was reached. Solution concentrations were determined using a standard boiling temperature vs. concentration curve as shown in Figure VI-4.

The temperature dependence of the etch can be observed in Figure VI-5, where the least squares etching rate line for each temperature is combined on one graph. The etching rate at each boiling temperature, K, measured as the slope of the least squares line in Figure VI-5, was presented in Table VI-2. In addition to measuring etching rate at equilibrium acid concentration for the particular temperature, etching rate was measured as a function of temperature at constant acid concentrations of 92 and 99.9 w/o, Table VI-2. The influence of temperature on the reaction rates was calculated from the Arrhenius equation:

$$K = K_o e^{-E_a/RT}$$

where K = reaction rate at the temperature T in ^{o}K

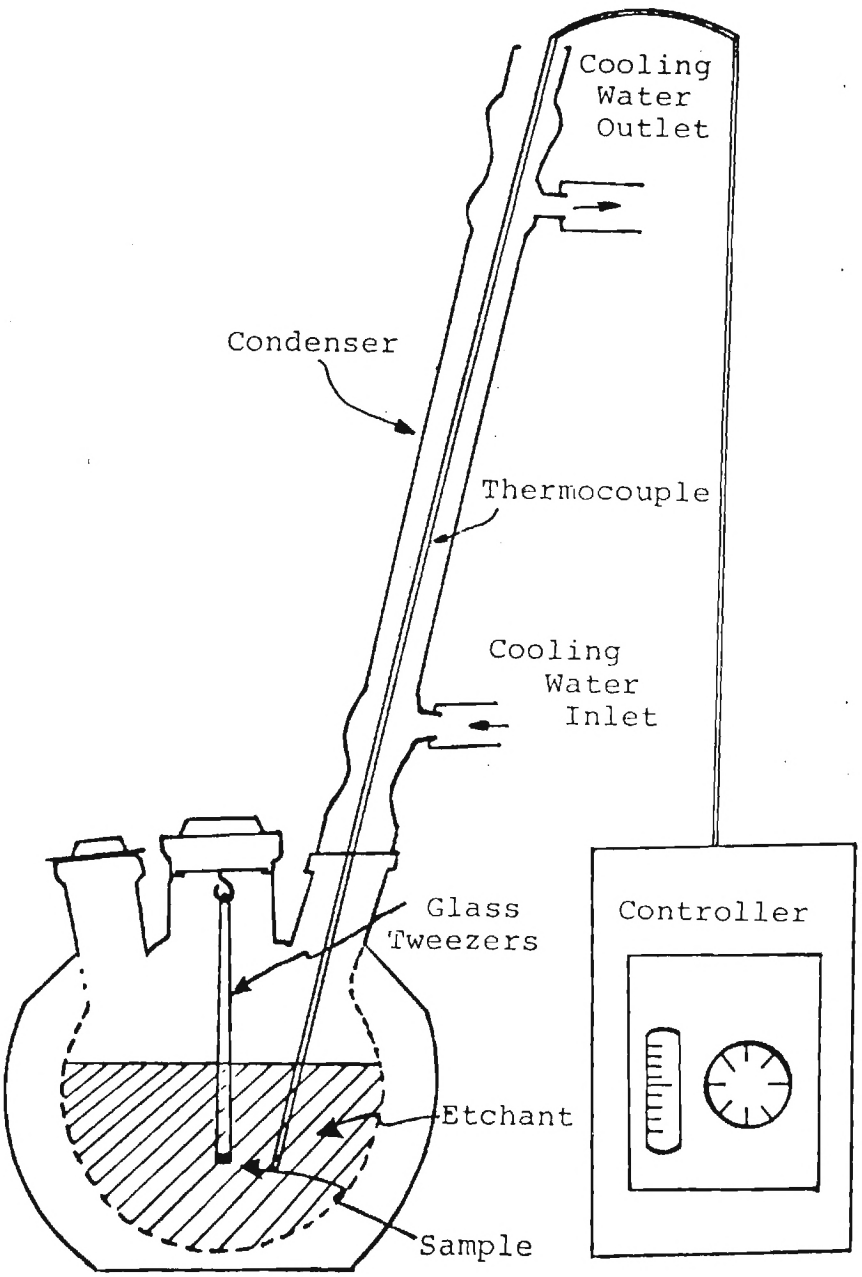

Figure VI-3. Schematic Diagram of Apparatus Used in the Reflux Etching System.

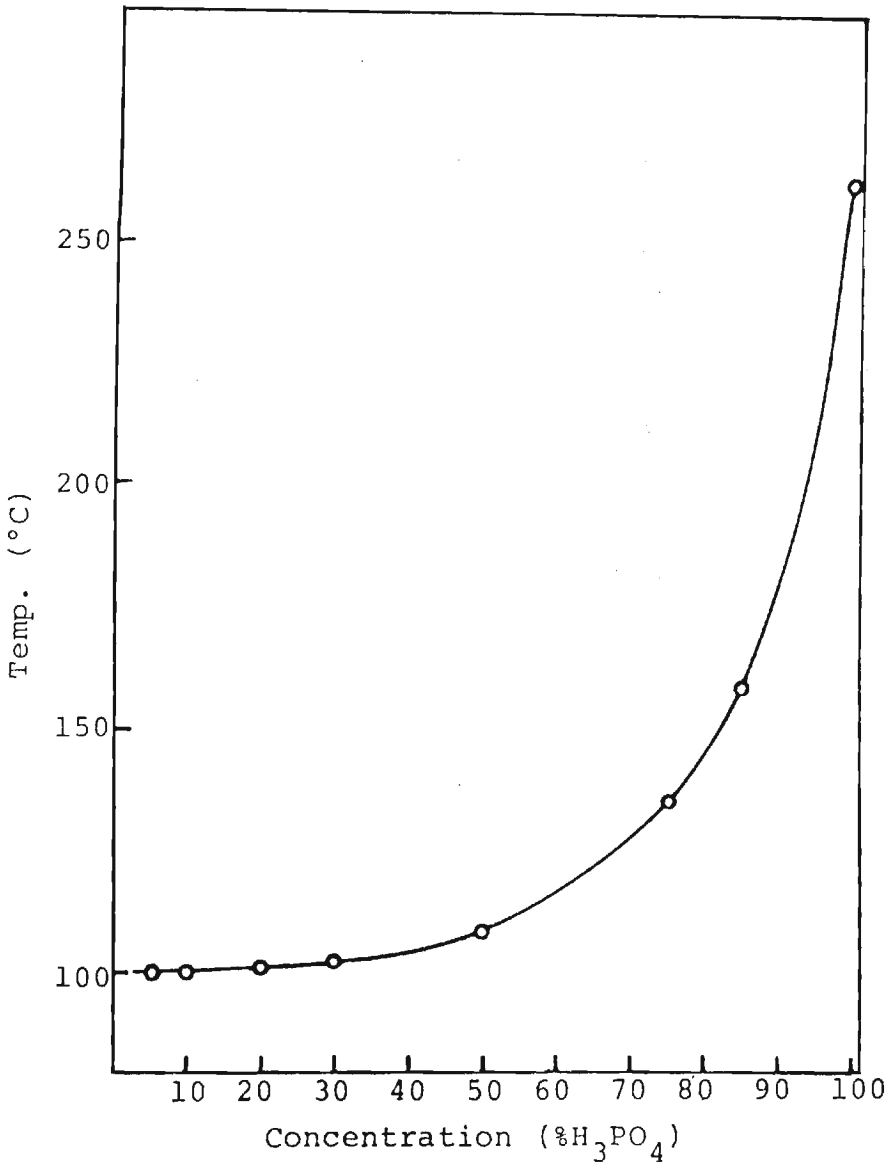

Figure VI-4. Standard Curve for Boiling Point vs. Concentration of Phosphoric Acid.

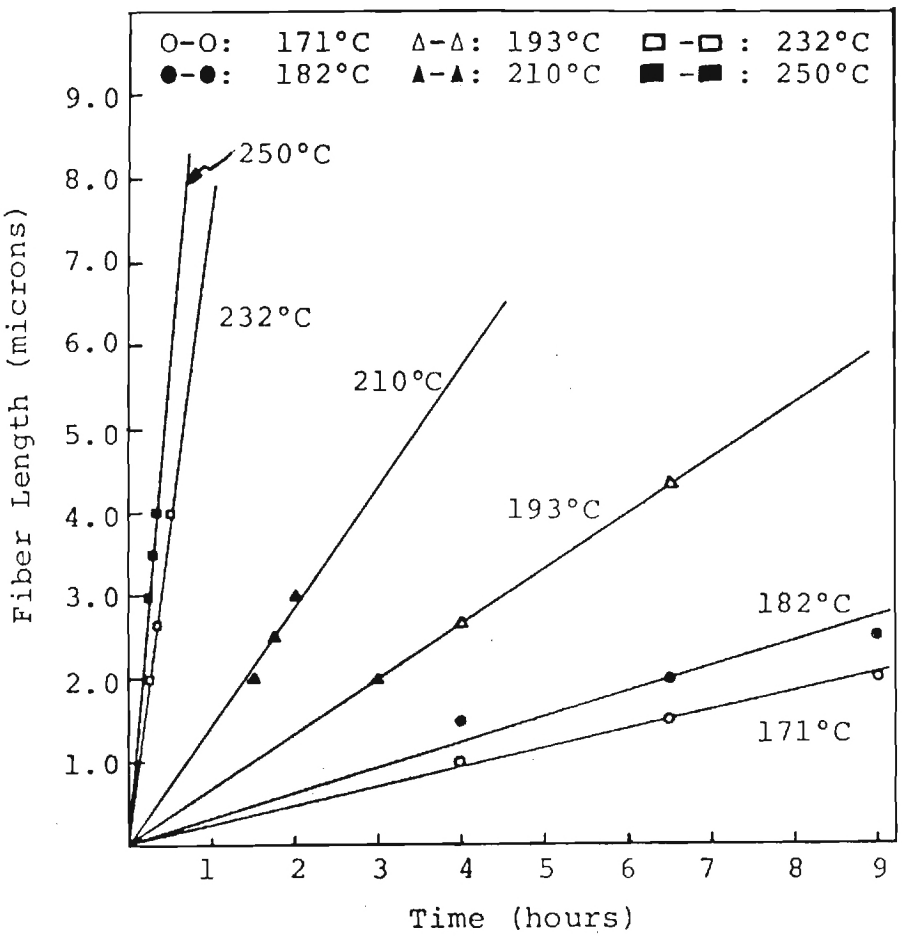

Figure VI-5. Least Squares Lines of Fiber Lengths vs. Etching Time at Various Temperatures Using Phosphoric Acid.

Table VI-2. Etching Rate for ZrO_2 Dissolved in Various Concentration of H_3PO_4 at Their Boiling Temperature.

Concentration (% H_3PO_4)	Boiling Temp. (^oC)	Etch Rate (μm/min.)
85	154	0.001
88	171	0.004
90	182	0.005
92	171	0.003
	182	0.005
	193	0.011
95	210	0.024
98	232	0.133
99	250	0.200
99.9	232	0.067
	250	0.133
	260	0.200

K_o = the pre-exponential factor.

R = the gas constant (1.987 cal/ K mole), and

E_a = the activation energy.

The least squares line for the Arrhenius graphs of ln K vs. 1000/T(^oK), Figure VI-6, provided an activation energy of (27.6, 28.9, and 23.0 J/mole) for the equilibrium concentrations, the 92 w/o and the 99.9 w/o H_3PO_4, respectively. The values of the activation energy and the pre-exponential factor of the dissolution process are frequently found to be dependent on the nature and concentration of an acid. The activation energy remains constant while the pre-exponential factor of dissolution changes markedly from one surface to another. Except at 99.9% H_3PO_4, the value of the activation energy for overall dissolution was constant (6.6 Kcal/mole), but that of the pre-exponential factor was dependent on the concentration of the etchant. In the temperature range of 232^o-260^{o}C, the value of activation energy for 99.9% H_3PO_4 was less than that for 92% H_3PO_4 concentration. The lower value of activation energy at 99.9% H_3PO_4 concentration in comparison with 92% H_3PO_4 suggests that at the higher concentration, the process may be diffusion limited.

An example of cylindrical tip fibers used for LVFE fabrication was presented in Figure VI-2. The surface topography of the matrix was smoothest in the H_3PO_4 concentration range 92-95%. Thus this concentration range was used for etching samples for LVFE fabrication.

2. Thermal Annealing to Produce Hemispherical Tips

In an attempt to provide field emission tips of more uniform geometry, cylindrical tipped fibers exposed by phosphoric acid were annealed in a

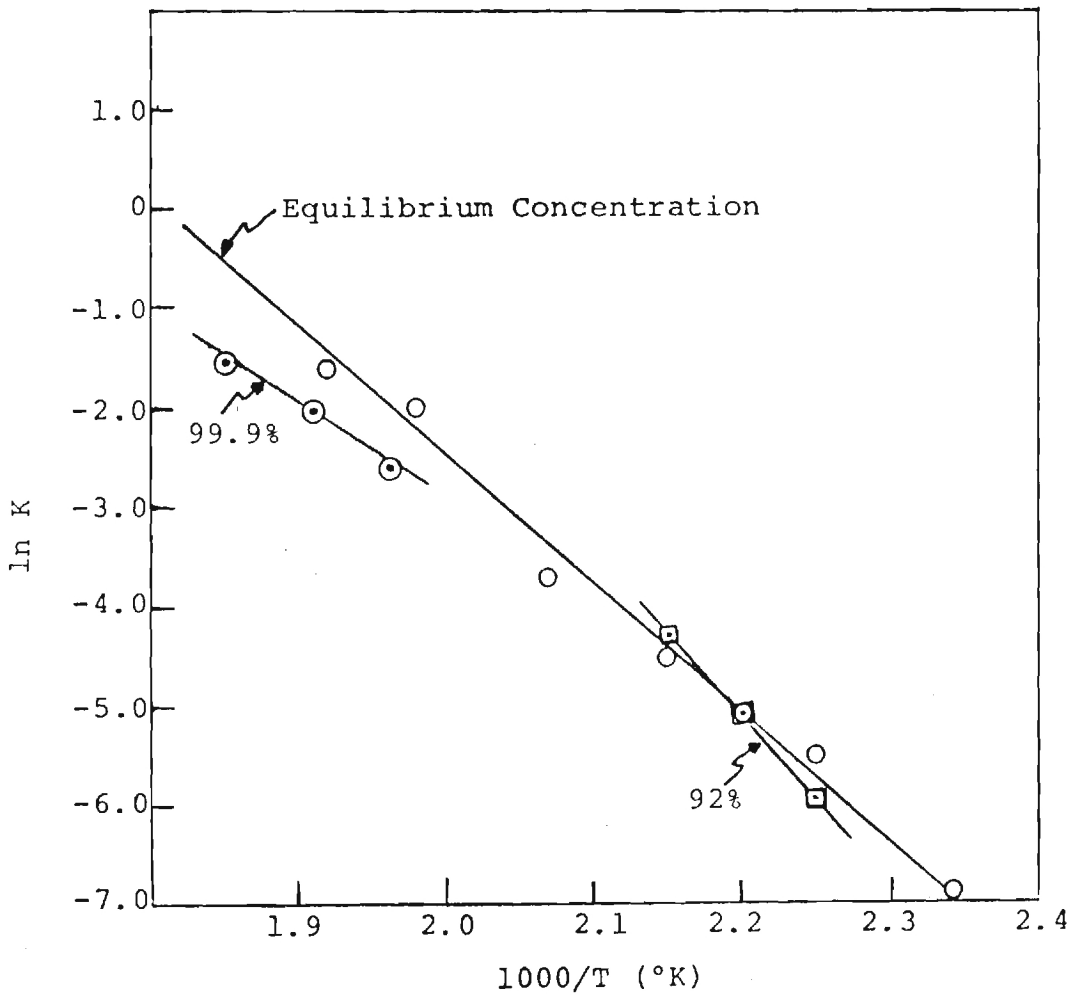

Figure VI-6. The Least Squares Line of Arrhenius Relationship for Etch Rate vs. Temperature.

H_2/N_2 atmosphere in a Mo element rf furnace at the times and brightness temperatures reported in Table VI-3. Initial rounding of the cylindrical corners occurred between 850 and 940°C. By 990°C, the tips formed complete hemispheres of the same diameter as the fiber. Above 1300°C, the fiber tips appeared to balloon slightly, i.e. to round to spheres slightly larger in diameter than the fiber. Since the tips quickly rounded to hemispheres and remained relatively unchanged over a wide range of times and temperatures, the rounding was due to surface diffusion as opposed to bulk diffusion. Otherwise, the entire fiber would have spheredized.

Thermal annealing produced the most uniform tip geometries used in LVFE fabrication as can be seen in Figure VI-7. However, emission testing of these 3000 Å radius tips did not indicate that emission uniformity was improved as is reported in section VI-C.

3. Chemical Etching to Produce Pointed Tips

This section describes an investigation of the solubility of tungsten in mixtures of hydrofluoric and nitric acids added to phosphoric acid in an effort to make reproducible, pointed pins of optimum height for LVFE applications. The effects of temperature and concentration of H_3PO_4, HNO_3 and HF on relative tungsten dissolution rate compared to matrix dissolution were investigated. Some success was attained and best pointing etches developed were etches L&M as presented in Table VI-4. Pointed fibers from these etches are shown in Figure VI-8.

Unfortunately pin uniformity was different from sample to sample and grain to grain even in the same sample. Some samples produced reproducible and uniform-sized pointed pins on a smooth matrix, and some samples produced considerable variation of pin size and shape even in the same grain. These

Table VI-3. Results of Pin Tip Annealing in a H_2/N_2 Atmosphere.

Annealing Temperature* (°C)	Annealing Time (min)	Final Tip Radius (Å)	Comments on Tip Geometry
850	60	----	No rounding
940	60	----	Corners rounding
990	60	2500	Complete Hemispheres
1030	30	2000	Complete Hemispheres
1200	30	2650	Complete Hemispheres
1300	60	2380	Complete Hemispheres
1400	15	2910	Tips Slightly Ballooned
1400	40	3440	Tips Slightly Ballooned
1500	30	2700	Tips Slightly Ballooned

*Brightness temperature on smooth, unoxidized Mo.

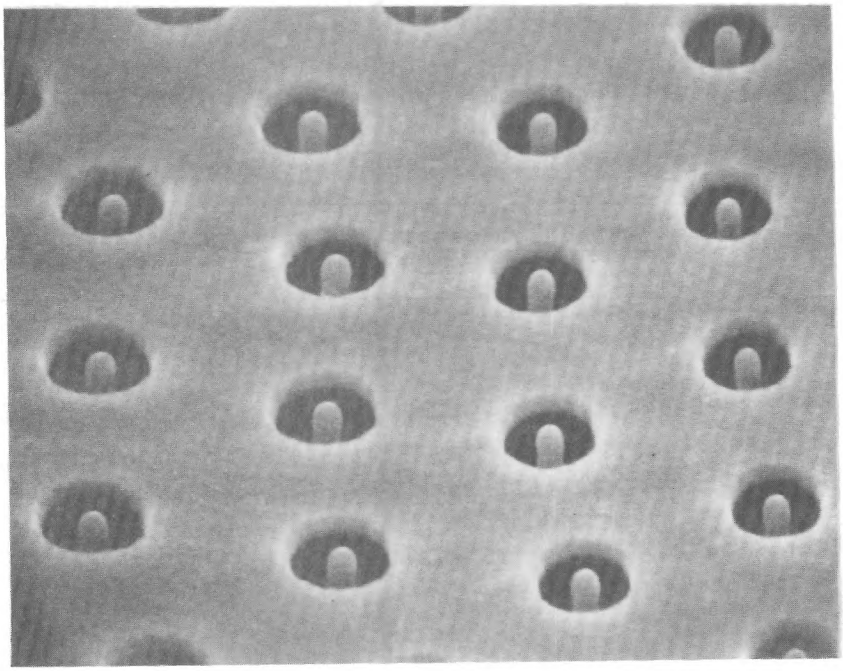

(a)

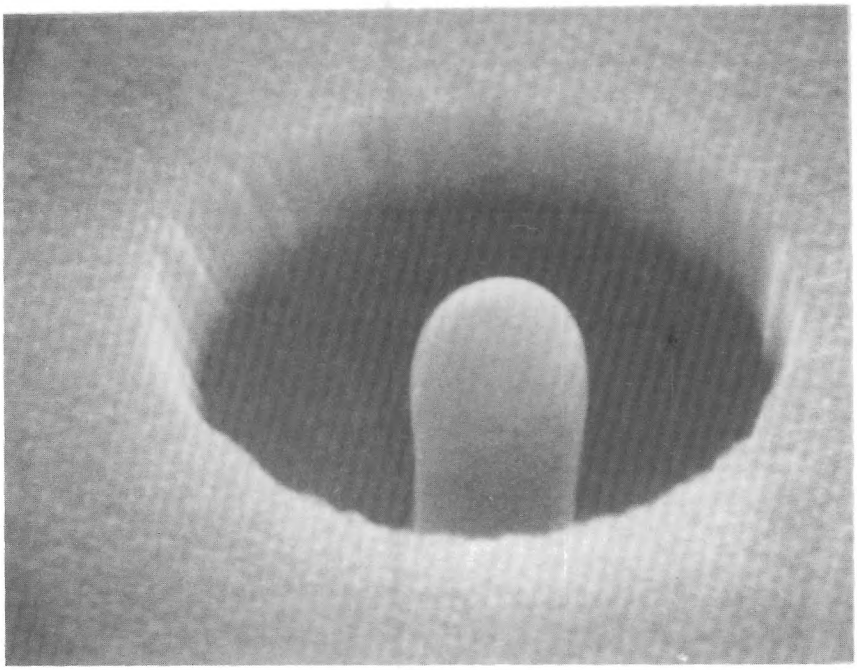

(b)

Figure VI-7. LVFEA Fabricated with Thermally Annealed W Fibers, Tip Radii ∿ 3000 Å; (a) 5000X, 45°, (b) 30,000X, 45°.

Table VI-4. Effect of HF Content on Pointing Etch at 210°C for a 1.75 Hour Etch.

Etch No.	Etch Composition		Fiber Length (μm)	Fiber Shape
	Acid*	Volume (ml)		
L	HF	1.0	2-3	Pointed
	HNO_3	2.5		
	H_3PO_3	100		
M	HF	2.5	4-5	Pointed
	HNO_3	2.5		
	H_3PO_4	100		

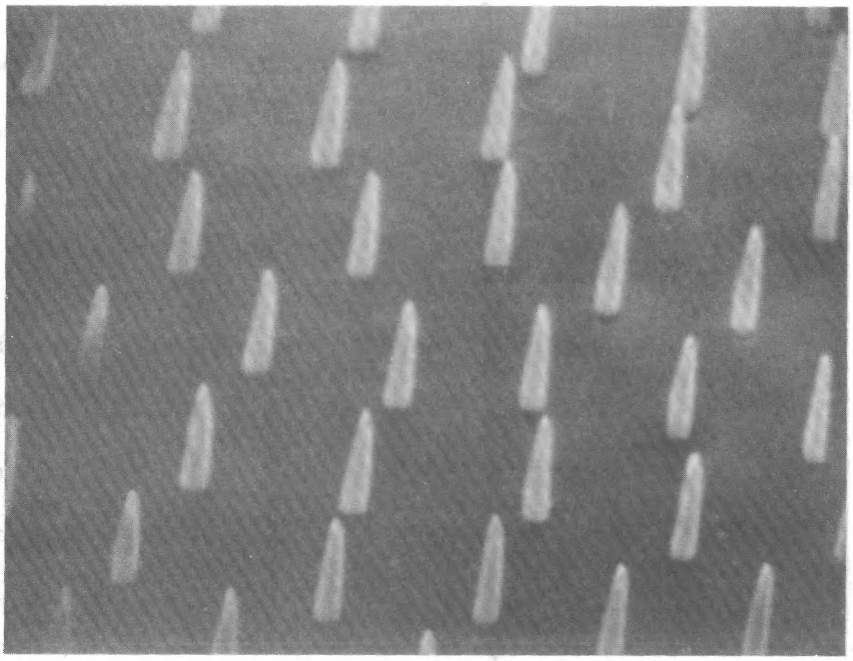

(a) Etch L, 5,000X, 45°.

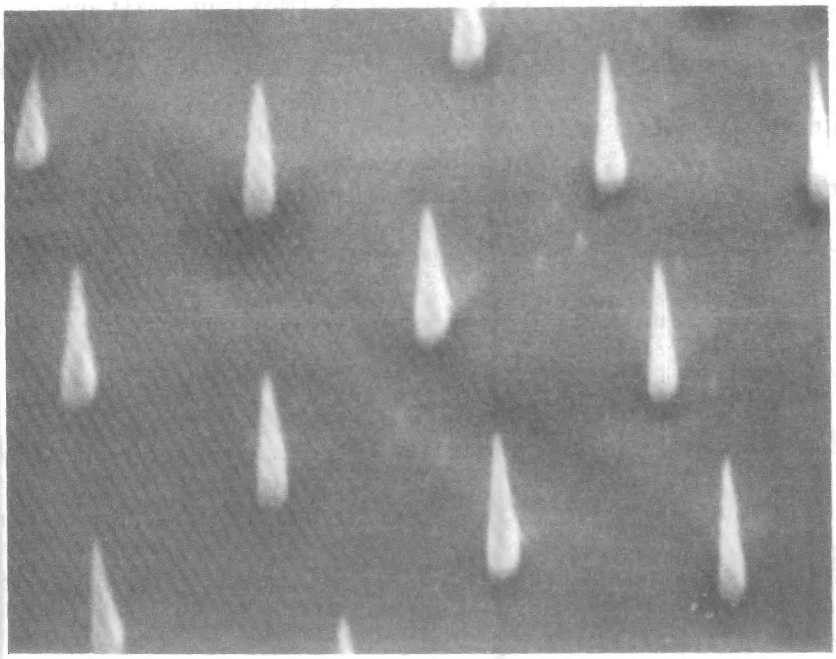

(b) Etch M, 7,500X, 45°.

Figure VI-8. Effect of HF Content in Acids Mixture on Formation of Pointed Tungsten Pins Etched at 210°C.

might be attributed to the surface strain energy in both the ZrO_2 matrix and possibly also in the tungsten fibers. Certainly, pointing etches need considerably more development.

C. EMISSION TESTING OF ZYW CATHODES

A total of fourteen ZYW cathodes were emission tested during the final six months of the project. All were tested in dc mode and, of the fourteen, eight produced significant emission current. The same test procedures and equipment were used as with the UO_2-W cathodes, with the important exception that an automated data acquisition system was completed and used to record some of the data.

A block diagram of the data acquisition system is shown in Figure VI-9. The experimenter specifies the curve parameters (maximum voltage, minimum voltage, etc.), which are input to the computer. Based on this operator input, the computer generates voltage commands for the digital-analog converter/high voltage operational amplifier. Voltages are equally spaced in reciprocal voltage so that Fowler-Nordheim curves are generated with equally spaced points. Upon command of the generator, the stored voltages are applied to the LVFE and the emission currents measured with the logarithmic amplifier and analog-digital converter. The apparatus determines a 50-point V-I curve in about 50 milliseconds. The data is then transmitted to the campus computer where Fowler-Nordheim curves are generated and plotted. Examples of two such curves are shown in Figure VI-10.

A summary of the emission performance data is given in Table VI-5. Note that all of the samples tested were from one ZYW ingot, Z-14, primarily because it had the most uniform arrays and the largest number of continuous

Table VI-5. Summary of ZYW Emission Test Results.

Cathode Designation	Dia. of Active Area (mm)	Pin Tip Geometry	Array Current Density @ 100V (A/cm^2)	Extractor Current @ 100V (μA)	Max. Array Current Density @ PK Extractor Voltage (A/cm^2)	Maximum Emission Current (mA)
Z-14-34-2	0.18	CYL	0.01	0.01	1.0 @ 168V	0.25
Z-14-34-4	0.18	CYL	0.01	0.01	0.6 @ 170V	0.15
Z-14-34-8	0.18	CYL	0.01	0.05	0.3 @ 140V	0.09
Z-14-34-11	0.18	CYL	0.01	0.01	0.08 @ 275V	0.02
Z-14-36-66	0.20	HEMI.	0.01	0.3	1.0 @ 200V	0.32
Z-14-36-71	1.0	HEMI.	0.01	1.2	1.14 @ 172V	1.1
Z-14-38-103	0.20	POINTED	0.11	1.1	5.0 @ 160V	1.6
Z-14-38-114	0.20	POINTED	0.40	1.5	3.4 @ 124V	1.1

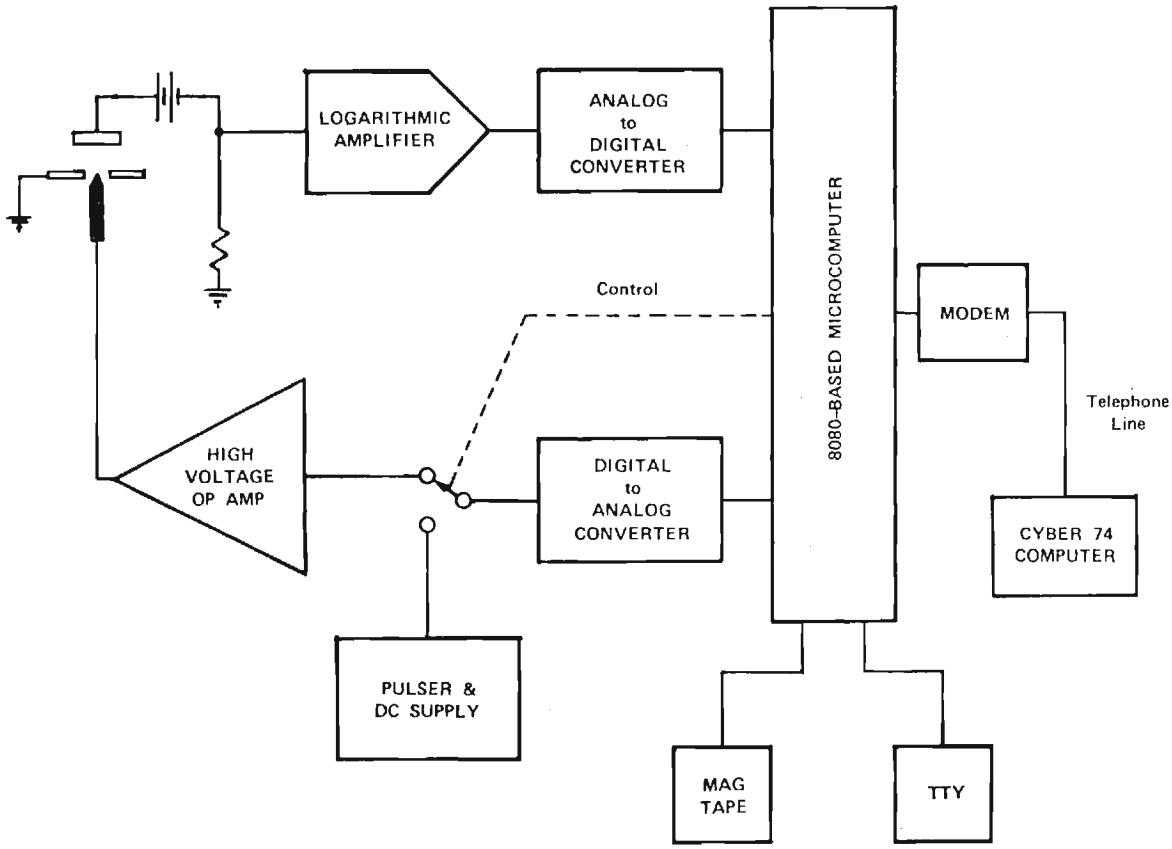

Figure VI-9. Block Diagram of the Automated LVFE Data Acquisition System.

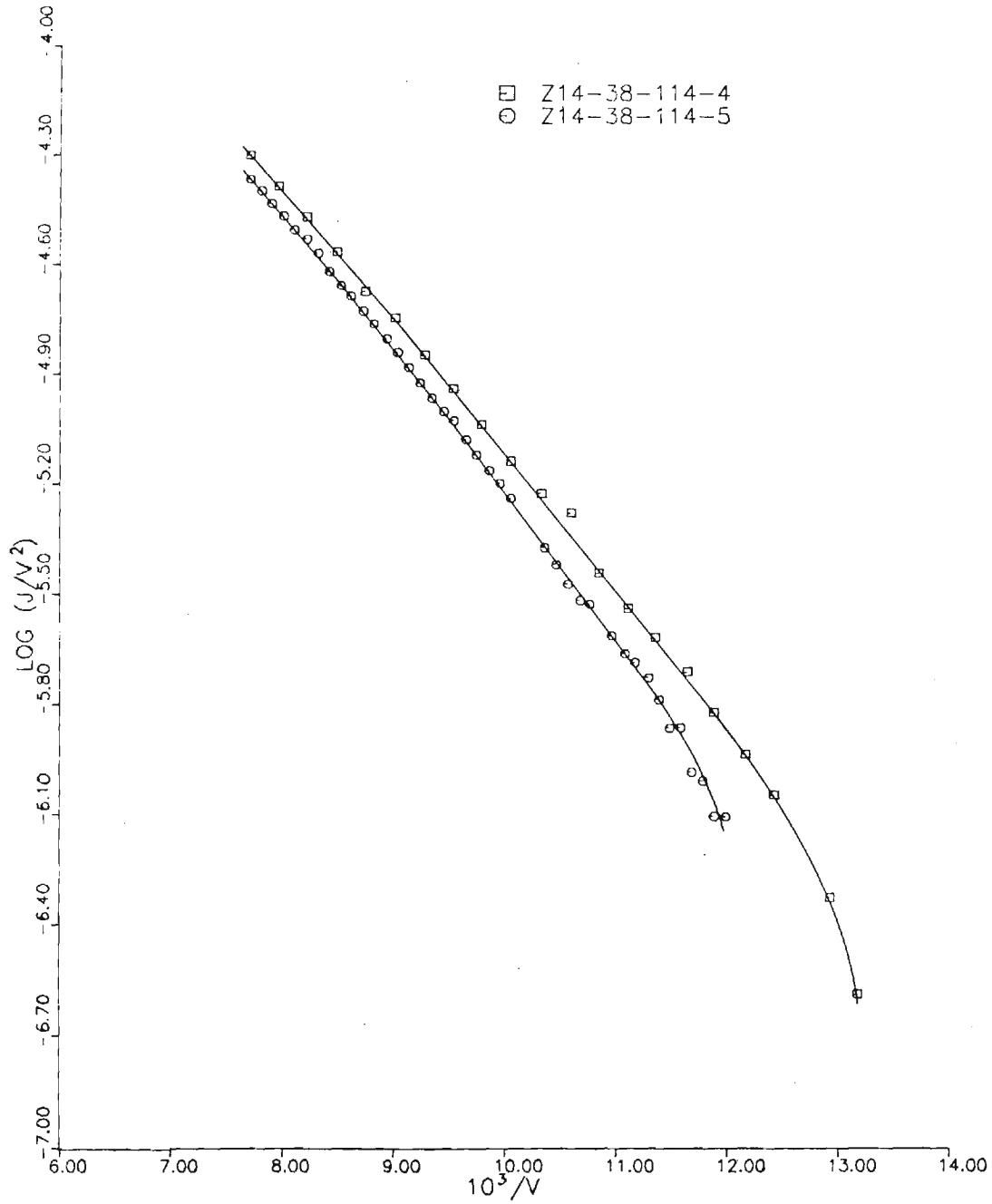

Figure VI-10. Examples of Fowler-Nordheim Plots Taken with the Automated Data Acquisition System.

fibers. The pin tip geometry has been specified in the table because it was one of the variables, and it had a significant effect on emission performance of the cathode.

As discussed in Section B, the initial etches used for the composite could only remove the ZrO_2 matrix without affecting the tungsten fibers. This produced a cylindrical pin geometry, illustrated in Figure VI-2 . All of the LVFE cathodes produced in Deposition Run 34 contained this pin geometry. It was relatively easy to go from the cylindrical to the hemispherical geometry simply by heating the etched substrate in H_2 to 1400°C for a few minutes to round the pin tips. This was done for all of the LVFE samples tested from Deposition Run 36.

The results of the emission tests of the cathodes with cylindrical and hemispherical pin tip geometries was anything but spectacular. The maximum emission current density achieved only 1 A/cm^2, at 170 V for the cylindrical geometry (Z-14-34-2) and 200 V for the hemispherical geometry (Z-14-36-66), and neither of the two cathodes operated at this level for more than a few minutes.

This gave further impetus to the search for a suitable pointing etch, and sufficient progress was made in this area during the final months of the contract that several LVFE cathodes were fabricated with at least a small percentage (~10%) of pointed pins in the active area. The pin tip radii were certainly not as small as the UO_2-W samples tested earlier, but they were considerably more favorable for emission than the previous ZYW samples tested. The results were extremely encouraging, with one sample (Z-14-38-114) producing 3.3 A/cm^2 @ 124 V and another (Z-14-28-103) 5 A/cm^2 @ 160 V. This was almost five times as much dc emission current density as any LVFE had

produced prior to these tests. Both of these cathodes operated at more than 2 A/cm^2 for over a hundred hours, and only failed when the emission current was increased.

Fowler-Nordheim curves for the cylindrical, hemispherical, and pointed pin tip geometries are shown for comparison in Figure VI-11. Curves of current density as a function of voltage are also given, in Figure VI-12, better illustrating the effect tip geometry on emission. These results confirm the conclusion drawn by Hill[2] in his work with UO_2-W LVFEA's, that sharply pointed pin tips give far better emission performance than any other tip geometry.

Perhaps the most significant result of the ZYW emission tests was the remarkable decrease in leakage current for these cathodes. Even at 200 volts dc the leakage current was generally less than 50 μA, and the majority of this current was probably intercepted emission current. At 100 volts dc, the leakage current was generally about 0.01 μA. In fact, when emission current was first detected, the leakage current generally reversed polarity. This was interpreted as being due to secondary emission from the extractor caused by the interception of electrons emitted from the pins. The secondary emission, which was recorded as a negative leakage current, was usually sufficient to mask the true leakage current until the latter reached several microamperes.

Since it was difficult, if not impossible, to separate the contributions of intercepted emission, secondary emission, and bulk electrical conduction through the film to the total extractor current, this measurement probably has little or no meaning once emission has commenced. Regardless, however, the extractor current in all the ZYW tests remained well below

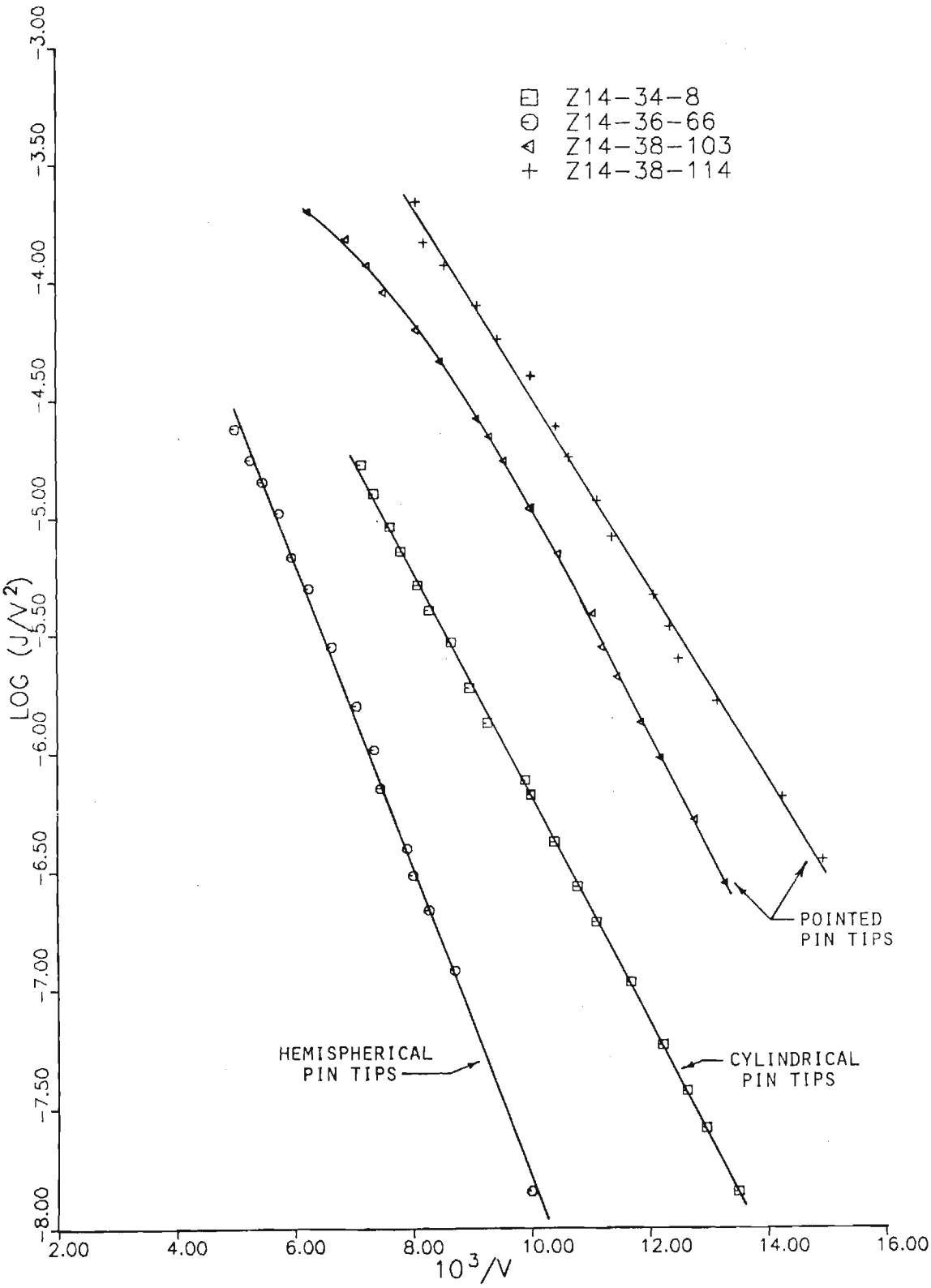

Figure VI-11. Fowler-Nordheim Plots Illustrating the Effect of Pin Tip Geometry on Emission Performance of ZYW LVFE Arrays.

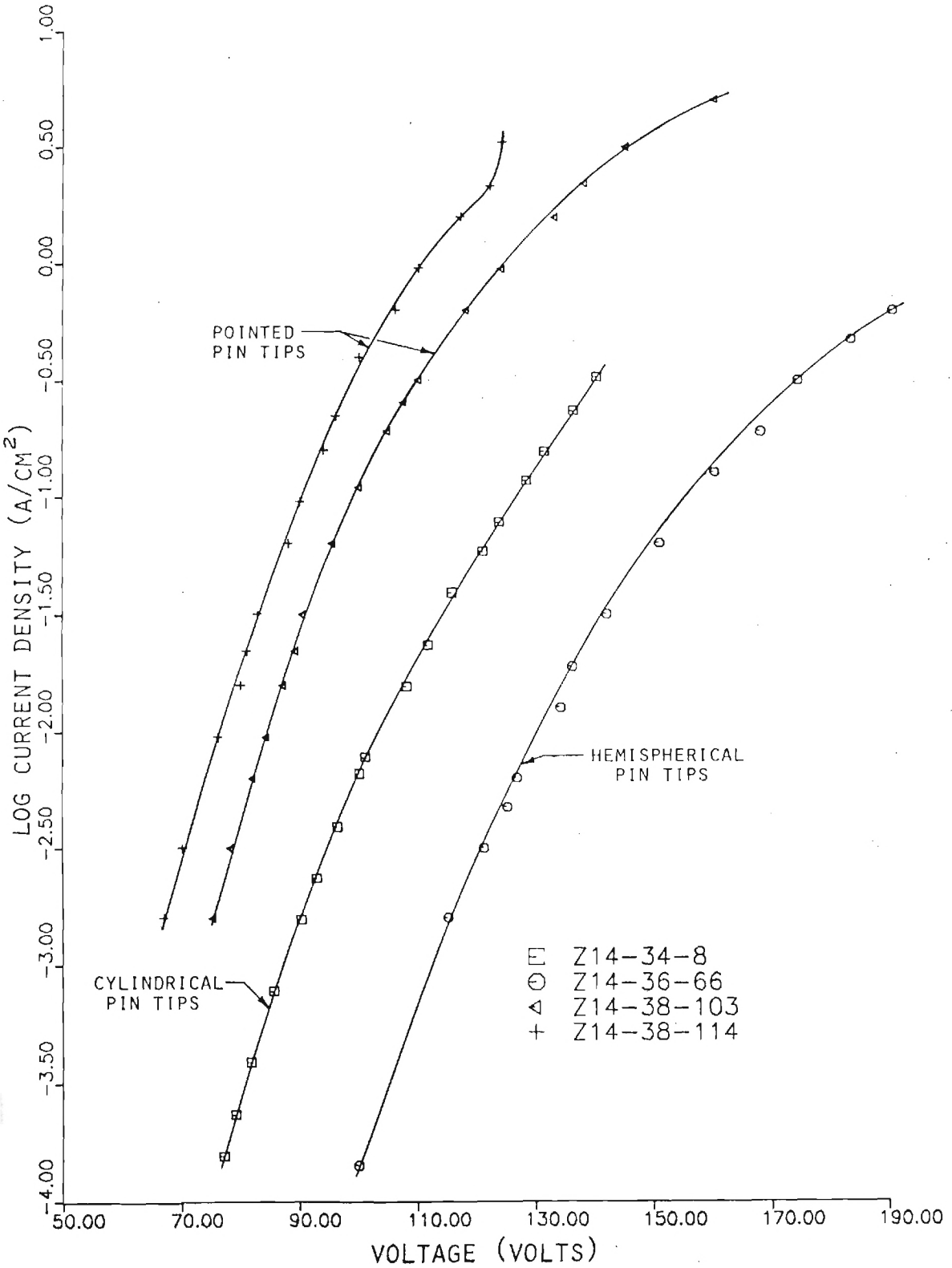

Figure VI-12. Data Plotted in Figure VI-11, Re-plotted Showing the Log of Current Density as a Function of Extractor Voltage.

the values recorded for the UO_2-W LVFEA's. The runaway situation of increasing leakage current due to bulk conduction and heating of the insulator film, commonly observed with the UO_2-W emitters, was never observed in any of the tests of the ZYW LVFEA's.

The reason for the reduced extractor current of the ZYW LVFEA's can best be explained by reference to Figure VI-13, which is a schematic diagram of an individual ZrO_2-W emitter after completion of the final etching step. Note that the conducting path from the extractor to ground, rather than being from a to b (as with the semiconducting UO_2 matrix), extends from a to c for the ZrO_2 matrix. Because of the high electrical resistivity of the ZrO_2 relative to the amorphous Al_2O_3 film, the voltage drop across the film is apparently reduced to something less than the 0.2 MV/cm level at which it begins to fail and the leakage current remains low.

The failures which occurred with the ZrO_2-W emitters were much more limited in extent than were seen with the UO_2-W composites. Rather than large areas of a dozen pins or more, in which the composite base, insulating and extractor films were all fused together (Figure IV-15), the ZrO_2-W emitters normally failed by the melting and/or vaporization of single emitting pins, as illustrated in Figure VI-14. If emission is relatively uniform over the active area, then failure of individual pins will have little or no effect on the total emission current (an active area one millimeter in diameter would typically contain about 75,000 emitters) until a substantial percentage of the pins have failed.

Occasionally, a pin in the active area of the ZrO_2-W LVFEA would fail in such a manner that it created a short-circuit path to the extractor film.

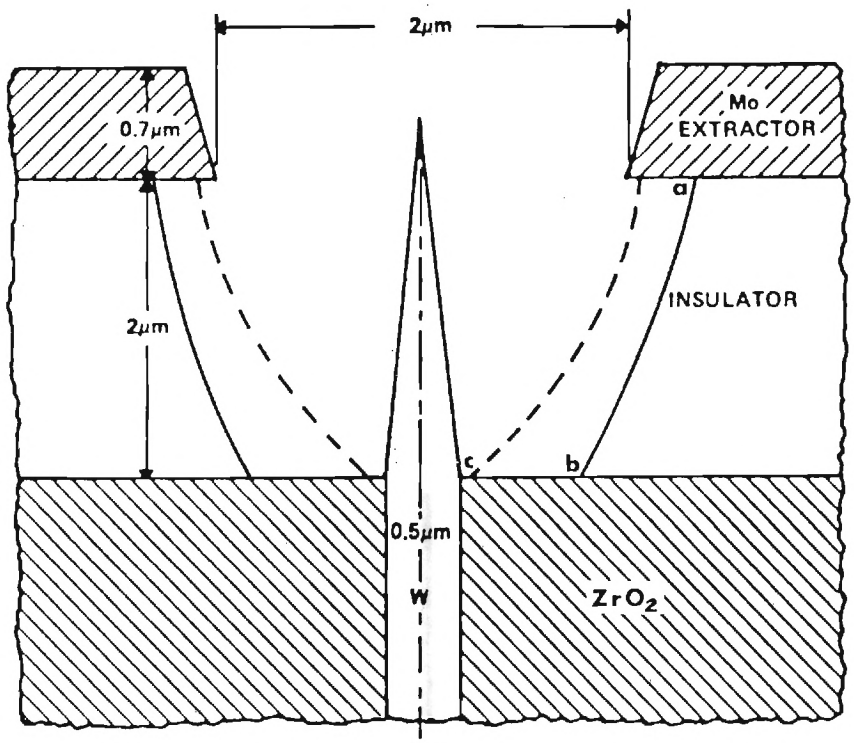

Figure VI-13. Schematic Diagram of a Single ZrO_2-W LVFE Subsequent to the Final Etching Step.

Frequently, however, these shorts could be opened by simply discharging a small capacitor through the circuit, and the cathode would continue to operate as before. In the case of the UO_2-W LVFEA's, removal of single-pin short circuits in this manner was less successful, often resulting in a large fused area as described above.

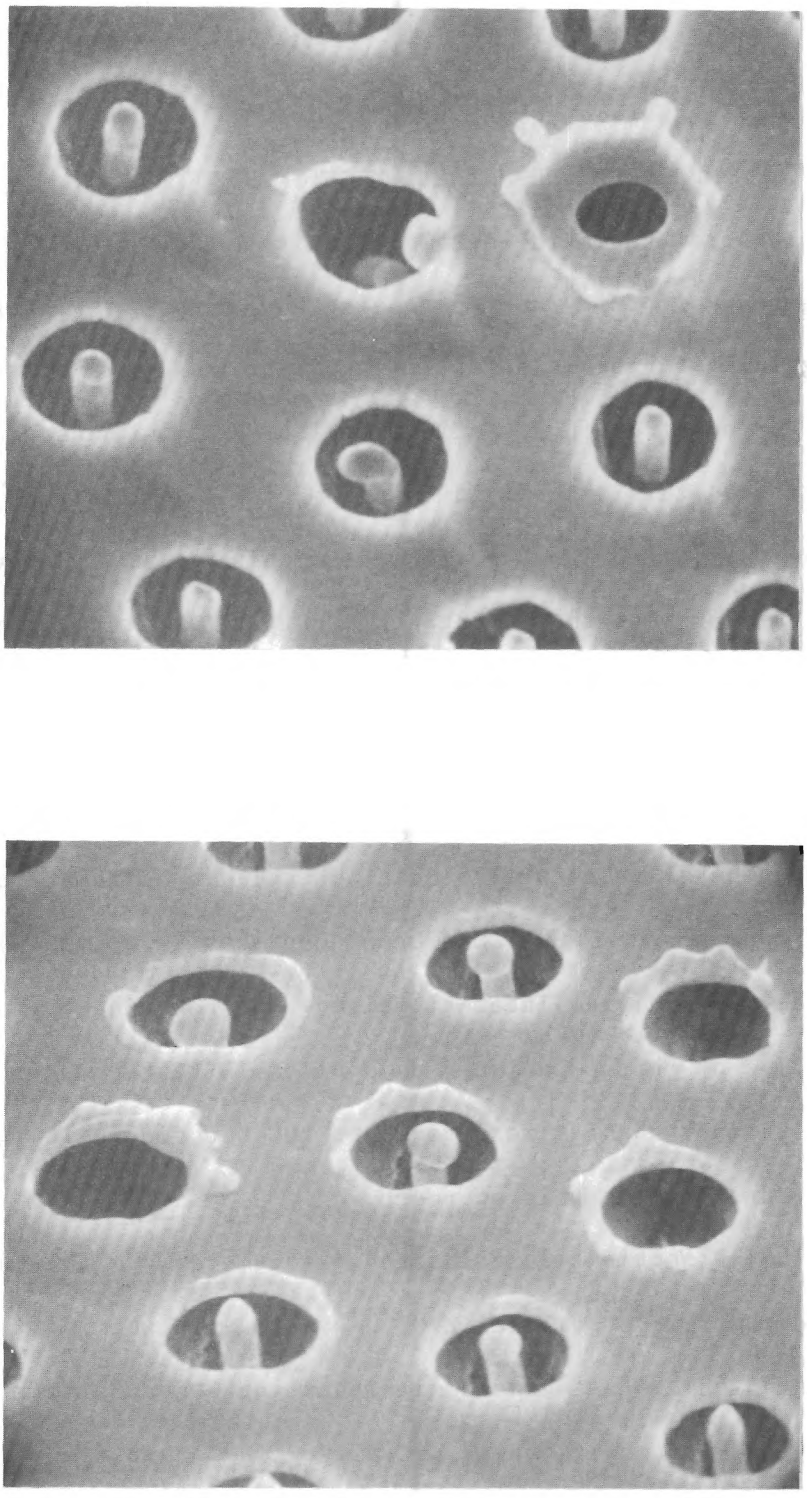

Figure VI-14. Typical Individual Pin Failures Observed in the ZYW LVFE Arrays During Post-Emission Failure Analysis.

CHAPTER VII

IMPROVE OXIDE-METAL COMPOSITE STRUCTURE

In this program the oxide-metal composite growth research was directed at improving the uniformity and increasing the area of the tungsten pin arrays, along with gaining further understanding of the role the various growth parameters play during directional solidification. At the outset of this program it was anticipated this work would be accomplished exclusively in the system UO_2-W and the initial work was performed in this system. However, about midway through this project the advantages a better electrically insulating substrate matrix would impart to the operating characteristics of the LVFE cathode were fully recognized. Consequently, most of the growth studies during the second year of this program were shifted from urania to zirconia based systems. The general procedure to melt and solidify oxide-metal ingots at temperatures approaching 3000°C has been described in detail elsewhere[5,6] and is basically a modified internal molten zone technique. In Chapter II A-1, an outline of this technique, as applicable to the UO_2-W system, is provided and only minor changes were required to induction melt Y_2O_3 stabilized ZrO_2-W (ZYW) ingots using this approach.

The following sections describe the oxide-metal growth studies in both the UO_2-W and the Y_2O_3 stabilized ZrO_2-W system. In the initial work with UO_2-W samples, problems associated with adapting a new 50 kw rf generator for the variable loading conditions, especially with larger (>40 mm) diameter ingots, consumed a significant effort. Difficulties also arose in the fabrication of the large diameter premelt UO_2-W samples. In the solidification studies in the Y_2O_3 stabilized ZrO_2-W system the major problem was selecting

conditions where excessive spills of the molten interior of the ZYW ingots could be prevented.

A. IMPROVE UO_2-W COMPOSITE

This section covers the work accomplished to improve the UO_2-W composite. As previously noted, the oxide-metal composite wafers serve as the major component in the LVFE device. Since there were unknown parameters active during the unidirectional solidification of the UO_2-W ingots and structural problems in the "state-of-the-art" composite, any program which attempted to improve the LVFE structure must incorporate work to improve the composite.

One of the limiting factors involved with enlarging the LVFE area was the size of the uniform tungsten pin arrays that could be produced. The specific problems limiting the array size were sample cracking and discontinuous and nonaligned fiber growth at the cell (grain) boundaries formed during solidification. By increasing the boule size some improvement in these problem areas was anticipated. In order to melt larger UO_2-W ingots a 50 kw rf generator was acquired and installed, and a new composite growth facility was assembled Using this facility some 25 UO_2-W ingots (both 25 and 31 mm in diameter) were solidified from which the LVFE samples were selected.

The following information outlines the installation of the 50 kw rf generator and the problems encountered in the effort to increase the size of the UO_2-W boules to 44 mm in diameter.

1. Install 50 kw rf Generator

In August 1979, a custom built 50 kw rf generator was delivered to Georgia Tech to provide the necessary power to melt UO_2-W ingots 31 mm in diameter and

larger. The existing 10 kw generators were only marginally useful with the 31 mm samples. In order to accomodate the generator, a special room was fitted with water, compressed air, and sufficient electrical power. In anticipation of possible rf interference, the room was enclosed with bronze wire cloth and grounded.

In addition to installing the generator, a sample translation apparatus was constructed from an existing fixture consisting of two metal plates mounted on 1½" diameter shafts by roller bushings and driven by two screwjacks as shown in Figure VII-1. This design allowed the independent and uniform movement of the sample and/or molybdenum preheater tube. Considerable effort was required to reduce mechanical vibrations to a level sufficient to minimize interference with steady-state eutectic growth.

A series of heating tests were conducted using a graphite cylinder as the inductive load to select the range of rf coil geometries and resultant megahertz frequencies available with the 50 kw generator. As a result of this testing, 4 and 6 turn coils formed from 3/8 o.d. copper tubing were selected. The approximate coil diameters were 80 mm for the 25 mm and 88 mm for the 31 mm diameter UO_2-W ingots resulting in operational rf frequencies between 2.5 and 3.5 MHz.

After several months of familiarization runs with the new generator, a few modifications were provided by the supplier. Changes included a second varaic for finer power control, an automatic heating and cooling rate controller and the addition of a variable tank coupling capacitor. One very serious problem arose because of the design need to keep the inductance in the tank circuit as small as possible. This was necessary because of the large inductance of the work coils, and since most of the inductance was

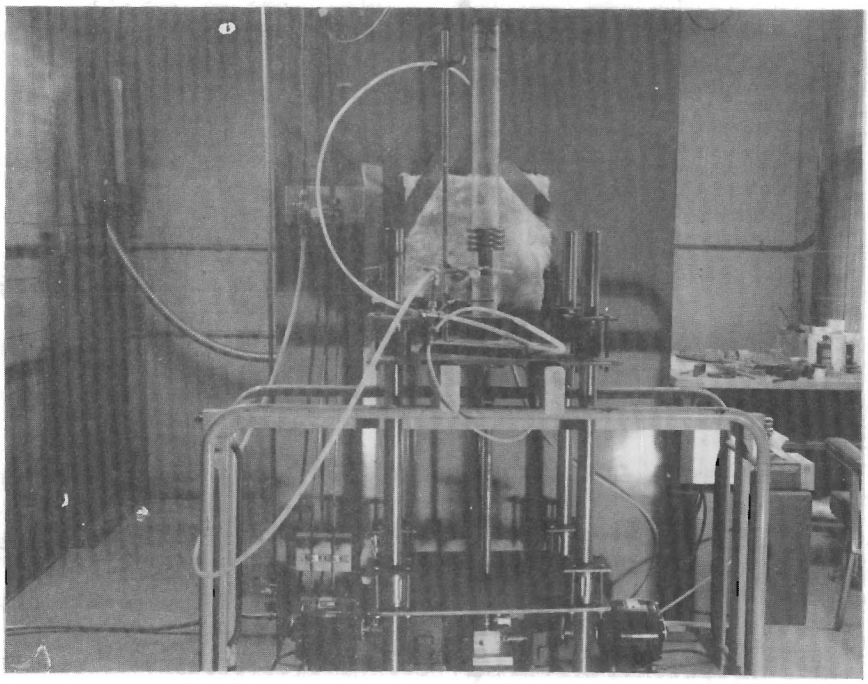

Figure VII-1. Unidirectional Solidification Equipment Used for the Growth of UO_2-W Composites.

present in the work coil, wide swings in the V-I characteristics of the oscillator tube occurred as the load changed (during sample translation). In most cases, this resulted in increased power to the UO_2-W ingot during the latter stages of solidification, leading to deformation of the sample and sometimes catastrophic spills of the molten interior (Figure VII-2). As a result of this problem, a feedback (clamping) circuit was designed and installed to maintain a constant output voltage from the saturable core reactor. This modification was a great benefit to securing uniform eutectic growth, especially during the latter stages of solidification.

Numerous growth experiments using 25 mm and 31 mm diameter UO_2-W samples were conducted to evaluate the performance of the 50 kw generator in comparison to the previously used 10 kw generators. In all cases, and especially with the 31 mm diameter samples, the extent of melting and molten zone uniformity were superior with the new 50 kw generator and a typical longitudinal section of a 31 mm diameter UO_2-W boule is shown in Figure VII-3.

2. Increase Boule Size

This task, initiated in January 1980, was designed to increase the UO_2-W ingot diameters to about 44 mm and was selected based on the consumption of UO_2 powder and rf frequency considerations. This change increased the volume to surface area ratio of the molten zone to a level where expected benefits, i.e. larger cell sizes, larger crack free areas, etc., could be adequately assessed.

To begin this work, a larger growth system was assembled and initial heating of the molybdenum preheater tube at a frequency of 1.9 MHz was accomplished using a 7 turn work coil 120 mm in diameter.

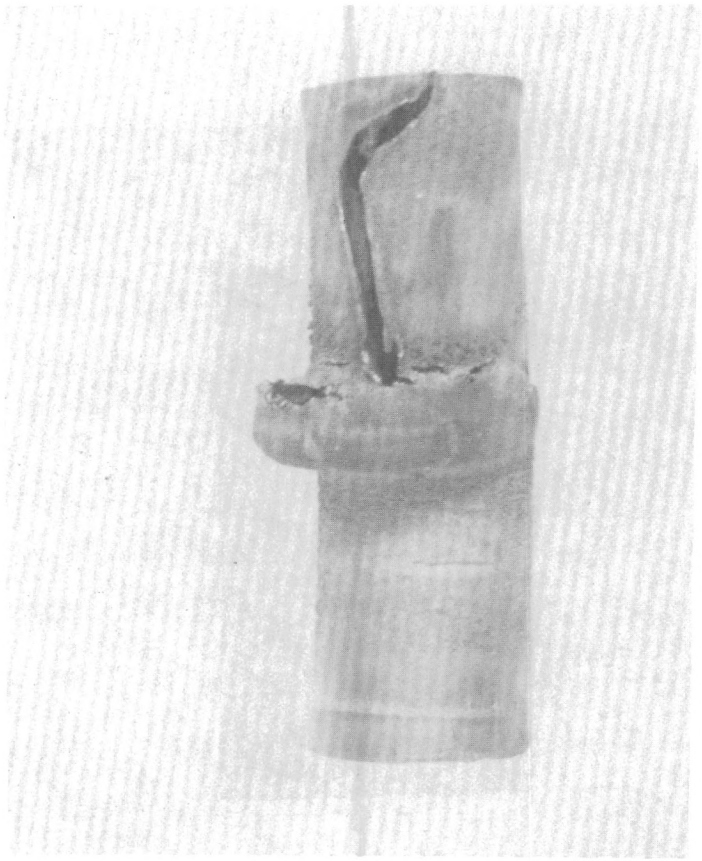

Figure VII-2. Deformed UO_2-W Ingot (25 mm in diameter) Resulting from Increased Input Power During the Latter Stages of the Molten-Zone Travel.

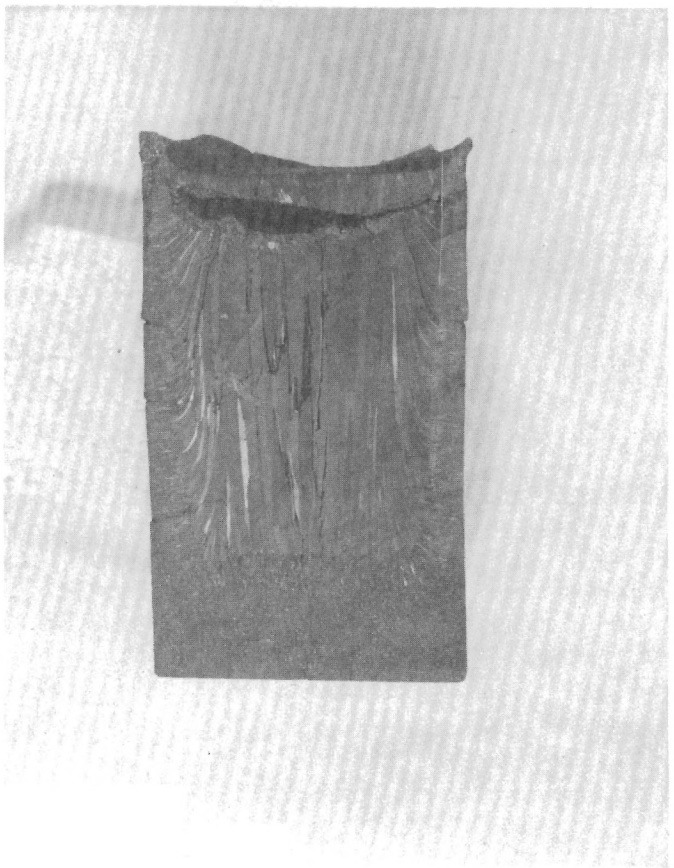

Figure VII -3. Typical UO_2-W Ingot (31 mm in diameter) Displaying a Completely Melted and Continuous Cell Structure.

Hot pressing was selected as the method of fabrication of the 44 mm diameter premelt samples since this technique should provide an excellent means of producing sound cylinders of controlled density. To test the hot pressing characteristics of the UO_2 and W powders, a 25 mm diameter sample was pressed in graphite dies to a density of 9.5 grams/cm^3. This sample was then subjected to the normal preheating cycle, in N_2, prior to the direct internal melting and composite growth. However the hot pressed UO_2-W sample failed by spalling and cracking before the temperature reached 1000°C. Possibly reaction of the oxide with the background oxygen pressure in the N_2 preheat atmosphere or nonuniform heating may have contributed to this behavior.

This cracking problem was unanticipated and was a major deterent for using hot pressing as a method of fabricating the large (44 mm) diameter premelt samples. As a consequence of this behavior, the large diameter samples were fabricated using conventional uniaxial pressing followed by sintering at 1400°C in a N_2 atmosphere. Accordingly, trial pellets were pressed and sintered to obtain shrinkage information necessary to design dies for the larger samples. Using this data, a set of graphite dies and punches were fabricated.

However, an additional problem occurred in the fabrication of the large UO_2-W samples. Because of the greater utilization of urania powder it was necessary to use a second source of depleted UO_2 powder. Unfortunately the pressing characteristics of this material, even after the standard reduction cycle, was poor. Excessive laminations occurred in the initial pressing trials and an effort was made to improve the pressing characteristics of this material. Techniques tested included pre-pressing, ball milling, and incorporating a binder with the urania powder. The ball milling operation proved to be most successful and this processing procedure follows: the urania powder was placed in

a gallon porcelain ball mill with twelve to eighteen alumina balls. The powder was milled approximately 24 hours which agglomerated and deaired the powder. After milling, the balls were removed and the powder scraped from the walls of the mill. The resultant powder pressed very satisfactorily. Using this procedure, four 250 grams UO_2-W wafers were green pressed, ∿51 mm in diameter, and sintered at 1400°C in nitrogen. The fired product shrunk to ∿41 mm in diameter and exhibited no gross deformation or cracking. These wafers were stacked together, yielding a one kg premelt sample for the initial melt trial with a large diameter UO_2-W sample.

The four UO_2-W discs were successfully induction melted and unidirectionally solidified although two internal melting attempts were necessary to accomplish this task. In the initial experiment a 7 turn rf coil (110 mm in diameter) was utilized, yielding an rf frequency of 1.9 MHz. The four sample stack was preheated to ∿1300°C in the molybdenum preheater; however, when the direct induction heating of the UO_2-W discs was attempted, grid exitation was lost and several additional melting attempts were made with various grid capacitor and inductance settings: all unsuccessful. Surprisingly, the UO_2-W discs withstood the thermal stresses generated during the wide temperature excursions associated with raising and lowering the molybdenum preheater tube during these melting attempts.

In the second melting trial the original four UO_2-W discs were reheated using a 5 turn work coil, raising the rf frequency to 2.3 MHz. Again some difficulty was encountered maintaining sufficient grid current during the direct melting of the UO_2-W sample; however, by slowly increasing the input power to the sample, while adjusting the grid controls, the four sample stack was internally melted and lowered through the rf coil (Figure VII-4). This sample was

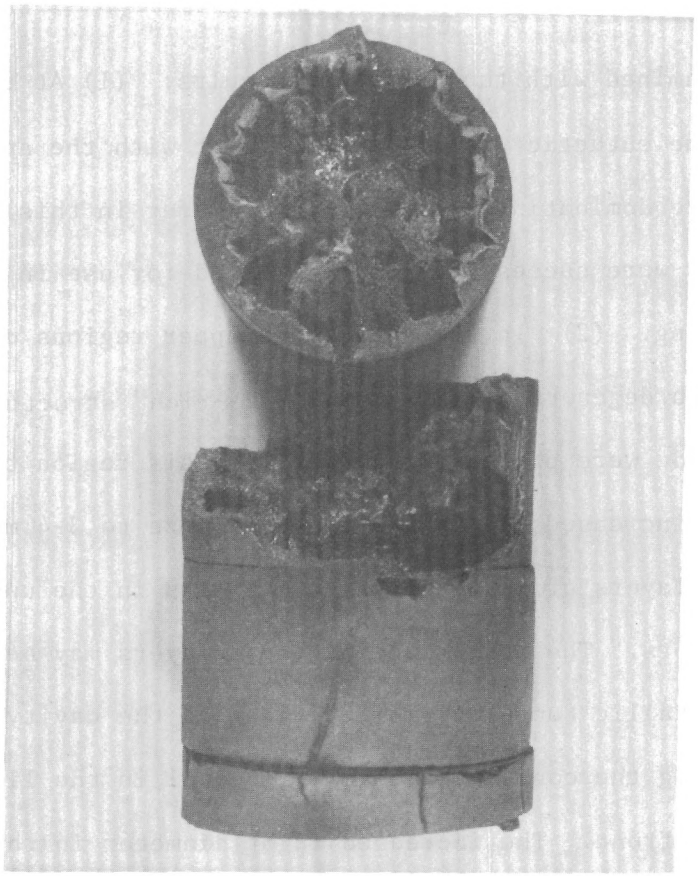

Figure VII-4. Exterior View of Upper Portion of 41 mm Diamter UO_2-W Ingot Showing Cellular Void Structure Above Molten Zone.

sliced and examined with the following results: (1) At the base of the molten zone the eutectic growth was excellent with the anticipated small diameter cell size dominating. From a single wafer in this growth region ten separate chips were successfully core drilled for use in LVFE fabrication and emission testing. (2) In the center and upper regions of this sample, the eutectic growth degenerated into the "oxide-rich" structures where large regions of primary oxide were present. However, in this region the cell diameter had substantially increased to an average cell size to 3-4 mm. (3) Noteworthy, there were no layers of heavy tungsten deposits in the upper regions of the solidified ingots. The appearance of these layers may be attributed to the dripping of metallic tungsten from the roof of the cavity during zone travel, greatly changing the concentration of the metal in the liquid just above the solidification front. The increased ingot diameter in this experiment apparently prevented the formation of a single large void above the molten zone, and replaced this geometry with a cellular void structure that helped redistribute the molten tungsten more evenly during the zone translation.

Prior to performing the last UO_2-W composite growth experiment, utilizing the 41 mm o.d. ingots, several trial induction heating runs with a modified load and tank inductance were made in an effort to improve the loading of oscillator tube and, hence, the grid exitation problem. A transformer type coil geometry was selected for use with the large diameter UO_2-W sample in this experiment. To fabricate the premelt sample, the reduced and milled urania powder was mixed with tungsten powder and sintered at 1400°C in nitrogen. Based on the eutectic growth behavior in the previous experiments, the tungsten content was increased to 10 w/o an increase of 4 w/o compared to the 6 w/o normally used in earlier experiments. During this experiment everything proceeded normally to 1300°C

when the moly tube was lowered out of the rf coil and the sample was internally melted and the internal molten zone stabilized. Translation of the UO_2-W ingot was initiated, and the sample ran exceptionally well for approximately 30 minutes (experiencing no unexpected grid or power excursions) when suddenly the grid current unexpectedly dropped to zero. This necessitated raising the moly preheat tube within the load coil to establish oscillation in the induction generator. The molten sample was lowered for an additional 15 minutes when the same behavior occurred, quenching the UO_2-W sample and completely destroying the growth experiment, except for a small section in the base of the molten zone.

Because of the grid exitation problem occurring with the large diameter UO_2-W samples, a decision was made to postpone further experiments until tank modifications were made to the 50 kw generator to alleviate this behavior. This problem resulted primarily because of the very different loading characteristics of the molybdenum preheater tube compared to the low resistivity of the molten UO_2-W solution. Eventually the tank circuit was redesigned to add more internal inductance to the circuit to provide more flexibility in the types of loads that could be successfully heated. This experiment turned out to be the last effort to directionally solidify UO_2-W compositions because of the interest the Y_2O_3 stabilized ZrO_2-W (ZYW) composite material for improved LVFE performance.

3. Reduce Cracking in UO_2-W Ingots

As stated earlier, one of the potential advantages of the larger (>40 mm) diameter UO_2-W boules was the prospect of increasing the content of "crack-free" composite growth from which LVFE chips could be core drilled. An indication of the improvement the large diameter ingots will provide is shown from the sketch (Figure VII-5) of the crack pattern in a UO_2-W wafer from the base of first 41 mm diameter UO_2-W sample directionally solidified. Based on the crack

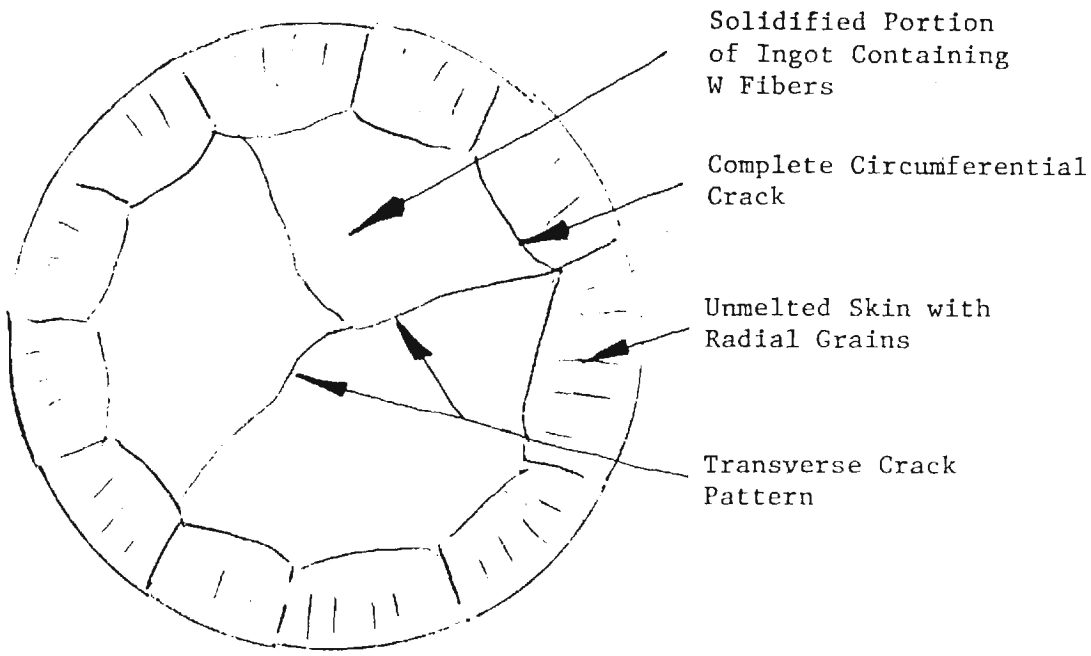

Figure VII-5. Wafer from Base of UO_2-W Ingot, 41 mm Diameter Showing Crack Pattern, Scale, X2.

pattern in this ingot, the wafers would yield 10 to 12 of the 4 mm diameter chips used in the fabrication of the LVFE emitters. This compares with the intermediate (31 mm diameter) and small (25 mm diameter) size UO_2-W samples were typically only 2 to 4 LVFE disks could be core drilled per wafer. Additional work with the large diameter UO_2-W ingots was terminated when the composite growth effort was shifted to the zirconia based systems.

4. Kinetic Processes

During the growth of the UO_2-W composites, one of the major problem areas has been the loss of W from the molten zone and the buildup of W on the roof of the cavity over the zone, as well as in the unmelted skin surrounding the zone. In an effort to analyze this process, molten pools of UO_2-W were held for various lengths of time and quenched. X-ray florescence analysis was employed to determine the W profiles. This type investigation should help to understand the effects of time, growth atmosphere, and growth rate on W losses and aid in understanding the kinetic processes active during directional solidification at the elevated temperature necessary to melt UO_2-W mixtures. Since a decision was made about the time this task started to shift most of the solidification efforts to the ZYW composites, only a limited amount of work was accomplished in this area.

In order to use x-ray florescence analysis, a series of UO_2-W standards of known tungsten content were prepared. Compositions containing up to 6 w/o W were run and a nearly linear relationship between the x-ray emission intensity and the W content was established. To check the validity of the florescence technique a series of previously grown UO_2-W samples were analyzed for W content using the x-ray analysis, as well as from simple geometric calculations from SEM micrographs. Very reasonable agreement was obtained between these two

techniques, and both methods established that most of the eutectic structures in the UO_2-W system contained about 1½ to 2½ w/o W.

In the first experiments performed specifically to evaluate W losses from molten UO_2-W mixtures, the samples initially containing 6 w/o tungsten, were held in the standard CO/ 1 v/o CO_2atmospheres. The sample remained stationary in the rf coil. The first sample was held for one hour and another for six hours to check the time dependence loss of W occurring under these conditions. Interestingly, both quenched samples contained approximately 2.1 w/o W and suggested that for reasonable periods there may be a tungsten-oxygen complex relatively stable in the molten uranium dioxide. These results suggest much of the tungsten observed concentrated in the unmelted skin surrounding the molten zone may result from the initial vaporization of W from samples initially containing 6 w/o W. In a second series of experiments, UO_2-W ingots similar to those run in the initial experiments were internally melted and held under identical conditions, except that the oxygen content in the system was increased by using a CO atmosphere containing 4.5 v/o CO_2. Since the solubility of W is known to increase as the o/u ratio increases[5], the experiment run for 6 hours indicated, as expected, that 3.1 w/o W was retained in solution. Again this result indicated it was possible to retain 2 to 3 w/o W in molten UO_2, and perhaps the loss of W from the molten internal zone is not as serious a problem as originally anticipated.

Again, because of the improved LVFE performance of the ZYW composites, the growth effort was shifted from the UO_2-W to the ZYW system and no additional work was done on the kinetic processes occurring in the UO_2-W system. The major conclusion from this work, although supported by a minimal amount

of evidence, is that it appears possible to maintain a relatively constant amount of tungsten in solution in molten urania, even at temperatures and oxygen pressures where the loss of metallic tungsten through vaporization and oxidation processes would be excessive.

B. Y_2O_3 STABILIZED ZrO_2-W (ZYW) COMPOSITE

Since initial performance of the LVFE samples fabricated from the Y_2O_3 stabilized ZrO_2-W (ZYW) composite was very positive, all the growth effort was shifted from the system UO_2-W to the ZYW material during the last 6-7 months of this program. A list of the comparative advantages and disadvantages of these two systems is presented in Table VII-1. Because of the very refractory nature of these systems, with eutectic temperatures greater than 2500°C, and lack of appropriate phase diagrams, much of the solidification work has been imperical in nature, and each system has presented its own unique set of problems. Based on previous experience solidifying Y_2O_3-stabilized ZrO_2-W (ZYW) composites, the major problem area preventing the continuous and extended growth of tungsten pin arrays can be broadly divided into two areas: (a) those associated with the general difficulty of establishing a well melted internal zone with a "flat" solidification front that can be translated uniformally through the center of the ZYW ingots, and (b) microstructural problems associated with the continuity of the tungsten fibers within the individual cells and, allied problems related to fiber geometries at the cell boundary. The following sections describe in some detail: (1) the major problem areas associated with the growth of the ZYW composites, and (2) the role the different growth parameters play in achieving aligned and continuous W fiber arrays in the zirconia matrix.

Table VII-1. Comparative Performance of Eutectic Growth in the Systems UO_2-W and Y_2O_3 Stabilized ZrO_2-W.

a. UO_2-W

Advantages

1. Forms a very stable molten zone when induction melted.
2. Readily control electrical conductivity with O/U ratio of oxide.
3. Forms regular W pin arrays when growth conditions "ideal".
4. Ten years experience accumulated growing the UO_2-W eutectic structures at Georgia Tech.
5. Multiple translation of molten zone possible.

Disadvantages

1. Metal (W) solubility in molten urania dependent on O/U ratio.
2. To maintain desired O/U ratio, P_{O_2} control necessary.
3. Controlled P_{O2} accelerates transport and vaporization processes.
4. Cell boundaries (and perhaps fibers) contain layer of UWO_x phase.
5. Suitable fabrication of premelt samples limited to sintering in N_2.
6. Source of urania powders limited and difficult to obtain.
7. Restrictions and limitations imposed because of radio-active source material.

b. Y_2O_3 Stabilized ZrO_2-W

Advantages

1. Zirconia powders of high purity readily available.
2. All sample fabrication and eutectic growth accomplished under reducing conditions.
3. Hot pressing (in graphite dies) utilized to produce premelt samples to close physical dimensions and controlled density.
4. Well ordered W pin arrays readily grown during unidirectional solidification.
5. "Good" eutectic growth achieved close to cell boundaries.
6. No foreign phase in cell boundary or on surface of W pins.

Disadvantages

1. Electrical conductivity of zirconia requires preheat temperatures >1600°C to initiate internal melting.
2. Spills often occur with the ZrO_2-W samples because of delicate balance between input power and heat loss processes.
3. Less than one year's experience at Georgia Tech melting large (> 1" o.d.) ZrO_2-W ingots.

1. ZYW Growth Problems

During the initial formation of the molten internal zone in ZYW ingots, several criteria must be adequately satisfied. Initially the material must possess the electrical conductivity to establish sufficient eddy current heating to sustain the internal zone. Obviously the starting composition and preheat temperature greatly influence the electrical conductivity, and ZYW samples were routinely internally melted utilizing preheat temperatures greater than 1600°C at rf frequencies between 2 and 4 MHz. However, large spills of the molten material often occurred producing a nonsymmetrical molten zone (Figure VII-6). After the zone was established, an impedence match between the load coil and the liquid and/or solid portions of the ingot controlled uniform translation of the molten zone through the ingot. An example is shown in Figure VII-7a where the zone did not remain fixed in the coil but translated down with the ingot until the liquid pool was out of the strongest part of the rf field. Suddenly and uncontrollably the molten zone moved up within the ingot to a position in the sample located at the center of the rf coil. These problems lead to discontinuous fiber growth with no possibility of ever obtaining well-ordered and continuous fiber arrays. In contrast, when the liquid-solid solidification front was well defined and translated under control, the ZYW ingot exhibited the molten zone geometry shown in Figure VII-7b.

Several types of discontinuities in the growth of the tungsten fibers are shown in Figure VII-8a and 8b. As evident in these pictures, wide bands of pure oxide layers, as well as heavy layers of tungsten metal formed during solidification. These wide horizontal bands resulted because of the inability to feed tungsten uniformly into the molten pool. As noted in the

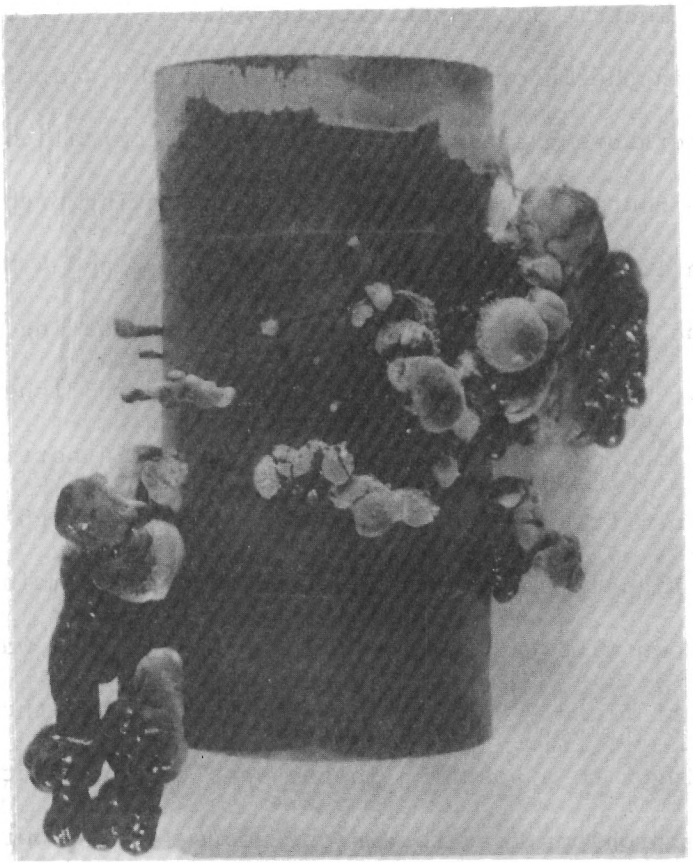

Figure VII-6. ZYW Ingot Displaying Excessive Spills From the Internal Molten Zone.

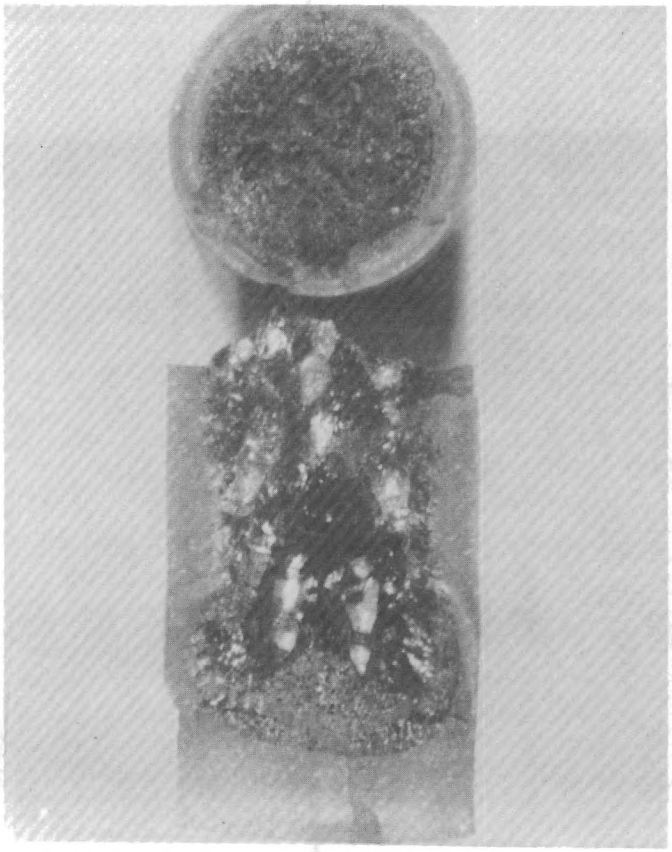

(a)

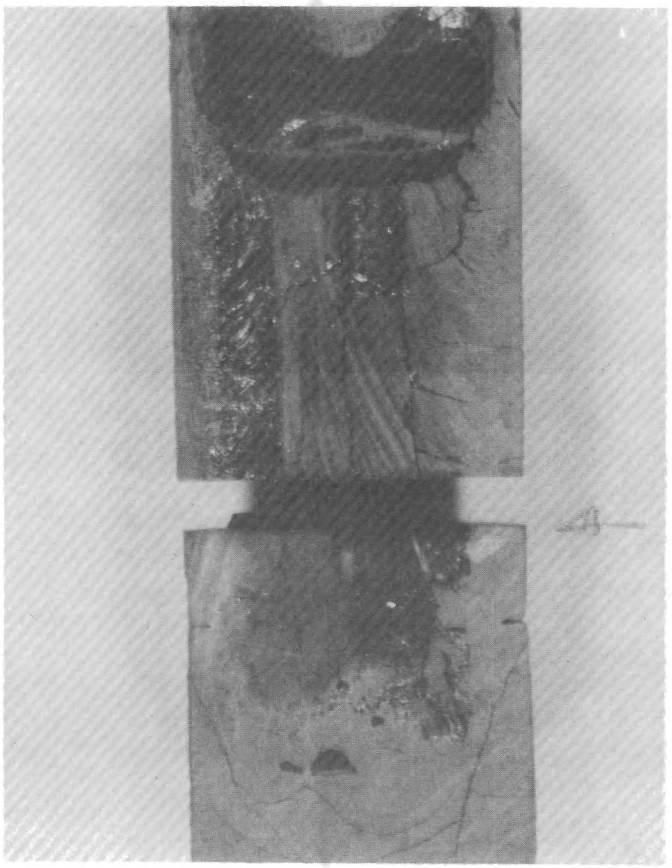

(b)

Figure VII-7. Longitudinal Section of ZYW Ingot
a. Sample with no Control of Solidification Front.
b. Well Melted Sample After Controlled Translation of Planar Solidification Front.

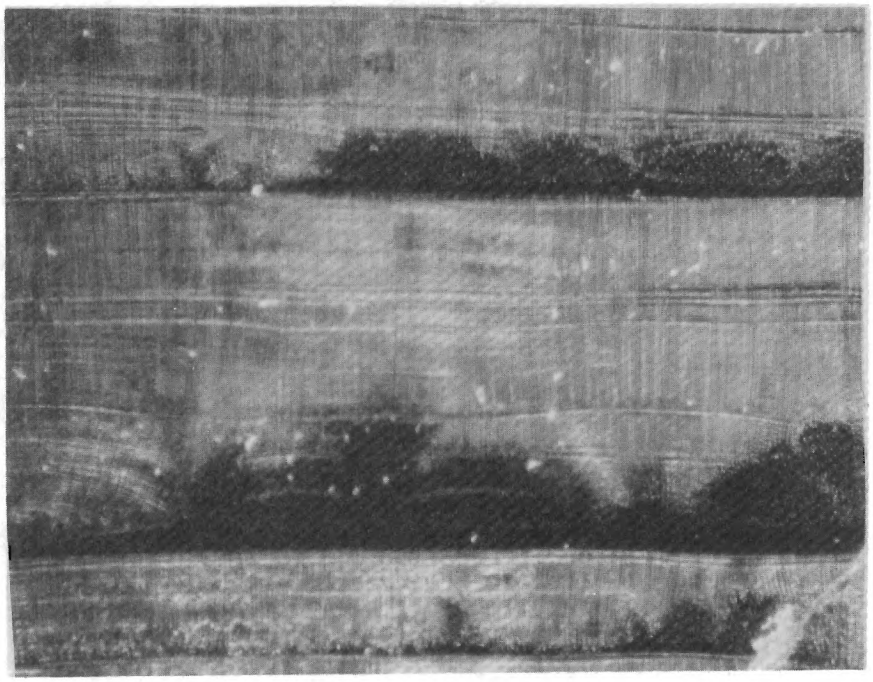

(a)

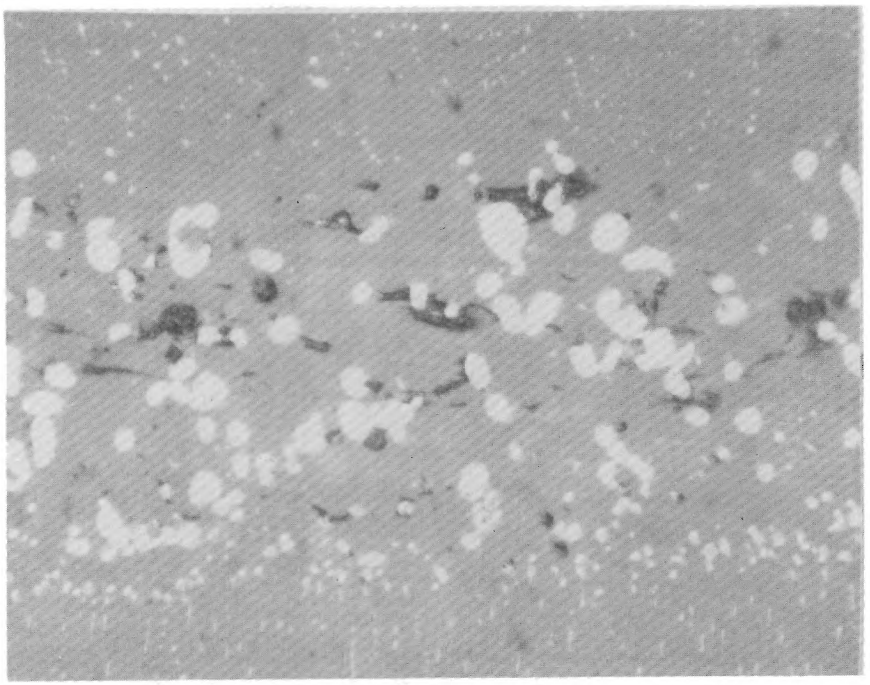

(b)

Figure VII-8. Discontinuous Tungsten Fiber Growth in the ZYW Ingots, Dark Field.
a. Oxide "Fan Banding, x 200.
b. Metal Precipitates, x 600.

description of the internal zone solidification process, a void travels ahead of the molten zone and this cavity was rapidly coated with a layer of metallic tungsten. During zone translation the uniform addition of the oxide and metal to the molten zone was responsible for these forms of "banding". An additional type of "banding", where the fiber continuity was interrupted for very short distances, is shown in Figure VII-9. The cause of this discontinuity is not as easily explained as the other microscopic defects. Possible causes included minor growth pertubations to the solidification front caused by fluctuations in rf power or a variation in the rate of solidification.

In addition to the problems described above, there was the problem of the ingot cracking basically because of the large temperature gradients necessary to contain the molten internal zone, as well as the mismatch in thermal expansions between the metal and oxide phases. Perhaps a more positive way to analyze eutectic solidification in refractory oxide-metal systems is to marvel at the ability to produce such ordered structures in systems where so many unknowns exist. The following section describes a list of parameters examined in an effort to minimize these growth problems.

2. Improved ZYW Growth

This section contains an analysis of the growth parameters which were studied during the unidirectional solidification of Y_2O_3 stabilized ZrO_2-W composites. Foremost was the need to establish conditions where sufficient metal (to form continuous fibers) was dissolved in the molten oxide. Then the necessary temperature gradients required to form a flat liquid-solid boundary must be established. Lastly, the mechanics of translating the solidification front while uniformily supplying the oxide and metal consti-

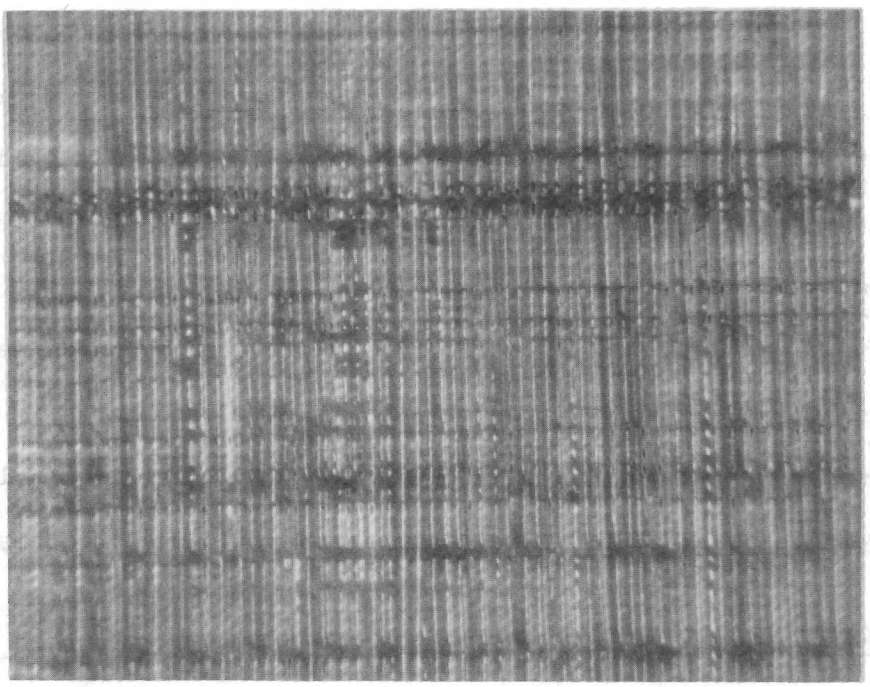

Figure VII-9. Interrupted Fiber Growth in the ZYW Ingots, Dark Field, x 600.

tuents in the molten zone was evaluated using the constraints of the internal zone technique.

Past experience solidifying ZYW composites indicated chemical parameters, such as the influence of oxide stoichiometry on tungsten solubility, were not nearly as important in the zirconia-based systems as with molten urania. Table VII-2 lists the parameters which were considered important to analyze in an effort to improve the W fiber continuity in the ZYW ingots. Time did not permit an extensive analysis of all these items and a summary of the more important findings follows.

Table VII-2. Parameters Analyzed During the Solidification of Y_2O_3-Stabilized ZrO_2 Composites.

a. Premelt sample density
b. Yttria and tungsten content
c. Zirconia purity
d. Melting geometry and rf frequency
e. Solidification rate
f. Atmosphere control and gas flow rate
g. Power excursions and uniform zone translation

The ZYW premelt samples were routinely prepared by hot pressing in graphite dies. This process permitted the accurate control of the premelt sample density and, to some extent the microstructure of the premelt samples. Past experience suggested premelt densities approximately 80-85% of theoretical were optimum because of the need to withstand the severe thermal shock during the initial formation of the internal molten zone, as well as the accompanying volume increase of the liquid. Using 31 mm diameter dies, a hot pressed

ZYW pellet with a starting density between 5.0 and 5.5 gms/cc and about 70-80 mm tall was employed in most of the ZYW solidification experiments. The degree of stabilization of the ZrO_2 with Y_2O_3 should play a major role in controlling the mechanical and electrical properties of the oxide. Conversely the metal (W) content was critical to assure the growth of continuous (non-interrupted) fibers. The "best" composition consisted of:

72 w/o ZrO_2

13 w/o Y_2O_3

15 w/o W

Efforts to systematically vary these components were plagued by the inability to always form a "stable" molten zone suitable for uniform translation.

The recent upsurge of interest in zirconia for a variety of applications (including gem stones) has lowered the raw material cost and made very pure zirconia powders available. Solidification theory suggests that the impurities segregate in the cell boundaries during unidirectional solidification. A series of experiments were conducted with ZrO_2 powders of different purity, but again, difficulties reproducing identical molten zone geometries and translation treatment masked any subtle structure differences.

Perhaps the most important factor in any effort to improve oxide-metal eutectic structures is the need to pass a flat liquid-solid solidification front uniformly through the interior of the ingots. In the ZYW system the translation of the molten zone was contingent upon uniformly feeding material from the roof of the cavity to the liquid pool. Any buildup of tungsten

layers or void pockets greatly impeded uniform movement. The positioning of pre and post heaters within the rf coil, as well as the rf frequency used for melting, were critical to achieve this objective. The best ZYW solidification runs were made using a top preheater tube positioned in the upper turns of the rf coil to prevent the zone from "running-up" (as shown in Figure VII-10). In addition the rf frequency was lowered to the 2.5 to 3.0 MHz range to facilitate a modest increase in skin depth to help prevent the "spills" of the molten zone, so disruptive to the translation of the liquid-solid interface.

All ZYW solidification experiments were accomplished in a dynamic atmosphere of H_2 and N_2. The ability to perform the premelt fabrication and melting steps in reducing conditions was one of the major advantages of the ZYW system. In addition, the cooling effects of H_2 especially at high flow rates (>1 liter/min) enhanced the heat loss from the surface of the ingots and helped maintain the solid skin necessary to prevent spills from the molten interior.

During this study some 33 separate ZYW solidification experiments were performed and a set of solidification parameters and premelt characteristics for the growth of the ZYW composites using the internal zone technique were established. However, the uncertainty of crack patterns within the ZYW ingots and accompanying spills never completely assured a reproducible translation of the liquid-solid interface so necessary for the growth of aligned composite structures. In addition, the upper portions of the ZYW ingots usually contained large regions of primary tungsten, thought to drip from the roof over the cavity above the liquid. However, in spite of these difficulties most ZYW samples contained narrow (5 to 10 mm) bands, usually toward

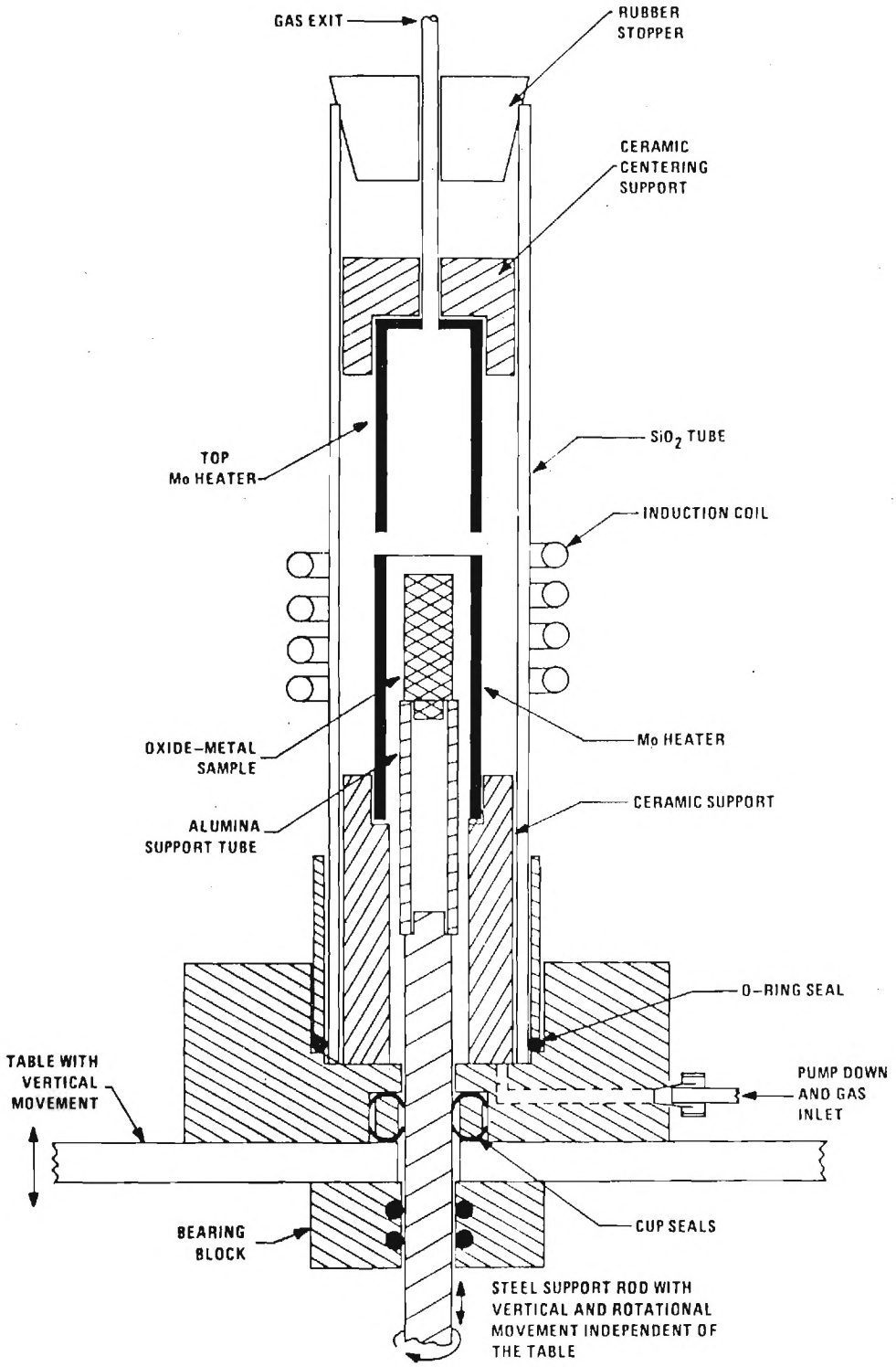

Figure VII-10. Schematic Diagram of the Facility Used to Unidirectionally Solidify the ZYW Composites.

the base of the ingots where the fibers displayed excellent regularity and sufficient continuity for processing to form the LVFE structures (Figure VII-11).

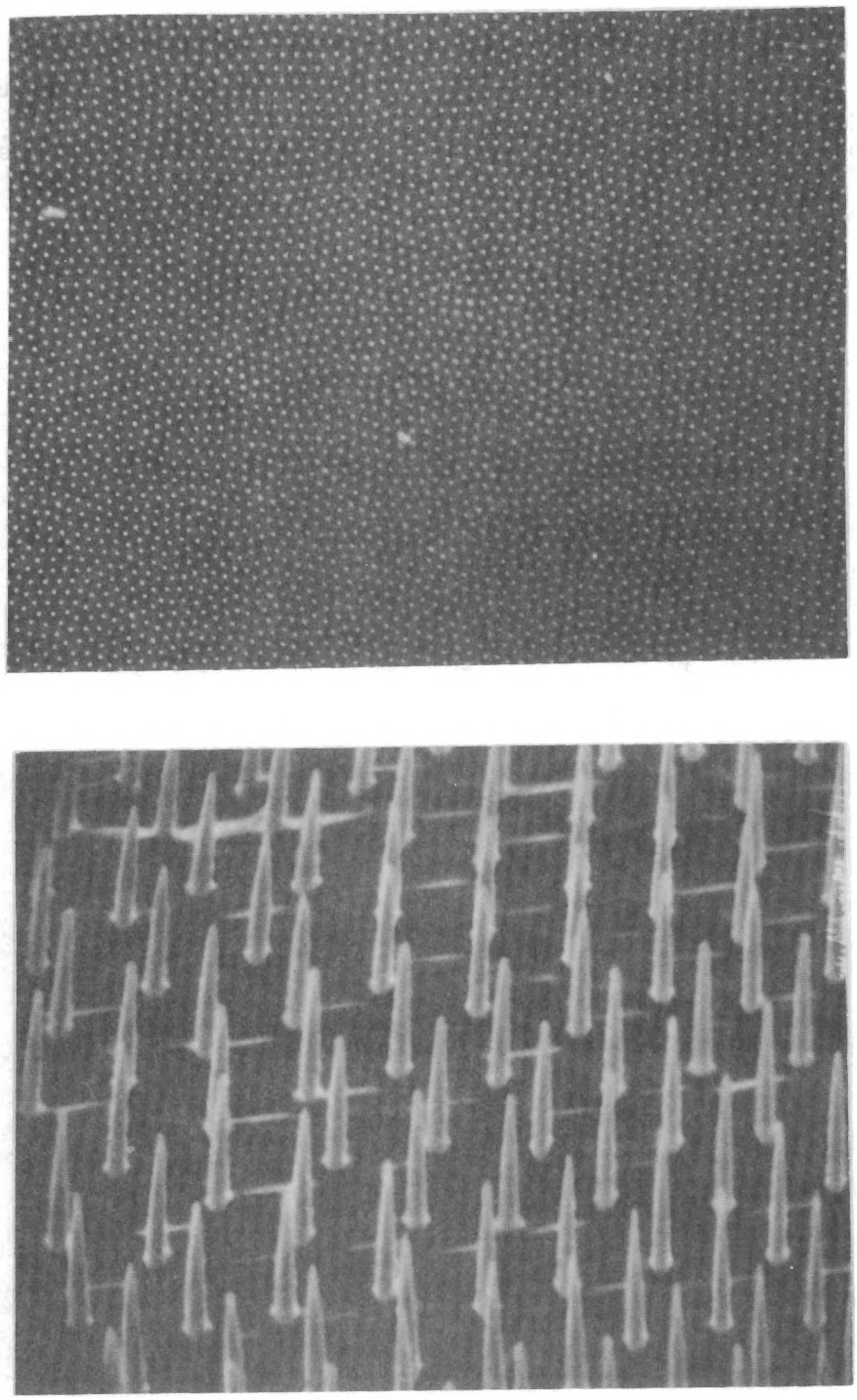

(a)

(b)

Figure VII-11. Eutectic Structure of Y_2O_3Stabilized ZrO_2-W Composites,
a. Tranverse section, dark field, X500 and
b. SEM of exposed W fibers after chemical etching, X5000.

BIBLIOGRAPHY

1. J. K. Cochran, et al., Final Report, U. S. Army Missile Command Contract DAAH01-75-C-0852, Georgia Institute of Technology, School of Ceramic Engineering, January 1979.

2. D. N. Hill, Ph.D. Dissertation, Georgia Institute of Technology, School of Ceramic Engineering (1979).

3. J. D. Lee, Ph.D. Dissertation, Georgia Institute of Technology, School of Ceramic Engineering (1978).

4. A. T. Chapman and G. W. Clark, J. Am. Ceram. Soc., 48, 494 (1965).

5. A. T. Chapman, et al., Reports 1-6 ARPA Contract DAAH01-70-C-1057, Georgia Institute of Technology, School of Ceramic Engineering, December 1977.

6. A. T. Chapman, et al., Final Technical Report, U. S. Army Missle Command Contract DAAH01-75-C-0852, Georgia Institute of Technology, School of Ceramic Engineering, December 1977.

7. R. V. Kolarik, "Electrical Properties of Amorphous Alumina Thin Films," Ph.D. Thesis, Georgia Institute of Technology, School of Ceramic Engineering, December 1981.

8. M. G. Mier and E. A. Buvinger, "A Comparative Study of Anodized, Evaporated and Sputtered Aluminum Oxide Thin Films," The Journal of Vacuum Science & Technology, (G), 4, 727-30 (1969).

9. H. Birey, "Dielectric Properties of Aluminum Oxide Films," J. Appl. Phys., (49) 5, 2898-2904 (1978).

10. C. A. Spindt, I. Brodie, L. Humphrey, and E. R. Westerberg, J. Appl. Phys., 47, 5248 (1976).

11. R. H. Fowler and L. W. Nordheim, Proc, Roy. Sco. (London) A119, 173 (1928).

12. F. B. Hildebrand, Finite-Difference Equations and Simulations (Prentice-Hall, New Jersey, 1968).

13. R. W. Hamming, Introduction to Applied Numerical Analysis, (Mcgraw-Hill, New York, 1981).

14. K. H. Moh, "Selective Chemical Etching of Unidirectional Zirconia-Tungsten Eutectic Composites," M.S. Thesis, Georgia Institute of Technology, School of Ceramic Engineering, June, 1981.

* U.S. GOVERNMENT PRINTING OFFICE: 1983 -659-062/717